3D Structural Controls of the Shear Zone Hosted Dugald River Zinc-Lead-Silver Deposit, Mount Isa Inlier, Australia

by

Pieter K. Creus

BSc. Hons, MSc (University of Stellenbosch)

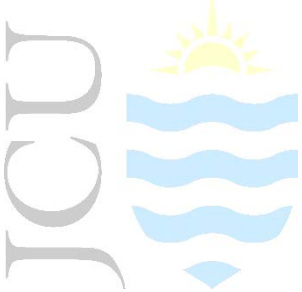

23 September 2022

For the degree of Doctor of Philosophy from the College of Science and Engineering, James Cook University

Statement of Access

I, the undersigned author of this thesis, understand that James Cook University will make this thesis available for use within the university library and allow access to other approved libraries after its submission. All users consulting this thesis will have to sign the following statement:

"In consulting this thesis, I agree not to copy or closely paraphrase it in whole or in part without the written consent of the author, and to make proper public written acknowledgement for any assistance that I have obtained from it".

Beyond this, I do not wish to place any restrictions on access to this thesis.

Pieter Koenraad Creus

23 September 2022

Declaration

I declare that this thesis is my work and has not been submitted in any form for another degree or diploma at any university or other institute of tertiary education. Information derived from the published or unpublished work of others has been acknowledged in the text and a list of references is given.

Pieter Koenraad Creus

23 September 2022

Acknowledgements

I want to thank my advisory panel: Dr. Ioan Sanislav, Prof. Paul Dirks and Dr. Brett Davis for their insights, editing and mentoring throughout the project.

Corey Jago from MMG is thanked for his numerous discussions about the geology of Dugald River. Dr. Nick Dyriw from Dugald River is thanked for reviewing the thesis and publications. The employees in mine technical services are also thanked for their support and discussions while undertaking field work. The two external reviewers are thanked for providing invaluable comments that improved the quality of the thesis.

MMG - Dugald River is thanked for providing logistical and financial support during my thesis. James Cook University is thanked for providing an International Postgraduate Research Scholarship. The Economic Geology Research Centre (EGRU), in particular Judy Botting, is thanked for logistical support. Seequent, Paradigm, Mira, Agisoft are thanked for providing academic licenses for software used in this thesis.

Finally, I wish to thank my family for their support during my thesis.

Statement of the Contribution of Others

Nature of Assistance	Contribution	Names	Affiliation
Intellectual Support	Proposal Writing	Prof. Paul Dirks Dr. Ioan Sanislav	James Cook University
	General Concepts and Ideas	Prof. Paul Dirks Dr. Ioan Sanislav	James Cook University
		Corey Jago	MMG
		Dr. Brett Davis	Ocina Gold
	Editorial and Writing Assistance	Prof. Paul Dirks Dr. Ioan Sanislav	James Cook University
		Corey Jago	MMG
		Dr. Nick Dyriw	
		Dr. Brett Davis	Ocina Gold
Financial Support	Tuition, Fees and Stipend	James Cook University – JCUPRS	
	Research Funds	MMG - Dugald River	
Data Collection	Drillcore Logging and Mapping	MMG Geologists	

Statement of the Contribution of Coauthors

Chapter	Paper	Authorship	Roles
2 To be submitted	The Dugald River type, shear zone hosted, Zn-Pb-Ag mineralization, Mount Isa Inlier, Australia	Creus, P. K. Sanislav, I. V. Dirks, P. H. G. M. Jago, C. J. Davis, B. K.	Major research concepts were developed by the authors. Creus conducted mapping and 3D modelling. Drafts were written by Creus and Sanislav, Dirks. Jago and Davis provided editorial reviews
3 To be submitted	3D geometry of the Dugald River Shear Zone: 3D modelling of a structurally complex, anastomosing shear zone	Creus, P. K. Sanislav, I. V. Dirks, P. H. G. M.	Major research concepts were developed by the authors. Creus conducted mapping and 3D modelling. Drafts were written by Creus and Sanislav. Dirks provided editorial reviews
4 Engineering Geology 10.1016/j.enggeo.2021.106314	Application of SfM-MVS for mining geology: Capture set-up and automated processing using the Dugald River Zn-Pb-Ag mine as a case study	Creus, P. K. Sanislav, I. V. Dirks, P. H. G. M.	Major research concepts were developed by the authors. Creus designed a procedure for capturing SfM-MVS and wrote the Python script to automate the processing. Sanislav and Dirks provided editorial reviews
5 Future Work	Visualisation and communication of geological data confidence in 3D geological modelling	Creus, P. K. Sanislav, I. V. Dirks, P. H. G. M.	Major research concepts were developed by the authors. Creus designed python scripts to process and visualise data confidence. Sanislav and Dirks provided editorial reviews

Table of Contents

List of Figures

Chapter 2: Structural Controls

Chapter 3: Shear Zone 3D Model

Chapter 4: Photogrammetry

Chapter 5: Data Confidence

List of Tables

Chapter 4: Photogrammetry

Chapter 5: Data Confidence

Thesis Abstract

The Dugald River deposit is situated in the globally significant base metal province, the Mount Isa Inlier. Previous studies at the mine, including the feasibility study to commence mining were done using surface-based drilling and mapping. Soon after reaching the ore body with underground development, it was realised that the structural complexity of the shear zone hosting the ore body was poorly understood and a decision was made to reduce the drill spacing to 15m along strike and 10m down dip. In addition, to ensure that development faces are mapped, they are captured as virtual outcrops using Structure-from-Motion Multiview Stereo. Thus, the result is dense data distribution, which allowed for a well-constrained 3D model to be constructed of the Dugald River Shear Zone. Furthermore, detailed mapping and observations of the ore body and shear zone relationship allowed for a structural paragenesis to be developed for the Dugald River deposit with regional implications on the genesis of Zn-Pb mineralisation during the Isan Orogeny of the Mount Isa Inlier.

The host rocks of the Dugald River deposit record several, successive deformation events of which we propose that the second to fourth (D_2 to D_4) were responsible for creating favourable dilational sites for mineralisation. Two phases of mineralisation are suggested with the first phase, Phase 1, occurring during D_2 and the second phase, Phase 2, occurring during D_4. While Phase 1 is a distinct mineralisation phase, we infer that the wallrock to sulphide ratio was high, thereby making this phase sub-economic. Phase 1 mineralisation records progressive deformation during D_2, which is associated with E-W directed shortening during the Isan Orogeny culminating in peak metamorphism and the regional N-S trending ductile fabric in the Mount Isa Inlier. At the Dugald River deposit, the regional fabric is expressed by progressive fold tightening (F_2) within the Dugald River Slates and the development of an associated axial planar slatey cleavage (S_2). The F_2 folds are E-verging, which is reflected in the dominantly W-dipping S_2 and localised east dips are inferred to be a result of co-planar D_4. During progressive fold tightening various secondary space accommodating mechanisms resulted in the development of quartz-carbonate veins of which flexural slip veins are the most striking. In addition to flexural slip veins, as folds continued to tighten during increasing D_2 strain, concurrent fold limb attenuation and hinge-zone thickening occurred.

Peak metamorphic conditions at Dugald River reached upper greenschist to lower amphibolite facies. Metamorphic/hydrothermal fluid produced during peak metamorphism is a probable transport mechanism for sulphide that replaced syn-tectonic quartz-carbonate veins and the frequency of quartz-carbonate veins increases with increasing fold tightening; hence sulphides were concentrated where folding was tightest. Quartz-carbonate veins congruently steepened with the folds, parallel to S_2 and at this high-angle to the sub-horizontal shortening, the veins were boudinaged with coalescing of veins and boudin necks. A noticeable D_2 strain gradient is observed in underground development moving from east to west and the coalescing of sulphide replaced quartz-carbonate veins within the areas of tight to isoclinal folds resembles a crackle breccia, which would have been future zones of high strain zone development that peaked during D_4. We infer that these areas resulted in a heterogeneous rock mass that was favourable sites for S_3 intensification during D_3, which in turn favoured early D_4 reactivation as low-angle thrusts and dilation for intense brecciation during the prevailing D_4 shear.

A period of orogenic collapse, between D_2 and D_4, is inferred by several authors in parts of the Mount Isa Inlier with an associated sub-horizontal fabric, herein referred to as D_3. A weak crenulation cleavage, S_3, with a consistent low to moderate southwest dip occurs throughout the deposit and is particularly noticeable where high concentrations of porphyroblasts occur in the limestone and the heterogeneous rock mass resulting from F_2 fold tightening and crackle breccia formation in the south of the mine provided favourable sites for zones of S_3 intensification. While the effects of D_3 are subtle within the Dugald River deposit, the fabric is generally a spaced crenulation cleavage. During early D_4, the continuation of bulk E-W directed sub-horizontal shortening resulted in reactivation of the zones of S_3 intensification as low-angle thrust arrays, which recorded top-to-the-NE sense of shear. Opposing shear along the stacked thrusts created areas of extension and contraction, which promoted the remobilisation of sulphides from areas of high mean rock stress (zones of contraction) to low mean rock stress (zones of dilation) and combined with synthetic shear along steeper, W-dipping S_0 and S_2 resulted in zones of concentrated sulphides.

The high grade Zn mineralisation that occurs at Dugald River is due to intense strain partitioning during D_4, which resulted in the development of the Dugald River Shear Zone as deformation transitioned from ductile to brittle-ductile. Mineralisation during D_4 is marked by a transition from coaxial to non-coaxial deformation and is recorded by the development of a transposed fabric and planar ore that is dominant in the steeper parts of the shear zone. Whereas the non-coaxial history is recorded by the development of breccia ore that is dominant in the lower angle parts of the shear zone. Transposition in the northern part of the deposit and towards the surface preserves the coaxial

deformation history during D_4 and developed high and low strain domains. The high strain domains are marked by the development of S_4 that transposed earlier fabric with rootless F_2 often observed.

The shift from coaxial to non-coaxial deformation is associated with the transition from ductile to brittle-ductile deformation, which we infer resulted in P-T conditions under which the sulphides could continue to deform through ductile mechanism versus the siliciclastic host rock that deformed through brittle mechanisms. This effect creates an interface with a pronounced competency contrast with the host rock and fractures developed in slate that was infilled by sulphides with clasts developing where fractures encircled the slate which was subsequently incorporated into the sulphide horizon. Through a process of kneading, milling and rotating the clasts were rounded. Furthermore, a strain rate incompatibility occurred between the thick ductile deforming sulphide horizon and the host slate, which resulted in the development of Riedel shear fractures. The first Riedel shear fractures to develop are R-shears with R'-shears developed within overlap zones of R-shears as displacement progressed. With increasing strain, P-shears developed and as the shear segments grew, they interconnected with R-shears to develop thoroughgoing Y-shears, eventually forming an anastomosing shear zone. The combination of a steeply developing Riedel shear zone with low-angle thrust arrays in the southern part of the deposit resulted in a pronounced flexure in the Dugald River Shear Zone with an average dip angle of ~45°, which is a highly favourable orientation for dilation. We suggest that the throughgoing Y-shears transported Zn-rich sulphides from depth and upon reaching the flexure ingressed into the progressively developing breccia horizon and further facilitating the thickening of the ore body.

The process of shear zone development and sulphide horizon thickening will have continued as the rock mass was exhumed until P-T conditions were no longer amenable to ductile deformation of the sulphides. This marks the transition from brittle-ductile to brittle deformation during D_5 and resulted in the reactivation of D_4 related shears and thrusts as well as the development of incohesive cataclastic and fault breccia rocks that create a poor rock mass quality in places. The poor rock mass quality is further compounded in areas where R- and P-shears developed into Y-shears as these areas underwent abrasion and adhesive wear to form cataclastic and fault breccia rocks as well as numerous small-scale shears. The poor rock mass can have negative implications for stope hangingwall stability.

A detailed structural analysis was conducted during this study and a high-resolution 3D model of the Dugald River Shear Zone was constructed. From the structural analysis and 3D model, a predictive model for mineralisation and areas of poor rock mass were derived. The eigenvalues from Bingham statistics of D_4 related shears provide an eigenvalue 1 of 23°-081° which can be used to orientate a slice view to guide the linking of structural data for shear zone construction and the statistics also provide an eigenvalue 3 of 40°-192° which is an important exploration vector as dilational zones within the shear zone will occur along that trend. Furthermore, areas of poor rock mass quality will also occur along the eigenvalue 3 and can assist in risk mitigation. Several Python scripts were developed during the study to assist in data visualisation and communication as well as a standalone executable that is integrated into Agisoft Metashape to automate the processing of Structure-from-Motion MultiView Stereo captures in underground mining.

Chapter 1

Introduction

Creus, P.K., Sanislav, I.V., Dirks, P.H.G.M.

The Dugald River deposit is situated in the Mount Isa Inlier, which is a globally significant base metal province and is the largest known repository of Zn in the world (Hutton et al, 2012). The deposit has been known since 1881 and has been the target of exploration since with ownership of the exploration licence changing several times. When MMG Ltd. took ownership, they proceeded to the feasibility study stage in 2008 and decided to commence underground operation in 2012 with the commercial pouring of Zn concentrate at the end of 2017. Thus, at the time of this study (starting in early 2019), the Dugald River mine was a newly exploited deposit with an annual production of Zn in Zn concentrate of 177 704 tonnes in 2020 (MMG, 2021).

1.1. Thesis Rationale and Objectives

Previous studies, including the feasibility study to commence mining was conducted using surface-based drilling and mapping. Shortly after reaching the ore body with underground development, the technical department at Dugald River mine realised that the structural framework of the shear zone and adjacent ore body was poorly understood and the mine was placed into care and maintenance while a technical risk mitigation study was conducted (Harris, 2015). A major result of the study was that the infill drill spacing was to be reduced to 15 m along strike and 10 m down-dip where the rock mass was deemed to be structurally complex after the primary drilling (spacing of 40 m along strike and 30 m down-dip). As a result, the drilling data is dense, which combined with virtual outcrops captured using Structure-from-Motion Multiview Stereo (SfM-MVS) results in a dataset that upon initial assessment is well-constrained.

While the decreased drill spacing and capturing of virtual outcrops resulted in increased confidence in the distribution of ore and identification of areas of reduced rock mass strength, excessive dilution of mined ore was still apparent. In simple terms, mining dilution is the incorporation of waste material within a mining block. Two major reasons are due to undercutting of stope hangingwall, or inadequate understanding of the geometry of an orebody within the mining block. Stope overbreak is simpler to quantify and can be done by comparing the stope void to the design shape of the stope, whereas geometrical issues with modelling of ore lenses are harder to quantify.

The overbreak of the stopes is clearly due to the proximity of ore lenses to the shear zone and often the shear zone truncates ore lenses. The Zn-Pb mineralisation at the Dugald River deposit is structurally controlled (e.g., Newbery et al., 1993; Xu, 1996), however before this study, a detailed high-level 3D structural analysis of the ore lenses had not been conducted. Thus, the primary focus of this thesis is the predictability of the 3D structural framework of the Dugald River Shear Zone and the ore lenses and can be grouped into two overarching research questions:

1. What is structural and mineral paragenesis and how does it affect the distribution of the ore lenses?
    a. Guides mine-scale exploration vectoring.
    b. Provides valuable insight into shear zone hosted mineralisation.

2. What is the 3D geometry of the shear zone?
    a. Helps in mine design as the ore body has a close spatial relationship to the shear zone.
    b. Dense drilling data provides a unique opportunity for high-resolution 3D modelling of a shear zone.

In essence, this is a 4D problem as the 3D fabric at a given point in time needs to be understood and how the fabric will respond to subsequent deformation. The significance of the thesis can be presented in two categories: 1) deposit scale; 2) regional scale.

1.2. Significance and Implications

To understand and predict the 3D geometry of the shear zone and the ore lenses a detailed structural analysis was undertaken to develop a structural paragenesis for the deposit and subsequently a genetic model for the mineralisation. The structural complexity of the shear zone in particular requires a non-conventional approach to structural logging of drillcore, and the dense drilling combined with the frequent capturing of the development headings with SfM-MVS resulted in a dense dataset. A high-resolution 3D model was generated and the methodology for generating the 3D model is included in this thesis. Further to the dense data is that the visualisation of the data can be cumbersome, especially when presenting 3D models to stakeholders and in this thesis, Python scripts were developed to assist in visualising and communicating 3D models and their underlying data.

1.2.1. Deposit Scale

During this study, several novel, applied methods were developed that can be readily incorporated into active mining operations. As part of the 3D modelling process, the SfM-MVS captures provided by Dugald River were digitally mapped to include smaller-scale structures that were not mapped by the mine geologists. However, the quality of the images used to generate the virtual outcrops was variable and upon investigation could be improved, which was the motivation for developing a new method for automated processing of SfM-MVS in underground mine geology, and the methodology can be extended to engineering geology and civil engineering (tunnels) solutions.

The dense data produced at the Dugald River mine can be cumbersome to view, which is a problem that is perpetuated when presenting 3D models and their underlying data to persons that do not have an intimate knowledge of the data. Several Python scripts and methods were developed that can be used to assist in communicating data and 3D models to non-geologists in particular.

A high-resolution 3D model was constructed to assist in understanding the 3D geometry of the shear zone. How 3D models are constructed in the mining industry is rarely published, particularly for complex shear zones.

1.2.2. Regional scale

The detailed structural analysis and paragenesis have regional significance as we describe how successive deformation events lead to forming of economic grade mineralisation. A new genetic model for Zn-Pb mineralisation in the Mount Isa Inlier was identified, which is based on sulphide remobilisation and enrichment during successive deformation events. For the Mount Isa Inlier this has implications for base metal exploration in the Eastern Fold Belt, which has fewer known Zn-Pb occurrences compared to the Western Fold Belt, and globally it adds to the understanding of shear zone hosted base metal mineralisation.

1.3. Thesis Structure

A thesis by publication was chosen as the thesis format with the structure following the guidelines of the Graduate Research School of James Cook University. At the time of thesis submission for review, Chapter 4 was published and covers the application of SfM-MVS in mining geology. Minor formatting changes were made to Chapter 4 to make it consistent with the rest of the chapters. Chapters 2 and 3 are the core data chapters for the thesis and are closely linked, with Chapter 2 covering the structural controls on the mineralisation during successive deformation events and Chapter 3 detailing the 3D modelling and shear zone development. Both chapters are formatted for publication and to be submitted for peer-review in appropriate journals, therefore, there is some repetition in the chapters, particularly in the regional and deposit geology sections.

The final data chapter, Chapter 5, details Python scripts developed during this thesis. The Python scripts and the methods described in the chapter can be considered future work as the scripts, in particular, could benefit from additional case studies to refine the scripts and methods. Chapter 6 is the concluding chapter of the thesis and integrates the main conclusions from the core chapters (Chapters 2 and 3).

At the time of the thesis submission, the Dugald River mine was an active mine. Thus, for confidentiality reasons the 3D model constructed as part of the study and the underlying data could not be included. Several samples were collected for thin section and analytical work, however, the results were inconclusive and a more in-depth study is suggested that can be done within the time frame and scope for this study. The sample locations and descriptions are included in Appendix A. The Python scripts in Chapter 5 are included as supplementary data in Appendix B. Note, that the Python script and additional supplementary data generated for Chapter 4 can be downloaded from the repository of Engineering Geology.

1.4. References

Harris, P. (2015). Dugald River case study - the importance of understanding your orebody and designing your mine for maximum value. In: Polvin, Y. (Ed.), Underground design methods. Australian Centre for Geomechanics, Perth. 21 - 36. doi:10.36487/ACG_rep/1511_0.2_Harris

Hutton, L., J., Denaro, T., J., Dhnaram, C. & Derrick, G., M. (2012). Mineral systems in the Mount Isa Inlier. Episodes 35(1). 120 - 130. https://doi.org/10.18814/epiiugs/2012/v35i1/011

MMG (2021). MMG Limited Annual Report 2020. 190pp

Newbery, S.P., Carswell, J.T., Allnutt, S.L. & Mutton, A.J. (1993). The Dugald River zinc-lead-silver deposit; an example of a tectonised Proterozoic stratabound sulphide deposit, in: International Symposium - World Zinc '93. Hobart, pp. 7–21.

Xu, G. (1996). Structural geology of the Dugald River Zn-Pb-Ag deposit, Mount Isa Inlier, Australia. Ore Geology Reviews, 11(6), 339–361. https://doi.org/10.1016/S0169-1368(96)00007-8

Chapter 2

The Dugald River-type, shear zone hosted, Zn-Pb-Ag mineralisation, Mount Isa Inlier, Australia

Creus, P.K., Sanislav, I.V., Dirks, P.H.G.M., Jago, C. M. and Davis, B. K.,

Keywords: Mount Isa Inlier, Shear Zone Hosted Mineralisation, Durchbewegung, Epigenetic Breccia Ore, Zn-Pb-Ag Mineralisation

2.1. Abstract

The Dugald River Zn-Pb-Ag mine is situated in the Mount Isa Inlier, a globally significant base metal province. Zn-Pb deposits in the Mount Isa Inlier are stratabound with four main genetic models, including SEDEX-style, remobilised SEDEX, epigenetic and Broken Hill-type mineralisation applied to interpret their formation. We propose that the Zn-Pb-Ag mineralisation at Dugald River represents a unique, shear zone hosted deposit type that formed through a series of successive deformation events during the Paleoproterozoic Isan Orogeny that concentrated the mineralisation within the Dugald River Shear Zone during two main mineralising phases. The first phase of mineralisation occurred during regional D_2 shortening, which is associated with the formation of large-scale F_2 folds and a regionally penetrative S_2 fabric. During this phase, progressive tightening of upright F_2 folds resulted in several sets of secondary space accommodating quartz-carbonate veins that were progressively rotated into parallelism with the pervasive, steep, W-dipping S_2 cleavage. The quartz-carbonate veins were coevally replaced by sulphides, which migrated to extensional sites (boudin necks and fold hinges) in tight folds thus creating a sulphide-rich horizon within a developing high strain zone, which during D_4 developed into the Dugald River Shear Zone. The second phase of mineralisation occurred during the regional D_4 transpressional deformation event and resulted in significant mineralisation enrichment and the current geometry of the ore bodies. The significant enrichment of the mineralisation during D_4 resulted from further fold tightening within the high strain zone, which resulted in the attenuation and dismembering of folds and produced a transposed fabric (S_4). The sulphide veins were transposed into parallelism with S_4 forming sulphide-rich planar ore textures. Strain partitioning at the contact between the ductile deforming sulphide horizon and the brittle deforming slates resulted in the development of an anastomosing shear zone, known as the Dugald River Shear Zone. A right-handed releasing bend in the shear zone produced a dilational jog and a thick, high-grade ore body. The mobilisation of sulphides within the dilational jog involved fragmentation of sulphides and wall rock, brecciation, rotation of fragments, rolling and the formation of durchbewegung texture.

2.2. Introduction

The Mount Isa Inlier, located in NW Queensland, is a globally significant base metal province (Fig. 2.1). World-class Zn-Pb deposits (Fig. 2.1c) include the Mt Isa deposit (e.g., Smith et al., 1978; Gulson et al., 1983; McGoldrick and Keays, 1990; Perkins, 1997; Davis, 2004; Cave et al., 2020), the Cannington deposit (e.g., Bodon, 1998, 2002; Roache et al., 2004; Walters and Bailey, 1998), the George Fisher and Hilton deposits (Valenta, 1994a, 1994b; Perkins and Bell, 1998; Chapman, 2004; Murphy, 2004; Cave et al., 2020) and the Dugald River deposit (Newbery et al., 1993; Xu, 1996; 1997; 1998a; 1998b; this chapter). The Zn-Pb mineralisation style extends further north to the McArthur Basin to include Century, McArthur River (HYC) and Teena deposits (Broadbent et al., 1998; Feltrin et al., 2009; O'Rourke et al., 2017; Sheldon et al., 2021). Together these deposits form the largest Zn-Pb province in the world (Huston et al., 2006).

Although the deposits display similarities in primary metal content (Zn-Pb), ore mineralogy (namely sphalerite and galena) and host rock type (mainly siliciclastic metasediments), the structural and metamorphic settings are variable. As a result, genetic models for the deposits vary as well. For example, in the Mount Isa town region in the west, the metamorphic grade of host lithologies varies from sub-greenschist facies in the George Fisher and Hilton deposits (see Rieger et al., 2021) to upper amphibolite facies in the Cannington deposit (see Chapman and Williams, 1998), thus the metamorphic grade increases from northwest to southeast (Fig. 2.2). Four genetic models for the Zn-Pb deposits have been proposed: 1) syngenetic-SEDEX style mineralisation (e.g., Smith et al., 1978; Large et al., 2005); 2) remobilised SEDEX style mineralisation (e.g., Finlow-Bates and Stumpfl, 1979; McGoldrick and Keays, 1990); 3) epigenetic mineralisation (e.g., Xu, 1996; Davis, 2004) and 4) Broken Hill type mineralisation (Walters and Bailey, 1998). It should be noted that all Zn-Pb deposits of the Mount Isa Inlier are stratabound, although the mineralisation can be discordant.

A syngenetic origin for some of the deposits (e.g. Mt Isa, George Fisher and Hilton) is supported by the preservation of syn-sedimentary textures. Fine-grained sphalerite and galena occur in thin laminae and bands parallel with the sedimentary layering as well as the preservation of textures suggesting intergrowth of sphalerite and galena with framboidal pyrite (e.g., Cave et al., 2020; Rieger et al., 2021). Although late metasomatic and metamorphic overprints affected these deposits, early syn-sedimentary textures are locally preserved. Conversely, the Cannington deposit underwent high-grade metamorphism and intense metasomatism, making the identification of syn-sedimentary textures nearly impossible (e.g., Chapman and Williams, 1998; Walters and Bailey, 1998) and thus being in general classified as Broken Hill-type mineralisation (Walters and Bailey, 1998).

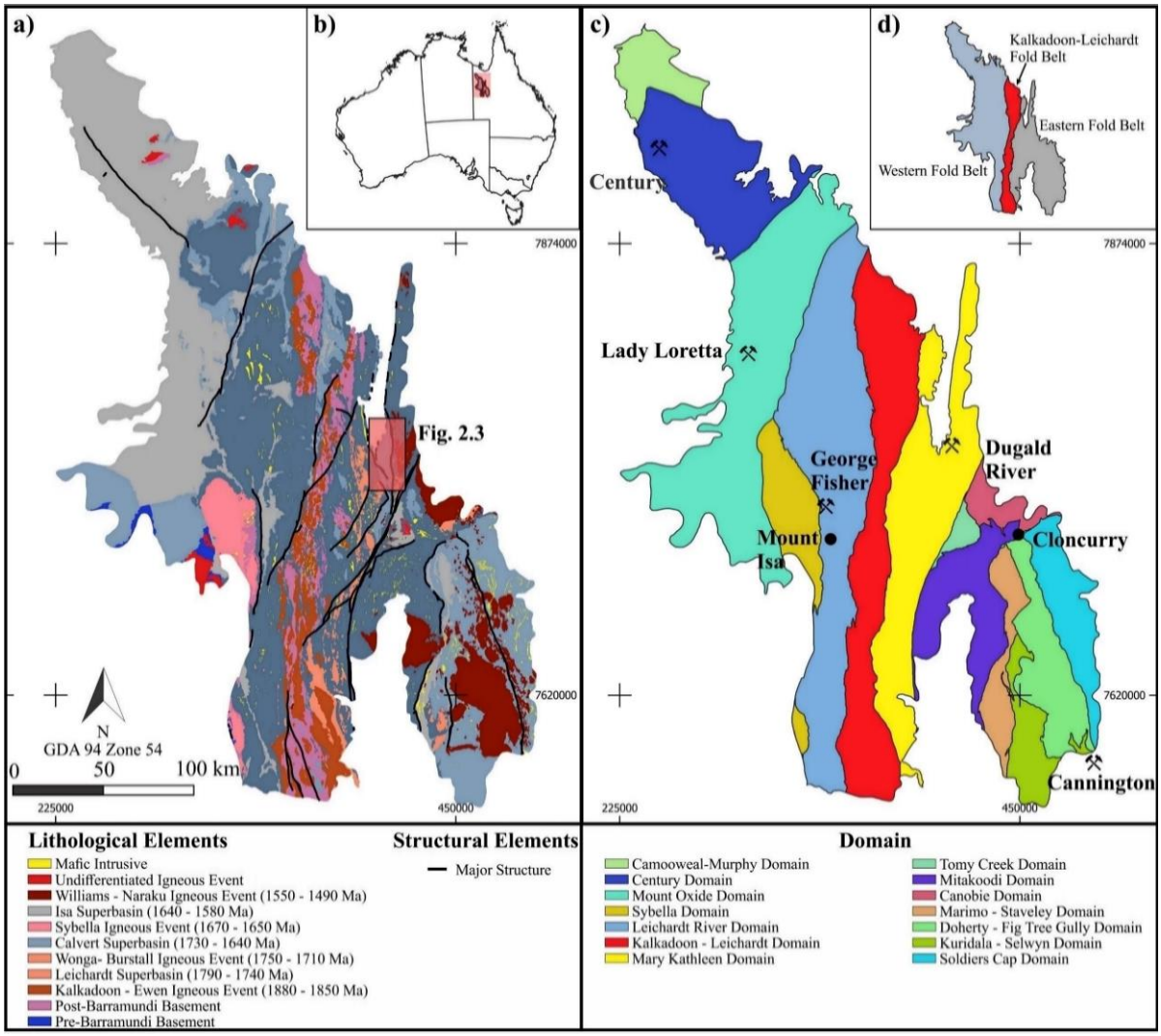

Fig. 2.1: a) Volcano-sedimentary and igneous rocks of the Mount Isa Inlier, NW Queensland, Australia (b) clipped to the outcrop pattern of the Mount Isa Inlier. c) The Mount Isa Inlier is sub-divided into sixteen domains (fourteen shown here) and is usually presented in a simplified format and grouped into three fold belts, namely, the Western and Eastern Fold Belts, which are separated by the Kalkadoon-Leichardt Fold Belt (d). d) Historical grouping of the Mount Isa Inlier modified after Blake (1987).

In this chapter, we discuss the structural controls that lead to the formation of the Dugald River deposit. The deposit represents an ideal case study for metamorphosed Zn-Pb mineralisation as it can be considered an intermediate between weakly metamorphosed end members such as the George Fisher deposit (sub-greenschist facies) and intensely metamorphosed end members such as the Cannington deposit (upper amphibolite facies) and may represent a new type of Zn-Pb mineralisation in the Mount Isa Inlier. Although the mineralisation is almost entirely hosted by a complex shear zone and the metamorphic grade reached amphibolite facies, the host rocks still preserve evidence of syn-sedimentary textures (*viz.* bedding and stratigraphy) and the structural evolution of the deposit can be reconstructed. The genetic model presented in this chapter not only has implications for understanding the genesis of Zn-Pb mineralisation in metamorphic terranes but also for shear zone hosted Zn-Pb deposits in general.

2.3. Regional Geology

The Dugald River Zn-Pb-Ag mine is hosted by Late Paleoproterozoic rocks of the Mount Isa Inlier in NW Queensland, Australia. The Mount Isa Inlier consists of a succession of volcano-sedimentary and intrusive rocks formed during a series of successive basin and orogenic events between ~1900 – 1500 Ma (see Blake, 1987; Blake and Stewart, 1992; Foster and Austin, 2008; Gibson et al., 2016). Three superbasin events are recognised that are separated by regional unconformities (Fig. 2.1a; Betts et al., 2006; Gibson et al., 2016): 1) Leichardt Superbasin (1790 – 1740 Ma); 2) Calvert Superbasin (1730 - 1640 Ma); and 3) Isa Superbasin (1640 – 1580 Ma) that were deposited over the basement Leichardt Metamorphics, which have a formation age of between 1900 – 1850 Ma. The superbasins are vertically stacked and inferred to have formed during ≥ 1840 Ma continental rifting (Betts et al., 2006, 2008; Gibson et al., 2008, 2012, 2016) within which the depositional environment changed from fluviatile-lacustrine to open marine (Jackson et al., 2000; Southgate et al., 2000).

Three major orogenic events have affected the Mount Isa Inlier, the 1880 – 1850 Ma Barramundi Orogeny, the 1750-1710 Ma Wonga Orogeny and the 1650 – 1490 Ma Isan Orogeny (see Blake, 1987; Blake and Stewart, 1992; Foster and Austin, 2008; Abu Sharib and Sanislav, 2013; Spence et al., 2021, 2022). The Barramundi and Wonga Orogenies have only affected the basement and the older sedimentary units whereas the Isan Orogeny has affected the entire Mount Isa Inlier. Recent studies have indicated that parts of the Mount Isa Inlier were also affected by shortening events and associated magmatism between 1800 – 1770 Ma (Le et al., 2021a, 2021b).

Four main periods of plutonism occurred in the Mount Isa Inlier. The plutons were emplaced along N-S trending linear belts with the first period between 1880 – 1850 Ma resulting in the

emplacement of the Kalkadoon and Ewen Batholiths (Page, 1983; Page and Williams, 1988; Bierlein et al., 2011). The second period occurred between 1750 – 1710 Ma and coincided with the emplacement of the Wonga and Burstall plutons (Neumann et al., 2009; Spence et al., 2021; 2022). The third period occurred between 1670 – 1650 Ma and coincided with the emplacement of the Sybella Batholith (Page and Bell, 1985; Connors and Page, 1995) and the fourth period occurred between 1550 – 1490 Ma with the emplacement of the Williams-Naraku Batholiths (Page and Sun, 1998; Wyborn, 2007).

The Mount Isa Inlier is sub-divided into a series of sixteen N-S trending geological domains (Fig. 2.1c; Wellman and Dooley, 1992; Withnall and Hutton, 2013), based on differences in basin sequences, metamorphism, structural and intrusive history. The domains are generally bounded by crustal-scale faults and shears. The Dugald River deposit is situated within the Mary Kathleen Domain (yellow domain in Fig. 2.1c) and the geology is dominated by sedimentary sequences deposited during the evolution of the Leichhardt Superbasin (Gibson et al., 2016) and intruded by the Wonga and Burstall plutons between 1750 – 1710 Ma (Neumann et al., 2009; Spence et al., 2021). A series of younger sedimentary sequences unconformably overlie the Leichhardt Superbasin sedimentary rocks in the north of the domain and are collectively assigned to the Mount Albert Group (Derrick et al., 1977), which is part of the Calvert Superbasin (Gibson et al., 2016).

Five main deformation events have been recognised in the Mount Isa Inlier and allocated to the Isan Orogeny. The first event, D_1, occurred during N-S shortening and produced E-W trending regional folds and thrusts (Bell, 1983; Bell et al., 1992; Page and Bell, 1986; Blake and Stewart, 1992; Abu Sharib and Sanislav, 2013). The second event, D_2, occurred during E-W shortening and produced the main N-S trending folds, shear zones and thrusts that define the dominant structural grain of the Isan Orogeny (e.g., Bell et al., 1992; Giles et al., 2006; Abu Sharib and Bell, 2011; Abu Sharib and Sanislav, 2013). The third event, D_3, has been described as an orogenic collapse phase that crenulated D_2 fabrics and produced a sub-horizontal cleavage (e.g., Bell and Hickey, 1998; Davidson et al., 2002) that was later overprinted, during the fourth deformation event, D_4, by a new N-S trending cleavage. D_4 occurred during renewed E-W shortening, but with a pronounced transpressive character marked by a transition from ductile to brittle-ductile deformation (O'Dea et al., 1997; Bell and Hickey, 1998; Spampinato et al., 2015). The last major deformation event, D_5, occurred during ESE-WNW shortening and resulted in brittle reactivation of major structures and the development of an open-to-close crenulation cleavage in higher-grade rocks.

Multiple metamorphic events have been recognised as part of the Isan Orogeny (e.g., O'Dea et al., 1997; Rubenach et al., 2008; Sayab, 2009; Abu Sharib and Sanislav, 2013), that are characterised

by low-pressure/high-temperature metamorphic assemblages (Connors et al., 1992; Foster and Rubenach, 2006). According to Abu Sharib and Sanislav (2013), high geothermal gradients (see Rubenach and Lewthwaite, 2002; Rubenach et al., 2008) are associated with the emplacement of magmatic bodies provided enough heat for metamorphism during successive phases of the Isan Orogeny. They suggested that the M_1 metamorphic event during D_1 was low-pressure and high-temperature metamorphism accompanied by a period of NE-SW bulk shortening during the early stages of the Isan Orogeny.

Peak metamorphic conditions reached upper amphibolite facies in the Eastern Fold Belt (Loosveld and Schreurs, 1987; Foster and Rubenach, 2006), during the later stages of the E-W shortening during D_2 (O'Dea et al., 1997), and possibly early into the D_3 (Stewart and Blake, 1992; Rubenach and Lewthwaite, 2002). Low-pressure and high-temperature clockwise P-T paths have been suggested for the M_2 metamorphic event during D_2 by numerous authors (e.g., Oliver et al., 1991; Reinhardt, 1992; Rubenach et al., 2008; Sayab, 2009; Abu Sharib and Sanislav, 2013). Foster and Rubenach (2006) provide a summary table of thermobarometric studies for select locations in the Mount Isa Inlier from which they suggest that the highest-grade zones are between 4 – 5 kbar and > 650 °C. Furthermore, they found that in an E-W transect through the Mount Isa Inlier, metamorphic grade varies from lower greenschist to upper amphibolite facies and that the overall pattern of metamorphism is a series of N-S orientated amphibolite facies belts separated by greenschist facies belts (Fig. 2.2). Further north of Mount Isa, lower greenschist are suggested (Gibson and Hitchman, 2005; Nortje et al., 2011) and substantiated by lower greenschist for the Century deposit and unmetamorphosed for HYC in the MacArthur Basin to the northwest of the Mount Isa Inlier.

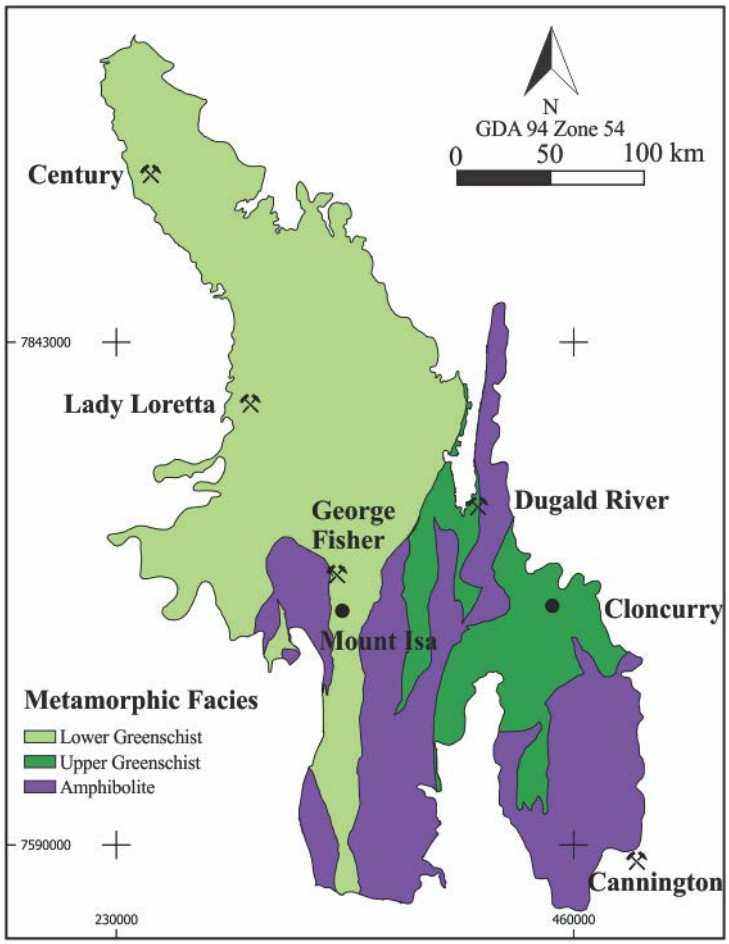

Fig 2.2: Metamorphic facies map of the Mount Isa Inlier modified from Foster and Rubenach (2006).

2.4. Dugald River Deposit

The Dugald River deposit outcrops as a Zn-Pb-Fe-Mn gossan and was first discovered in 1881 and became a drill target since 1948 (Connor et al., 1982; Xu, 1998b). Ownership of the exploration license for the deposit has changed several times and in 2009 MMG Ltd. undertook a feasibility study to commence mining. Underground development commenced in 2012 and production of Zn concentrate in 2017 with the 2020 resource stated at 66Mt with 11.7% Zn, 1.3% Pb and 26 g/t Ag (MMG, 2021). The deposit is wholly underground and accessed via two declines: one accessing the northern extent of the deposit ("North Mine") and the second, the southern extent of the deposit ("South Mine").

2.4.1. Lithostratigraphy

The Dugald River deposit is situated within the Mount Roseby Corridor (Fig. 2.3; Newbery et al., 1993). The Mount Roseby Corridor is a narrow, N-S trending zone of high strain rocks of the Mount Albert Group and bounded by major faults, the Mount Roseby Fault to the east, the Coolullah Fault to the west, and the Pinnacle Fault to the southwest.

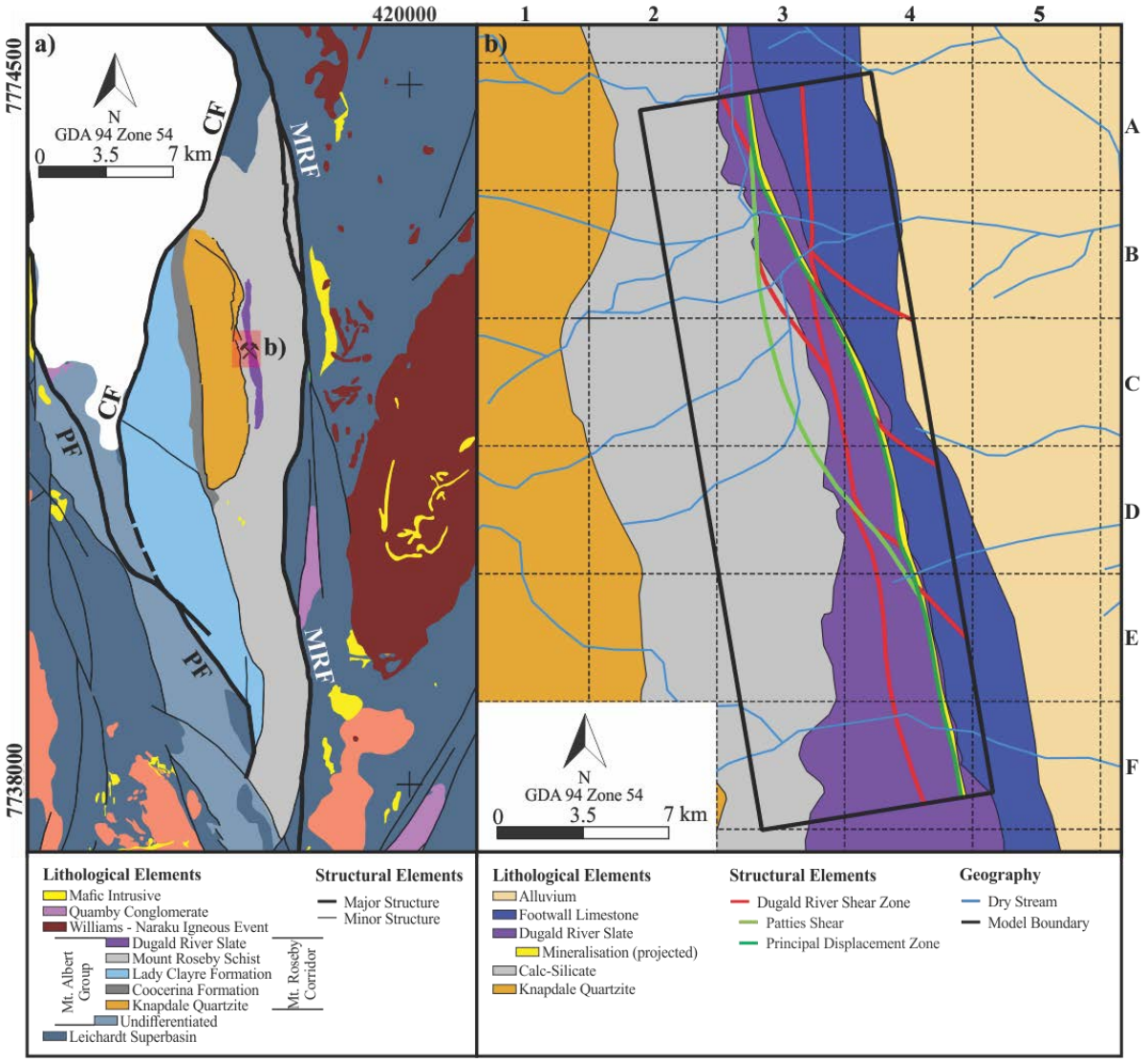

Fig. 2.3: a) The Mount Roseby Corridor is an N-S trending high strain corridor of Mount Albert Group rocks, bounded to the east by the Mount Roseby Fault (MRF), the west by the Coolulah Fault (CF) and the southwest by the Pinnacle Fault (PF). b) Simplified geological map of the Dugald River deposit. The black outline is the 3D model boundary and envelopes the majority of the available data. The geological map has a local grid system used as a reference in this chapter. Note, that the Patties Shear and principal displacement zone form part of the Dugald River Shear Zone.

The Mount Albert Group in the Mount Roseby Corridor has been subdivided into 4 main units: the Knapdale Quartzite, Lady Clayre Dolomite, Coocerina Formation, and the Mount Roseby Schist (Fig.

2.3a). The Mount Roseby Schist is a time equivalent of the Coocerina Formation and Lady Clayre Dolomite (Withnall and Hutton, 2013). The Knapdale Quartzite is interpreted to represent the oldest unit, flanked by the Mount Roseby Schist to the east and by the Coocerine Formation and Lady Clayre Dolomite to the west. The Dugald River deposit is hosted by the Dugald River Shale, which is a member of the Mount Roseby Schist Formation (ASUD, 2021). However, the Mount Roseby Schist has been metamorphosed to amphibolite facies and the Dugald River Shale has a prevalent slatey cleavage and will be referred to as the Dugald River Slate in this chapter (also see Connor et al., 1982; Newbery et al., 1993; Xu, 1996).

The Mount Roseby Schist within the mine volume of interest (Fig. 2.3b) is subdivided into four main units (also see Connor et al., 1982; Newbery et al., 1993; Xu, 1996). From oldest to youngest these are: 1) Knapdale Quartzite; 2) a calc-silicate unit; 3) the Dugald River Slate and 4) the Footwall Limestone. Note, the Footwall Limestone is a mining term as it occurs along the footwall of the lode, but it is stratigraphically younger than the Dugald River Slate that hosts the mineralisation. Minor lithological units found near the deposit include a mafic feldspar porphyry dyke and muscovite schists (Spelbrink and George, 2017).

The calc-silicate unit comprises two main varieties, biotite-garnet-scapolite schist and a carbonate-rich banded biotite-scapolite schist (Spelbrink and George, 2017). The scapolite and garnet form porphyroblasts observable in the hand sample. Under the petrographic microscope, they preserve a well-developed internal foliation defined by inclusion trails of unknown composition (Davis, 2017). The transition from calc-silicate to the Dugald River Slate is marked by high strain zone and consists of medium- to coarse-grained, banded biotite-epidote schist pods that have a strong schistosity. Within the high strain zone, lenses of a weakly deformed mafic feldspar porphyry dyke are common and the geometry of these lenses and the localisation of intense deformation along their margins suggest that the mafic dyke was boudinaged during shearing.

The Dugald River Slate is massive and fine-grained with a dark grey to black appearance depending on the graphite content. The slate has a spotted appearance in places due to scapolite porphyroblasts (Williams, 2017), which tend to have strain shadows (Fig. 2.4) with variable concentrations of carbonate, quartz, and sulphides. The scapolite porphyroblasts within the Dugald River Slate are aligned parallel to the main foliation. The muscovite schist forms discrete lenses within the Dugald River Slate that are inferred to be structurally controlled and display a strong anastomosing fabric (Spelbrink and George, 2017) and red garnet porphyroblasts are common.

The limestone occurs to the east of the lode. It is light to dark grey, with flattened sulphide streaks defining a trend similar to the main foliation (Newbery et al., 1993; Xu, 1996) and fine-grained, wispy discontinuous white carbonate veinlets (Spelbrink and George, 2017) defining an S_3 spaced cleavage. Bedding is preserved within the limestone and is defined by dark grey, massive dolomitic layers intercalated with mica, quartz and K-feldspar rich layers. Scapolite porphyroblasts are common and contain strain shadows which are aligned sub-parallel to the main fabric.

2.4.2. Deformational History

The Mount Roseby Schist at Dugald River has been subjected to up to five deformational events. Structures produced during the first deformation event, D_1, have largely been overprinted by E-W directed, co-planar shortening during D_2 and D_4. The first three deformational events are inferred to be ductile, followed by brittle-ductile deformation during D_4, and D_5 which represents a period of brittle reactivation of mainly D_4 structures. Recognising primary textures and features in the underground workings (including drill intersections) is difficult not only due to the dark colour of the rock but mainly due to the intense deformation which has obliterated earlier tectonic fabric, including those produced during D_1.

2.4.2.1. D_1 structures

The earliest deformation event, D_1, recognised at the Dugald River deposit is defined by a series of E-W trending folds (F_1) and associated axial planar cleavage (S_1) which resulted from N-S directed shortening (Xu, 1996). Broad F_1 folds are observed to the south of the deposit where they occur as metre-scale folds refolded during D_2 along N-S trending axes in Type 1 interference pattern and F_1 are exposed 10 km south of the Dugald River deposit (see Xu, 1996; GDA94 coordinates: 410098, 7752960). S_1 is preserved as inclusion trails in D_2 related porphyroblasts (Fig. 2.4c).

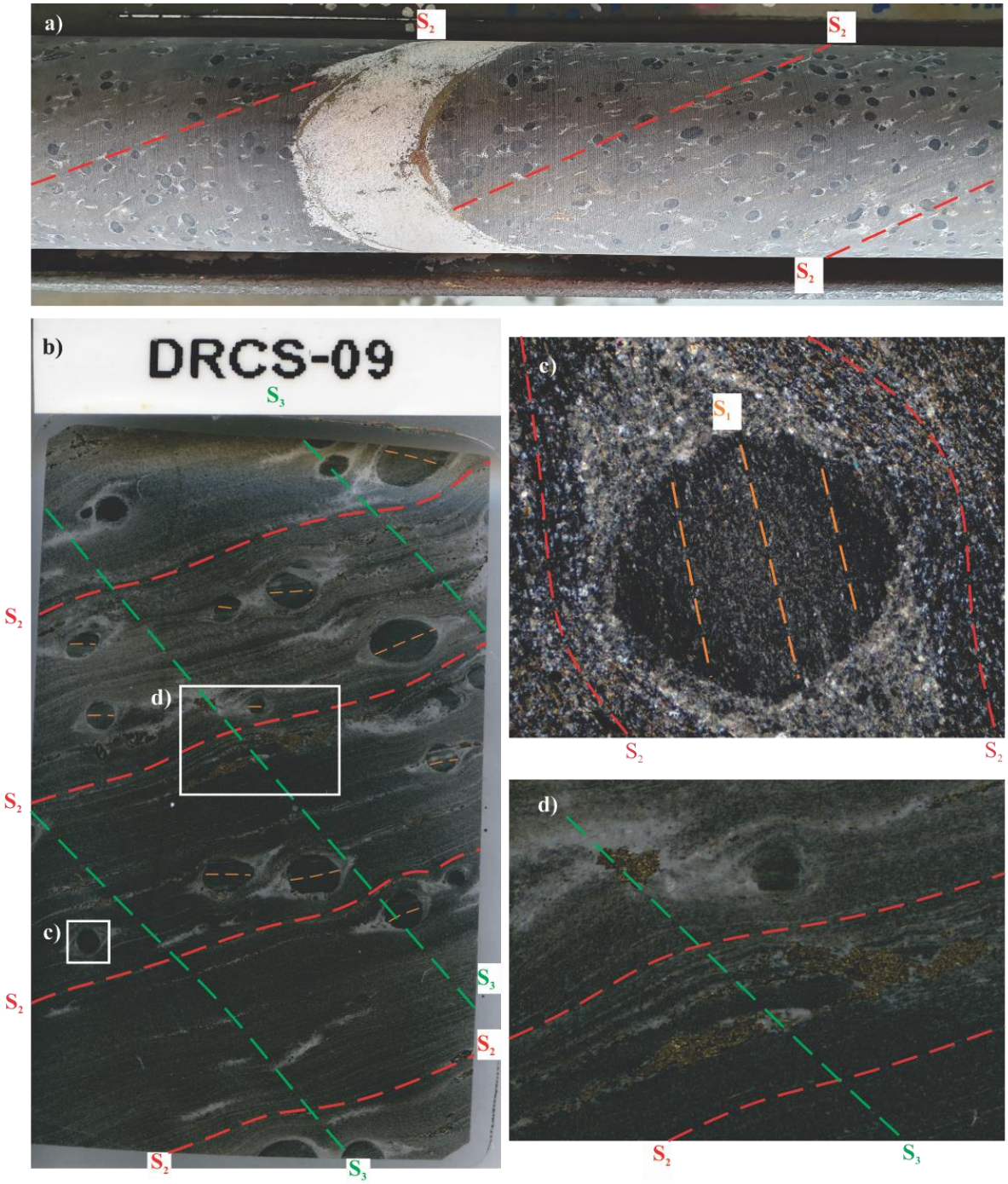

Fig. 2.4: Low-angle truncation of S_1 (orange dashed lines) preserved in syn-D_2 porphyroblasts (dark spots). a) Drillcore (DU2639 - 112.04 m; grid reference 4D) in black slate. Porphyroblasts are aligned parallel to S_2 (red dashed lines) and provide an easily recognisable texture for measuring S_2. Porphroblasts typically have carbonate-rich strain shadows that are commonly partially replaced by sulphides (typically pyrrhotite). b) High-resolution scan of a polished thin section of (a). In areas of dense porphyroblast development, a crenulation cleavage has developed (S_3; green dashed lines) and has a consistent SW-dip. Porphyroblasts are gently rotated, resulting in S_1 occurring at a low angle to S_2, which itself in this section has formed a composite S_0/S_2 fabric. c) Cross-polarised photomicrograph of the white box in (b) showing low-angle truncation of S_1 inclusion trails by matrix S_2. Reaction rims indicated by strain caps and shadows have increased carbonate alteration. b) Layer-parallel boudinage with pyrrhotite infill in boudin necks.

The interaction between D_1 and D_2 is preserved in low-strain domains. A good example is in the north of the mine (North Mine), observable over multiple levels. Here, a large-scale F_1 fold of unknown amplitude is preserved, which is refolded by an F_2 fold. Axial planar S_2, together with bedding and an orthogonal, N-facing joint set create rhomboid blocks (Fig. 2.5). Bedding-parallel slip has occurred along the bedding planes showing E-plunges, suggesting slip during E-W directed D_2 compression.

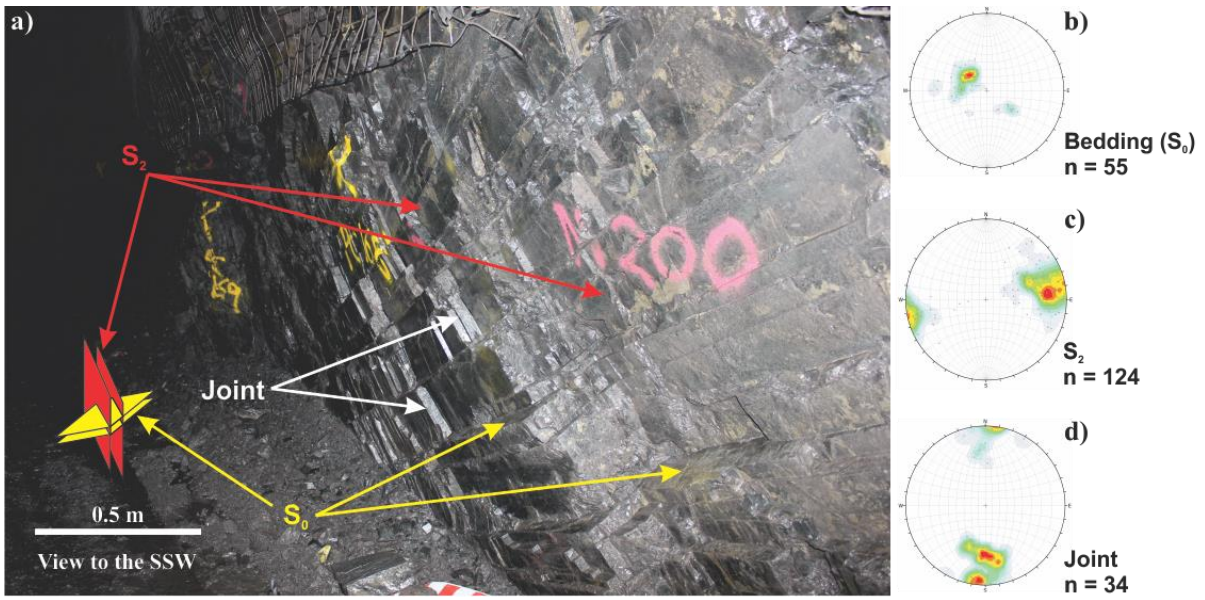

Fig. 2.5: a) Part of a large amplitude F_1 and F_2 Type 1 interference fold preserved in a low strain domain in the North Mine (grid reference 3B). Here, over successive levels, the interaction of three prominent planes results in the development of rhomboid blocks. Photo was taken in the approximate position of the main shear zone. b, c, d) Equal angle, lower hemisphere stereoplots of S_0 (b), S_2 (c) and joint (d) from levels N125 – N220 (125 – 220 m below surface). S_0 has a consistent southeast dip and small-scale low-angle thrusts are developed within the beds and propagate between them. Steep, S_2 undulates with dominant west dips and is marked by thin, sulphide veins, which combined with the chlorite alteration, causes slabbing along the S_2 planes. The joint set has a general north dip and occurs orthogonal to the bedding.

2.4.2.2. D_2 structures

The dominant structural element at Dugald River and the surrounding area consists of a well-developed N-S trending fabric attributed to the regional E-W directed shortening D_2 (Newberry et al., 1993, Xu, 1996). D_2 consists of regional to mesoscale, close to isoclinal, N-S trending folds (F_2) and a well-developed axial planar cleavage (S_2). The folding pattern in the Dugald River area has been disrupted during D_4 by the formation of high- and low-strain domains. Macroscale F_2 folds are well exposed on the surface to the north of the deposit as a series of synform-antiform pairs of tight to isoclinal folds preserved in a D_4 low strain domain (GDA94 coordinates: 411504, 7762204; Fig 3.3 in Chapter 3). Within D_4 higher strain domains, F_2 tends to be isoclinal, with synform-antiform pairs disrupted and rootless folds common.

In the northern part of the deposit, F_2 occur as tight isoclinal folds with steep axial planes and north plunges. In the southern part of the deposit, F_2 geometries are more complex with inclined, non-cylindrical folds varying between close to isoclinal (Fig. 2.6) and having variable plunges towards the north and south.

Associated with the F_2 folds are a series of quartz-carbonate veins that formed through various secondary space accommodating mechanisms during progressive fold tightening (Fig. 2.6). Tightening of folds is associated with hinge-zone thickening and concurrent limb attenuation. Some veins occur as crosscutting structures along fold limbs and developed in the more competent lithological layers, such as silicified slate beds (Fig. 2.6b), or as en-echelon veins within beds. Flexural slip along bedding planes in folds has resulted in thin, strike extensive layer-parallel veins (Fig. 2.6b - c, e - f) and in some isoclinal folds a series of steep, conjugate, and axial planar orthogonal veins formed as well as sub-horizontal quartz-carbonate veins (Fig. 2.6d), indicating that principal and intermediate stretching axes are similar ($X \approx Y >> Z$, i.e., prolate strain).

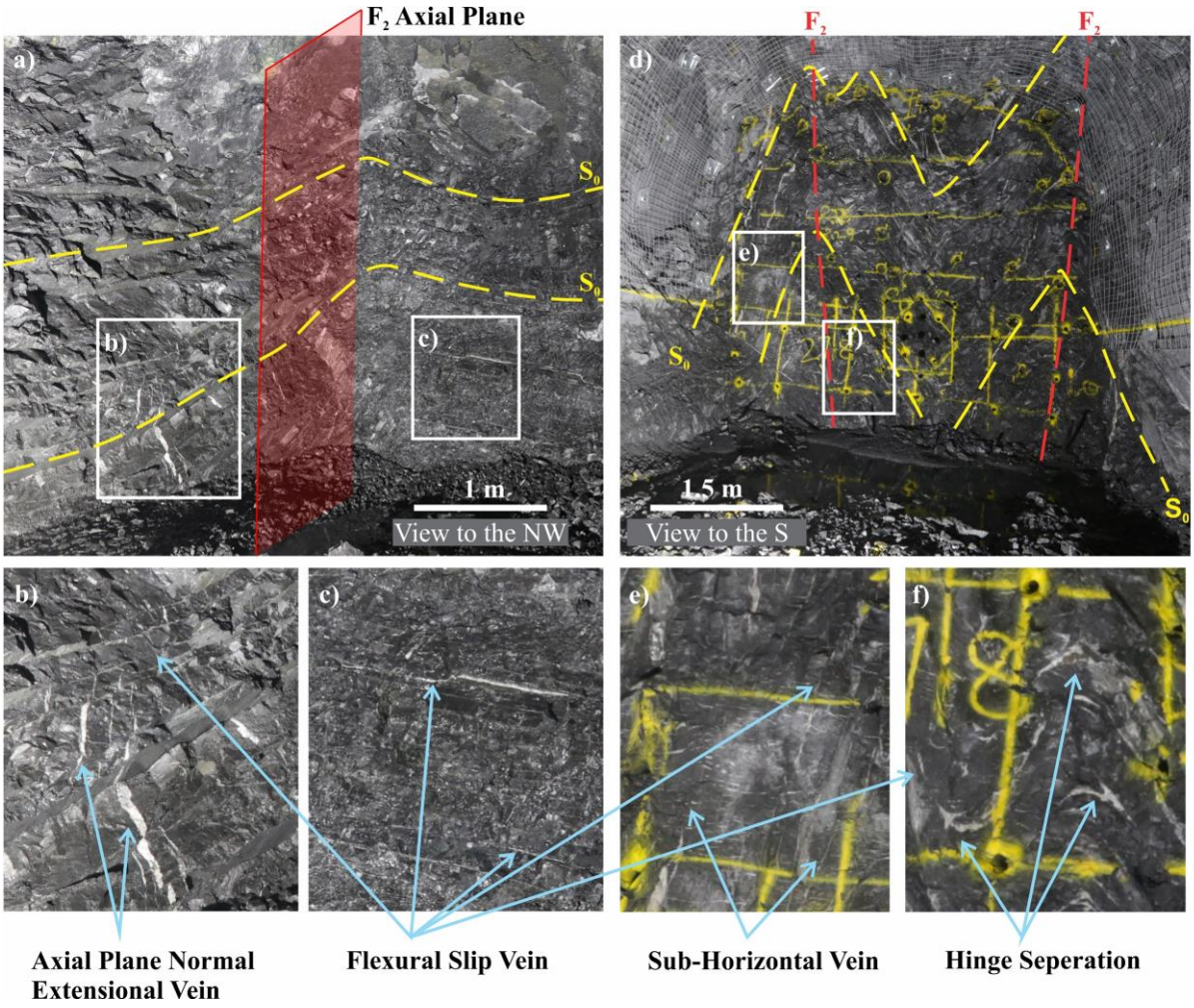

Fig. 2.6: F_2 folds in the South Mine. Folds are open (a) to close (d) with folds away from the ore body typified by lower dipping eastern limbs (a). Several space-accommodating mechanisms resulted in the development of quartz-carbonate veins (b-c, e-f). Hinge separation occurs where folds are close to isoclinal (f; also Fig. 2.13f, 14a).

A penetrative S_2 foliation occurs in all rock units. It is generally ~N-S trending with steep, west dips and local east dips due to D_4 (Fig. 2.7). In slates, it occurs as a slaty cleavage whereas in all the other rock types it occurs as a well-developed schistosity (Newbery et al., 1993, Xu 1996). Pressure solution during D_2 is evident by the development of carbonate strain shadows of porphyroblasts, which themselves are aligned within S_2 (Fig. 2.4), and strain shadows are commonly partially replaced by sulphides.

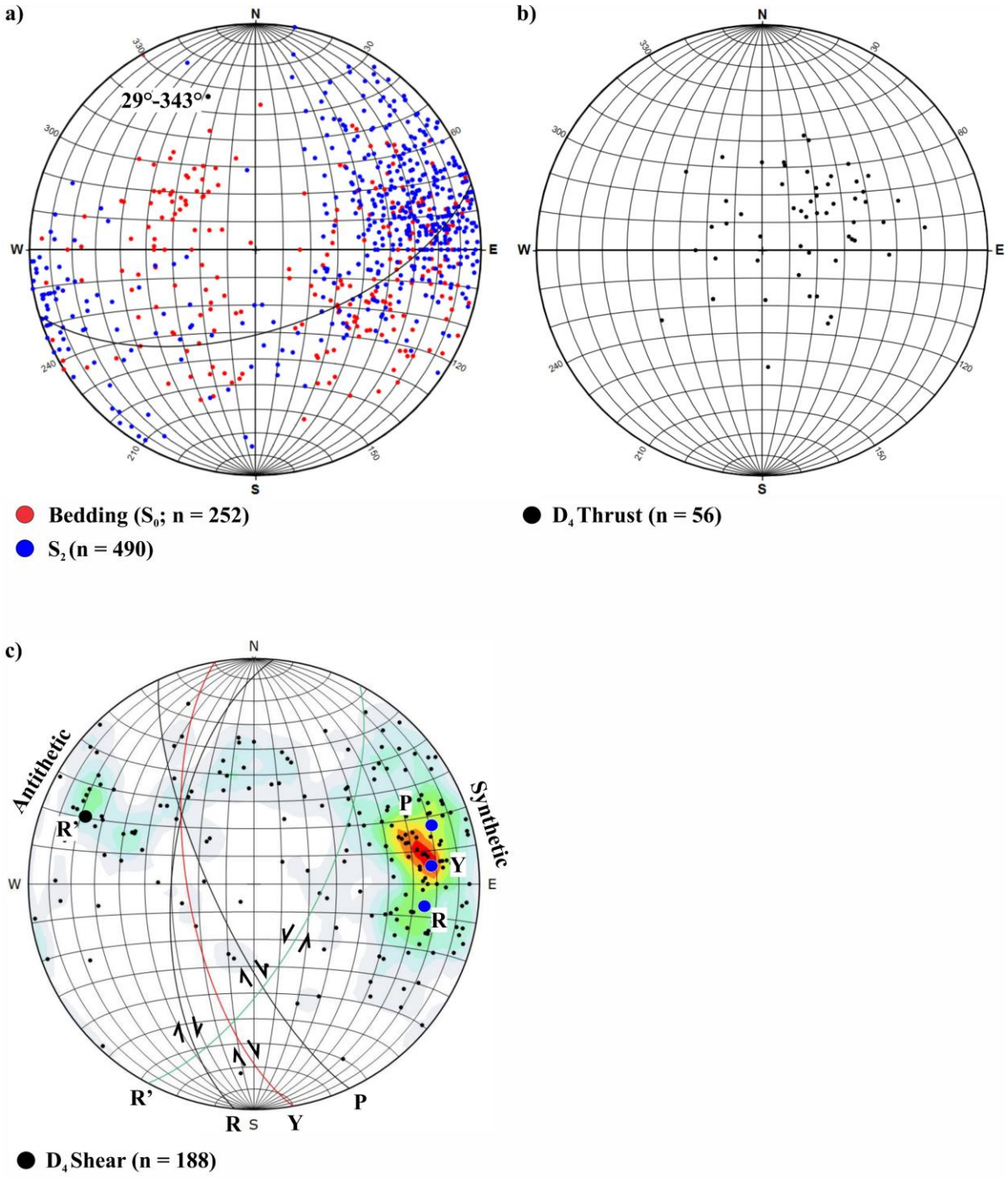

Fig. 2.7: Equal area, lower hemisphere stereoplots for poles to planes. a) The planar fabric at Dugald River is NW-SE trending with dominant WSW dips due to east verging folding during D_2. Low strain domains of D_4 preserve F_1 and F_2 Type 1 interference folds highlighted by the SE- and NW-dipping bedding (S_0) b) SW-dipping zones of S_3 intensification were reactivated early D_4 as thrusts with a top-to-the-NE sense of shear. c) The Dugald River Shear Zone developed as a dextral Riedel shear network with both synthetic and antithetic structures developed.

2.4.2.3. D_3 structures

A weak crenulation cleavage (S_3) commonly occurs in the limestone and slate (Fig. 2.4b). S_3 has a consistent, low-to-moderate southwest dip and is particularly noticeable where high concentrations of porphyroblasts occur in the limestone, causing the localised intensification of S_3 (also Xu, 1996, Spelbrink and George, 2017). The porphyroblasts created a more competent layer in which extensional sites in the crenulations were infilled with carbonate-rich material - in effect creating a domainal cleavage in calc-silicate portions of the limestone versus that in relatively more schistose layers.

A top-to-the-E sense of shear is suggested by Xu (1996) and Davis (2017). On the surface, Xu (1996) described F_3 folds with sub-horizontal axial planes, which together with the low-angle S_3 suggests that D_3 had a localised sub-vertical shortening direction – a similar observation was made by Davis (2017). At George Fisher mine (Murphy, 2004) and the Monakoff deposit (Davidson et al., 2002) similar observations of flat-lying S_3 crenulations and sub-horizontal F_3 were observed. A possible explanation for this may be a period of orogenic collapse between two major shortening events with co-axial top-to-the-E shearing and referred to as $D_{2.5}$ by Bell and Hickey (1998) and Davidson et al. (2002). While F_3 folds were not directly observed in underground development during this study, the effects of D_3 are apparent in the South Mine as S_0 and axial planar S_2 are locally rotated to moderate southwest dips, which suggest recumbent folding.

2.4.2.4. D_4 structures

The orebody at Dugald River is truncated by a strike-extensive graphitic shear system that transposed all earlier fabrics. The NNW-ESE trending, anastomosing shear system (the Dugald River Shear Zone; Fig. 2.3b, 2.12) is marked by increased graphite and chlorite. In places, graphite represents a significant concentration, giving the rock a shiny grey, polished appearance and occurring in metre-scale pods. Curvi-planar discrete shear zones within the shear system range from sub-centimetre scale striated fractures that have highly polished, graphitic walls to metre-scale high strain zones with well-developed S-C' fabrics (Fig. 2.8, 2.9b). These curvi-planar shear zones link together to form the anastomosing shear system hosting the high-grade mineralisation.

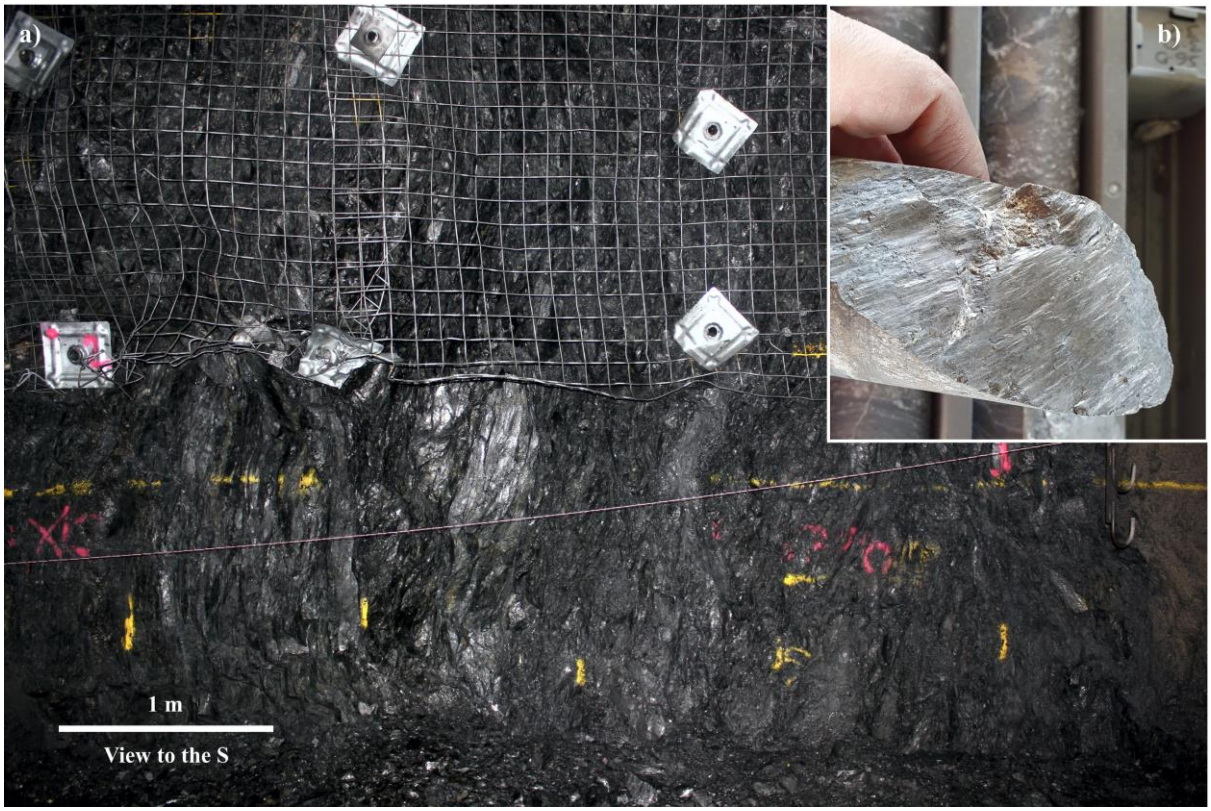

Fig. 2.8: Characteristic range of discrete shears within the Dugald River Shear Zone. The shear zones are marked by increased graphite and chlorite. a) Metre-scale high strain zones are common in the South Mine (grid reference 4E) and marked by a well-developed S-C' fabric that has been a focus for D_5 brittle reactivation. b) Thin, shears with highly polished walls that are typically striated. Notably, a discrete structure can commonly pinch from a metre-scale high strain zone to a sub-centimetre shear.

Strain partitioning in discrete shear zones, resulting in pinch-and-swell, is evident over metre scales (Fig. 2.9). In relatively lower strain domains, which are less than one metre wide, numerous shear bands (C'-planes) can be observed that occur parallel to the shear zone margin. The incipient S-foliation is sub-parallel to S_2 and can be difficult to differentiate given the dark colour of the slates in the shear zone. In high strain domains, which can be several metres wide, a well-developed S-C' fabric has developed. . The asymmetry of sigmoidal lenses in the S-C' fabric is consistent with a top-to-the-NE sense of shear during D_4, with an overall oblique-dextral slip (i.e., transpression or the Phase 3 wrench tectonics described by O'Dea et al. 1997). Sigmoidal lenses within the S-C' fabric typically contain a core of sulphide accumulation with wings of graphite-rich material, and within the South Mine, the cores may contain significant sphalerite. Thin mylonites (centimetre scale) occur away from the orebody and are recognisable by the occurrence of highly stretched porphyroblasts.

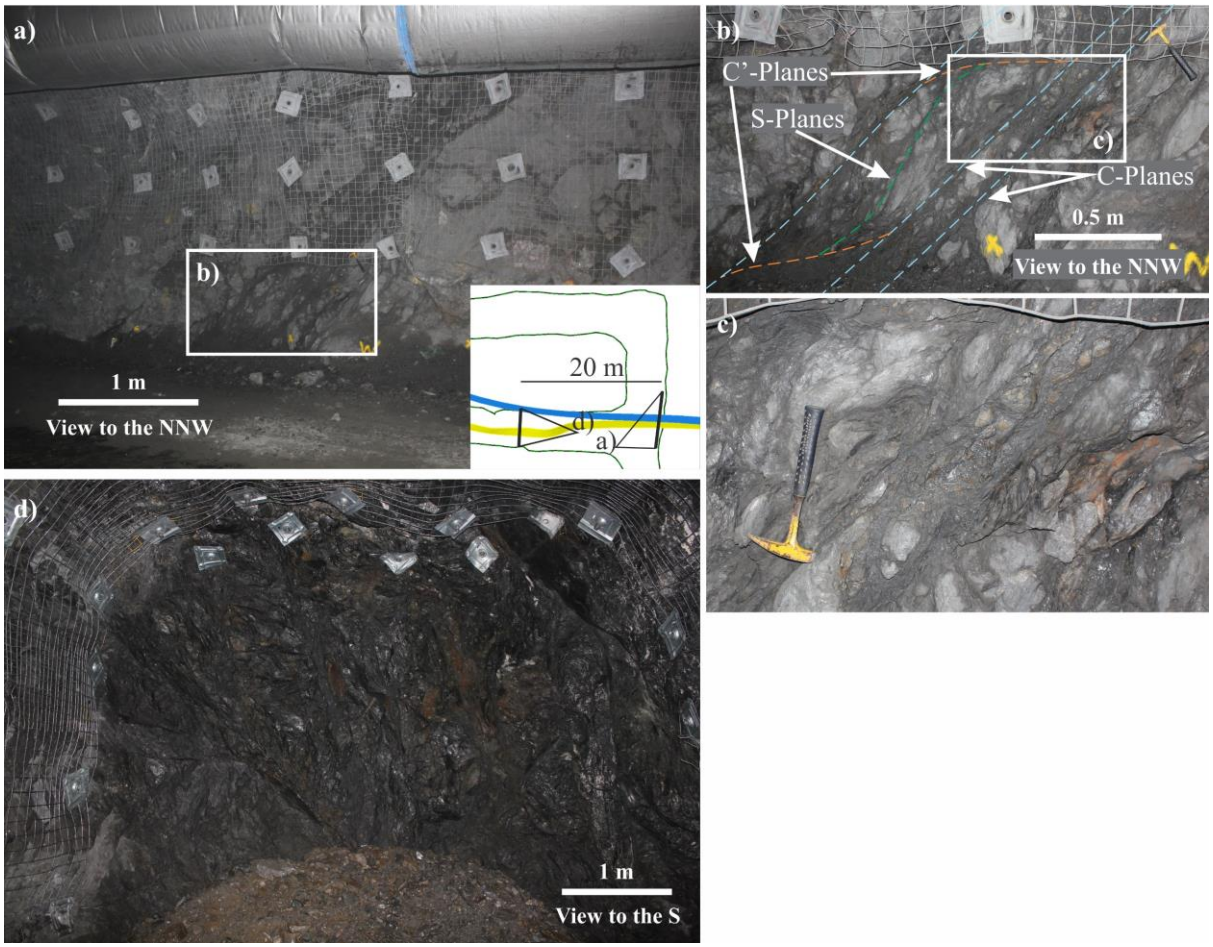

Fig. 2.9: Example of pinch and swell of a discrete shear within the Dugald River Shear Zone (grid reference 4D). a) and d) occur 20 m along strike (see insert in a). The yellow and blue planes in the insert are the footwall and hangingwall of the shear zone, respectively. a) Shear zone, while narrower displays a well-developed S-C' fabric (b and c; geopick for scale) that has been reactivated during D_5 to form an incohesive cataclasite with rounded sigmoidal lenses. d) Here the shear zone is thicker with thinner discrete shears that are sympathetic to the shear zone.

Transposition in the northern part of the deposit and towards the surface is prominent and resulted in high and low strain domains (Fig. 2.10a, 2.19). The high strain domains are marked by the development of S_4 that transposed earlier fabric with rootless F_2 folds often observed. Due to the co-planarity of D_2 and D_4, S_4 is observed sub-parallel to S_2 and can be difficult to differentiate. Low strain domains preserve F_2 folded S_0 and quartz-carbonate veins developed during fold tightening.

D_4 cleavages occur as zones of crenulation cleavage and transposed fabric observed at the microscale. Domanial cleavages commonly result in preferential development of late D_4 cleavages in favourable bands such as micaceous bands. In slates proximal to the ore body, strain partitioning into biotite-rich layers resulted in the development of a composite $S_{2/4}$ foliation, whereas in graphitic layers a crenulated cleavage is observed with S_4 micro-folding S_2 in lower strain domains of F_2 hinges.

Rare folding at the contact of limestone and slate can be attributed to D_4 with black porphyroblasts, that are aligned parallel to S_2, providing evidence of post-D_2 folding. The outcrop-scale folds are disharmonic and contain carbonate-infilled fold-accommodation faults within the fold hinges. Axial planes are moderate, E-dipping and have moderate northwest plunges and rare southeast plunges.

2.4.2.5. D_5 structures

The final major deformational event to affect the Dugald River deposit is associated with the reactivation of earlier shears and faults (Fig. 2.10), as well as the development of small-scale shears within thicker ore bodies and D_4-related tension gashes. Reactivation of shears resulted in the development of incohesive fault rocks (Fig. 2.10c) and metre-scale displacement of ore lenses and limestone/slate contact zones. Offsets are particularly noticeable along SW-dipping shear/fault planes. Generally, steeper structures tend to display cataclasis and low-angle structures display brecciation, particularly along the footwall. Near the limestone contact, the reactivated low-angle thrusts typically involve a damage zone with quartz-carbonate infill and may have chlorite alteration.

The wings of sigmoidal lenses within the S-C' fabric were mechanically sheared leaving the cores as well-rounded clasts within the cataclastic zones with a matrix of graphite-rich brecciated carbonate, quartz and sulphide (Fig. 2.9c). Striations on fault-walls are ambiguous with both strike-slip and dip-slip vectors recorded and cannot be attributed to D_4 or D_5, however, kinematics largely indicate a dextral sense of shear.

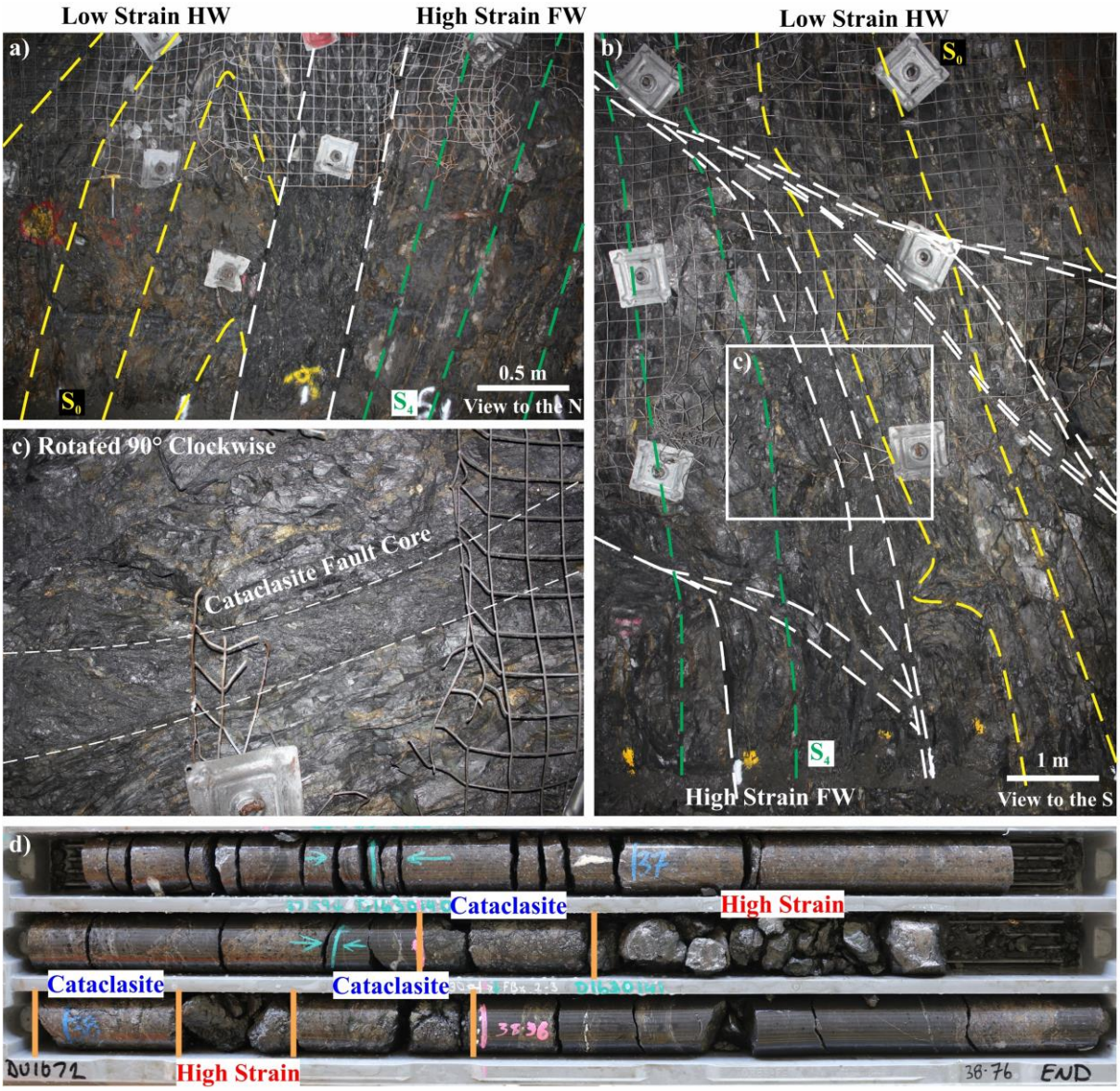

Fig 2.10: Strain partitioning during D_5 resulted in variable development of fault rocks. a) and b) are outcrop expressions of a reactivated part of a mine-scale shear and are on opposite sides of S150_XC423_W (grid reference: 4C). a) The northern side of the drive shows that the high strain character of the D_4 shear is still recognisable as an S-C' fabric. Note, the D_4-related truncation of F_2 folded bedding (S_0) in the hangingwall (HW) of the principal displacement zone. In the footwall (FW) of the principal displacement zone, S_0 is no longer distinguishable from S_2 and transposition has occurred with boudinage of sulphide veins common. b) In the southern side of the drive, the S-C' fabric has been mechanically sheared to form incohesive cataclasite (c; note image is rotated 90° clockwise). d) Drill-core example of a reactivated shear, which includes high-grade matrix breccia texture that typically maintains cohesion as opposed to relatively more graphite-rich parts of shear zones.

2.4.2.6. Metamorphism

The stratigraphic sequence contains abundant garnet and scapolite porphyroblasts which indicate that the minimum P-T conditions reached upper greenschist to lower amphibolite facies. According to Foster and Rubenach (2006) and Whittle (1998), peak metamorphism at Dugald River may have reached mid-amphibolite facies (Fig. 2.2). Foster and Rubenach (2006) placed the host sequence at Dugald River in a belt that they assigned to the diopside zone. Moreover, staurolite- and sillimanite-bearing rocks have been described from the coarse-grained mica schists that occur west of the deposit implying temperatures of up to 600 °C (Whittle, 1998). Calcite grains analysed by George (2011), associated with the carbonate-slate contacts, have MgO-contents up to 2.7 wt % equivalent to 7 mol % $MgCO_3$. Metamorphic calcites with this composition can only be stable at temperatures > 600° C (Anovitz and Essene, 1987) and is the only petrological indication that the metamorphic grade of the Dugald River Slate may be as high as recorded in the mica schists that occur to the west of the deposit. A detailed metamorphic study is recommended for the deposit.

2.5. The Dugald River Shear Zone

The Dugald River Shear Zone is an NNW-trending structure situated to the east of the Knapdale Quartzite within the Mount Roseby Schist (Fig. 2.3b). The surface expressions of the shear zone include a 5 m thick Zn gossan that is approximately 2.5 km long and disappears under cover along strike and at depth, the shear zone was intercepted by drilling at 1 km below the surface.

At the deposit scale, the shear zone has an overall sigmoidal geometry, dipping at 40° - 90° to the west (Fig. 2.11). In the North Mine, the shear zone is steeper compared to the South Mine and has localised east dips. In the South Mine, at ~290 m below the surface, the dip of the shear zone flattens and steepens again at depth (Fig. 2.11, 2.12b) and this change in dip from steep to moderate to steep manifests as a pronounce flexure zone in the geometry of the shear zone. The thickness of the shear network is related to the dip angle of the shear zone: where the dip is steeper, the shear zone is thinner, and conversely, where the dip is at a lower angle the shear zone is wider. In addition, the flexure of the shear zone is associated with low to moderate, SW-dipping thrusts, which are D_4 reactivated zones of intense S_3 development (see section 2.7.3).

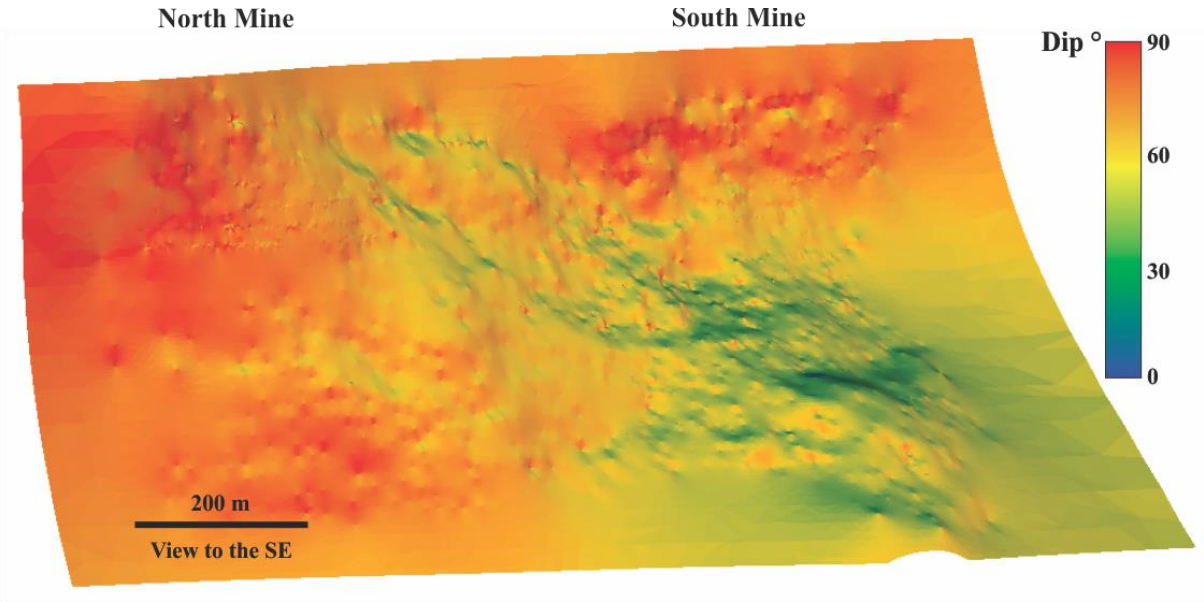

Fig. 2.11: Wireframe triangle faces of the principal displacement zone colour coded according to dip angle. The shear zone in the South Mine is marked by a flexure with moderate dips to the southwest. Towards the north and surface, the shear zone steepens and in the North Mine, local east dips occur.

The shear zone is characterised by anastomosing shears and fractures that reflect a fractal pattern. The geometry of metre-scale shears which locally comprise well-developed S-C' fabrics is reflected in the large-scale geometry of the shear zone. Discrete shear planes within the shear zone can be traced, and modelled, based on drill logging and underground face and drive mapping, including digitised shear planes from Structure-from-Motion – Multiview Stereo (SfM-MVS) photogrammetry (Creus et al., 2021).

In the South Mine, moving towards the west (grid reference: 4C and 4D), several shear zones occur at a variety of scales and are separated by lower-strain zones that may preserve D_2 related fabric elements, thereby creating an anastomosing system of high strain zones bounding lower strain domains (Fig. 2.20). Furthest west, a mine-scale shear (light green polyline on Fig. 2.3b and purple plane on Fig. 2.12) bifurcates from the principal displacement zone (purple polyline on Fig. 2.3b and red plane on Fig. 2.12) at grid reference: 4D. The shear merges with the principal displacement zone in the north at grid reference 3A. In the North Mine, where the shear system is steep and sub-parallel to the pervasively developed S_2, fewer discrete shears are splaying off the principal displacement zone and they tend to disappear into S_2 within a few meters.

2.5.1. Riedel Shear Network

The Dugald River Shear Zone developed as a Riedel shear network. Riedel shears develop with distinctive geometric arrangements and are given different names based on their kinematics and orientations (R, P, R', P', Y and T; Riedel, 1929; Tchalenko, 1968; Naylor and Sijpesteijn, 1986; Davis et al., 2000). Idealised models for Riedel shear networks propose that strike-slip movement within a basement fault is propagated into flat-lying, relatively homogenous cover sequences where strike-slip shear strain is imposed, with slip surfaces developing in distinctive geometries (Fig. 2.12c). Field-based studies of Riedel shear networks suggest that basement faults are not necessary for Riedel shears to develop (e.g, Davis et al., 2000; Mueller, 2020) and may also develop in inclined to steep dipping strata (Swanson, 2006; Dirks et al., 2009; 2013; Mueller, 2020).

Riedel shears develop en-echelon and stepwise and at Dugald River, R-, R'-, P- and Y-shears have been recognised. The first Riedel shears to develop are R-shears, which are synthetic to the shear direction and develop at ~15°, clockwise to the shear direction. R'-shears developed within overlap zones of R-shears and are antithetic to the shear direction and occur at ~75°, clockwise to the shear direction (Davis et al., 2000). With increasing strain, P-shears develop at ~15°, anticlockwise to the shear direction. Finally, as the R- and P-shear segments grow, they interconnect to form throughgoing Y-shears, which at Dugald River is responsible for the anastomosing pattern of the Dugald River Shear Zone.

2.6. Ore Body Geometry and Textures

2.6.1. Ore Body Geometry

The elevated Zn-grades that define the Dugald River ore body have a close spatial relationship with the Dugald River Shear Zone (Fig. 2.3b, 2.12). The ore body, defined by the Inferred resource volume, consists of a ~2.5 km, NNW-trending continuous major ore body and several smaller bodies to the west that are hosted within, and parallel to the shear zone. The main ore body has been intersected to a depth of 1 km below the surface and potential remains to the north, south and at depth. The mineralisation is orientated at a low angle relative to the stratigraphy (Fig. 2.12b). At depth in the South Mine, mineralisation is proximal to the contact between the calc-silicate and slate. Towards the surface and the North Mine, mineralisation gradually shifts towards the contact with the limestone and slate. The gradual shift is marked by a flexure and thickening of the deposit, which represents a dextral step-over in the shear zone (i.e., a releasing bend; Chapter 3). In addition, subordinate ore bodies bifurcate from the major ore body at the flexure.

Individual ore bodies typically occur along the footwall of major Y-shears (e.g. Fig. 2.3b, 2.12). In addition, the geometry of the shear zone and thickness of the ore body has a direct relationship: where the shear zone is steep and thin, the ore body is steep and thin whereas, where the shear zone has a lower dip angle – and thickens – the ore body is thicker and has a lower dip angle.

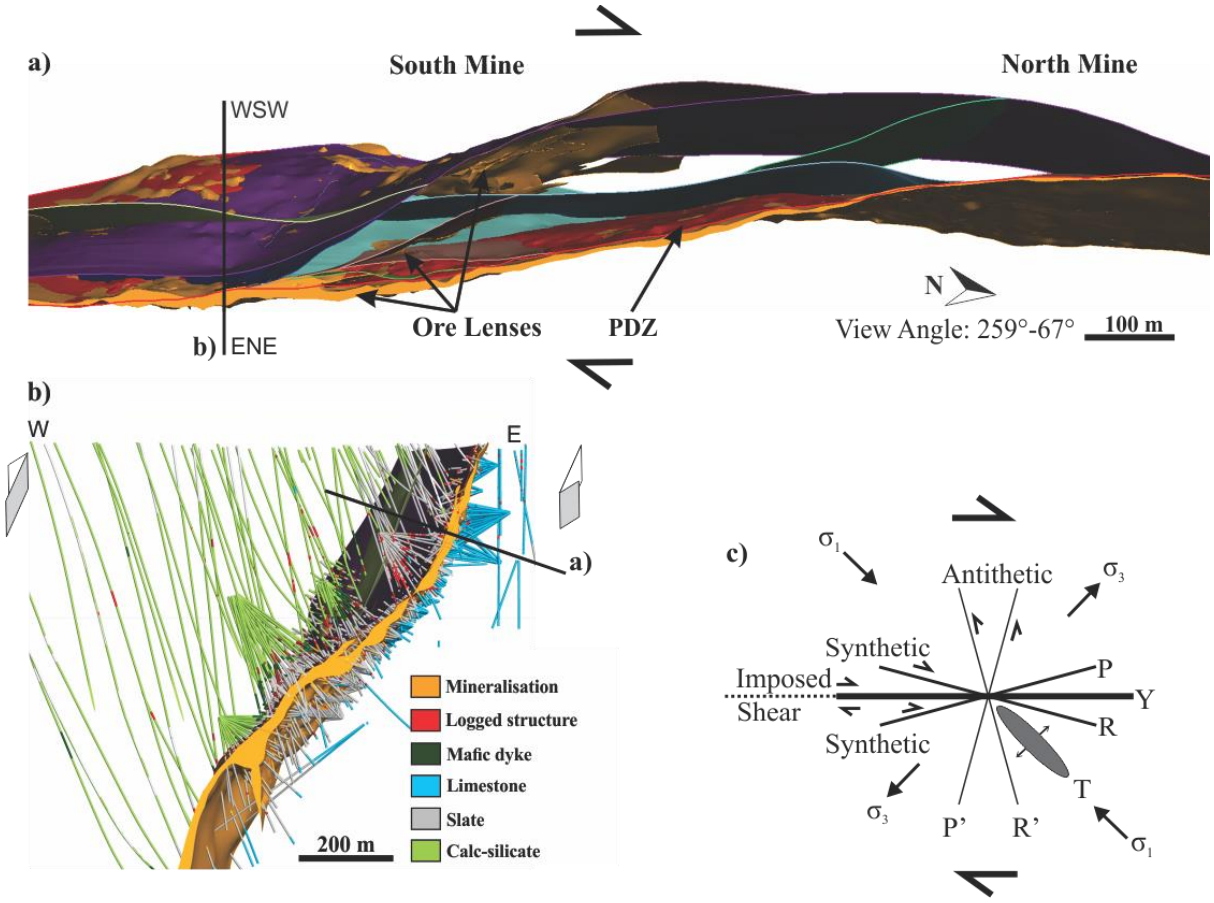

Fig. 2.12: a) Down-dip overview of the Dugald River Shear Zone and high-grade Zn volume (> 7% Zn). The shears bifurcate and merge to form an anastomosing shear zone with an oblique dextral sense of shear. Note the thinning of the mineralisation towards the north and the surface. b) Cross-sectional view looking north through the South Mine. The location of the cross-section is shown in (a). c) Schematic representation of Riedel shears developed within a dextral, transpressional strike-slip shear zone.

2.6.2. Ore Textures

The geometry of the ore zone parallels the Dugald River Shear Zone and has an apparent tabular shape (Fig. 2.12). The ore textures vary along the ore zone and can be categorised into breccia and planar ore (e.g., Newbery et al., 1993; Xu, 1996; Spelbrink and George, 2017; this chapter). The rest of section 6.2 is a summary of Newbery et al. (1993), Xu (1996), Spelbrink and George (2017) and observations during this study. The breccia ore represents the most economic style of mineralisation, highest grade and thicker ore zones, and is particularly abundant in the southern end of the deposit where the ore body is thicker and has a lower dip angle, while planar ore is abundant in the northern end of the deposit where the ore body is thinner and has a sub-vertical dip (Fig. 2.13a).

End-member types for the breccia ore texture include clast supported and matrix-supported. The clast-supported breccia is characterised by centimetre- to metre-scale sub-angular clasts of slate and sub-centimetre clasts of quartz and pyrite in a matrix dominated by sphalerite, however other matrix sulphides include pyrite, pyrrhotite and galena. Clasts of folded slate are common and the presence of an axial planar cleavage in some of the clasts indicates that the shearing occurred after the main folding event. Most slate clasts contain bedding parallel carbonate veins and veinlets that are partly to completely replaced by sulphides, mainly sphalerite (Fig. 2.13e). The matrix-supported breccia is characterised by variably sized, rounded slate, pyrite, quartz and rare fluorite clasts (Fig. 2.13b) in a fine-grained matrix of sphalerite with subordinate amounts of galena, pyrite and pyrrhotite. Clasts rarely exceed 10 cm in length. In the South Mine, where the ore body thickens, the footwall to the ore body consists of a thick zone of carbonate matrix-supported breccia with trace amounts of pyrite, sphalerite, pyrrhotite and galena (Fig. 2.13b). Locally, pyrrhotite-rich matrix-supported breccia occurs and is associated with a pronounced drop in the Zn grade and the appearance of visible chalcopyrite. The pyrrhotite-rich breccia is usually fine-grained and displays evidence of shearing and appears to overprint the earlier sphalerite-rich breccia (e.g., Fig. 2.13g).

Planar ore textures are common in the northern part of the deposit and include banded and stringer ore. Banded ore consists of alternating bands of sulphides and black slate (Fig. 2.13d). The sulphides occur as both fine-grained crystals and coarse-grained annealed aggregates, suggesting replacement and remobilisation during deformation. Some clasts within the breccia ore consist of banded type ore suggesting that the banded ore predates the breccia ore.

Stringer ore represents a widely distributed ore texture usually occurring along the periphery of breccia type ore. The stringers have variable thicknesses and commonly occur as a series of bands that are sub-parallel to the S_2 fabric, suggesting that this ore type may represent replacement ore of the S_2 fabric or D_2 carbonate veins. The main sulphide phases within the stringer ore are sphalerite and pyrite with subordinate pyrrhotite and rare galena.

In general, the ore textures have a zonation pattern that appears to correlate with the geometry of the ore body/shear zone (Fig. 2.13a). In the North Mine where the ore body is steep, ore textures are dominated by planar ore with thin, discontinuous lenses of breccia ore. Towards the south, where the ore body has a lower dip angle, breccia type ore dominates and weaves around planar ore.

Fig. 2.13: Main ore textures observed in the Dugald River deposit. a) Oblique section through grid reference 4D and the "back" of the section showing the distribution of the main ore textures as colour-coded drillhole intervals. The footwall plane of the principal displacement zone (PDZ) is coloured according to the wireframe triangle face dip. b) High-grade matrix-supported breccia that is dominant in the South Mine. Here the matrix comprises sphalerite (sp) and minor pyrrhotite (po). c) Carbonate breccia forms an eastern zone of low-grade mineralisation and is only found in the South Mine and represents a quartz-carbonate brecciation front that was replaced by sulphides. In this sample, the rounding effect due to sulphide remobilisation of competent wall rock, including pyrite (py) is highlighted. In the carbonate breccia, the pyrite is largely euhedral. d) The North Mine is dominated by transposed sulphide veins that are parallel to S_2 and form the planar ore. e) Clast-supported mineralisation is found throughout the deposit – mainly in the South Mine - and is marked by clasts of D_2-related folds. Folded clasts often contain thin veinlets of bedding parallel carbonate veins that are partially to completely replaced by sulphides. f) Hand-scale example of a tight fold where flexural slip along bedding planes has resulted in veining. With fold tightening sulphides migrate into extensional sites such as fold hinges (saddle reefs; (i)) and boudin necks (ii). Pyrite grains in the flexural slip veins, boudin necks and hinges are fine-grained, whereas, in S_2 parallel veins, pyrite is coarse-grained. g) Post-breccia shearing can develop in matrix-supported breccia as pyrrhotite bands within fine-grained sphalerite. The pyrrhotite bands can be thicker and contain rounded fragments of wall rock, quartz and fluorite. Abbreviations: pyrite (py), sphalerite (sp), host rock (hr); quartz (qtz), fluorite (fl), carbonate (cb), pyrrhotite (po), galena (gn).

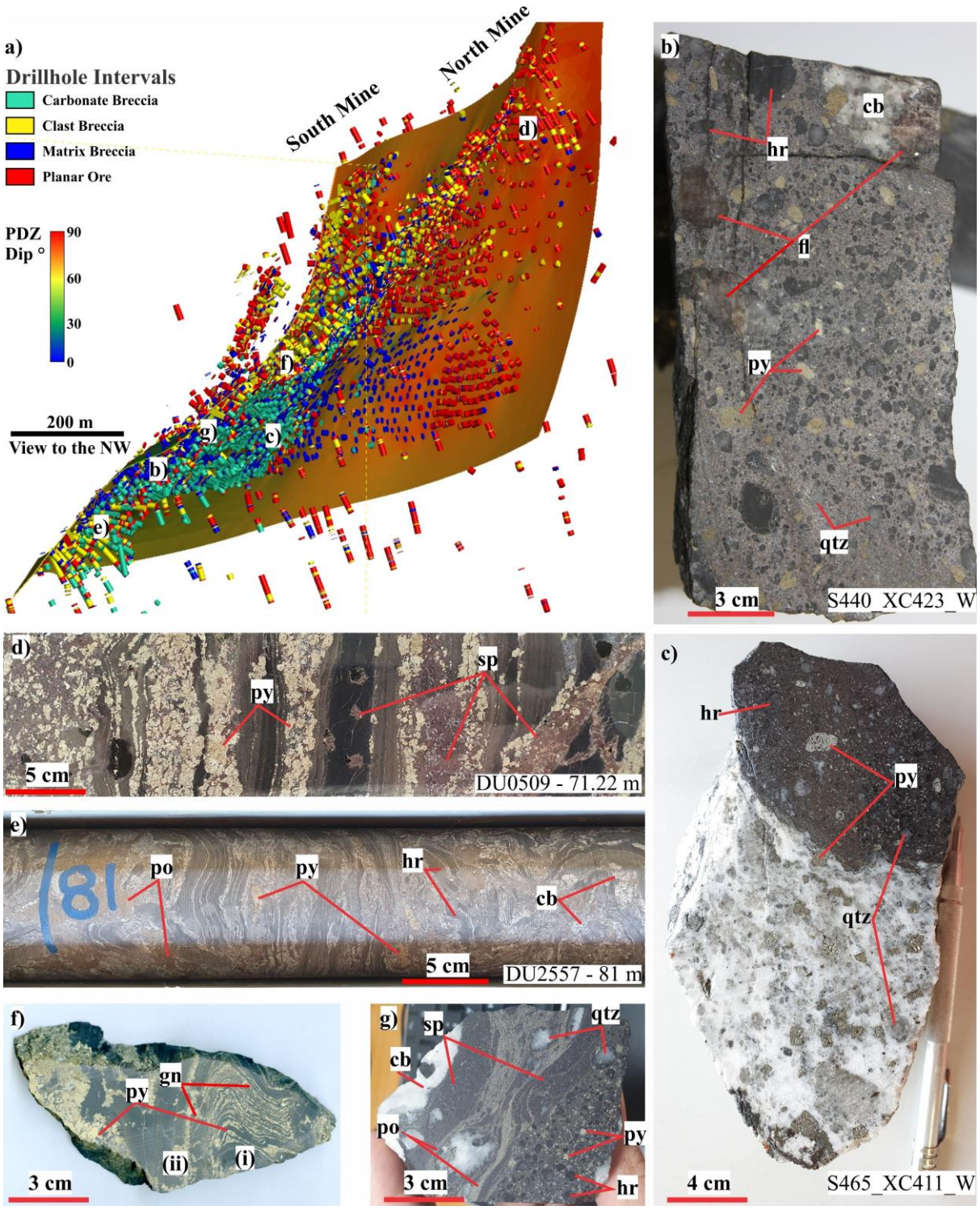
a)
Drillhole Intervals
Carbonate Breccia
Clast Breccia
Matrix Breccia
Planar Ore
PDZ Dip °
90
60
30
0
200 m
View to the NW
South Mine
North Mine
b)
cb
hr
fl
py
qtz
3 cm
S440_XC423_W
c)
hr
py
qtz
4 cm
S465_XC411_W
d)
py
sp
5 cm
DU0509 - 71.22 m
e)
po
py
hr
cb
5 cm
DU2557 - 81 m
f)
gn
py
(ii)
(i)
3 cm
g)
sp
qtz
cb
po
py
hr
3 cm

2.6.3. Boudinage

Sulphide accumulation into dilational sites created by boudinage is common within the deposit (Fig. 2.4d, 2.14; Davis, 2017; this chapter). Layer-parallel boudinage of attenuated limbs of tight to isoclinal F_2 folds is common and boudin necks are characteristically cross-shaped and infilled with quartz-carbonate, which has subsequently been replaced by sulphides during mineralisation. Foliation boudinage is a possible mechanism for the cross-shaped boudin necks given the lack of rheological contrast within the slate (Fig. 2.14d – e; e.g., Aerden, 1991; Arslan et al., 2008; 2012). Infill of pyrite, pyrrhotite and sphalerite in boudin necks combined with a lack of deformation of the sulphide grains suggests precipitation coeval with boudin formation (Davis, 2017). However, it should be noted that while boudin necks contain sulphides, the arms of boudins are typically comprised of quartz-carbonate suggesting the replacement of carbonate by sulphides (Fig. 2.14e). Torn boudins are common in the planar ore and larger clasts of the breccia ore (Fig. 2.14a – c). Here the slate layers, which are competent layers enveloped by sulphides resulted in strain rate incompatibilities, which caused layer extension, resulting in angular, block-shaped boudins with necks infilled by sulphides.

Fig. 2.14. Common boudinage patterns observed at Dugald River where boudin necks are generally infilled with sulphides. a) Hinge separation of a close fold with infill of sulphides to create a saddle reef which in this instance is infilled with coarse-grained pyrite and fine-grained sphalerite. Adjacent to the saddle reef is cross-shaped boudin necks infilled by coarse-grained pyrite and fine-grained pyrite. a, b, c) Torn boudins with sulphide infill in the necks occur where thicker (centimetre-scale) slate layers are enveloped by sulphide layers. d, e) Foliation boudinage within slate (e) and limestone (d).

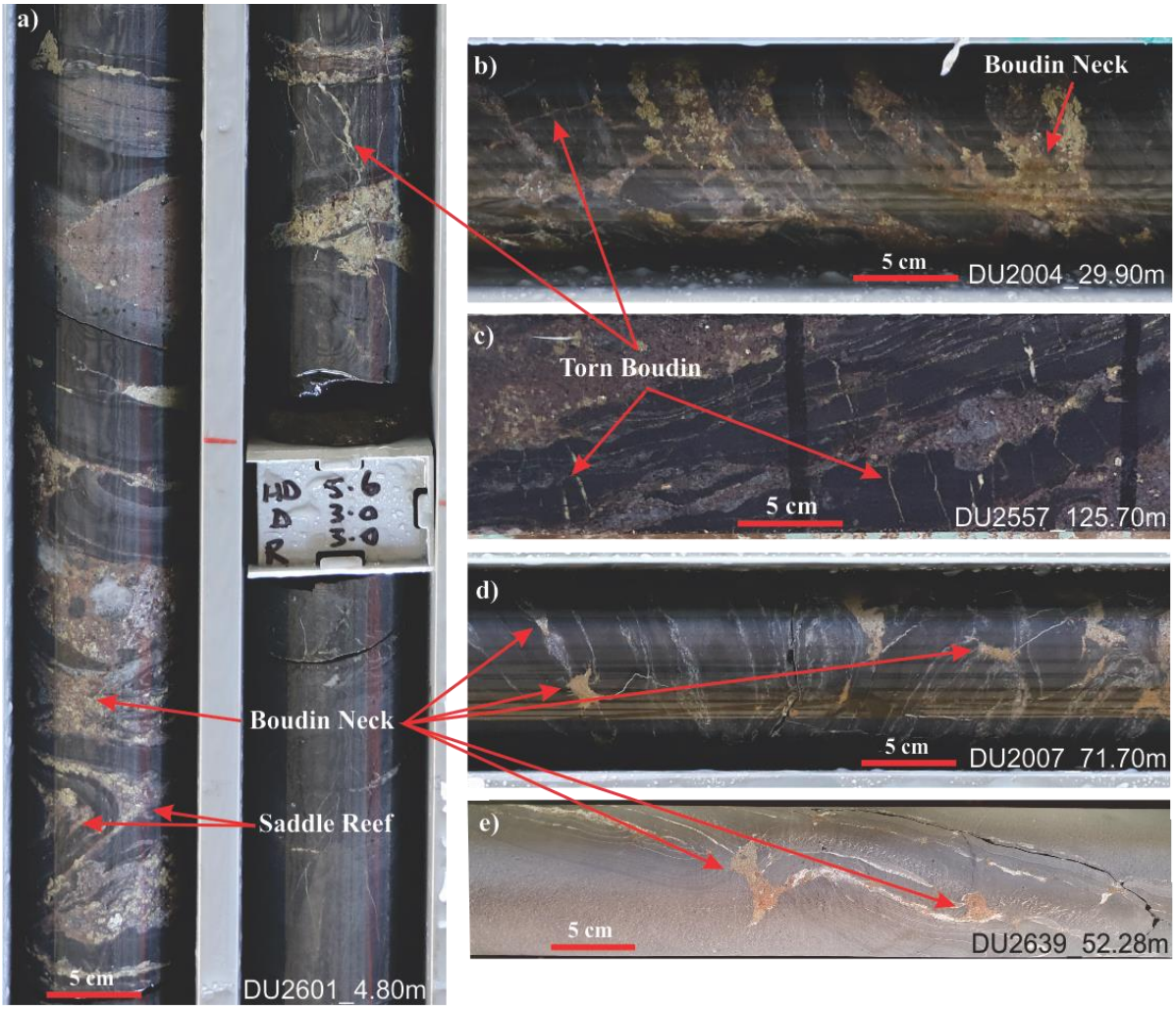

2.6.4. Ore Paragenesis

Microscale and hand-specimen analysis of high-grade breccia ore indicate that there were at least two main phases of sulphide mineralisation. The first phase is associated with the replacement of carbonate in quartz-carbonate veins during late D_2, and the second phase is associated with intense brecciation during D_4 with associated quartz-carbonate fluid injection.

Observations of D_2-related mineralisation, herein referred to as Phase 1 mineralisation, under the microscope and at outcrop-scale indicate that during this phase, pyrite was the dominant sulphide species with significant sphalerite and minor galena and pyrrhotite. Pyrite, sphalerite and galena crystals are preserved as rounded clasts in breccia ore and are typically coarse-grained.

During the second phase of mineralisation, herein referred to as Phase 2 mineralisation, sphalerite was the dominant sulphide species together with significant pyrite and galena. Episodic injection of sulphide-rich fluid is indicated by the variable grain size of matrix sphalerite, and the observation that in many rounded clasts of D_2 related veins, the clasts are surrounded by fine-grained polycrystalline quartz and inclusions, some of which are sulphides. In general, where finer-grained matrix sphalerite occurs the number of rounded clasts is greater. Pyrrhotite is inferred to have precipitated late during D_4, but at a time when the sulphides were still ductile as indicated by sheared pyrrhotite within matrix-supported sphalerite breccia (e.g., Fig. 2.13g). It appears that away from the orebody, pyrrhotite is the dominant sulphide and tends to infill micro-fractures in slates and limestone. Furthermore, selvedge's of pyrrhotite are stretched and dismembered into smaller segments, parallel to S_2 and S_4.

2.7. Discussion

The close spatial-temporal relationship of the Zn-Pb mineralisation to the Dugald River Shear Zone suggests that the Dugald River deposit can be classified as an epigenetic, shear zone hosted deposit. While the data presented in this chapter indicates a strong structural control on the development of the deposit in its current setting, the question remains whether or not precursor mineralisation existed and if so, was it initially in a SEDEX or diagenetic environment as proposed for other deposits in the Mount Isa Inlier and McArthur River areas (e.g., Newbery et al., 1993; Dixon and Davidson, 1996; Large et al., 2005; Spinks et al., 2020; Rieger et al., 2021). For example, the banded ore texture (*viz.* planar ore, Fig. 2.13a), common in the North Mine, was used to argue for a genetic model of early, syngenetic or diagenetic, stratabound mineralisation with a later hydrothermal overprint (Newbery et al., 1993; Dixon and Davidson, 1996). Newbery et al. (1993) suggested that the laminations in the banded ore represent sedimentary layering and the layers containing equant grains of sulphides indicate uniform recrystallization and limited remobilisation, whereas the coarse-grained, sulphide-rich bands represent remobilisation and recrystallization during deformation. Dixon and Davidson (1996) argued that the fine-grained pyrite that occurs as “minute” subhedral grains enclosed by anhedral sphalerite and pyrrhotite indicates that the base-metal sulphides were introduced after the growth of the pyrite within the sediment. Furthermore, they suggest that high δ^{34} sulphur in sulphides was inherited from a component of earlier diagenetic sulphur and that the limestone acted as an impermeable layer trapping Zn-Pb brines within the slate package.

We suggest that the banded ore represents quartz-carbonate-sulphide veins that were progressively flattened, attenuated, dismembered, and transposed into parallelism with S_2 (Fig. 2.13d). During

progressive deformation, the veins were boudinaged as they were rotated into parallelism with S_2, and the boudin necks acted as dilational sites where pyrite, sphalerite and galena migrated and crystallised (Fig. 2.16). Although, the Dugald River deposit is completely shear zone hosted we cannot exclude the possibility of early syngenetic or diagenetic mineralization that was subsequently upgraded during deformation and continuous tectonism. In the following section we propose a structural model for the formation of the Dugald River ore deposit based on detailed mapping, core logging and 3D modelling of the ore body and structures.

Our observations indicate that the Zn-Pb mineralisation at the Dugald River deposit is hosted within the Dugald River Shear Zone and the sulphide mineralisation comprised at least two depositional phases. The first phase of sulphide deposition involved transport in hydrothermal/metamorphic fluids and is represented by mineralisation hosted in syn-D_2 quartz-carbonate veins. The second and the main phase of sulphide deposition involved a combination of fluid-assisted transport and mechanical remobilisation and is represented by the breccia, planar and the stringer ore hosted by the D_4 Dugald River Shear Zone.

2.7.1. Sulphide mobility during hydrothermal and deformation events

Sulphides undergoing deformation and metamorphism can be mobilised by fluids and by solid-state deformation, often both processes occurring simultaneously and known as mixed-state solution (e.g., Hobbs, 1987; Marshall and Gilligan, 1987, 1989, 1993; Marshall et al., 2000; Tomkins, 2007; Zhang et al., 2014). Mechanical remobilisation (i.e., solid-state solution) involves a process of translocating sulphides from zones of high mean rock stress to zones of lower mean rock stress during ductile deformation (e.g., Tomkins, 2007). Usually, this process involves the migration of sulphides from fold limbs to hinge zones (e.g., Marshall and Gilligan, 1987; Tomkins, 2007) and the same principle applies to dilational jogs in shear zones and boudin necks.

According to Tomkins (2007), mechanical remobilisation is effective at redistributing massive sulphides as they act as single units that are more ductile than the surrounding silicate rocks. In this manner, sulphides can be remobilised on the scale of 10's metres when compared to the movement of disseminated ore, which occurs on the scale of centimetres (Marshall et al., 2000; Tomkins, 2007; Zhang et al., 2014). Experimental results indicate that sulphides undergoing deformation have a strength order, *viz.*, galena (weakest) < chalcopyrite < pyrrhotite < sphalerite < pyrite (strongest) with the middle 3 interchangeable (Marshall and Gilligan, 1987). Furthermore, all sulphides but pyrite undergo several deformation processes starting from greenschist facies and include ductile deformation, solid/liquid state remobilisation and annealing (Craig et al., 1998). At higher metamorphic grades, i.e., at amphibolite facies and higher, massive sulphides tend to migrate as a whole with little mechanical fractionation of the ore (Tomkins, et al., 2007). The relative strength between different sulphide phases also has a bearing on the preferential remobilisation of metals within the sulphide horizons (Marshall and Gilligan, 1987).

The breccia ore represents the highest grade of mineralisation, particularly the matrix-supported breccia. Rounded clasts of wall rock, vein quartz-carbonate, fluorite, and pyrite are inferred to have formed through the process of mechanical remobilisation. Initially, competent rock fragments (including pyrite and quartz-carbonate veins) cracked through brittle deformation (e.g., cataclasis) with ductile sulphides migrating into the cracks, forming the clast-supported breccia (e.g. Fig. 2.15). The competent fragments were mechanically deformed through kneading, milling and rotation to form the matrix-supported breccia as the massive sulphide horizon thickened. This process is often referred to by the German term "durchbewegung" first described by Vokes (1963) and further discussed by e.g., Maiden et al. (1986), Klemd et al. (1987), McQueen (1987), Cook et al. (1993) and Zhang et al. (2014). Durchbewegung is an internal feature of ore deposits and is the result of intense progressive simple shear within fault and shear zones (Marshall and Gilligan, 1987) with two endmembers described (e.g., Maiden et al., 1986; Klemd et al., 1987; McQueen, 1987):

1. Progressive fold tightening to isoclinal folds where alternating layers of silicate rocks and massive sulphides become disrupted and separated, with the migration of sulphides between the silicate clasts, which includes disrupted folds and boudins. The clasts then undergo rotation within the sulphide matrix.
2. Progressive brittle fracturing of competent wallrock at the interface with a sulphide horizon results in the migration of sulphides into the fractures, and wallrock clasts are incorporated into the sulphide matrix and rotated.

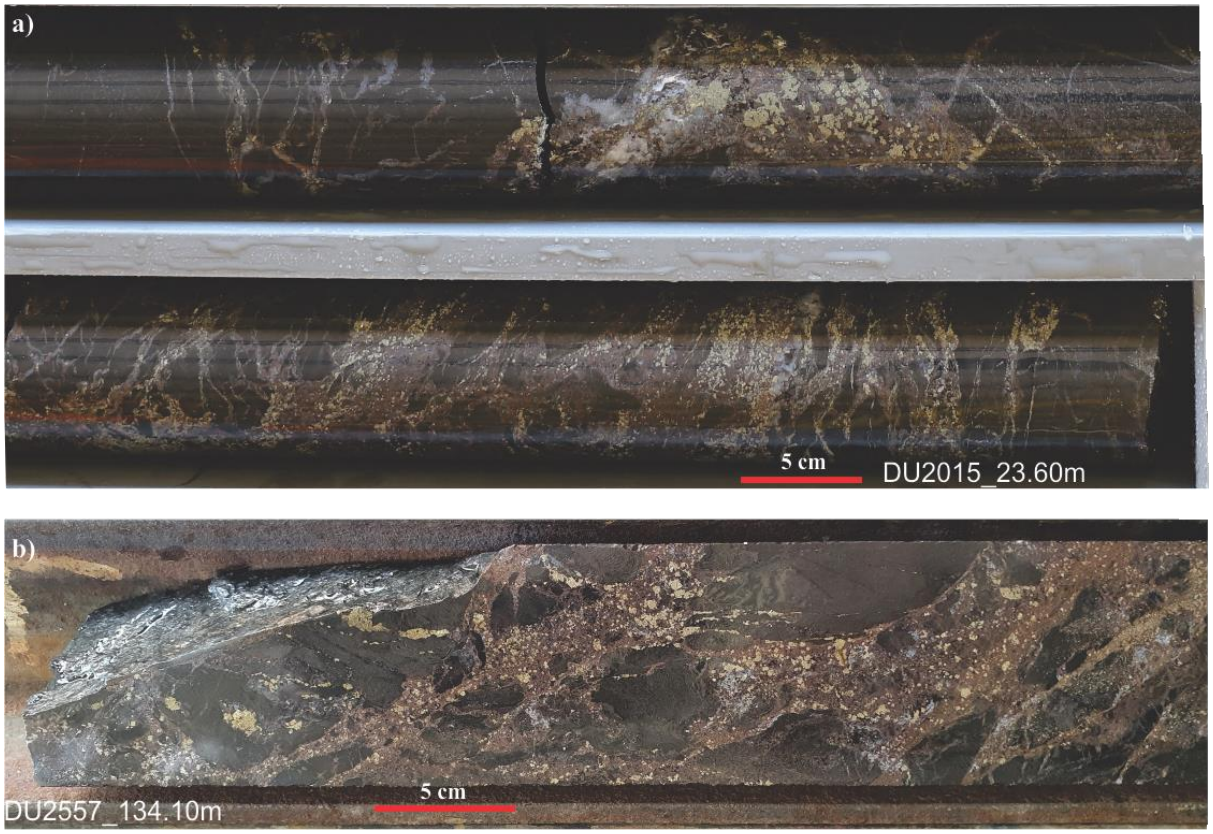

Fig. 2.15. Hand specimen representation of a durchbewegung structure. At the interface of a sulphide layer and slate, the slate fractures with the cracks infilled with sulphides, whereas the sulphides can deform through ductile means and flow through the rocks. Slate clasts are incorporated into the sulphide layer and through a process of kneading, milling and rolling are rounded. The inferred temperature range falls within 350 – 500 °, which is the temperature at which most sulphides deform in a ductile manner except for pyrite. Here, this is illustrated by the abundance of pyrite within the sulphide layers and sphalerite infilling the cracks. Furthermore, some pyrite grains in (a) are sub-rounded. a) Grid reference: 3C. b) Grid reference: 4E.

2.7.2. Phase 1 Mineralisation

Phase 1 mineralisation marks the first evidence for mineralisation and occurs during late D_2, following quartz-carbonate veining and peak metamorphism and is inferred to have been sub-economic. Underground mapping and core logging of structures, veins and mineralisation textures allow for the reconstruction of progressive, ductile deformation and mineralisation during D_2 (Fig. 2.16). D_2 folds become tighter proximal to the Dugald River Shear Zone which resulted in the progressive steepening of veins, parallel to S_2, followed by boudinage and the coalescing of veins and boudin necks. The formation of quartz-carbonate veins, sulphide deposition and deformation were coeval as indicated by progressive migration of veins and sulphides into dilational sites where folding has intensified (i.e. fold hinge separation and boudinage along fold limbs; Davis, 2017). Away from the ore body, layer-parallel veins (flexural slip veins) are spaced (> 10 cm) and thinner and relatively evenly distributed, but the sulphide concentration is negligible. Closer to the ore body the spacing between quartz-carbonate veins becomes increasingly smaller, veins are thicker, and the concentration of sulphides increases. Folds are close to isoclinal with hinge separation (saddle reef) and boudinage in fold limbs (e.g., Fig. 2.14a).

Increasing D_2 strain resulted in progressive fold tightening and cumulative fold accommodation veins that were rotated into parallelism with S_2. Zones of tight to isoclinal folds with associated, coalesced sulphide replaced quartz-carbonate veins resemble a crackle breccia. We infer that this zone of incipient brecciation produced a heterogenous rock mass that was favourable for S_3 intensification during D_3, which in turn favoured early D_4 reactivation as low-angle thrusts and initial dilation for intense brecciation during prevailing D_4 shearing. In other areas, like the North Mine, fold amplification and steepening of F_2 fold limbs resulted in vein rotation into parallelism with S_2 and form the precursor to planar ore during D_4.

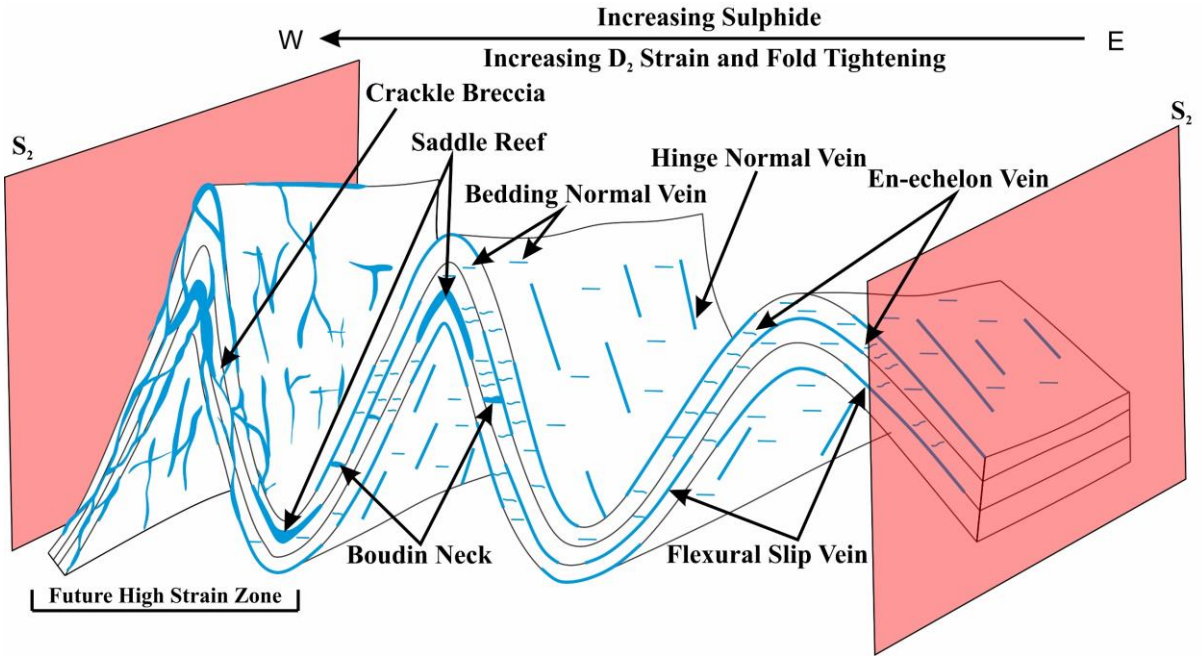

Fig. 2.16: Cartoon sketch of Phase 1 mineralisation. Progressive tightening of folds resulted in secondary space accommodating quartz-carbonate veins (blue lines and polygons), progressively steepening parallel to steep, W-dipping S_2 planes. Where fold interlimb angles are tight, veins create interconnected networks that are now sub-parallel to S_2, and a crackle breccia developed where wall-rock to sulphide ratios are lower. Zones of crackle breccia and closely spaced, interconnected veins created a favourable heterogeneous rock mass for strain partitioning during D_3 and D_4. Notably, these zones are sites for future high strain zone development.

2.7.3. Intervening phase

Following D_2 is an inferred period of orogenic collapse. In orogenic collapse, the stress exerted by an overthickened orogen exceeds the compressive stress and in the Mount Isa Inlier this resulted in sub-vertical principal stress with a suggested top-to-the-E sense of shear (e.g., Xu, 1996; Bell and Hickey, 1998; Murphy, 2004). Notably, this involved a switch from a sub-horizontal principal stress direction and associated sub-vertical fabric development (i.e. S_2 and upright F_2 folds) to a sub-vertical principal stress direction and associated sub-horizontal fabric development (S_3).

The effects of D_3 are subtle and within the Dugald River deposit generally occur as a spaced crenulation cleavage. In the South Mine, the heterogenous rock mass resulting from F_2 fold tightening and crackle breccia formation provided favourable sites for zones of S_3 intensification (Fig. 2.17a). The zones of S_3 intensification locally rotated steeply dipping S_0 and S_2 orientations to lower angle, ~west dipping orientations (also Xu, 1996). In addition, this would have rotated F_2 to more recumbent

orientations with sub-horizontal axial planes, however, this was not observed during underground mapping and drillcore analysis but was described by Xu (1996) away from the deposit on the surface.

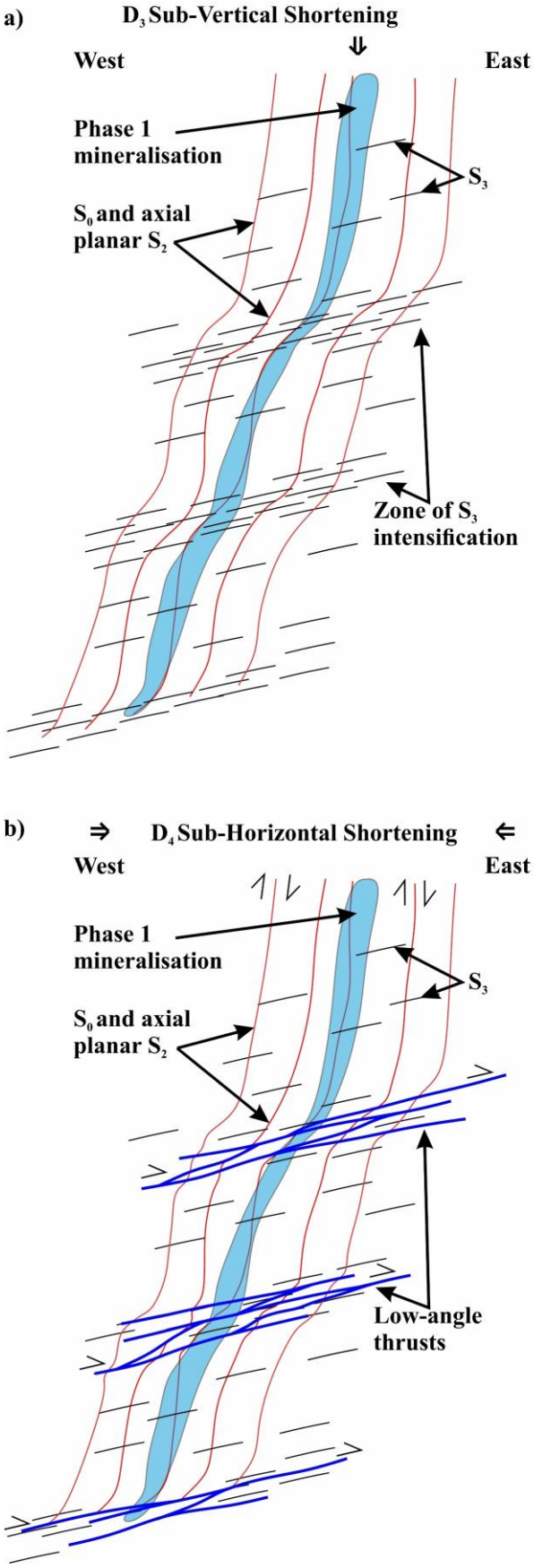

Fig. 2.17: a) During a period of inferred orogenic collapse, the D_3 principal stress direction was sub-vertical, which produced sub-horizontal S_3 planes. In the South Mine, zones of S_3 intensification locally rotated Phase 1 mineralisation (in blue) and steep S_0 and S_2 to lower angle, ~ west dips. b) During D_4, with the resumption of E-W directed shortening, the cleavage planes within the zones of S_3 intensification were reactivated and linked to form low-angle thrusts that ramp to form low-angle lenses. Low-angle thrusts are common in grid reference 4D.

2.7.4. Phase 2 Mineralisation

Phase 2 mineralisation is inferred to have occurred during retrograde metamorphism, during the waning stages of the Isan Orogeny. Thus, this involved a transition from ductile to brittle-ductile deformation (e.g., O'Dea et al., 1997). Following the period of orogenic collapse, the continuation of bulk E-W directed sub-horizontal shortening resulted in the reactivation of zones of intensified S_3 in the South Mine as low-angle thrusts with a top-to-the-NE sense of shear (Fig. 2.17). Opposing shear along stacked thrusts created zones of contraction and extension, i.e. areas of high and low mean rock stress, respectively, promoting remobilisation of sulphides. Additionally, synthetic shear along steeper S_0 and S_2 created additional zones of dilation with subsequent remobilisation of sulphides into the zones.

The asymmetry of sigmoidal lenses in the S-C' fabric is consistent with a top-to-the-NE sense of shear. Notably, given that D_4 was ~E-W directed (O'Dea et al., 1997), steep W-dipping S_0 and S_2 planes were in favourable orientations for synthetic, dextral shear and S_3 planes to accommodate dip-slip movements. Furthermore, increasing strain during D_4 is marked by a progression from coaxial to non-coaxial strain.

Fabric formation during early D_4 involved a coaxial strain history. The effects are best preserved in the North Mine where further tightening of F_2 resulted in textures that are similar to Phase 1 mineralisation (i.e. attenuation of fold limbs and migration of sulphides into extensional sites; Fig. 2.19b). The steep fabric elements (S_0, isoclinal F_2 folds, and an axial planar S_2 fabric), combined with progressive tightening of folds into parallelism with S_2, resulted in the development of a transposition fabric and eventually high strain zones that wrapped around low strain zones with preserved F_2 folds (Fig. 2.18, 2.19b). In the South Mine, the effects of coaxial strain have been preserved in zones away from low-angle thrusts where opposing shear along steep, W-dipping S_0 and S_2 versus top-to-the-NE movement along the thrusts resulted in dilation and areas of low mean rock stress.

With the exhumation of the deposit and a transition from ductile to brittle-ductile deformation, the P-T conditions were within the range for ductile deformation of sulphides versus brittle deformation of the slate. The transition from ductile to brittle-ductile deformation was marked by a switch from coaxial to non-coaxial deformation largely due to the thickened sulphide horizon in the South Mine. The sulphides could deform in a ductile manner versus the host slate that had to accommodate the strain in a brittle manner. Riedel shears developed within the slates and in an en-echelon manner. The first Riedel shears to develop are R-shears with R'-shears developed within overlap zones between R-shears – an effect that is prominent in the South Mine. Thus, opposing shear along numerous Riedel shears and low-angle thrusts resulted in the widespread development of contractional and extensional sites within the South Mine promoting mechanical remobilisation of sulphides and durchbewegung structures to develop. With increasing strain, P-shears developed and as the shear segments grew, they interconnected with R-shear segments to develop throughgoing Y-shears eventually forming an anastomosing shear zone (discussed in detail in Chapter 3).

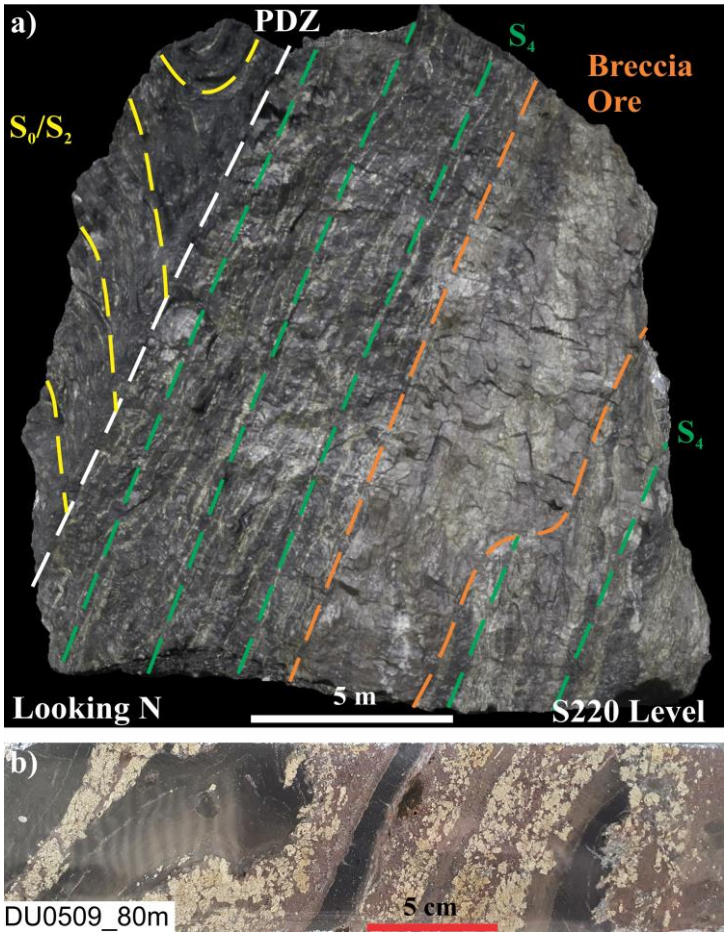

Fig. 2.18: a) SfM-MVS capture of S220_OD430_S1 level (grid reference 4C). In the South Mine the planar ore is preserved where the shear zone is steep and commonly disrupted by metre-scale lenses of breccia ore. The principal displacement zone (PDZ) shown on the capture is relatively thin compared to other examples in this thesis (e.g., Fig. 2.8 – 2.10). The shear zone truncates a low strain domain to the west, which preserves folded S_0, as well as sulphide replaced flexural slip veins that were rotated into parallelism with S_2 as folds tightened. b) Hand specimen example of transposition of folded slate and sulphide. In addition strength contrasts in the sulphides has resulted in banding of sphalerite and pyrite. Sphalerite at the inferred P-T conditions was susceptible to plastic flow hence the finer-grained crystals compared pyrite that annealed to form larger crystals.

Shear zones are effective channel ways for transporting fluids. The shear zone is largely developed within impermeable slates and it is plausible that the Dugald River Shear Zone transported fluids from depth and given that the South Mine represents a bulk area of low mean rock stress, ingress of fluids into this zone may have occurred (Fig. 2.20). Thus, while numerous fracture planes developed within the host rock during which opposing and converging shear created zones of dilation and contraction, respectively, the inferred fluid injection coupled with mechanical remobilisation will have significantly enriched mineralisation.

Phase 2 mineralisation is inferred to have been episodic and probably long-lived given helical inclusion trails and polycrystalline growth of quartz around rounded, vein quartz. Micro-textural and hand specimen investigations indicate that during this period sphalerite was the dominant sulphide species and formed the matrix of high-grade breccia ores. Wall-rock clasts include polycrystalline quartz with sulphides (pyrite, sphalerite, galena and pyrrhotite) and are commonly folded, which includes Phase 1 mineralisation indicated by course-grained sulphides in the matrix (Fig. 2.13e).

2.7.4.1. North Mine

The North Mine is characterised by a steep fabric disrupted by F_2 folds (Fig. 2.19). Here flattening strain dominates, which progressively tightened F_2 folds and rotated veins into parallelism with S_2 (Fig. 2.14b), which given the co-planar D_2 and D_4 are at a high angle to the bulk sub-horizontal E-W shortening of D_4. In underground development, a significant strain gradient can be observed when moving west from the limestone towards the shear zone. Near the limestone contact within the slates, S_0 is distinguishable from axial planar S_2 to F_2 folds. Within meters of the shear zone, F_2 folds are observed to be isoclinal and contained within the transposed fabric, creating high and low strain domains.

The North Mine has a general lack of breccia ore. An explanation for this is that the North Mine lacks a major structural control for breccia ore to have developed, namely, the low-angle thrusts. Thus, zones of contraction and extension were lacking, and the strain was accommodated by progressive fold tightening leading to transposition. The planar ore (stringer and banded ore textures) represents transposed Phase 1 mineralisation and the wallrock to sulphide ratio is too low for durchbewegung structures to develop. Furthermore, given the steep fabric, the development of dilational jogs is limited to undulations in the shear zone and the South Mine acted as a sink for ingress fluid ingress along the shear zone.

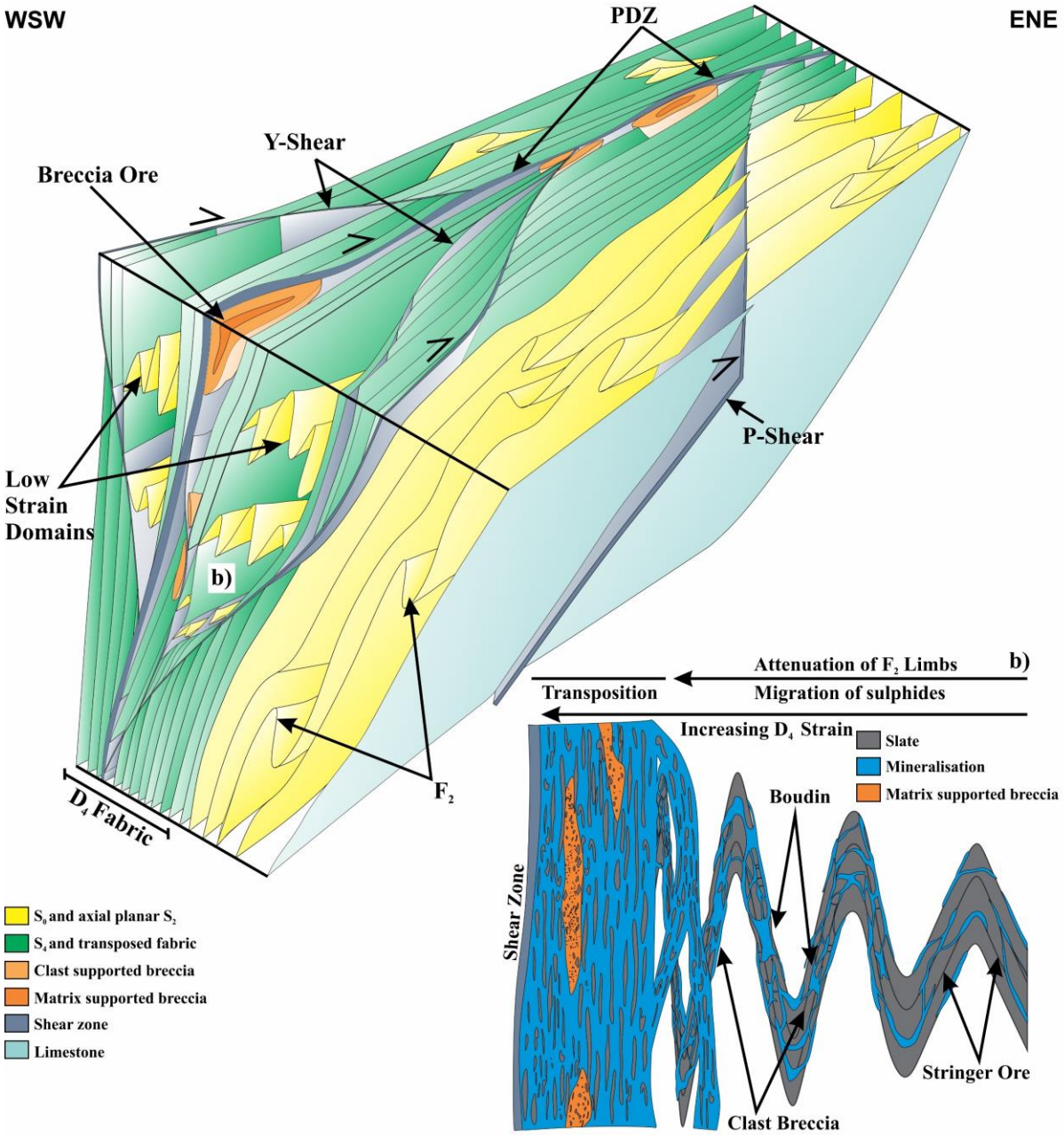

Fig. 2.19: Cartoon sketch of the North Mine. In the North Mine, steeper S_0 and axial planar S_2 with upright folds, which have arrays of sub-parallel veins were transposed during D_4 (b). Transposition has resulted in the development of high and low strain domains. High strain domains have preferentially developed in the sulphide horizon and are marked by the development of a transposition fabric, S_4, with alternating slate and sulphide veins (Fig. 2.13d, 2.18b). Rootless F_2 folds occur within high strain domains and low strain domains are marked by preserved synform-antiform pairs of F_2. Dextral shearing during D_4 resulted in the development of the anastomosing Dugald River Shear Zone. In the North Mine, planar ore is the dominant ore texture and breccia ore is developed in undulations in the shear zone. b) The progressive tightening of folds resulted in the development of a transposition fabric with increasing strain. Attenuation of fold limbs and boudinage resulted in interlinking of veins. The ratio of wallrock to veins and the orientation of the veins are used to label the ore textures (i.e. stringer and planar ore, clast breccia) with overlap between the named textures.

2.7.4.2. South Mine

The South Mine is dominated by breccia ore (Fig. 2.13a). While planar ore is observed in the South Mine, this type of ore texture is limited to steep parts of the shear zone where the effects of S_3 reactivation are limited and has been largely disrupted by durchbewegung textures responsible for the breccia ore. The initial stages of Phase 2 mineralisation in the South Mine follow those of the North Mine, with the exception that along intersection zones of opposing low-angle thrusts to steep, W-dipping fabric, areas of low mean rock stress developed with associated migration of sulphides.

With the onset of shearing, the combination of low-angle thrusts, flattened S_0 and S_2 resulted in a favourable geometry for a step-over to develop in the shear zone. Thus, fluid migrating up the channel way created by the shear zone, which is enveloped by impermeable lithologies, eventually reached the dilational zone created by the step-over. A high sulphide to wall rock ratio resulted and given the ductile nature of the sulphides versus the more brittle nature of the host rocks, durchbewegungs structures developed. Notably, this step-over represents a significant area of low mean rock stress over the rest of the deposit, and it is inferred that most of the Zn-rich fluid migrated here via mixed-state solution.

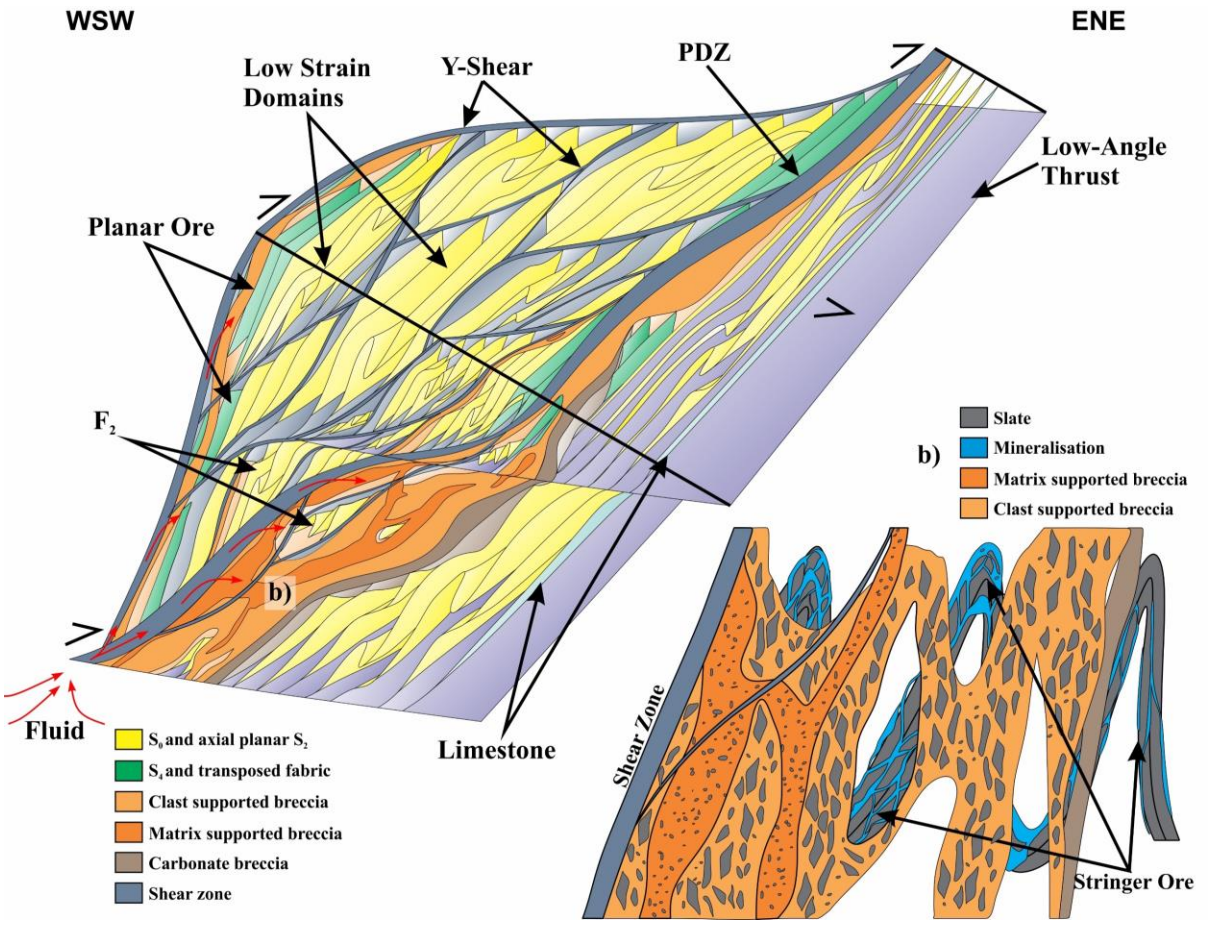

Fig. 2.20: Cartoon sketch of the South Mine. The South Mine is marked by a thicker and higher-grade ore zone, which is dominated by breccia type ore. The dextral step-over in the shear zone resulted in the formation of a dilational jog and a favourable geometry for durchbewegung structures to develop. Early D_4 involved the reactivation of moderate SW-dipping S_3 to form low-angle thrusts with a top-to-the-NE sense of shear. Where the low-angle thrusts intersected steep, W-dipping S_0 and S_2, opposing shear directions resulted in dilation. In areas where low-angle thrusts do not occur, increasing strain during D_4 resulted in transposition and development of planar ore (shown in green). With the onset of shear development, the shear zone acted as a channel way for Zn-rich fluid (red arrows) with the step-over acting as a preferential depositional site. b) With an increase in the sulphide to wall-rock ratio, mechanical shearing (durchbewegung) resulted in enrichment of sulphides and a significant increase in the Zn-grade.

2.8. Conclusion

- The Dugald River deposit has been subjected to several deformation events during the Isan Orogeny. Co-planar progressive deformation during D_2 and D_4 provided favourable extensional sites for the mineralising fluid to deposit sulphides including sphalerite during two phases of mineralisation, namely, Phase 1 and Phase 2 mineralisation.
- Phase 1 mineralisation is associated with progressive tightening of folds during a regionally extensive, ductile deformation event (D_2). Flexural slip, hinge-normal and bedding-normal quartz-carbonate veins were progressively rotated into parallelism with the pervasive S_2 fabric and replaced by sulphides. This phase was sub-economic.
- An inferred period of orogenic collapse, D_3, provided an important structural control for high-grade mineralisation during D_4. Zones of S_3 intensification were heterogeneously developed and prominent in the South Mine. Reactivation of S_3 planes during D_4 produced low-angle thrusts along which opposing shear resulted in contractional and extensional sites, promoting sulphide migration and thickening of the sulphide horizon in the South Mine.
- Early Phase 2 mineralisation was deposited during D_4 ductile shearing as a result of progressive fold tightening which produced a transposed fabric of sulphides and slate (planar ore). The North Mine lacks the structural control of low-angle thrusts, however, the concentration of the sulphides due to transposition resulted in economic grade mineralisation.
- With the exhumation of the deposit and a transition to D_4 brittle-ductile shearing, there was a significant enrichment of the deposit through mixed-state solution, particularly in the South Mine. Zn-enriched fluid exploited channel ways developed by the shearing and the step-over created in the shear zone by low-angle thrusts. Mechanical remobilisation migrated sulphides that deformed in a ductile manner from areas of high to low mean rock stress, infilling cracks in the competent wall rock fragments that were progressively kneaded, milled and rolled into smaller and rounder fragments.

2.9. References

Abu Sharib, A. S. A. A. & Bell, T. H. (2011). Radical changes in bulk shortening directions during orogenesis; significance for progressive development of regional folds and thrusts. Precambrian Research, 188(1-4), 1–20. https://doi.org/10.1016/j.precamres.2011.03.008

Abu Sharib, A. S. A. A. & Sanislav, I. V. (2013). Polymetamorphism accompanied switching in horizontal shortening during Isan Orogeny; example from the Eastern fold belt, Mount Isa Inlier, Australia. Tectonophysics, 587, 146–167. https://doi.org/10.1016/j.tecto.2012.06.051

Aerden, D. G. A. M. (1991). Foliation-boudinage control on the formation of the Rosebery Pb-Zn orebody, Tasmania. Journal of Structural Geology, 13(7), 759–775. https://doi.org/10.1016/0191-8141(91)90002-Z

Anovitz, L. M. & Essene, E. J. (1987). Phase Equilibria in the System CaCO3-MgCO3-FeCO3. Journal of Petrology, 28(2), 389–415. https://doi.org/10.1093/petrology/28.2.389

Arslan, A., Koehn, D., Passchier, C. W. & Sachau, T. (2012). The transition from single layer to foliation boudinage; a dynamic modelling approach. Journal of Structural Geology, 42, 118–126. https://doi.org/10.1016/j.jsg.2012.06.005

Arslan, A., Passchier, C. W. & Koehn, D. (2008). Foliation boudinage. Journal of Structural Geology, 30(3), 291–309. https://doi.org/10.1016/j.jsg.2007.11.004

ASUD (2021). Australian Stratigraphic Units Database

Bell, T. H. (1983). Thrusting and duplex formation at Mount Isa, Queensland, Australia. Nature (London), 304(5926), 493–497. https://doi.org/10.1038/304493a0

Bell, T. H. & Hickey, K. A. (1998). Multiple deformations with successive subvertical and subhorizontal axial planes in the Mount Isa region; their impact on geometric development and significance for mineralization and exploration. Economic Geology, 93(8), 1369–1389. https://doi.org/10.2113/gsecongeo.93.8.1369

Bell, T. H., Reinhardt, J. W. & Hammond, R. L. (1992). Multiple foliation development during thrusting and synchronous formation of vertical shear zones. Journal of Structural Geology, 14(7), 791–805. https://doi.org/10.1016/0191-8141(92)90041-T

Betts, P. G., Giles, D. & Schaefer, B. F. (2008). Comparing 1800-1600 Ma accretionary and basin processes in Australia and Laurentia; possible geographic connections in Columbia. Precambrian Research, 166(1-4), 81–92. https://doi.org/10.1016/j.precamres.2007.03.007

Betts, P. G., Giles, D., Mark, G., Lister, G. S., Goleby, B. R. & Ailleres, L. (2006). Synthesis of the Proterozoic evolution of the Mt Isa Inlier. Australian Journal of Earth Sciences, 53(1), 187–211. https://doi.org/10.1080/08120090500434625

Bierlein, F. P., Maas, R. & Woodhead, J. (2011). Pre-1.8 Ga tectono-magmatic evolution of the Kalkadoon-Leichhardt Belt; implications for the crustal architecture and metallogeny of the Mount Isa Inlier, northwest Queensland, Australia. Australian Journal of Earth Sciences, 58(8), 887–915. https://doi.org/10.1080/08120099.2011.571286

Blake, D.H. (1987). Geology of the Mount Isa Inlier and environs, Queensland and NorthernTerritory. BMR Bull. 225, 83

Blake, D.H. & Stewart, A.J. (1992). Stratigraphic and tectonic framework, Mount Isa Inlier. Detailed Studies of the Mount Isa Inlier. Australian Geological Survey Organisation, 1–11

Bodon, S. B. (1998). Paragenetic relationships and their implications for ore genesis at the Cannington Ag-Pb-Zn deposit, Mount Isa Inlier, Queensland, Australia. Economic Geology, 93(8), 1463–1488. https://doi.org/10.2113/gsecongeo.93.8.1463

Bodon, S. B. (2002). Geodynamic Evolution and Genesis of the Cannington Broken Hill-type Ag-Pb-Zn deposit, Mount lsa Inner, Queensland. Unpublished PhD thesis. University of Tasmania. 443p

Broadbent, G. C., Myers, R. E. & Wright, J. V. (1998). Geology and origin of shale-hosted Zn-Pb-Ag mineralization at the Century Deposit, Northwest Queensland, Australia. Economic Geology, 93(8), 1264–1294. https://doi.org/10.2113/gsecongeo.93.8.1264

Cave, B., Lilly, R. & Barovich, K. (2020). Textural and geochemical analysis of chalcopyrite, galena and sphalerite across the Mount Isa Cu to Pb-Zn transition: Implications for a zoned Cu-Pb-Zn system. Ore Geology Reviews, 124, 103647–. https://doi.org/10.1016/j.oregeorev.2020.103647

Chapman, L. H. (2004). Geology and mineralization styles of the George Fisher Zn-Pb-Ag deposit, Mount Isa, Australia. Economic Geology, 99(2), 233–255. https://doi.org/10.2113/gsecongeo.99.2.233

Chapman, & Williams, P. J. (1998). Evolution of pyroxene-pyroxenoid-garnet alteration at the Cannington Ag-Pb-Zn deposit, Cloncurry District, Queensland, Australia. Economic Geology, 93(8), 1390–1405. https://doi.org/10.2113/gsecongeo.93.8.1390

Connor, A. G., Johnson, I. R. & Muir, M. D. (1982). The Dugald River zinc-lead deposit, northwest Queensland, Australia. Proc. Australas. Inst. Min. Metall. No 283, 1 - 19

Connors, K. A. & Page, R. W. (1995). Relationships between magmatism, metamorphism and deformation in the western Mount Isa Inlier, Australia. Precambrian Research, 71(1-4), 131–153. https://doi.org/10.1016/0301-9268(94)00059-Z

Connors, K. A., Proffett, J. M., Lister, G. S., Scott, R. J., Oliver, N. H. S. & Young, D. J. (1992). Geology of the Mount Novit Ranges, southwest of Mount Isa mine, in: Stewart, A.J. & Blake, D.H. (Eds.), Detailed Studies of the Mount Isa Inlier. Bureau of Mineral Resources, Geology and Geophysics, pp. 137–160.

Cook, N. J., Halls, C. & Boyle, A. P. (1993). Deformation and metamorphism of massive sulphides at Sulitjelma, Norway. Mineralogical Magazine, 57(1(386)), 67–81. https://doi.org/10.1180/minmag.1993.057.386.07

Craig, J. R., Vokes, F. M. & Solberg, T. N. (1998). Pyrite; physical and chemical textures. Mineralium Deposita, 34(1), 82–101. https://doi.org/10.1007/s001260050187

Creus, P. K. Sanislav, I. V. & Dirks, P. H. G. M. (2021). Application of SfM-MVS for mining geology: Capture set-up and automated processing using the Dugald River Zn-Pb-Ag mine as a case study. Engineering Geology, 293, 106314–. https://doi.org/10.1016/j.enggeo.2021.106314

Davidson, G. J., Davis, B. K. & Garner, A. (2002). Structural and geochemical constraints on the emplacement of the Monakoff Oxide Cu-Au(-Co-U-REE-Ag-Zn-Pb) deposit, Mt Isa Inlier, Australia, in: Porter, T. M. (Ed.), Hydrothermal Iron Oxide Copper-Gold & Related Deposits: A Global Perspective. PGC Publishing, Adelaide, pp. 49–75.

Davis, B. K. (2017). Dugald River - Orebody Knowledge Study (DROKS). Unpublished report by Orefind

Davis, G. H., Bump, A. P., Garcia, P. E. & Ahlgren, S. G. (2000). Conjugate Riedel deformation band shear zones. Journal of Structural Geology, 22(2), 169–190. https://doi.org/10.1016/S0191-8141(99)00140-6

Davis, T. P. (2004). Mine-Scale Structural Controls on the Mount Isa Zn-Pb-Ag and Cu Orebodies. Economic Geology, 99(3), 543–559. https://doi.org/10.2113/99.3.543

Derrick, G.M., Wilson, I.H. & Hill, R. (1977). Revision of stratigraphic nomenclature in the Precambrian of northwestern Queensland. VII: Mount Albert Group. Queensl. Gov. Min. J. 77, 113–116

Dirks, P. G. H. M., Charlesworth, E. G. & Munyai, M. R. (2009). Cratonic extension and Archaean gold mineralisation in the Sheba-Fairview mine, Barberton Greenstone Belt, South Africa. South African Journal of Geology, 112(3 - 4), 291 - 316. https://doi.org/10.2113/gssajg.112.3-4.291

Dirks, P. H. G. M., Charlesworth, E. G., Munyai, M. R. & Wormald, R. (2013). Stress analysis, post-orogenic extension and 3.01 Ga gold mineralisation in the Barberton greenstone belt, South Africa. Precambrian Research, 226, 157–184. https://doi.org/10.1016/j.precamres.2012.12.007

Dixon, G. & Davidson, G. J. (1996). Stable isotope evidence for thermochemical sulfate reduction in the Dugald River (Australia) strata-bound shale-hosted zinc-lead deposit. Chemical Geology, 129(3-4), 227–246. https://doi.org/10.1016/0009-2541(95)00177-8

Feltrin, L., McLellan, J. G., & Oliver, N. H. S. (2009). Modelling the giant, Zn-Pb-Ag Century Deposit, Queensland, Australia. Computers & Geosciences, 35(1), 108–133. https://doi.org/10.1016/j.cageo.2007.09.002

Finlow-Bates, T. & Stumpfl, E. F. (1979). The Copper and Lead-Zinc-Silver orebodies of Mt Isa Mines, Queensland: Products of One Hydrothermal System. Ann. la Soc. Geol. Belgique, 102, 497 - 517

Foster, D. & Austin, J. (2008). The 1800–1610Ma stratigraphic and magmatic history of the Eastern Succession, Mount Isa Inlier, and correlations with adjacent Paleoproterozoic terranes. Precambrian Research, 163(1-2), 7–30. https://doi.org/10.1016/j.precamres.2007.08.010

Foster, D. R. W. & Rubenach, M. J. (2006). Isograd pattern and regional low-pressure, high-temperature metamorphism of pelitic, mafic and calc-silicate rocks along an east-west section through the Mt Isa Inlier. Australian Journal of Earth Sciences, 53(1), 167–186. https://doi.org/10.1080/08120090500434617

George, K-L. (2011). Mineralisation processes at the Dugald RIver Pb-Zn-Ag deposit, Mount Isa Eastern Inlier, NW Queensland. Unpublished honours thesis. James Cook University of North Queensland. 143pp

Gibson, G. M. & Hitchman, A. P., 2005. Project I1 Final Report. Geoscience Australia. Canberra

Gibson, G.M., Henson, P.A., Neumann, N.L., Southgate, P.N. & Hutton, L.J. (2012). Paleoproterozoic-earliest Mesoproterozoic basin evolution in the Mount Isa region, northern Australia and implications for reconstructions of the Nuna and Rodinia supercontinents. Episodes 35, 131–141. https://doi.org/10.18814/epiiugs/2012/v35i1/012

Gibson, G. M., Rubenach, M. J., Neumann, N. L., Southgate, P. N. & Hutton, L. J. (2008). Syn- and post-extensional tectonic activity in the Palaeoproterozoic sequences of Broken Hill and Mount Isa and its bearing on reconstructions of Rodinia. Precambrian Research, 166(1-4), 350–369. https://doi.org/10.1016/j.precamres.2007.05.005

Gibson, Meixner, A. J., Withnall, I. W., Korsch, R. J., Hutton, L. J., Jones, L. E. A., Holzschuh, J., Costelloe, R. D., Henson, P. A. & Saygin, E. (2016). Basin architecture and evolution in the Mount Isa mineral province, northern Australia; constraints from deep seismic reflection profiling and implications for ore genesis. Ore Geology Reviews, 76, 414–441. https://doi.org/10.1016/j.oregeorev.2015.07.013

Giles, D., Betts, P. G., Ailleres, L., Hulscher, B., Hough, M. & Lister, G. S. (2006). Evolution of the Isan Orogeny at the southeastern margin of the Mt Isa Inlier. Australian Journal of Earth Sciences, 53(1), 91–108. https://doi.org/10.1080/08120090500432470

Gulson, B. L., Perkins, W. G., & Mizon, K. J. (1983). Lead isotope studies bearing on the genesis of copper orebodies at Mount Isa, Queensland. Economic Geology, 78(7), 1466–1504. https://doi.org/10.2113/gsecongeo.78.7.1466

Hobbs, B. E. (1987). Principles involved in mobilization and remobilization. Ore Geology Reviews, 2(1-3), 37–45. https://doi.org/10.1016/0169-1368(87)90022-9

Huston, D. L., Stevens, B., Southgate, P. N., Muhling, P. & Wyborn, L. (2006). Australian Zn-Pb-Ag ore-forming systems; a review and analysis. Economic Geology, 101(6), 1117–1157. https://doi.org/10.2113/gsecongeo.101.6.1117

Jackson, M. J., Scott, D. L. & Rawlings, D. J. (2000). Stratigraphic framework for the Leichhardt and Calvert superbasins; review and correlations of the pre-1700 Ma successions between Mt Isa and McArthur River. Australian Journal of Earth Sciences, 47(3), 381–403. https://doi.org/10.1046/j.1440-0952.2000.00789.x

Klemd, R., Maiden, K. J. & Okrusch, M. (1987). The Matchless copper deposit, South West Africa/Namibia; a deformed and metamorphosed massive sulfide deposit. Economic Geology, 82(3), 587–599. https://doi.org/10.2113/gsecongeo.82.3.587

Large, R. R., Bull, S. W., McGoldrick, P. J., Walters, S., Derrick, G. M. & Carr, G. R. (2005). Stratiform and stratabound Zn-Pb-Ag deposits in Proterozoic sedimentary basins, northern Australia. Econ. Geol. 100th Anniv. Vol. 931 - 963

Le, T, X., Dirks, P. H. G. ., Sanislav, I. V., Huizenga, J. M., Cocker, H. A. & Manestar, G. N. (2021a). Geochronological constraints on the geological history and gold mineralization in the Tick Hill region, Mt Isa Inlier. Precambrian Research, 366, 106422–. https://doi.org/10.1016/j.precamres.2021.106422

Le, T. X., Dirks, P. H. G. ., Sanislav, I. V., Huizenga, J. M., Cocker, H. A. & Manestar, G. N. (2021b). Geological setting and mineralization characteristics of the Tick Hill Gold Deposit, Mount Isa Inlier, Queensland, Australia. Ore Geology Reviews, 137, 104288–. https://doi.org/10.1016/j.oregeorev.2021.104288

Loosveld, R. & Schreurs, G. (1987). Discovery of thrust klippen, northwest of Mary Kathleen, Mt. Isa Inlier, Australia. Australian Journal of Earth Sciences, 34(3), 387–402. https://doi.org/10.1080/08120098708729419

Maiden, K. J., Chimimba, L. R., Smalley, T. J. (1986). Cuspate ore-wall rock interfaces, piercement structures and the localization of some sulfide ores in deformed sulfide deposits. Economic Geology, 81(6), 1464–1472. https://doi.org/10.2113/gsecongeo.81.6.1464

Marshall, B. & Gilligan, L. B. (1987). An introduction to remobilization; information from ore-body geometry and experimental considerations. Ore Geology Reviews, 2(1-3), 87–131. https://doi.org/10.1016/0169-1368(87)90025-4

Marshall, B. & Gilligan, L. B. (1989). Durchbewegung structure, piercement cusps, and piercement veins in massive sulfide deposits; formation and interpretation. Economic Geology, 84(8), 2311–2319. https://doi.org/10.2113/gsecongeo.84.8.2311

Marshall, B. & Gilligan, L. B. (1993). Remobilization, syn-tectonic processes and massive sulphide deposits. Ore Geology Reviews, 8(1-2), 39–64. https://doi.org/10.1016/0169-1368(93)90027-V

Marshall, B., Vokes, F. & Larocque, A. (2000). Regional metamorphic remobilization: upgrading and formation of ore deposits. Rev Econ Geol 11, 19–38

McGoldrick, P. J. & Keays, R. R. (1990). Mount Isa copper and lead-zinc-silver ores; coincidence or cogenesis? Economic Geology, 85(3), 641–650. https://doi.org/10.2113/gsecongeo.85.3.641

McQueen, K. G. (1987). Deformation and remobilization in some Western Australian nickel ores. Ore Geology Reviews, 2(1-3), 269–286. https://doi.org/10.1016/0169-1368(87)90032-1

MMG (2021). MMG Limited mineral resources and ore reserves statement as at 30 June 2021. 220pp

Mueller, A. G. (2020). Structural setting of Fimiston- and Oroya-style pyrite-telluride-gold lodes, Paringa South Mine, Golden Mile, Kalgoorlie; 1. Shear zone systems, porphyry dykes and deposit-scale alteration zones. Mineralium Deposita, 55(4), 665–695. https://doi.org/10.1007/s00126-017-0747-3

Murphy, T. E. (2004). Structural and stratigraphic controls on mineralization at the George Fisher Zn-Pb-Ag Deposit, Northwest Queensland, Australia. Unpublished PhD thesis. James Cook University. 443p

Naylor, M. A., Mandl, G. & Sijpesteijn, C. H. K. (1986). Fault geometries in basement-induced wrench faulting under different initial stress states. Journal of Structural Geology, 8(7), 737–752. https://doi.org/10.1016/0191-8141(86)90022-2

Neumann, N. L., Gibson, G. M. & Southgate, P. N. (2009). New SHRIMP age constraints on the timing and duration of magmatism and sedimentation in the Mary Kathleen fold belt, Mt Isa Inlier, Australia. Australian Journal of Earth Sciences, 56(7), 965–983. https://doi.org/10.1080/08120090903005410

Newbery, S.P., Carswell, J.T., Allnutt, S.L. & Mutton, A.J., 1993. The Dugald River zinc-lead-silver deposit; an example of a tectonised Proterozoic stratabound sulphide deposit, in: International Symposium - World Zinc '93. Hobart, pp. 7–21

Nortje, G. S., Oliver, N. H. S., Blenkinsop, T. G., Keys, D. L., McLellan, J. G. & Oxenburgh, S. (2011). New faults v. fault reactivation; implications for fault cohesion, fluid flow and copper mineralization, Mount Gordon fault zone, Mount Isa District, Australia. Geological Society Special Publication, 359(1), 287–311. https://doi.org/10.1144/SP359.16

O'Dea, M. G., Lister, G., MacCready, T., Betts, P. G., Oliver, N. H. S., Pound, K. S., Huang, W. & Valenta, R. K. (1997). Geodynamic evolution of the Proterozoic Mount Isa terrain. Geological Society Special Publications, 121(1), 99–122. https://doi.org/10.1144/GSL.SP.1997.121.01.05

Oliver, N. H. S., Holcombe, R. J., Hill, E. J. & Pearson, P. J. (1991). Tectono-metamorphic evolution of the Mary Kathleen fold belt, Northwest Queensland; a reflection of mantle plume processes? Australian Journal of Earth Sciences, 38(4), 425–455. https://doi.org/10.1080/08120099108727982

O'Rourke, A. J., Johnson, B. N. B. & King, S. (2017). Century Zn-Pb-Ag, in: Pjillips, G. N. (Ed.), Australian Ore Deposist. Australian Institute of Mining and Mettalurgy, 485 - 492

Page, R. W. (1983). Timing of superposed volcanism in the Proterozoic Mount Isa Inlier, Australia. Precambrian Research, 21(3/4), 223–245. https://doi.org/10.1016/0301-9268(83)90042-6

Page, R. W. & Bell, T. H. (1986). Isotopic and structural responses of granite to successive deformation and metamorphism. The Journal of Geology, 94(3), 365–379. https://doi.org/10.1086/629035

Page, R. W. & Sun, S. S. (1998). Aspects of geochronology and crustal evolution in the Eastern Fold Belt, Mt Isa Inlier. Australian Journal of Earth Sciences, 45(3), 343–361. https://doi.org/10.1080/08120099808728396

Page, R. W. & Williams, I. S. (1988). Age of the Barramundi Orogeny in northern Australia by means of ion microprobe and conventional U-Pb zircon studies. Precambrian Research, 40-41, 21–36. https://doi.org/10.1016/0301-9268(88)90059-9

Perkins, W. G. (1997). Mount Isa lead-zinc orebodies; replacement lodes in a zoned syndeformational copper-lead-zinc system? Ore Geology Reviews, 12(2), 61–111. https://doi.org/10.1016/S0169-1368(97)00004-8

Perkins, W. G. & Bell, T. H. (1998). Stratiform replacement lead-zinc deposits; a comparison between Mount Isa, Hilton, and McArthur River. Economic Geology, 93(8), 1190–1212. https://doi.org/10.2113/gsecongeo.93.8.1190

Reinhardt, J. (1992). Low-pressure, high-temperature metamorphism in a compressional tectonic setting; the Mary Kathleen fold belt, northeastern Australia. Geological Magazine, 129(1), 41–57. https://doi.org/10.1017/S0016756800008116

Riedel, W. (1929). Zur mechanik geologischer Brucherscheinungen. Zentralblatt fur Mineral. Geol. und Palaontolgie 354–368.

Rieger, P., Magnall, J. M., Gleeson, S. A., Oelze, M., Wilke, F. D. H. & Lilly, R. (2021). Differentiating between hydrothermal and diagenetic carbonate using rare earth element and yttrium (REE+Y) geochemistry: a case study from the Paleoproterozoic George Fisher massive sulfide Zn deposit, Mount Isa, Australia. Mineralium Deposita, 57(2), 187–206. https://doi.org/10.1007/s00126-021-01056-1

Roache, T. J., Blenkinsop, T. G., Vearncombe, J. R. & Reddy, S. M. (2004). Shear zone versus fold geometries at the Cannington Ag-Pb-Zn deposit; implications for the genesis of BHT deposits. Journal of Structural Geology, 26(6-7), 1215–1230. https://doi.org/10.1016/j.jsg.2003.11.013

Rubenach, M. J. & Lewthwaite, K. A. (2002). Metasomatic albitites and related biotite-rich schists from a low-pressure polymetamorphic terrane, Snake Creek Anticline, Mount Isa Inlier, north-eastern Australia; microstructures and P-T-d paths. Journal of Metamorphic Geology, 20(1), 191–202. https://doi.org/10.1046/j.0263-4929.2001.00348.x

Rubenach, M. J., Foster, D. R. W., Evins, P. M., Blake, K. L. & Fanning, C. M. (2008). Age constraints on the tectonothermal evolution of the Selwyn Zone, Eastern fold belt, Mount Isa Inlier. Precambrian Research, 163(1-2), 81–107. https://doi.org/10.1016/j.precamres.2007.08.014

Sayab, M. (2009). Tectonic significance of structural successions preserved within low strain pods; implications for thin- to thick-skinned tectonics vs. multiple near-orthogonal folding events in the Palaeo-Mesoproterozoic Mount Isa Inlier (NE Australia). Precambrian Research, 175(1-4), 169–186. https://doi.org/10.1016/j.precamres.2009.09.007

Sheldon, H. A., Schaubs, P. M., Blaikie, T. N., Kunzmann, M., Poulet, T. & Spinks, S. C. (2021). 3D thermal convection in the Proterozoic McArthur River Zn-Pb-Ag mineral system, northern Australia. Ore Geology Reviews, 133, 104093–. https://doi.org/10.1016/j.oregeorev.2021.104093

Smith, J. W., Burns, M. S., & Croxford, N. J. W. (1978). Stable isotope studies of the origins of mineralization at Mount Isa; I. Mineralium Deposita, 13(3), 369–381. https://doi.org/10.1007/BF00206570

Southgate, P. N., Bradshaw, B. E., Domagala, J., Jackson, M. J., Idnurm, M., Krassay, A. A., Page, R. W., Sami, T. T., Scott, D. L., Lindsay, J. F., McConachie, B. A. & Tarlowski, C. Z. (2000). Chronostratigraphic basin framework for Palaeoproterozoic rocks (1730-1575 Ma) in northern Australia and implications for base-metal mineralisation. Australian Journal of Earth Sciences, 47(3), 461–483. https://doi.org/10.1046/j.1440-0952.2000.00787.x

Spampinato, G. P. T., Betts, P. G., Ailleres, L. & Armit, R. J. (2015). Structural architecture of the southern Mount Isa Terrane in Queensland inferred from magnetic and gravity data. Precambrian Research, 269, 261–280. https://doi.org/10.1016/j.precamres.2015.08.017

Spelbrink, L. & George, K-L. (2017). Dugald RIver Orebody Knowledge Study (DROKS). Unpublished internal MMG report

Spence, J. S., Sanislav, I. V. & Dirks, P. H. G. M. (2021). 1750-1710 Ma deformation along the eastern margin of the North Australia Craton. Precambrian Research, 353. https://doi.org/10.1016/j.precamres.2020.106019

Spence, J. S., Sanislav, I. V. & Dirks, P. H. G. . (2022). Evidence for a 1750–1710 Ma orogenic event, the Wonga Orogeny, in the Mount Isa Inlier, Australia: Implications for the tectonic evolution of the North Australian Craton and Nuna Supercontinent. Precambrian Research, 369, 106510–. https://doi.org/10.1016/j.precamres.2021.106510

Spinks, S. M., Pearce, M. A., Liu, W., Kunzmann, M., Ryan, C. G., Moorhead, G. F., Kirkham, R., Blaikie, T., Sheldon, H. A., Schaubs, P. M. & Rickard, W. D. A. (2020). Carbonate replacement as the principal ore formation process in the Proterozoic McArthur River (HYC) sediment-hosted Zn-Pb deposit, Australia. Economic Geology, 116(3), 693–718. https://doi.org/10.5382/econgeo.4793

Swanson, M. T. (2006). Late Paleozoic strike-slip faults and related vein arrays of Cape Elizabeth, Maine. Journal of Structural Geology, 28(3), 456–473. https://doi.org/10.1016/j.jsg.2005.12.009

Tchalenko, J. S. (1968). The evolution of kink-bands and the development of compression textures in sheared clays. Tectonophysics, 6(2), 159–174. https://doi.org/10.1016/0040-1951(68)90017-6

Tomkins, A. G. (2007). Three mechanisms of ore re-mobilization during amphibolite facies metamorphism at the Montauban Zn-Pb-Au-Ag deposit. Mineralium Deposita, 42(6), 627–637. https://doi.org/10.1007/s00126-007-0131-9

Valenta, R. (1994). Deformation of host rocks and stratiform mineralization in the Hilton Mine area, Mt Isa. Australian Journal of Earth Sciences, 41(5), 429–443. https://doi.org/10.1080/08120099408728153

Valenta, R. (1994). Syntectonic discordant copper mineralization in the Hilton Mine, Mount Isa. Economic Geology, 89(5), 1031–1052. https://doi.org/10.2113/gsecongeo.89.5.1031

Vokes, F.M. (1963). Geological studies on the caledonian pyritic zinc-lead orebody at Bleikvassli, Nordland, Norway, 222nd ed. Norges Geologiske UndersØkelse

Walters, S. & Bailey, A. (1998). Geology and mineralization of the Cannington Ag-Pb-Zn deposit; an example of Broken Hill-type mineralization in the eastern succession, Mount Isa Inlier, Australia. Economic Geology, 93(8), 1307–1329. https://doi.org/10.2113/gsecongeo.93.8.1307

Wellman, P. & Dooley, J. C. (1992). Structure of the Mount Isa region inferred from gravity and magnetic anomalies. Exploration Geophysics (Melbourne), 23(1-2), 417–421. https://doi.org/10.1071/EG992417

Whittle, M. A. (1998). Aspects of the geology of the Dugald River (zinc-lead) deposit, northwest Queensland, Australia. Unpublished MSc. thesis James Cook University of North Queensland. 163pp

Williams, P. (2017). Dugald River Petrography: Summary of Key Observations from the 2017 Knowledge Study. Unpublished report by Clump Mountain Geoscience

Withnall, I. W. & Hutton, L. J. (2013). North Australian Craton, in: Jell, P.A. (Ed.), Geology of Queensland. Geological Survey of Queensland, pp. 23–112

Wyborn, L. (1998). Younger ca 1500 Ma granites of the Williams and Naraku batholiths, Cloncurry District, eastern Mt Isa Inlier; geochemistry, origin, metallogenic significance and exploration indicators. Australian Journal of Earth Sciences, 45(3), 397–411. https://doi.org/10.1080/08120099808728400

Xu, G. (1996). Structural geology of the Dugald River Zn-Pb-Ag deposit, Mount Isa Inlier, Australia. Ore Geology Reviews, 11(6), 339–361. https://doi.org/10.1016/S0169-1368(96)00007-8

Xu, G. (1997). Microstructural evidence for an epigenetic origin of a Proterozoic zinc-lead-silver deposit, Dugald River, Mount Isa Inlier, Australia. Mineralium Deposita, 32(1), 58–69. https://doi.org/10.1007/s001260050072

Xu, G. (1998a). A fluid inclusion study of syntectonic Zn-Pb-Ag mineralization at Dugald River, Northwest Queensland, Australia. Economic Geology, 93(8), 1165–1179. https://doi.org/10.2113/gsecongeo.93.8.1165

Xu, G. (1998b). Geochemistry of sulphide minerals at Dugald River, NW Queensland, with reference to ore genesis. Mineralogy and Petrology, 63(1-2), 119–139. https://doi.org/10.1007/BF01162771

Zhang, Y., Sun, F., Li, B., Huo, L. & Ma, F. (2014). Ore textures and remobilization mechanisms of the Hongtoushan copper-zinc deposit, Liaoning, China. Ore Geology Reviews, 57, 78–86. https://doi.org/10.1016/j.oregeorev.2013.09.006

Chapter 3

3D geometry of the Dugald River Shear Zone, Mount Isa Inlier, Australia: 3D modelling of a structurally complex, anastomosing shear zone

Creus, P.K., Sanislav, I.V. and Dirks, P.H.G.M.

Keywords: Mount Isa Inlier, Transpression, Riedel Shear Network, 3D Geological Modelling, Mineral Exploration

3.1. Abstract

The Dugald River Shear Zone is a structurally complex, anastomosing shear zone that hosts high-grade Zn mineralisation within the Dugald River Slate. The Dugald River Zn-Pb-Ag mine is situated within the Mount Isa Inlier, Australia and developed through two phases of mineralisation with high-grade Zn mineralisation intimately associated with the development of the brittle-ductile Dugald River Shear Zone. The first phase of mineralisation occurred during the regionally extensive, D_2 ductile fold and axial planar cleavage forming event and resulted in the development of a sulphide horizon that was a preferential site for strain partitioning during early D_4 ductile deformation, which resulted in a transposition related concentration and thickening of a sulphide horizon and marks the second phase of mineralisation. The Dugald River Shear Zone developed during D_4 where strain rate incompatibilities between a ductile deforming sulphide horizon and the brittle deforming Dugald River Slate resulted in the development of a Riedel shear zone. A high-resolution 3D model of the shear zone was constructed from robust drilling and mapping datasets in which releasing and restraining bends highlight the thickening and thinning of ore lenses, respectively. The 3D model with detailed structural analysis and observations allows for predictive modelling of dilational zones within thoroughgoing Y-shears and are prospective sites for remobilisation of high-grade Zn sulphides as the ore body developed coevally with progressive shearing.

3.2. Introduction

The Dugald River Shear Zone, situated in the metallogenic significant Mount Isa Inlier, hosts the Dugald River Zn-Pb-Ag mine (Fig. 3.1). The elevated Zn grade has a close spatial and temporal relationship with the anastomosing shear zone (see Chapter 2) which is hosted within the graphitic Dugald River Slate of the Mount Albert Group that was deposited during the 1730 – 1640 Ma Calvert Superbasin event (Gibson et al., 2016). The entire Mount Isa Inlier was subjected to the 1650 – 1490 Isan Orogeny (Blake, 1987; Blake and Stewart, 1992; Foster and Austin, 2008) with regionally extensive strike-slip shears and faults developing during wrench tectonics (O'Dea et al., 1997), which we suggest was responsible for the development of the Dugald River Shear Zone.

In Chapter 2, we describe the Zn-Pb mineralisation at Dugald River and that it can be grouped into two phases. The first phase of mineralisation developed during progressive fold tightening during which secondary fold accommodations structures developed and were preferential sites for sulphide deposition and the second phase was associated with sulphide mobilisation and remobilisation during brittle-ductile shearing and resulted in significant enrichment of the deposit. There is abundant research into the role of geological structures in producing economic concentrations of mineralisation (Roache, 2004; Davis, 2004; Murphy, 2004, Kisters, 2005; Creus, 2011; Dirks et al., 2013; Hill et al., 2014; Vollgger et al., 2015; 2020; Basson et al., 2018a, 2018b; Koegelenberg et al., 2019; Blenkinsop et al., 2020; Hillacre et al., 2020) with important geological structures controlling mineralisation including faults, folds and veins with stress, strain, P-T conditions and fluid pressure governing their formation within a progressively deforming host rock.

In this chapter, we are concerned with the role of progressive shear zone development in controlling the distribution of sulphide lenses. Shear and fault zones have been recognised as important channel ways for focussing and transporting fluids from depth (e.g., Hobbs, 1987; Sibson, 1990) and for creating stepovers and bends (Davis and Reynolds, 1996; Swanson, 2005; Ford et al., 2009; Micklethwaite et al., 2015; Hillacre et al., 2020). Stepovers occur where one fault segment overlaps with another of the same trend and bends are curvatures within a fault or shear zone and depending on the shear direction and curvature geometry, are termed restraining or releasing bends. Restraining bends represent areas of high mean rock stress and releasing bends areas of low mean rock stress with fluids migrating from areas of high to low mean rock stress. Thus, identifying releasing bends within a shear zone is paramount for optimised mining as these areas will represent localities of enriched mineralisation and may be associated with thicker ore lenses. Furthermore, the efficacy of releasing bends at hosting mineralisation is dependent on several factors including dip angle of the structure, lithological contrast, width of structure and geometry of the bend and demonstrated using numerical modelling by Ford et al. (2009).

The Dugald River Shear Zone is structurally complex and combined with the graphitic nature of the slate, necessitates close drill spacing to delineate the shear zone and ore body to ensure safe and optimised underground mining. Detailed in this chapter is the methodology adopted to construct a high-resolution, 3D model of a complex, anastomosing shear zone. The robust drilling data combined with mapping data provides an ideal case study of how to interpret structural data to extract information that can be used in 3D modelling and exploration vectoring. Furthermore, with a good understating of the structural framework and geometry of a shear zone, predictive modelling can be applied to determine

where releasing bends may occur within a shear zone and therefore where the highest grades of mineralisation may potentially be found.

3.3. Regional Geology

The Late Paleoproterozoic Mount Isa Inlier together with the MacArthur Basin to its northwest is the largest Zn-Pb province in the world (Huston et al., 2006). Thus, has been the focus of detailed research over decades, mainly to understand the basin and tectonic framework of the Mount Isa Inlier with emphasis on Zn-Pb mineralisation genetic models (e.g., Newbery et al., 1993; Xu, 1996; Murphy, 2004; Roache, 2004; Cave et al., 2020; Chapter 2). Key publications in understanding the regional framework include (e.g., Blake, 1987; Blake and Stewart, 1992; Jackson et al., 2000; Scott et al., 2000; Foster and Austin, 2008; Rubenach et al., 2008; Withnall and Hutton, 2013; Gibson et al., 2016; Le et al., 2021a, 2021b; Spence et al., 2021, 2022), which describe the succession of volcano-sedimentary and igneous rocks formed during a series of successive basin and orogenic events during ~1900 – 1500 Ma. Sixteen tectonic domains have been described with a general N-S trend that has been grouped into the Western and Eastern Fold Belt, separated by the Kalkadoon – Leichhardt Belt (Fig. 3.1b). The domains are superimposed on major depositional basins and basement deposited during three main depositional events (e.g., Gibson et al., 2016); namely, the Leichhardt Superbasin (1790 – 1740 Ma), Calvert Superbasin (1730 – 1640 Ma) and the Isa Superbasin (1640 – 1590 Ma). Two major orogenic events have affected the Mount Isa Inlier (see Blake, 1987; Blake and Stewart, 1992; Foster and Austin, 2008), namely, the 1880 – 1850 Ma Barramundi Orogeny and the 1650 – 1490 Ma Isan Orogen. More recently additional, minor shortening events between 1800 – 1770 Ma (Le et al., 2021a, 2021b) and 1750 – 1710 Ma (see Spence et al., 2021, 2022) have been proposed with associated magmatism.

Five regional deformation events have been recognised as part of the Isan Orogeny. An initial phase of N-S directed shortening (D_1) produced E-W trending regional folds and thrusts (e.g., Bell, 1983; Page and Bell, 1986; Bell, 1991; Lister et al., 1999; Abu Sharib and Sanislav, 2013). The second event (D_2) has been regarded as the main deformational event that produced the N-S trending structural grain of the Mount Isa Inlier (e.g. Bell et al., 1992; Giles et al., 2006; Abu Sharib and Bell, 2011; Abu Sharib and Sanislav, 2013). D_2 structures formed due to E-W directed shortening that resulted in regional N-S trending folds, shears and thrusts, together with a pervasively developed S_2 foliation and peak metamorphism (M_2). The third deformational event (D_3) is associated with an inferred period of orogenic collapse that produced a subtle, sub-horizontal fabric, which includes low-angle thrusts, F_3 folds that locally rotate earlier fabric elements, and a spaced S_3 cleavage (e.g., Xu, 1996; Bell and Hickey, 1998; Davidson et al., 2002; Murphy, 2004; Chapter 2). A fourth deformational event (D_4)

marks the transition from ductile to brittle-ductile deformation during renewed E-W directed shortening and had a pronounced transpressional character (e.g., O'Dea et al., 1997; Bell and Hickey, 1998; Stampinato et al., 2015; Chapter 2). This event is defined by the development of high strain fabrics (S_4) and anastomosing shear zones. The final major deformation event (D_5) resulted from ENE-WSW directed shortening and involved brittle reactivation of major structures (e.g., Xu, 1996; Chapter 2).

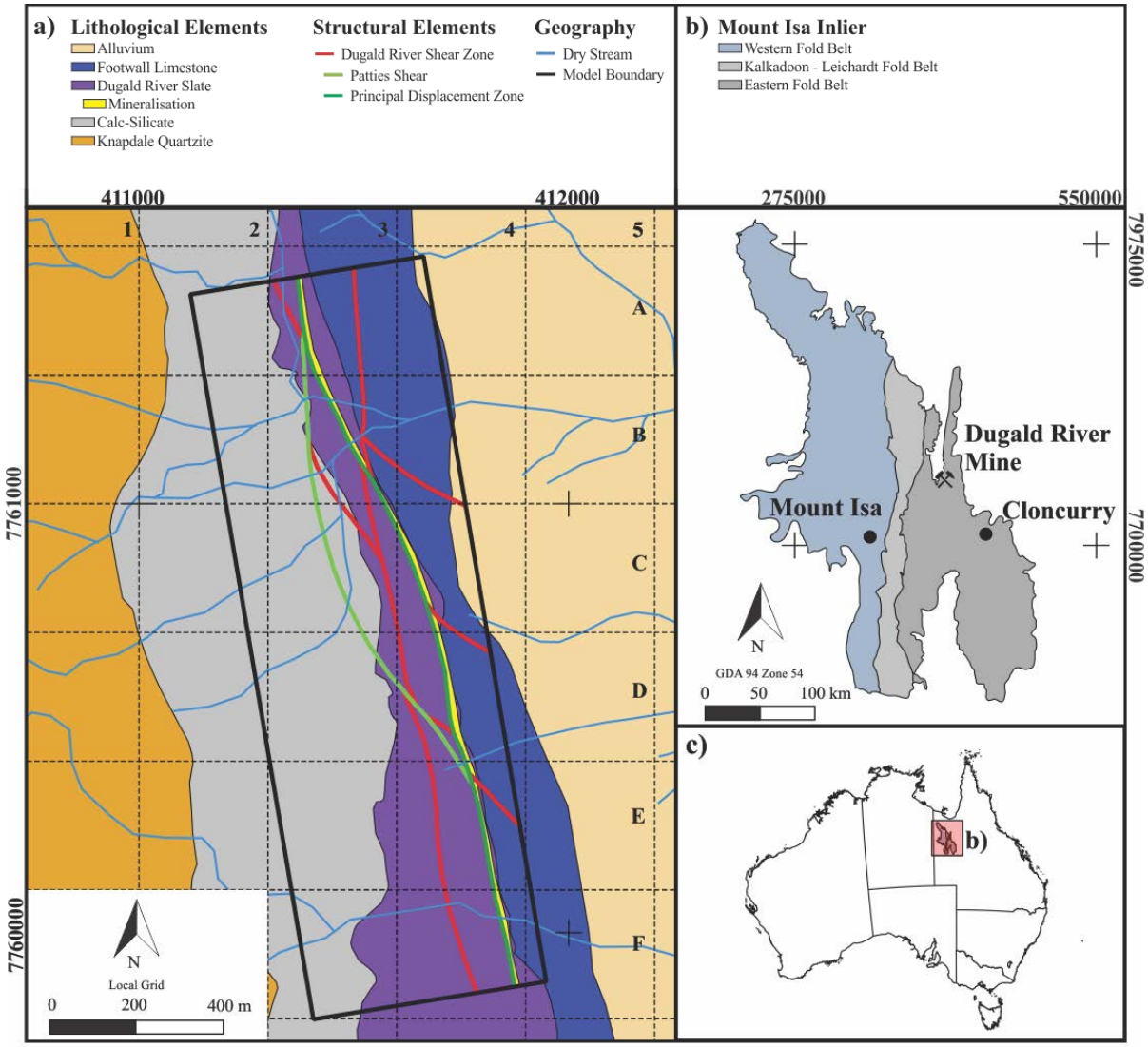

Fig. 3.1: a) Geological map of the Dugald River deposit. A local grid comprising the letters A – F and numbers 1 – 5 are used in this chapter to provide a spatial reference for figures. The Patties Shear Zone and the Principal Displacement Zone are significant shears that form part of the Dugald River Shear Zone. b) Outline of the Mount Isa Inlier using the traditional sub-division of three fold belts. c) Location of the Mount Isa Inlier in NW Queensland, Australia.

3.4. Dugald River Geology

The Dugald River Shear Zone developed within the Mount Albert Group of the Mary Kathleen Domain. The Mount Albert Group comprises mixed carbonate-siliciclastic rocks that were deposited towards the end of the Calvert Superbasin infill and have been sub-divided into four main units, *viz*., the Knapdale Quartzite, the Lady Clayre Dolomite, the Coocerina Formation and the Mount Roseby Schist (Foster and Austin, 2008; Withnall and Hutton, 2013). Age dating by Carson et al. (2009, 2011) provided ages for the Lady Clayre Dolomite and Mount Roseby Schist of 1691 Ma and 1686 Ma, respectively, leading to a suggestion by Withnall and Hutton (2013) that the two units are time equivalents.

The Mount Albert Group underlies a complexly deformed high strain corridor referred to as the Mount Roseby Corridor (Newbery et al., 1993; Chapter 2), characterised by generally steep, W-dipping strata with local variations to the east that is related to east verging folding. The Mount Roseby Corridor is bounded by strike extensive faults with the Mount Roseby Fault defining the eastern boundary and the Coolullah Fault, the western boundary. The Mount Roseby Schist constitutes the eastern half of the Mount Roseby Corridor and comprises a thick package of limestone, calc-silicate and the Dugald River Slates, which host the deposit (Fig. 3.1a).

Up to six deformational (D_1 to D_6) events have been suggested with successive deformation events progressing from ductile (D_1 to D_3) to brittle-ductile (D_4) and lastly brittle (D_6; Newbery et al., 1993; Xu, 1996; Chapter 2). The first deformation event, D_1, is associated with N-S directed shortening in the Mount Isa Inlier (e.g., Bell, 1983, 1991; Page and Bell, 1986; Stewart and Blake, 1992; Abu Sharib and Sanislav, 2013). At Dugald River, structural elements associated with D_1 include E-W trending folds (F_1) and an axial planar cleavage (S_1) preserved 10 km to the south of the deposit (see Xu, 1996) and as inclusion trials within syn-D_2 porphyroblasts (Chapter 2). However, within the deposit, D_1 structural elements have largely been overprinted by subsequent deformation events.

The second deformation event, D_2, represents the dominant fabric observed in the Mount Isa Inlier (e.g., Bell et al., 1992; Betts et al., 2006; Abu Sharib and Bell, 2011; Abu Sharib and Sanislav, 2013) and the Mount Roseby Corridor (Newbery et al., 1993; Xu, 1996; Chapter 2). Structural elements associated with D_2 consist of multi-scale, close to isoclinal, N-S trending folds (F_2) and a well-developed axial planar cleavage (S_2) developed during E-W directed ductile shortening. F_1 and F_2 overprinted one another and developed a Type 1 interference pattern (Xu, 1996; Chapter 2), which was disrupted during D_4 (Chapter 2). D_2 is responsible for the overall steep, W-dipping stratigraphy observed in the Mount Roseby Corridor, and resulted from macro-scale, overturned and isoclinal folding with east directed vergence. A penetrative N-S trending S_2 foliation developed in all rocks, and it has a steep westerly dip, with localised easterly dips. An initial phase of mineralisation occurred towards the end of D_2 (Phase 1 mineralisation of Chapter 2) and is associated with progressive fold tightening during which flexural slip, hinge-normal and layer-normal quartz-carbonate veins were progressively rotated into parallelism with the pervasively developed S_2 fabric, and coevally replaced by sulphides. In addition, during fold tightening, hinge separation occurred as well as boudinage along the fold limbs.

An inferred period of orogenic collapse, D_3, resulted in heterogeneously developed low strain deformation and associated subtle structures (e.g., Xu, 1996; Bell and Hickey, 1998; Davidson et al., 2002; Murphy, 2004; Chapter 2). In the Mount Roseby Corridor, a weak S_3 cleavage developed in the Dugald River Slate where it is associated with mm-scale crenulations, and a disjunctive cleavage developed in the Footwall Limestone. The S_3 cleavage has consistent southwest dips and Xu (1996) and described sub-horizontal folds (F_3) on the surface and Davis (2017) in underground development. Zones of S_3 intensification are heterogeneously developed within the southern part of the Dugald River mine with localised rotation of S_0 and S_2 into moderate southwest dips (Xu, 1996; Chapter 2). D_3 is associated with a sub-vertical principal stress direction (Chapter 2) and a top-to-the-E sense of shear (Xu, 1996; Davis, 2017). Notably, zones of intense S_3 were reactivated during early D_4 as low-angle thrusts with a top-to-the-NE sense of shear (Chapter 2) and segmented the Phase 1 mineralisation and major stratigraphic horizons (e.g., the slate and limestone contact).

Brittle-ductile deformation during D_4 is responsible for the development of the Dugald River Shear Zone. In this chapter, we provide a detailed analysis of the progressive deformation during D_4 that resulted in the development of the graphitic, anastomosing shear zone. The final deformation event, D_5 (D_6 of Xu, 1996), is marked by the reactivation of the earlier fabric (Chapter 2). The most striking is the development of fault rocks (breccia and cataclasite) with cohesive and incohesive varieties indicating active deformation into upper crustal levels.

3.5. Dugald River Shear Zone

In Chapter 2, we describe brittle-ductile deformation during D_4 which we suggest culminated in the development of an anastomosing shear zone with coeval high-grade Zn mineralisation. Associated with D_4 is the development of high and low strain domains, where high strain domains are marked by S-C' and transposition fabrics, which includes attenuation of F_2 limbs and S_2 parallel veins. The low strain domains preserve earlier fabric elements, mainly related to D_2 events such as F_2 folds and its associated axial planar S_2 cleavage.

3.5.1. Riedel Shear Network

A detailed structural analysis was undertaken on D_4 related structural elements from which we concluded that the Dugald River Shear Zone developed as a transpressional dextral Riedel-like shear network (Fig. 3.2a). We use the term Riedel-like shear network because Riedel shear networks were defined using analogue experiments of clay (Riedel, 1929) and repeated numerous times over the decades using either clay or sand (e.g., Tchalenko, 1968; Naylor et al., 1986; Barcos et al., 2016) and with the aid of computers, numerical experiments (e.g., Mckinnon and de la Barra, 1998; Cho et al., 2008; Chemenda et al., 2016).

The classic interpretation of Riedel shear zone geometries is that in the early stages of strike-slip fault formation, displacement within basement rocks produces characteristic fault geometries within the overlying cover (e.g., Tchalenko, 1968, 1970; Tchalenko and Ambraseys, 1970; Arboleya and Engelder, 1995). In these idealised models, rigid blocks are moved past each other, simulating strike-slip movement in a basement fault, with the clay/sand layer above representing a homogenous, flat-lying cover sequence. A vertical Riedel shear zone forms in the clay/sand layer where strike-slip shear strain is imposed with slip surfaces developing in predictive geometries and with time sequences (Fig. 3.2b). While the stratigraphy in Dugald River mine is steep, W-dipping (Fig. 3.6b) and currently there is no evidence to suggest a basement fault, there are field-based descriptions in the literature of Riedel shear zones that do not propagate from a basement fault (e.g., Mueller, 2020), or at the very least have not found evidence of a basement fault (e.g., Davis et al., 2000). Furthermore, several publications describe Riedel shear zones for inclined to steep dipping strata that have undergone folding (e.g, Swanson, 2006; Dirks et al., 2009, 2013; Mueller, 2020).

Within Riedel shear zones, fracture surfaces develop in distinctive geometric arrangements and are given names based on their kinematics and orientations (R, P, R', P', Y and T; Fig. 3.2b; e.g., Riedel, 1929; Tchalenko, 1968; Davis et al., 2000; Passchier and Trouw, 2005). R- and P- shears develop synthetic to the shear direction with Y-shears developed within the imposed shear direction. R'- and P'- shears are antithetic to the shear direction and are generally less well-developed than synthetic shears and R'- shears tend to develop in overlap zones between R-shears (Davis et al., 2000). T-shears, or T-fractures, develop parallel to the principal stress direction ($\sigma 1$) with extension parallel to the maximum instantaneous stretching axis (ISA1; Davis and Reynolds, 1996; Passchier and Trouw, 2005). Fractures within Riedel shears zone develop in an en-echelon pattern (e.g., P-shears in Fig. 3.2a) and interconnecting segments (usually R'- and P- shears) develop an anastomosing pattern of shears that envelop lenses (Tchalenko, 1968; Naylor et al., 1986). At Dugald River, P-shears are inferred to have developed as oblique-reverse shears with top-to-the-NE movement as indicated by minor displacement observed at the limestone and slate contact.

In the literature, the geometric arrangement of fractures within a Riedel shear zone is defined by the angle a fracture occurs at with respect to the bulk shear direction (e.g. Tchalenko, 1970; Tchalenko and Ambraseys, 1970; Davis et al., 2000). The angle is described in terms of the internal friction angle (ϕ) of the deforming material relative to the shear direction. In a dextral Riedel shear zone, which is the case for the Dugald River Shear Zone, these are $\phi/2$ for R-shears and $90° - \phi/2$ for R'-shears in a clockwise direction to the shear zone. P-shears develop at $\phi/2$ and $90° - \phi/2$ for P'-shears in an anti-clockwise direction to the shear zone. Extensional T-fractures form at ~45° to the shear direction.

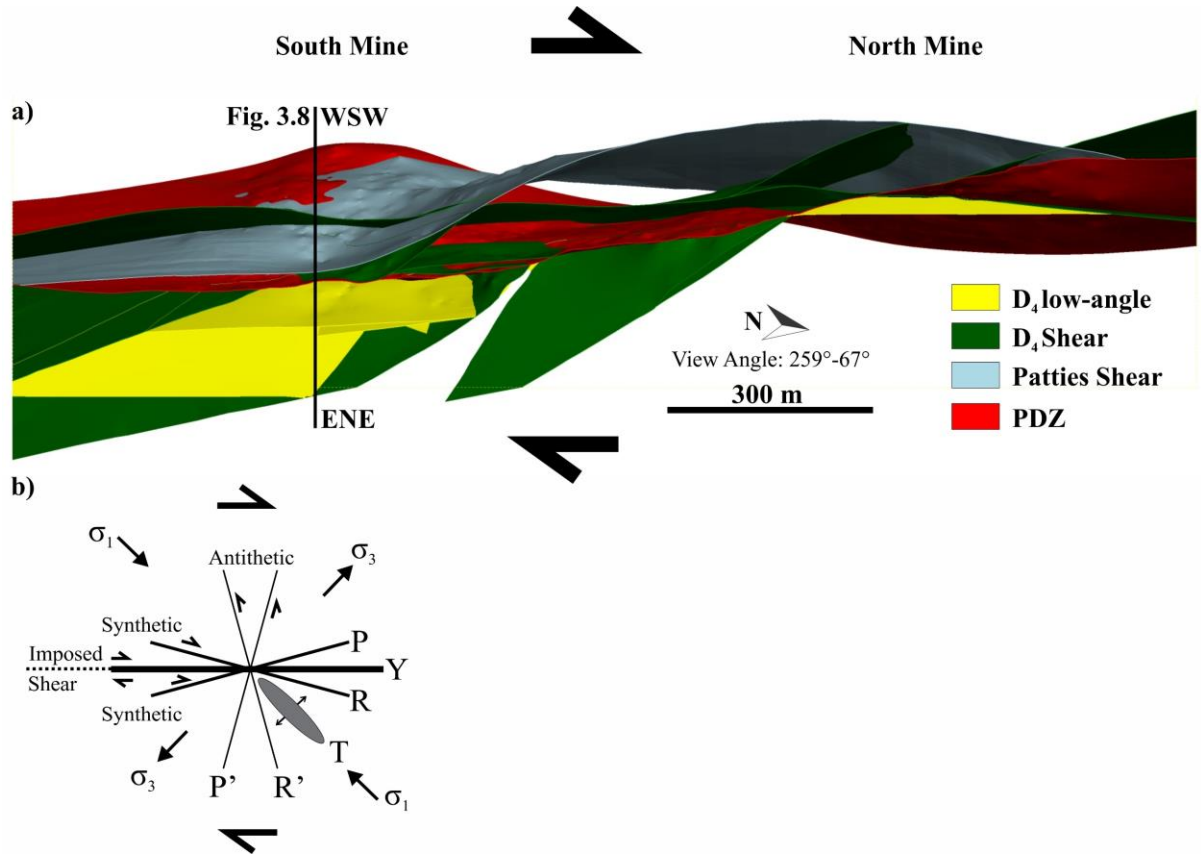

Fig. 3.2: a) Down dip view of the Dugald River Shear Zone within the model boundary. The mine is subdivided into a North and South Mine with each mine accessed by a decline and linked occasionally by thoroughgoing development drives. Zones of intensified S_3 were reactivated during D_4 as arrays of low-angle thrusts (yellow planes) and are pronounced in the South Mine (grid reference: 4D). The location of the cross-section (Fig. 3.8) is shown. b) Schematic diagram of a Riedel shear network within compressional dextral shear. Synthetic structures (R-, P-, Y- shears) develop at a low angle to the shear direction and antithetic structures (R', P'- shears) develop at a high angle to the shear direction. PDZ: principal displacement zone.

3.5.2. Structural Elements

In the northern part of the mine (Fig. 3.2a), high strain zones are marked by transposed fabric that forms S_4 domains from centimetre to metre scale that wraps around low strain domains that preserve older fabric elements (Fig. 3.3; also Xu, 1996). In the zones of transposed fabric, S_0, S_2 and Phase 1 mineralisation were transposed to form metre-scale zones of planar ore which we refer to as early Phase 2 Mineralisation in Chapter 2 (Fig. 3.3b).

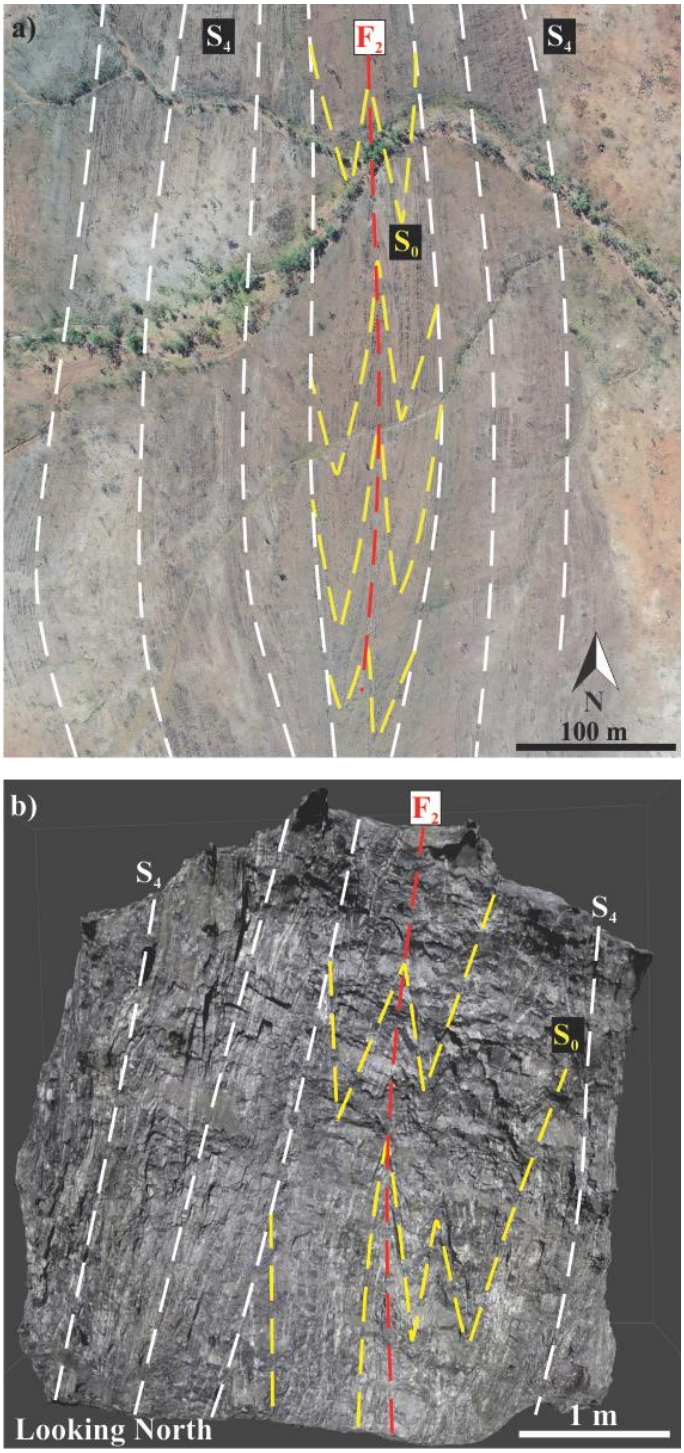

Fig. 3.3: D_4-related transposition of earlier fabric (S_0, F_2, S_2 and Phase 1 mineralisation). a) Drone image was captured to the north of the deposit (coordinates GDA 94 Zone 54: 411520; 776227). Intense progressive deformation resulted in the transposition of S_0 and F_2 into high strain domains representing S_4 that wrap around a lower strain domain with preserved S_0 and F_2. b) Structure-from-Motion Multiview Stereo (SfM-MVS) capture of N150_OD486_S level (grid reference: 3B). Here S_4 comprises transposed S_0, S_2, F_2 and Phase 1 mineralisation and represents a high strain domain that wraps around lower strain domain with preserved S_0 and F_2 folds and D_2 related secondary accommodation mechanism veins. The veins are sulphide replaced quartz-carbonate infill.

Mesoscale shear zone-related lozenge-shaped domains are common in the northern part of the mine (Fig. 3.4). The lozenges represent low strain domains that are enveloped by high strain shear bands that curve into the D_4 fabric. Within low strain domains, rotation of alternating layers has occurred and shear bands are regarded by Williams and Price (1990) as indications of transpression when the main plane of anisotropy (here steep, W-dipping S_2) is sub-parallel to the shear margin (also see Ponce et al., 2013). The oblique shearing during transpression results in a sigmoidal geometry for the lozenges and synthetic slip with respect to the bulk shear direction along the shear bands has resulted in antithetic rotation. Notably, the shear bands are analogous to R-shears and occur as en-echelon arrays.

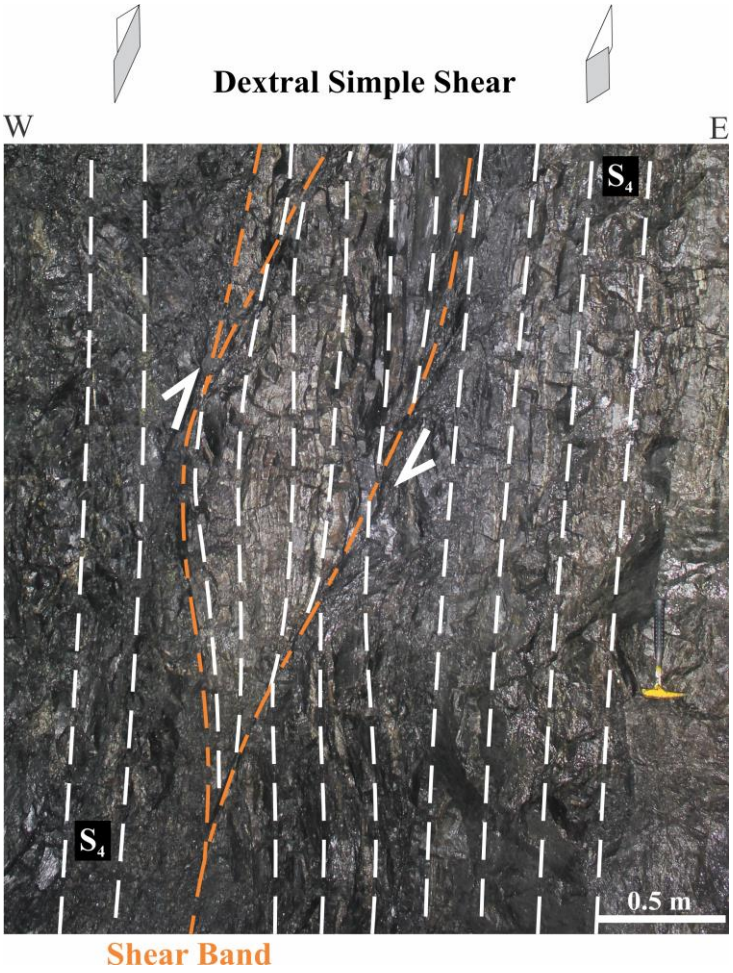

Fig. 3.4: Simple shear related lozenge that is common in the North Mine. The image was captured on the N220_OD491_N level (grid reference: 3A). The asymmetry of the lozenges suggests a top-to-the-NE sense of shear, thus ENE-WSW directed shortening during D_4.

The S-C' fabric lenses are marked by sigmoidal penetrative S-foliation displaced C'-planes. The overall asymmetry of lenses indicates a top-to-the-NE sense of shear. Localised reversal of shears indicates that top-to-the-W shear along steep E-dipping segments of shears has occurred (Fig. 3.5a). The main S-foliation is penetrative and in part defined by the preferred orientation of graphite. Sigmoidal lenses in the S-C' fabric have a fractal characteristic and when picked up, the lenses crumble into smaller lenses along the S-foliation and C'-planes (Fig. 3.5b). The core of lenses is composed of sulphides, including sphalerite. Notably, the C'-planes are parallel to the shear bands that envelope lozenges and are analogues to R-shears. The presence of high and low strain domains and sporadic distribution of S-C' fabric zones within high strain zones are indicative of strain partitioning.

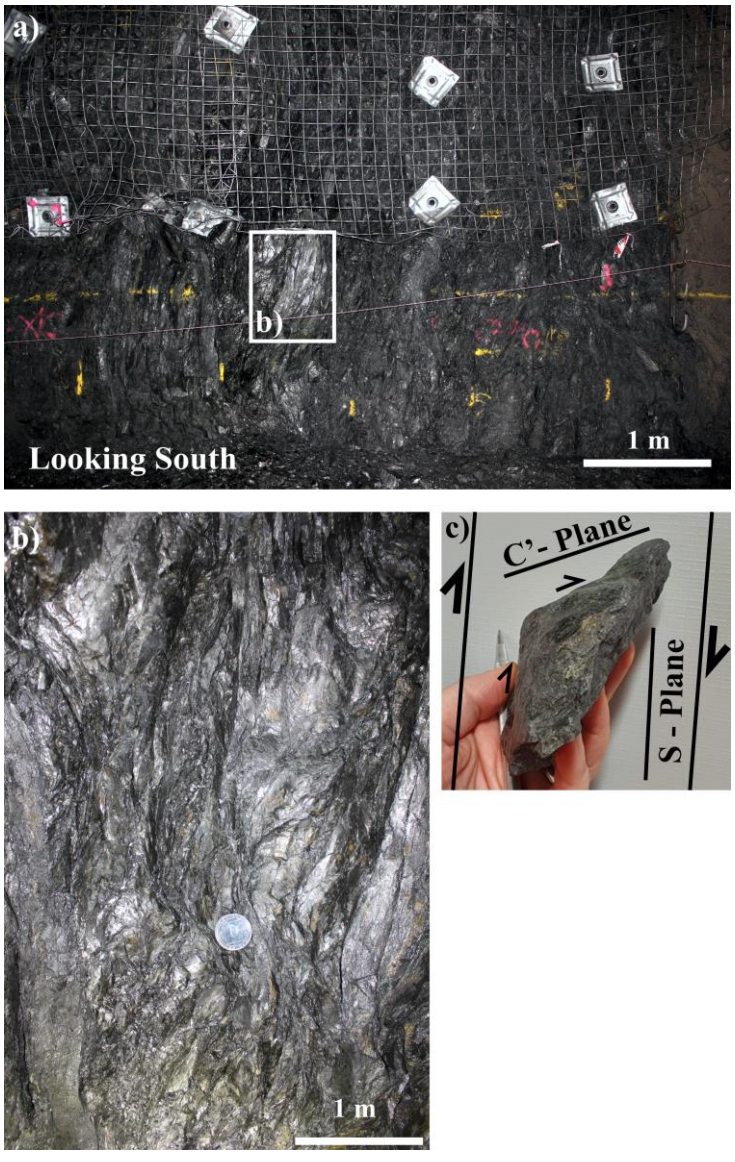

Fig. 3.5: S-C' fabric developed within a D_4-related high strain zone. a and b) The principal displacement zone on the S390_XC395_W level has a localised steep, east dip (grid reference: 4E). c) Example of a sigmoidal lens created by the interaction of S-foliation and C'-planes.

3.5.2.1. D_4 Structural analysis

Several key values are obtained from the structural analysis of D4-related fractures and are presented on equal area, lower hemisphere stereonets (Fig. 3.6). The majority of the D_4 shears plot within the same orientation as the pervasively developed S_2 fabric reaffirming the co-planarity of D_2 and D_4. Shown in Fig. 3.6b, is a best-fit girdle to poles of S_0 and S_2 indicating a gentle northwest plunge due to D_4, which is similar to the plunge observed in inflections in discrete shears and the S-C' lenses. The e1 eigenvalue derived from Bingham Statistics (Fig. 3.6c) provides a view angle for modelling the Riedel shear zone by providing a value to create a sectional view (slice plane) that in this instance is orientated at 081°/23°, which has a perpendicular view that is parallel to the shear zone dip direction and dip of 259°/67° (e.g., Fig. 3.2). The importance of using an appropriate view angle when modelling structural features such as faults and shears is illustrated in Fig. 3.7.

Contour highs on the stereonets for synthetic R- and P- shears have steep, west to southwest dips and antithetic R'-shears have steep, southeast dips (Fig. 3.6a). The acute bisector, e3 at 40°-198° (Fig. 3.6c) of the contour highs for synthetic and antithetic structures provides an important exploration vector as it is sub-parallel to the bulk shear direction and releasing bends may develop along that trend.

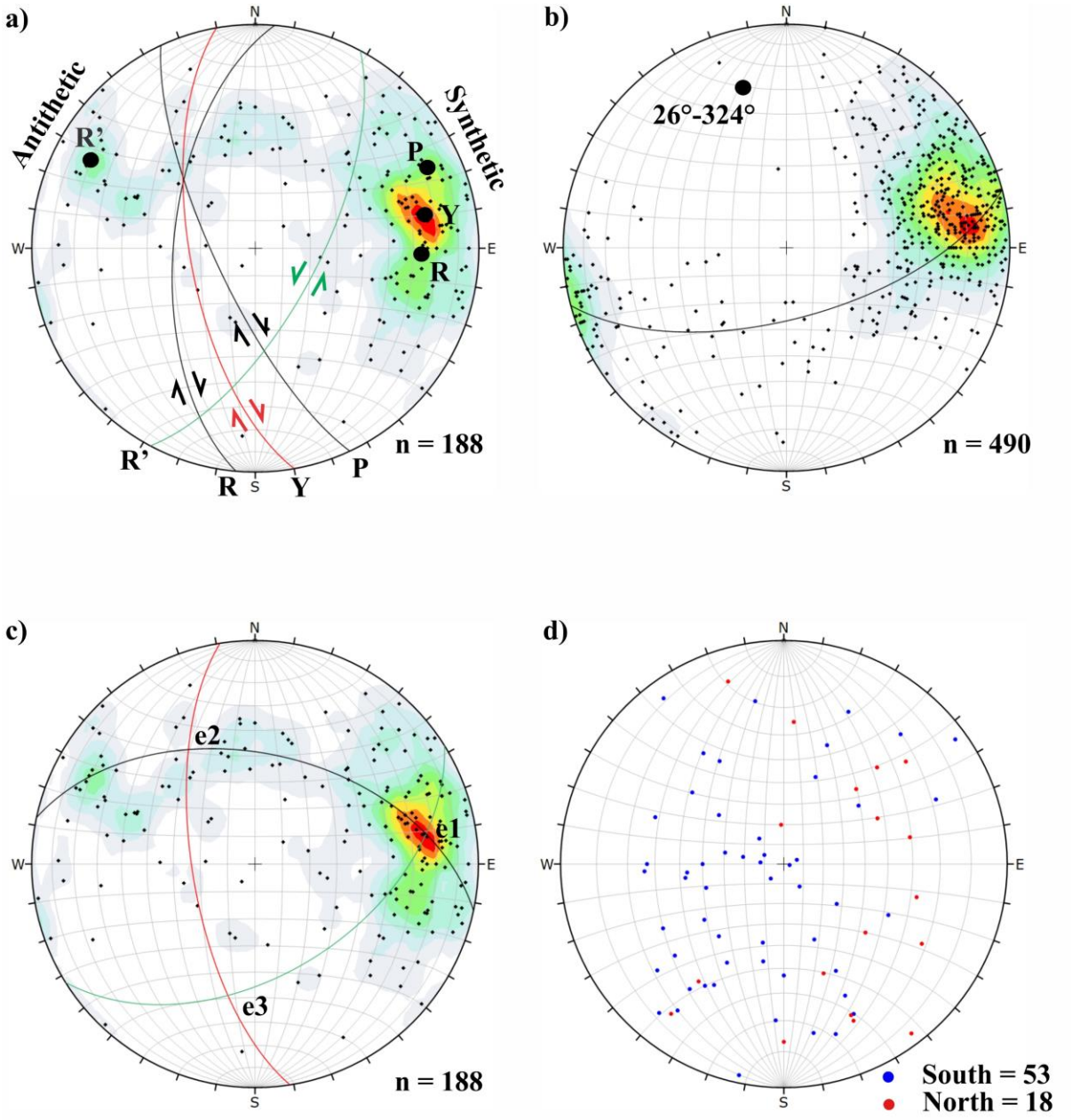

Fig 3.6.: Equal area, lower hemisphere stereoplots of poles to planes. The data were collected during underground face mapping and covered both the North and South Mine. The data used in the stereoplots is filtered to only include measurements with descriptive comments, particularly the scale of the structure measured. a) Poles to D_4 shears show a distinctive Riedel shear network pattern. b) Poles to S_0 and S_2. The synthetic shears plot within the same region as the S_2 cleavage indicates that D_2 and D_4 are co-planar. c) Poles to D_4 shears. Bingham statistics provide three eigenvalues, e1, e2, and e3. e1 at 23°-081° provides a perpendicular modelling view which is parallel to the down-dip of the imposed shear direction (259°/67°; Fig. 3.7a). e2 at 41°-328° is parallel to the intermediate stretching axis defined by the plunges of inflections within steep, W-dipping shears and provides a localised trend for plunges within ore lenses. e3 at 41°-192° is a useful vector as releasing bends in the shear zone will occur along that trend. d) Striations recorded on D_4 shears and low-angle thrusts. The lineations are sub-divided into North Mine (red points) and South Mine (blue points).

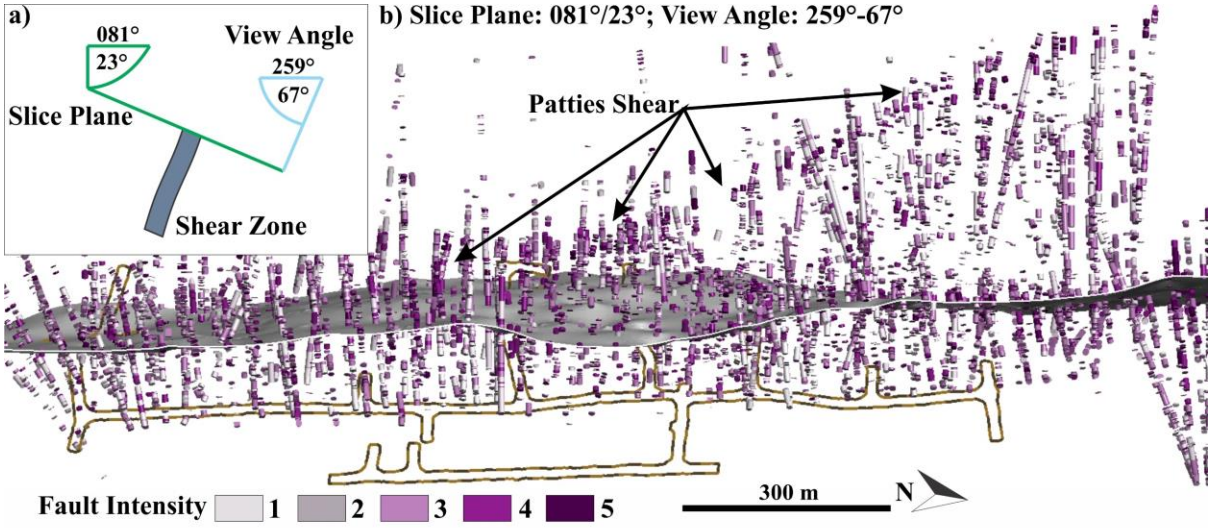
a)
081°
23°
View Angle
259°
67°
Slice Plane
Shear Zone
b) Slice Plane: 081°/23°; View Angle: 259°-67°
Patties Shear
Fault Intensity
1
2
3
4
5
300 m
N

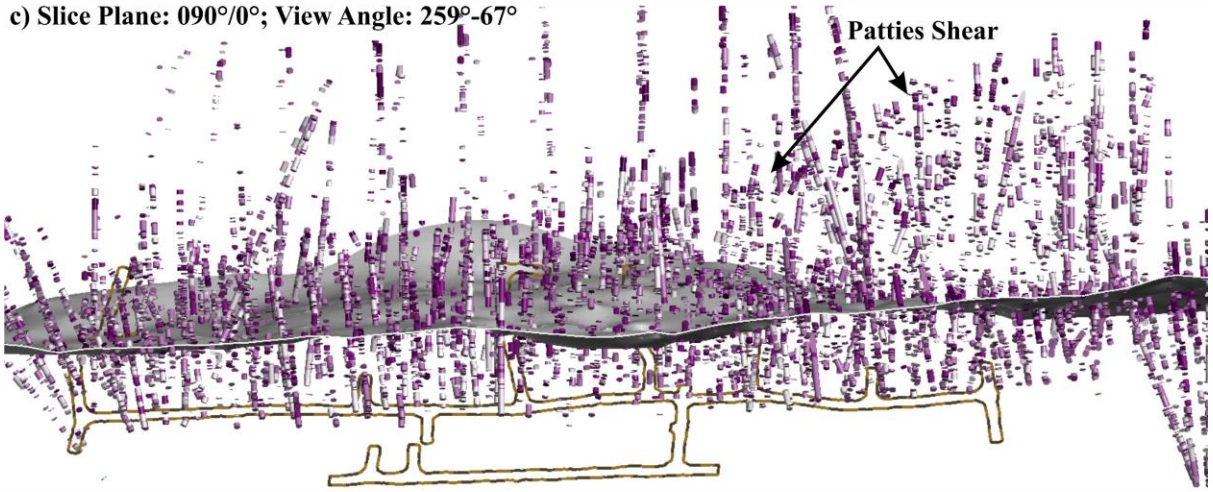
c) Slice Plane: 090°/0°; View Angle: 259°-67°
Patties Shear

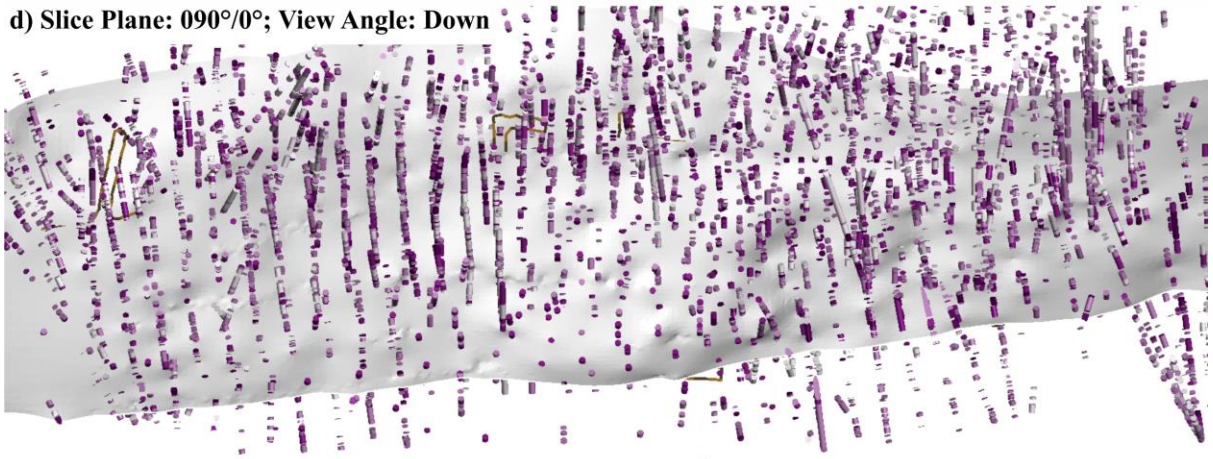
d) Slice Plane: 090°/0°; View Angle: Down

Fig. 3.7: Sectional view of the South Mine to illustrate why choosing an appropriate slice and view angle are important when modelling shears. The development level in the sections is the S365 level (i.e. 365 m below the surface). The shears are logged as categorical data using an intensity rating of 1 to 5. See sub-section 3.6.1.1 for a description of how structures are logged at Dugald River. a) Sketch showing the difference between the slice and view angle. b) The, e1, eigenvalue derived from the stereoplot in Fig. 3.6c provides a slice plane of 081°/23°, which has a perpendicular view angle of 67°-259° and the ideal view for assigning drillhole interval data to discrete shears. c) In this image the slice angle is changed to horizontal and the view angle is the same as (b) and Patties Shear which is clear in (b) is harder to visualise. d) The perpendicular view for a horizontal slice is a down view and in this instance assigning drillhole interval data would be difficult.

Evolved Riedel shear zones may result in the development of Y-shears, which as displacement progresses form throughgoing structures that wear parallel to the bulk shear direction (here 259°/67°; Fig. 3.2a; 3.6a; 3.14). At Dugald River mine, Y-shears are well developed in the southern part of the deposit and are inferred to have been largely driven by the presence of a thick sulphide horizon that acted as a weak horizon within the host slate and provided an ideal site for focused strain partitioning, which were coupled with zones of S_3 intensification that were reactivated as low-angle thrust lenses during early D_4 (Chapter 2). Consequently, in the southern part of the deposit, the shear zone has numerous anastomosing shears developed at all scales (Fig. 3.8). Thus, while a mapping point may suggest for instance a P-shear, the shear plane may 'bend' into the imposed shear direction within the rock mass and further along strike 'bend' into a general R-shear direction (see Fig. 3.11b and c), which makes modelling complex, anastomosing shear zones using dense 3D data intricate. The anastomosing nature of the shears while maintaining steep dips resulted in numerous, multi-scale releasing and restraining bends, with releasing bends providing ideal sites for syntectonic sulphide remobilisation and subsequent high-grade Zn brecciation during D_4 (Fig. 3.13; Chapter 2).

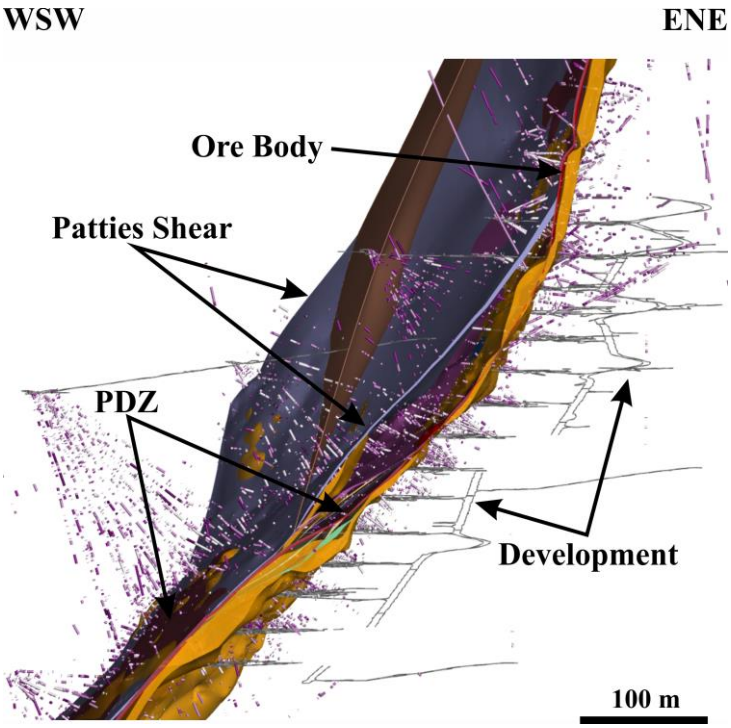

Fig. 3.8: Cross-section through the South Mine (see Fig. 3.2 for location). The shears are randomly coloured and generated as closed surfaces. Included are logged intervals for drilling data (see Fig. 3.7 for colour codes for the intervals) and illustrates the decreased drilling data away from the ore body, particularly towards the west (viz. hangingwall). Mapping data is biased towards the east of the shear zone due to the development that is mainly designed in the footwall of the shear zone/ore body. PDZ: principal displacement zone.

Striations recorded on shear planes are inconclusive (Fig. 3.6d). This is in part due to the graphitic characteristic of the shear zone and the fact that graphite has a low friction coefficient and is suggested to play an important role in fault development as a lubricant (e.g., Rutter et al., 2013; Kirilova et al., 2018). Another reason is that the anastomosing shear zone is comprised of multiple shear planes (Chapter 2), including low-angle thrusts with a top-to-the-NE sense of shear (i.e. dip-slip) that are prevalent in the South Mine. Nonetheless, observations in the North Mine suggest that most of the striations on the steep, W-dipping shears are sub-horizontal (blue points on Fig. 3.6d) indicating predominately strike-slip in this part of the shear zone. In contrast, in the South Mine, the striations also include dip-slip along low-angle thrusts and steeper shear planes (red points on Fig. 3.6d). The presence of both sub-horizontal and sub-vertical striations along steep, D_4 related shears in the South Mine may be a result of initial strike-slip shear which rotated to dip-slip as the finite strain increased. However, more work will need to be done to confirm this.

3.6. 3D Geological Model

In the mining industry, 3D models of the sub-surface form the foundation for optimised mining. Before the widespread adoption of implicit modelling engines by software companies, models were generated using explicit modelling methods using a process of manually digitising and wireframing from data using a largely subjective perspective. While it allows for interpretations to be directly applied during modelling, which includes its own inherent risk, it is laborious, single surface at a time and generally results in wireframes that are jagged where the geology is complicated and lacks the detail required for modern, optimised mining. Furthermore, modelling datasets from varied sources with irregular distribution can be difficult with explicit modelling as the construction of surfaces is done using 2D sections.

With implicit modelling, multiple surfaces and volumes are generated automatically and rapidly using interpolation. The algorithms powering implicit modelling engines allow for millions of data points to be incorporated to solve a scalar function $f(x) = C$, where x is a 3D position vector and is used to return scalar values where coordinates are on the surface (= 0), inside (< 0) or outside (> 0) (see Cowan et al., 2003; Hillier et al., 2014, 2017; Vollgger et al., 2015; Cuomo et al., 2017; Grose et al., 2021). A triangulated surface is then rendered using algorithms such as least marching cubes (Lorensen and Cline, 1987) everywhere the scalar field is 0 and negative/positive values denote inside/outside of the curve. The result is a smooth surface (depending on the resolution defined for the triangulation). The resolution, set by the user, is generally a balance between computational time requirements and data density. A major advantage of implicit models is that more time can be spent testing hypotheses, and the models are reproducible, given the same dataset and parameters.

Lithological data is well-suited to implicit modelling as lithology is generally classified during mapping or logging and all that is required when modelling is choosing which lithology represents positive or negative values for a given contact surface, allowing for lithological models to be generated quickly. To generate lithological volumes, a hierarchy is defined for the lithologies, e.g., Lithology A is younger than Lithology B, which is younger than Lithology C. Planar structural data such as bedding and foliation measurements can be incorporated when solving the scalar function to adjust the gradient of the scalar field (e.g., Vollgger et al., 2015). Incorporating planar structural measurements during implicit modelling allows for complex geometries such as folds and faults to be produced (Cowan et al., 2003; Hillier et al., 2014; Laurent et al., 2016; Grose et al., 2021).

Structural data such as faults and shears are generally not classified during mapping and logging. Exceptions are where distinct markers are present such as juxtaposed lithologies and simple fault

networks. The Dugald River Shear Zone occurs within a single lithology, namely, the Dugald River Slate and as shown on many figures in this thesis (e.g., Fig. 3.7 and 3.8), a single drillhole can intercept numerous shears making classification difficult and time-consuming during logging. Thus, classifying of discrete shears at Dugald River is done explicitly during modelling with the methodology described in this section and surfaces representing the shears produced using implicit interpolation.

Publications using implicit 3D models as a basis for presenting complex structural and orebody geometries have recently gained traction. In part due to workflow-based implicit modelling software, which allows researchers to quickly produce a model and discuss a wide range of topics such as ore body geometries (e.g., Hill et al., 2014; Vollgger et al., 2015, 2020; Basson et al., 2017, 2018a, 2018b; Kitt et al., 2018; Stoch et al., 2018; Hillacre et al., 2021) and country-rock framework to intrusive bodies such as kimberlites and carbonatites (e.g., Basson et al., 2016, 2017; Creus et al., 2018). Due to the smooth surfaces that are produced from implicit modelling, they can be confidently used in "downstream" applications such as geohazard modelling (e.g., Creus et al., 2019).

In this study, we used Leapfrog Geo (Seequent, 2021) and SKUA-GOCAD (Paradigm, 2021) with the GOCAD Mining Suite extension (Mira Geoscience, 2021) for interpreting structural data and modelling the Dugald River Shear Zone.

3.6.1. Structural Data

The structural data used in modelling the Dugald River Shear Zone included dense drilling data, traditional surface and underground mapping, and digitised polylines of structures obtained from Structure-from-Motion Multiview Stereo (SfM-MVS) captures. In this section, we detail the structural datasets that were incorporated into the 3D model and refer to inadequacies with the dataset types that should be considered when constructing surfaces.

3.6.1.1. Drilling data

Prior to the commencement of mining activities in late 2012, there were 467 pre-collared diamond core drillholes used to delineate the ore body. In subsequent years an additional 2546 diamond drill holes were completed, mostly during the period 2015 to late 2019 (taken as the data cut-off date for the 3D model presented here) in underground development (see Fig. 5.4 in Chapter 5). The significant increase in drilling follows a period of care and maintenance while the structural complexities at Dugald River mine were resolved, after which a decision was made to reduce drillhole spacing (see Harris, 2015).

Drill programs at the mine use a fan pattern with a primary investigation (primary drillholes) followed by infill drillholes. Only the primary drillholes were orientated, and these have a spacing of 40 m along strike and 30 m down dip. This was followed by non-orientated infill drilling at 15 m intervals along strike and 10 m intervals down dip in places where the structure is complex (Fig. 3.9; Harris, 2015). However, while primary drillholes are orientated, the graphitic nature of the shear zone and reactivation of discrete shears can be problematic and result in criteria failure for recording orientated point data. For a structure to be recorded as acceptable, orientation marks need to be linked over three successive drillcore runs. Thus, Spelbrink and George (2017) developed a method to record structural data as intervals with a structure (fault, breccia, shear, fracture) given a damage intensity rating increasing from 1 to 5 (Fig. 3.10). In this manner, structural data can be imported as a categorised interval table and used within applicable modelling software. It should be noted that adjacent drillholes with logged intervals of for example fault intensity rating 5 do not necessarily intersect the same structure, considering that discrete structures in the shear zone can pinch and swell completely at a metre scale (Fig. 3.10). An advantage of logging structures as intervals in this manner allows for modelling of the shear system as a closed surface that incorporates the damage zone of discrete structures (e.g., Fig. 3.8).

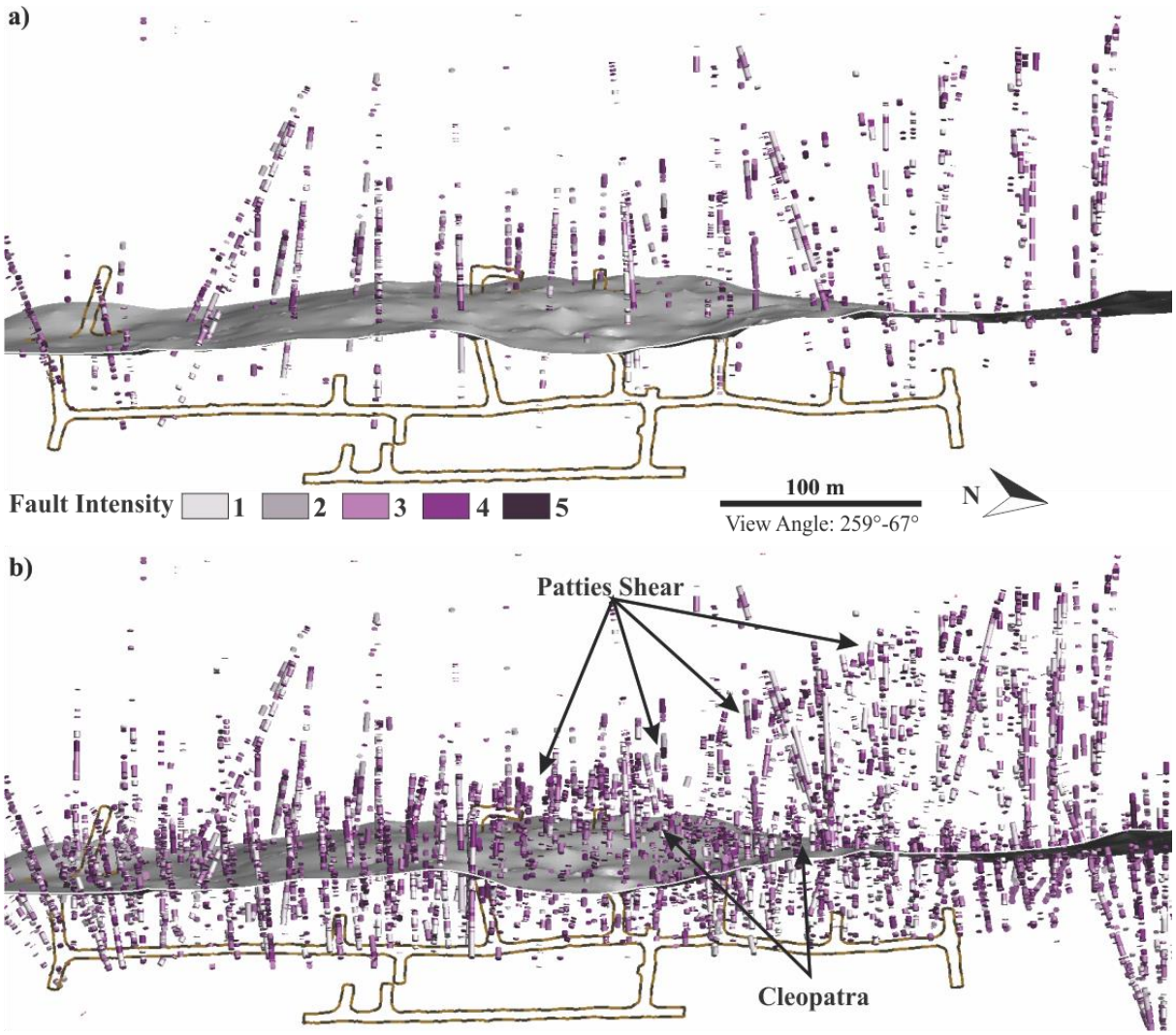

Fig. 3.9: Comparison between (a) primary drilling at 40 m along strike and 30 m down-dip and (b) including infill drilling at 15 m along strike and 10 m down-dip as this is a structurally complex area (South Mine). The figure illustrates why there was a need to reduce the drill spacing as shears are easier to visualise and assign drilling intervals to discrete shears. The development level shown here is S365 (i.e., 365 m below the surface).

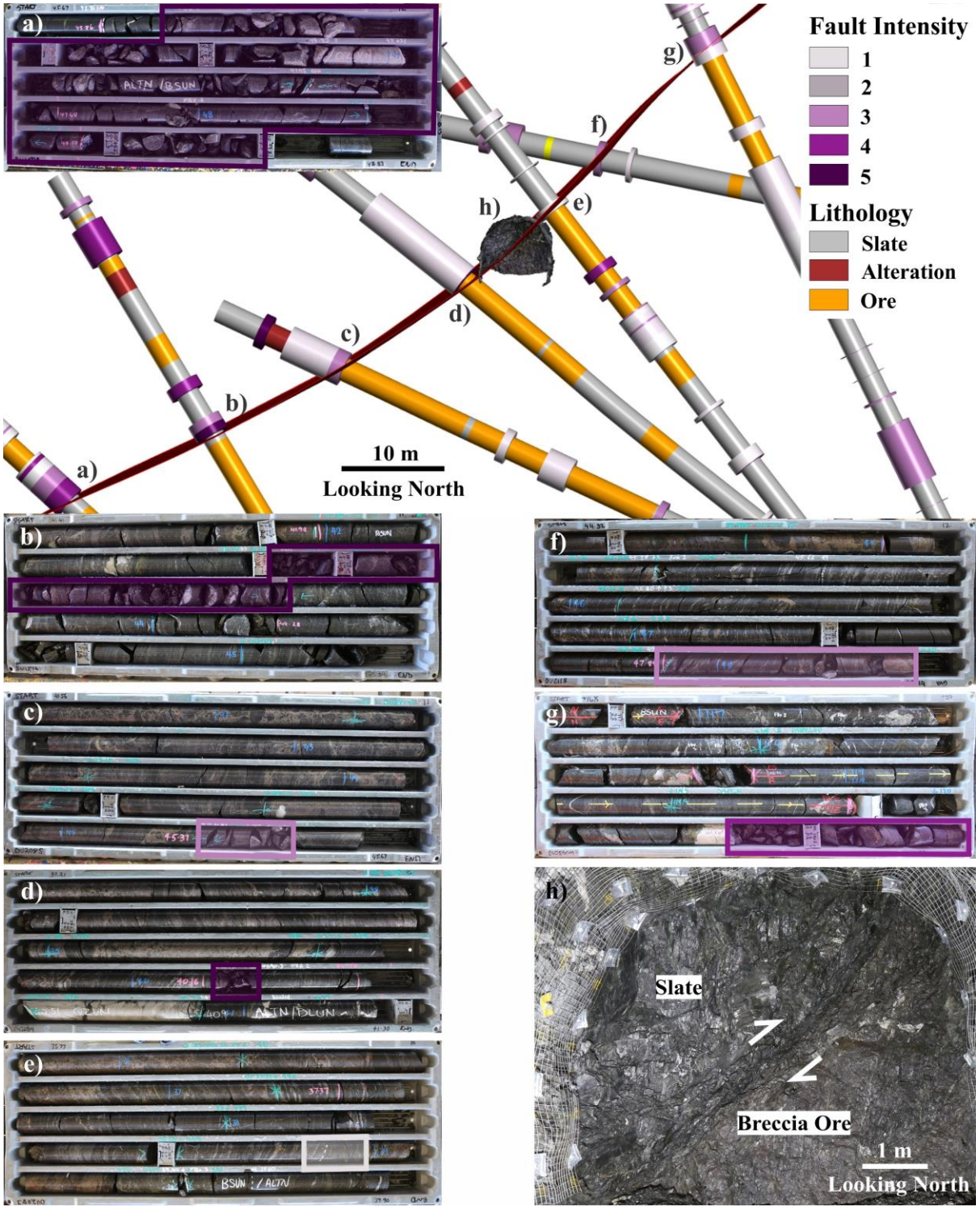

Fig. 3.10: Example of logged intervals for shears and faults (grid reference: 4D). The structures are categorised as shears, faults or fault breccia and assigned an intensity rating. Shown in this figure is the footwall plane of the principal displacement zone, which over a down-dip distance of several 10's of metres has highly variable thicknesses which makes modelling structures with such characteristics difficult without orientation data. The variation of thickness is partly due to reactivation of the structures during D_5 with metre-scale displacements observed (e.g., (h)).

3.6.1.2. Mapping Data

In general mapping data represents a dataset with a high degree of variability in the quality of observations, and measurements may also have a strong bias inherited from the availability of outcrop. In underground mining, geoscientists are limited to active mining areas and safe mining practices limit accessibility to unsupported development faces. Thus, in a deposit like Dugald River where the ore body is adjacent to a sub-vertical shear zone (e.g. Fig. 3.9 - 11), the geological features required to be mapped are typically on development faces (e.g. Fig. 3.3, 3.10 – 11) that cannot be directly measured due to safety concerns. Modern technology such as SfM-MVS has gained popularity in underground mining (see Creus et al., 2021 and references therein) as it allows for virtual outcrops to be recorded as 3D reconstructions (e.g. Fig. 3.3, 3.10 – 11) and measurements digitised using software such as Leapfrog Geo. Thus, it allows for augmenting of standard mapping, however, it should be treated separately from standard mapping as only orientation, scale and type of structure can be recorded with confidence and limitations in what can be recorded for material properties (i.e., lithology, alteration, etc.). In contrast, standard mapping allows for descriptive data collection which includes coordinates, orientation, structure type, kinematic information, comments, material properties and classification of what is recorded and importantly small-scale features such as striations, crenulations, porphyroblasts etc.

When considering mapping data to be used in 3D modelling, we suggest that input data are subdivided into characterised and orientation-only datasets (see Chapter 5). Characterised mapping data refers to descriptive data which includes coordinates, orientation, structure type, kinematic information, comments, material properties and classification of what was recorded. Accordingly, the characterised dataset represents high-confidence data that can be used in interpretations and to determine modelling parameters (e.g. Fig. 3.6c). Orientated mapping data generally only includes coordinates, orientation, and structure type. It represents lower confidence data that may potentially create uncertainty in a model.

Most of the orientated mapping data is from digitised structural discs on SfM-MVS 3D reconstructions. 3D reconstructions from SfM-MVS provide a continuous virtual outcrop of underground development (Fig. 3.11; see Creus et al., 2021). SfM-MVS has been employed at Dugald River since 2017 and has resulted in a significant increase in orientated mapping data. While it allows for continuous structural data in drives, it should be excluded in structural analysis as it can create a statistical bias. Thus, on an individual structure basis, i.e., for constraining a structure while modelling it is useful, but plotting the data on a stereonet even in a sub-sampled manner creates a bias. At Dugald River, the bias is due to the NNW-trending, sub-vertical character of the shear zone and its adjacent ore

body, which allows for NNW-trending development to be designed within the ore zone (Fig. 3.7 – 3.11). Thus, multiple measurements are recorded for the roughly NNW-trending R-, P- and Y- shears. In contrast, R'-shears are at a high angle to the NNW-trending development and are generally only intersected by a single development cut.

Polylines were digitised in Leapfrog Geo, which allows for importing of object files and associated jpeg files. Digitising in Leapfrog Geo permits setting the "inside and outside" of a structure, which is necessary when modelling undulating, steep structures within Leapfrog Geo itself.

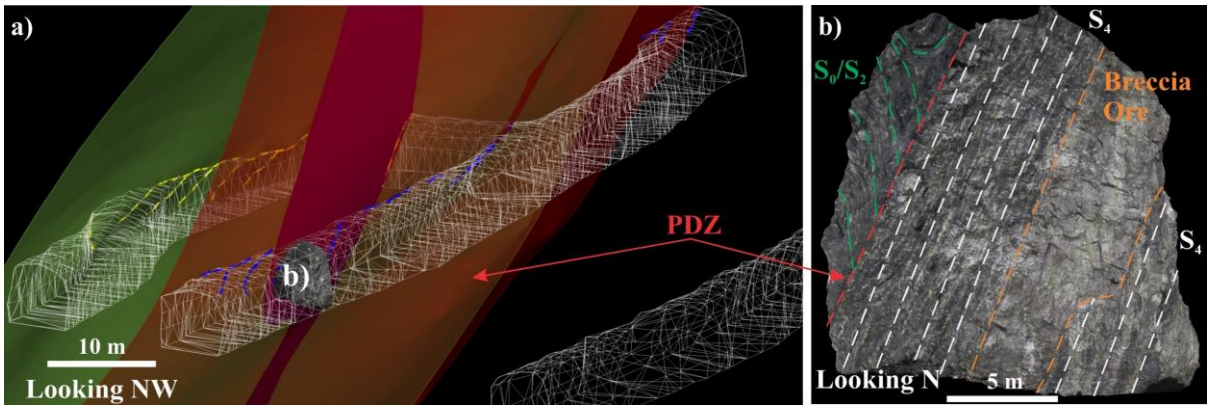

Fig. 3.11 Example of digitised polylines and associated modelled shears (transparent) on the S220 level (220 m below surface; grid reference: 3C). Successive captures using SfM-MVS allows for polylines to be digitised directly on the face of the drives and incorporated into modelled shears. b) In addition, ore lenses can be digitised and modelled as closed volumes with polylines set with inside/outside tangents. PDZ: principal displacement zone.

3.6.2. Model Construction

The Dugald River Shear Zone is a complicated structure to model. In part, due to the numerous shears and faults that comprise the anastomosing shear system, but mainly due to its graphitic and reactivated character. The metre-wide ore lenses in the deposit tend to occur along the footwall of discrete shears with the main ore lens positioned along the footwall of the principal displacement zone (e.g., Fig. 3.8 - 11; Chapter 2). The principal displacement zone is also the furthest east, significant discrete shear with most shears modelled to its west (Fig. 3.1 – 2, 3.8, 3.10). Thus, long-term mine development (Fig. 3.8) generally occurs to the east of the principal displacement zone resulting in a mapping data distribution that is biased towards the footwall, and therefore adjacent to the shear zone. West-trending cross-cuts required to exploit ore lenses to the west, provide valuable information into the geometry and spacing of discrete shears as they intersect the sidewall of drives and can be observed directly using standard mapping. The South Mine at lower levels provides good examples as the anastomosing shear zone has been modelled in detail with a high degree of confidence (Fig. 3.8).

Only discrete shears that can be linked across multiple levels and drives were modelled. A wireframe surface resolution of 4 (i.e., 4 metres in the mine coordinate system) was set, which is roughly the development cut spacing. Two models for the Dugald River Shear Zone were constructed; 1) footwall planes of discrete shears (Active Model, e.g., Fig. 3.2 and 3.12); and 2) closed surface model (e.g., Fig. 3.8).

3.6.2.1. Active Model

The active model was built using wireframe surfaces that represent the footwall planes of discrete shears. The footwall planes were used because observations in drill core and underground development indicate that sulphide mineralisation is concentrated along the footwall of discrete shears. Furthermore, by modelling individual wireframe surfaces, structural domains can be defined to allow for discretised modelling of ore lenses and the generation of form surfaces broadly representing the main plane of anisotropy (e.g., Creus et al., 2019).

Discrete shears were identified using mapping data, which as a minimum has orientation information associated with it, but higher confidence data was given priority. For instance, it is common that multiple data points within proximity to one another will have variable orientation and due to the higher confidence rating of characterised data, they should be preferentially included in wireframe construction. In the construction of the Dugald River Shear Zone, mapping data that could be linked across multiple levels and drives were assigned to the same shear (Fig. 3.12). The principal displacement zone is the primary surface with all other, relevant surfaces terminating against it. A second prominent Y-shear (Patties Shear) developed towards the west of the principal displacement zone (e.g., Fig. 3.1 – 2, 3.8, 3.15).

Intervals from drilling data were added to the shears by using the 'Vein' tool in Leapfrog Geo. The vein tool generates a hangingwall and footwall wireframe surface from either the start or endpoints of a drillhole interval - depending on the orientation of the connection points. The necessary points were added to the wireframe surfaces. This process requires iterations of selecting and adding data to the wireframe surfaces to extend them into the rock mass (Fig. 3.12b) and as the Dugald River Shear Zone is anastomosing, the extended wireframe surfaces may closely overlap with another one. In these instances, the wireframe surfaces are merged to create a single wireframe surface (Fig. 3.12c).

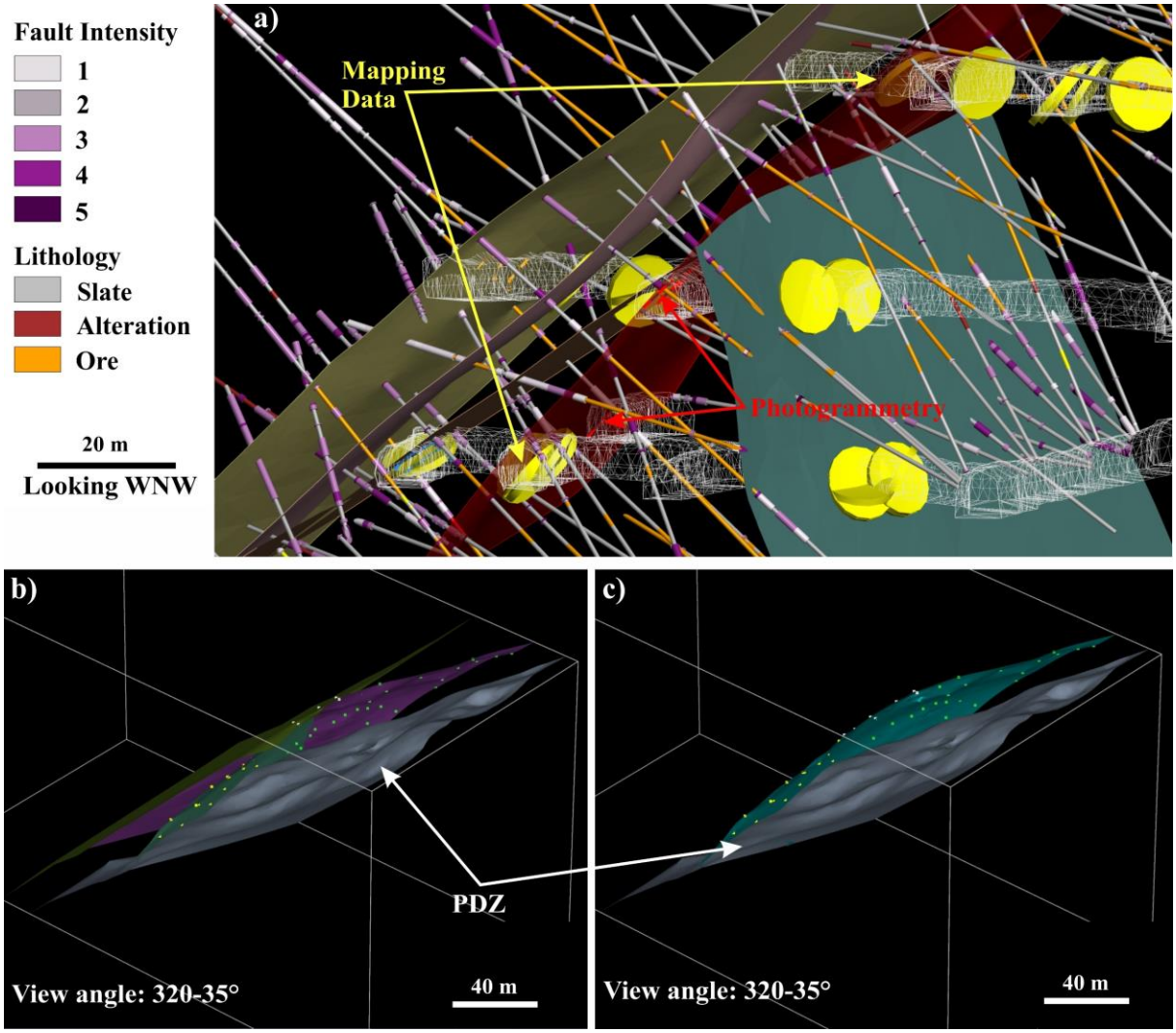

Fig. 3.12: Modelling methodology to illustrate how the footwall planes of the Active Model were modelled. a) Mapping, including traditional techniques and SfM-MVS were used to build initial surfaces, which were then used to guide what intervals from drilling should be assigned to the surface. The cross-section is 50 m thick and occurs within grid reference: 4D. b) The shears as modelled in (a) eventually "connect" with another shear, usually with one that is within a geometric arrangement of a Riedel shear network. The data used to construct the relevant surfaces are then merged to form a single surface that is curvi-planar (c).

3.6.2.2. Closed Surface Model

The closed surface model (e.g., Fig. 3.8) was generated in the same manner as the Active Model, with hangingwall data included in the 'Vein Tool' of Leapfrog Geo. Using the same shear hierarchy as the active model, a continuous shear zone was modelled that realistically represents the discrete shears of the Dugald River Shear Zone. The closed surface model was done after the active model was completed as it is computationally intensive to process at 4 m resolution. With the closed surface model, the damage zones of the shears can be represented in 3D, and these can be used to represent potentially problematic zones for stope mining. Notably, where shears merge poor rock mass may occur as these are zones where sidewall rip-out has occurred (see Swanson, 2005, 2006) forming lenses of rock enveloped by minor shears that may breakout to major shears and cause stope wall instability (Fig. 3.15).

3.7. Discussion

The structural analysis in this study combined with dense drilling data and 3D modelling of the Dugald River Shear Zone provides a unique opportunity to visualise how progressive deformation led to the development of an evolved Riedel shear zone with coeval high-grade Zn mineralisation. From the structural analysis and kinematic observations underground, it can be inferred that the Dugald River Shear Zone developed as a Riedel shear zone in a dextral transpressional system. In transpression, there is kinematic partitioning of simple shear parallel to the shear direction and coaxial flattening orthogonal to the shear zone (e.g., Dewey et al., 1998; Fossen, 2010).

The Dugald River Shear Zone developed during D_4 brittle-ductile deformation. However, pre-existing fabric and competency contrast enacted a pivotal role in the position and development of the shear zone. During the regional D_2 folding and with the coeval development of axial planar cleavage, the stratigraphy in the Mount Roseby Corridor was rotated to sub-vertical orientations by isoclinal, overturned E-verging folds with an associated well-developed axial planar cleavage (S_2). The Dugald River Slates are less competent than the enveloping limestone to the east and the calc-silicate to the west (Fig. 3.1a). While all Mount Albert Group lithologies in the Mount Roseby Corridor were subjected to folding and cleavage development, the slates as a "softer" unit preferentially accommodated strain via fold tightening and limb attenuation. The progressive fold tightening resulted in the formation of quartz-carbonate infill secondary accommodation structures such as flexural slip veining, layer-normal veins, hinge separation and boudinage along fold limbs of tighter folds. The development of the secondary accommodation structures during fold tightening was coeval with the replacement of carbonate by sulphides and in tighter folds resulted in the interlinking of secondary

accommodation structures, which in Chapter 2 we refer to as Phase 1 mineralisation that resembles a crackle breccia, which was preferential sites for future high strain zone development. Notably, Phase 1 mineralisation was sub-economic given an inferred high wall rock to sulphide ratio.

During inferred D_3 orogenic collapse, the principal stress was sub-vertical, which resulted in the development of a subtle sub-horizontal fabric. Of particular importance is the heterogeneous development of a crenulation cleavage, that in the South Mine developed zones of S_3 intensification that locally rotated earlier fabric to flatter, southwest dips. These zones were reactivated early during D_4 as low-angle thrust arrays with a top-to-the-E to NE displacement. Opposing shear along overlapping thrusts resulted in contractional and extensional sites, which promoted the remobilisation of sulphides and marked the onset of Phase 2 mineralisation (see Chapter 2). Notably, early Phase 2 mineralisation records two different sulphide concentration mechanisms during D_4:

1) In the South Mine, the reactivation of zones of S_3 intensification resulted in the mechanical migration of sulphides from areas of high to low mean rock stress due to the development of contractional and extensional zones, respectively.

2) In zones where S_3 spacing was not close enough to develop into thrust arrays, coaxial flattening deformation dominated and resulted in transposition and the development of high strain zones into which sulphides were concentrated. A good example of this is observed in the North Mine where a 100's metre strike extent transposed sulphide horizon developed that in places can be several metres wide (e.g. Fig. 3.3b).

Early Phase 2 mineralisation is inferred to have occurred while the deposit was deforming through ductile means and mineralisation continued while the deposit was exhumed through the brittle-ductile transition. The result of this transition is that the rheological contrast that existed between the host slate and the pre-existing mineralisation produced strain incompatibilities leading to the fracturing of the slate. The rheological stiffer slates had slower strain rates and combined with lower tensile strengths; the slates were prone to fracturing to accommodate the strain rate of the sulphide horizon. Notably, the brittle-ductile transition is marked by the regional wrench tectonics that developed dextral strike-slip shears observed on regional maps (e,g., O'Dea et al., 1997).

Increasing D_4 strain combined with the varying strain rate between the ductile deforming sulphide horizon and the brittle deforming slate resulted in the development of the Dugald River Shear Zone as a Riedel shear zone and can be presented in four steps:

1) Initiation of simple shear resulting in the development of the R-shears, and R'-shears within overlap zones between R-shears.
2) Increasing displacement along R-shears resulted in the development of P-shears.
3) Interconnection between R- and P-shears developed into through-going Y-shears.
4) Eroding of Y-shears into parallelism with the shear direction where R- and P-shears connected to form the Y-shears. Development of a principal displacement zone that accommodated the bulk of the displacement.

The following section discusses the four steps and it should be noted that the first three steps are associated with mostly mechanical remobilisation of sulphides on the scale of 10's of metres. Whereas, the fourth step is inferred to be associated with significant enrichment of the deposit through migration of sulphides from depth through high-permeability Y-shears and resulted in the concentration of sulphides via mixed-state solution (see Chapter 2). Lastly, the Dugald River Shear Zone represented a high-permeability channelway that was enveloped by impermeable slates and dilational sites proximal to the shear zone were preferential sites for sulphide accumulation.

3.7.1. Step 1 – R- and R'- Shears

The first step is inferred to have occurred due to incompatible strain rates between the sulphide horizon and the slates. The first shears that developed are R-shears that are synthetic with respect to the bulk shear direction (Fig. 3.13a) and have a contour high on stereonets of 276°/61° (Fig. 3.6a). In the overlap zones of R-shears, R'-shears developed due to the high compressive stress that occurs in these zones (e.g., Davis et al., 2000) and have a contour high on stereonets of 118°/70° (Fig. 3.6a). At Dugald River, the development of R'-shears in the overlap zones appears to have been heterogeneous, given the available data, as we suggest that the South Mine represents an overlap between at least two R-shears and the North Mine between another two. Furthermore, we suggest that the heterogeneous development of R'-shears in the South Mine was due to the low-angle thrust arrays continuing to develop with the Riedel shear zone and that this will have compounded the compressive stress in the overlap zones between R-shears as opposed to the North Mine where fewer R'-shears have developed. The low-angle thrusts combined with the development of R'-shears in the South Mine is an important structural control on Phase 2 mineralisation by creating additional opposing and converging slip planes that further promoted sulphide remobilisation.

3.7.2. Step 2 – P-Shears

The increasing D_4 strain resulted in R-shear growth which reached a point where the shears were unfavourably orientated to sustain large relative displacements (e.g., Tchalenko, 1970) and P-shears developed to accommodate the strain (Fig. 3.13b). Good examples of P-shears are observed in the footwall development with macro-scale discrete shears modelled (e.g., Fig. 3.1 – 3.2) and have a consistent spacing of ~350 m. The P-shears are synthetic to the dextral shear direction and will have created additional dilation sites, albeit not as effective as the combination of low-angle thrusts and R'-shears prevalent in the South Mine. However, as the P-shears developed en-echelon with regular spacing in response to the rotation of the local principal stress (e.g., Tchalenko, 1970) their distribution is widespread in the shear zone and promoted mechanical remobilisation of sulphides at a local scale, particularly where they intersected R-shears.

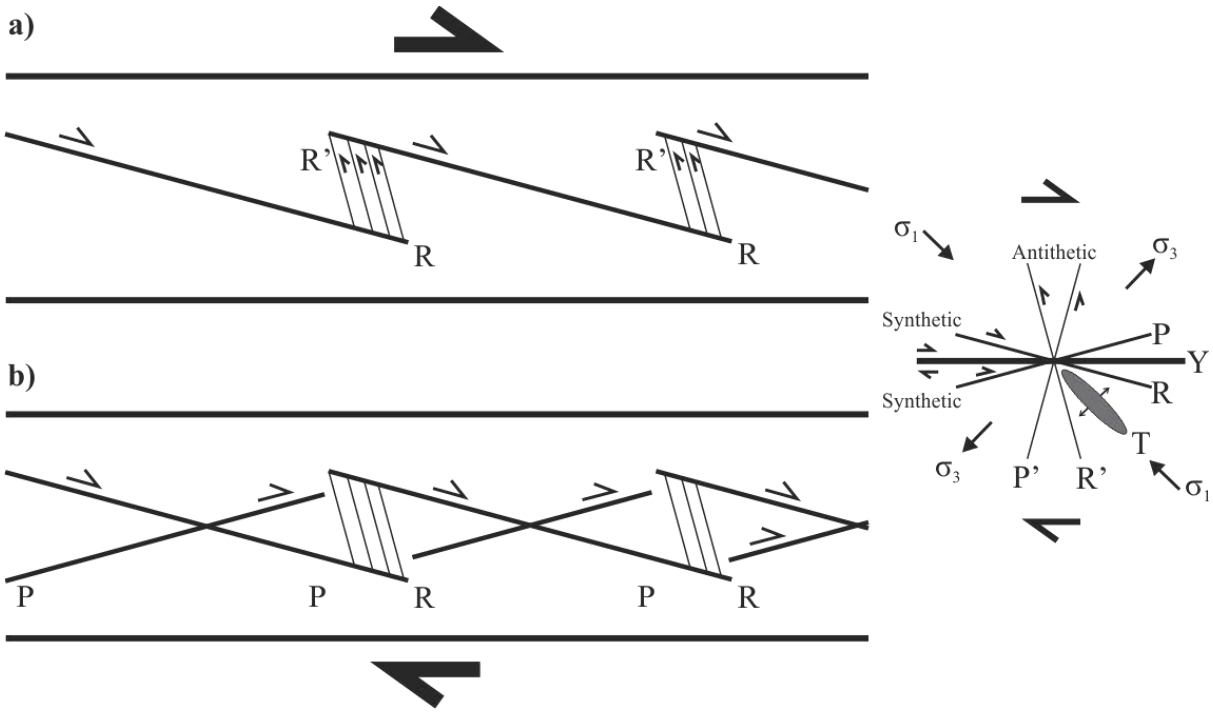

Fig. 3.13: Steps 1 and 2 of Riedel shear zone development. a) R-shears develop first and are the only criteria for a Riedel shear zone to develop and may have R'-shears developed in high compressive areas in overlap zones. At Dugald River, R'-shears develop within the overlap zones of R-shears and are characterised by discontinuous, but thick shears with well-developed cataclastic fault cores. b) P-shears developed when the displacement along R-shears could no longer be sustained. Notably, R- and P-shear displacement occurs in a pulsating manner with local stress switching between R- and P-shear segments. Good examples of P-shears are observed along the footwall of the principal displacement zone within the long-term development of underground workings.

3.7.3. Step 3 – Y-shears

In evolved Riedel shear networks, throughgoing shears (Y-shears) develop by interconnected R- and P- shear segments (Fig. 3.14a, 3.15a). Early development of Y-shears has sharp angles at merger points of R- and P-shears (Fig. 3.14a, 3.15a) and with progressive development starts to wear parallel to the bulk shear direction (Fig. 3.14b, 3.15b), which involves modification through both abrasive and adhesive wear. Abrasive wear results in cataclastic core growth, brecciation and gouge development, and adhesive wear results in sidewall rip-out that create asymmetric lenses of wall rock (Swanson, 2005, 2006). At Dugald River these zones are represented by high-strain zones with a well-developed S-C' fabric (e.g., Fig. 3.5a) with the S- and C'-planes parallel to R- and P-shears, respectively. Abrasive wear is responsible for the development of cataclastic fault cores and was reactivated during late D_5 brittle deformation to form incohesive cataclasites and fault breccia. Furthermore, the sidewall rip-outs pose a geotechnical concern as they will have developed at the scale of stopes with numerous small-scale shears that may result in breakout of stope walls to development level-scale Y-shears (Fig. 3.16).

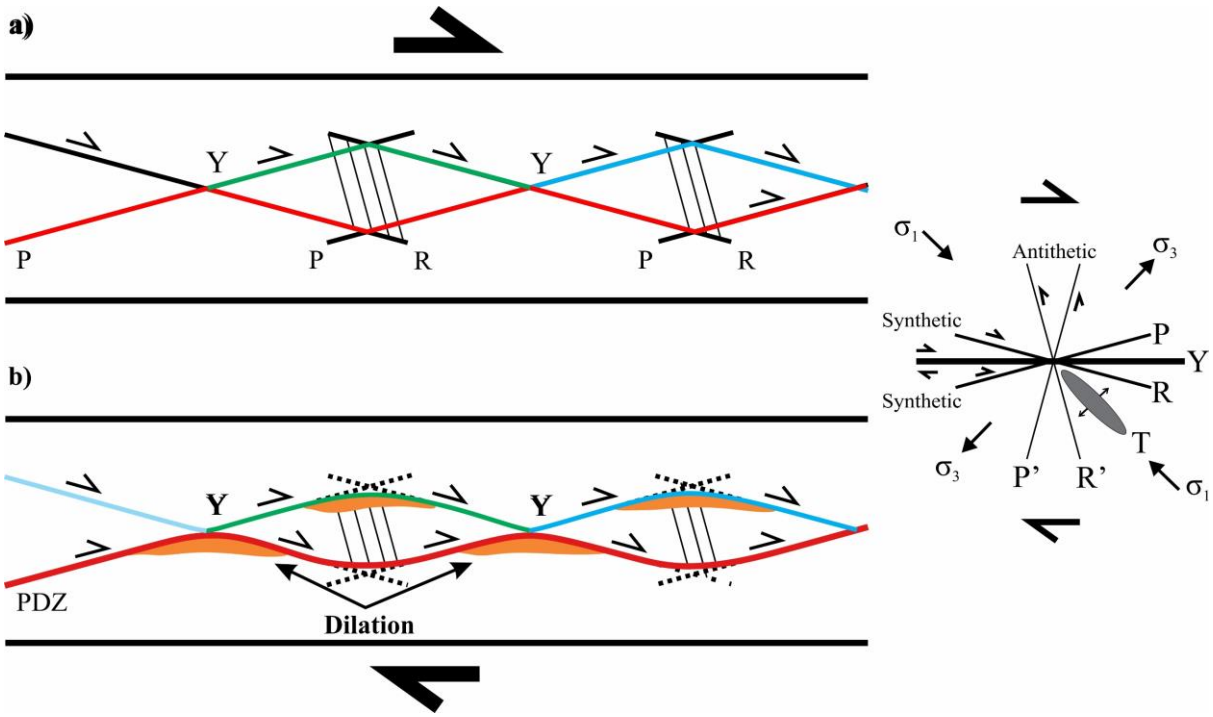

Fig. 3.14: Steps 3 and 4 of Riedel shear zone development (also Fig. 3.15). a) Increasing displacement along R- and P-shears eventually resulted in segments terminating and overlapping with each other. At this stage, a throughgoing Y-shear developed and displacement propagated along the Y-shear. Initially, the Y-shear has sharp segments, which will wear down parallel to the bulk shear direction (b). Depending on the bend direction with respect to the bulk shear direction, a releasing or restraining bend may develop. In dextral shear zones, right-handed bends develop as dilational zones and left-handed bends as contractional. b). A Y-shear develops into a principal displacement zone, which then accommodates the bulk of the displacement. At Dugald River, the principal displacement zone developed along the interface between a thick sulphide horizon and Dugald River Slates.

Fig. 3.15: Idealised 3D representations to assist in visualising steps 3 (a) and 4 (b) of Riedel shear zone development. The surfaces were generated using the contour highs from the stereonets (Fig. 3.6) thus accurately represent the geometry of the R-, P- and Y- shears of the Dugald River Shear Zone, including the principal displacement zone (PDZ).

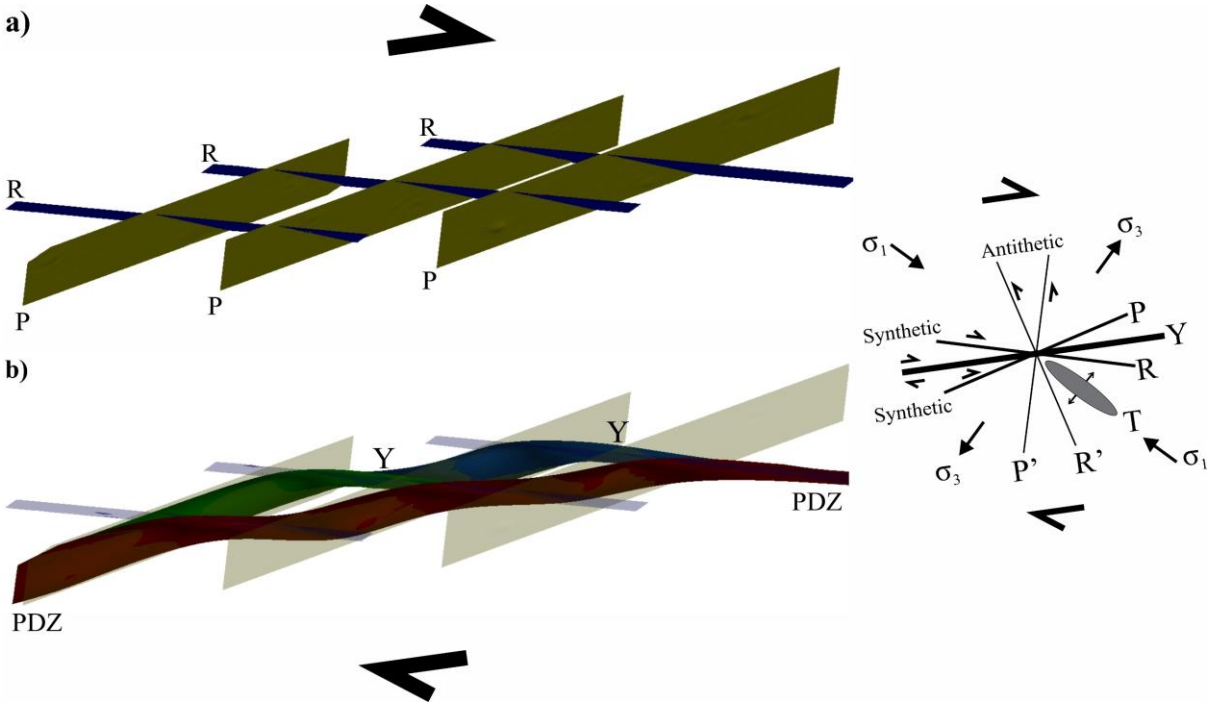

3.7.4. Step 4 – Principal Displacement Zone

During the final step, most of the strain was accommodated along Y-shears, which widened, and one of the Y-shears developed into a principal displacement zone (Fig. 3.14b, 3.15b). At Dugald River, the principal displacement zone developed along the hangingwall of a strike extensive, continuous sulphide horizon. Y-shears are common to the west of the principal displacement zone and bifurcate and merge with it (Fig. 3.7). The principal displacement zone represents a continuous high permeability channel way through which sulphides migrated and dilational zones developed along the structure (Fig. 3.14). At Dugald River, the dilational zones are responsible for high-grade Zn brecciation in the South Mine as well as hangingwall lenses that occur along the footwall of other major Y-shears like the Patties Shear (Fig. 3.14).

Fig. 3.16: As Reidel shear zone development progresses R- and P-shear segments merge to form throughgoing Y-shears. a) At the Dugald River the terminations of R- and P-shears eroded to form zones of abrasion that when drilled through are marked by numerous intersections that are difficult to link to discrete shears. Furthermore, the intervals comprised fault cores of cataclasite and fault breccia. b) View of the S340 stope voids in the South Mine showing the distance of the void walls to the design surface. The zones of abrasion are of geotechnical concern as stopes that are designed in these zones are subject to overbreak. c) Idealised 3D representation of the eroding of R- and P- shear termination zones to develop Y-shears, which also results in the development of abrasion zones. The half arrows indicate the propagation direction of the principal displacement zone (PDZ) which may develop into an extensional and contractional zone.

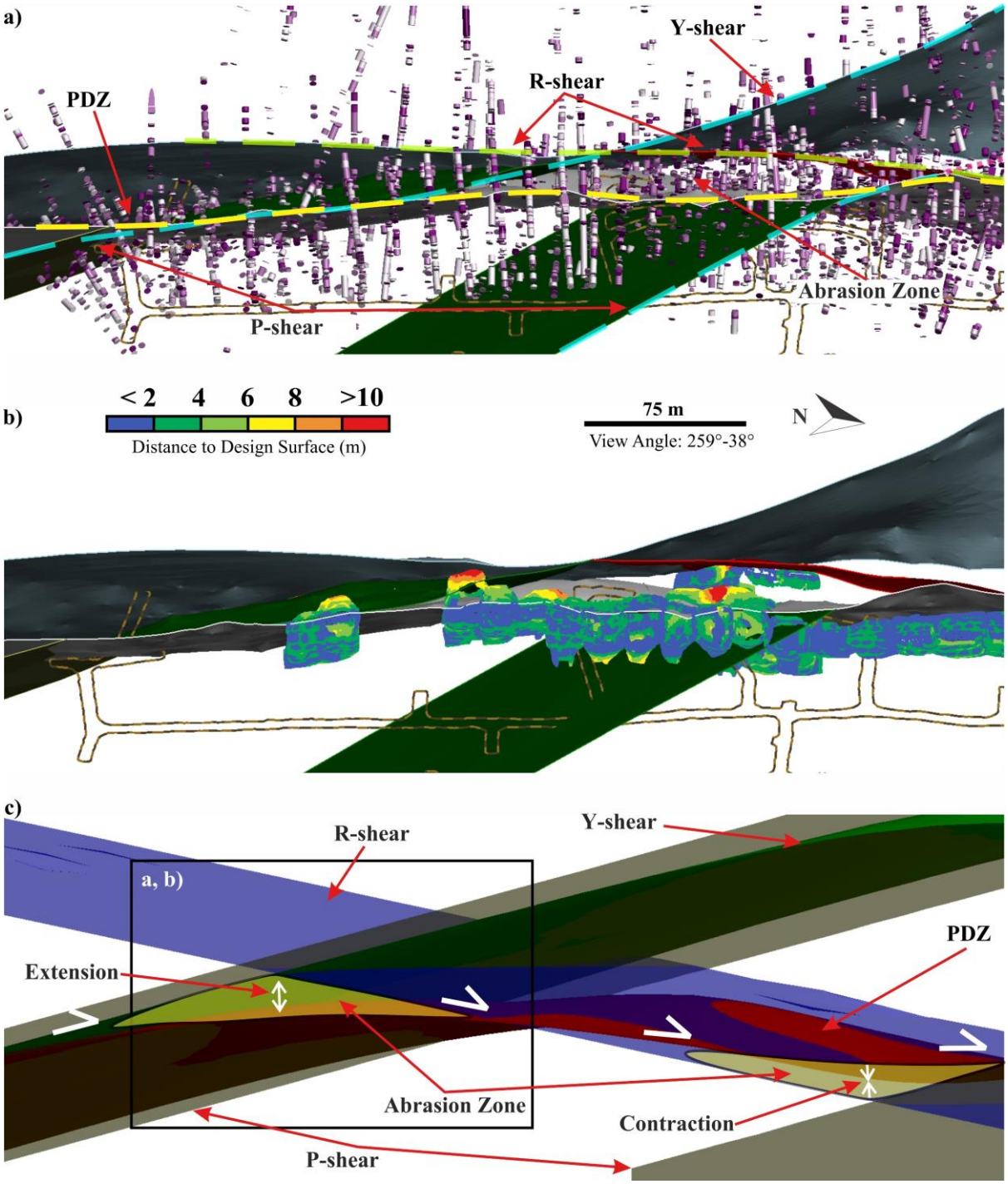
a)
PDZ
R-shear
Y-shear
P-shear
Abrasion Zone
b)
< 2 4 6 8 >10
Distance to Design Surface (m)
75 m
View Angle: 259°-38°
N
c)
R-shear
Y-shear
a, b)
Extension
PDZ
Abrasion Zone
Contraction
P-shear

3.7.5. Predictive Modelling

The en-echelon characteristic of Riedel shear networks allows for predictive modelling from both a resource definition and geotechnical perspective. The Dugald River Shear Zone represents an evolved Riedel shear zone with well-developed Y-shears, which allows for predicting localised areas that were under contraction or extension, i.e., dilational zones in the form of restraining and releasing bends along the throughgoing Y-shears (Fig. 3.17, 3.19).

The areas of contraction and extension are governed by the intersection of P-shear with R-shear segments with respect to the bulk dextral shear sense of the Dugald River Shear Zone, while the Y-shears continued to develop. The development of restraining and releasing bends are governed by the propagation of the Y-shears as they develop and as displacement continued (e.g., Fig. 3.16c). Figure 3.18 is a series of depth slices through the deposit and highlights how releasing bends develop along throughgoing structures. Releasing bends developed where a throughgoing Y-shear propagated from a P-shear to an R-shear and further along the R-shear to create a right-handed bend in the Y-shear (e.g. Fig. 3.14b, 3.15b, 3.16c, Fig. 3.17d - g), whereas restraining bends developed where a throughgoing Y-shear propagated along an R-shear to a P-shear and further along the P-shear to create a left-handed bend in the Y-shear (e.g. Fig. 3.14b, 3.15b, Fig. 17d – e, g). In dextral shears, right-handed bends and jogs are dilational, whereas left-handed bends and jogs are compressional (Blenkinsop, 2000). Releasing bends can be expected where drilling intersects NNW-trending shears with N-trending shears to the north. In contrast, restraining bends can be expected where drilling intersects NNW-trending shears with N-trending shears to the south. Lastly, the releasing bends may occur along the e3 direction, which in the case of the Dugald River Shear Zone is 41°-192° (Fig. 3.6c).

Fig. 3.17: Depth sections through the Dugald River Shear Zone with the high grade ore volume. The ore volume was provided by Dugald River Mine and is current as of December 2020. The depth of each section is in the mine grid coordinate system and the location of each slice is shown in (h). The view angle for each section is different due to the curvi-planar character of the shear zone to ensure that each section has a down-dip view of the principal displacement zone. Releasing and restraining bends are best illustrated towards the lower levels of the mine where the flexure in the shear zone is best developed (e.g. d – f).

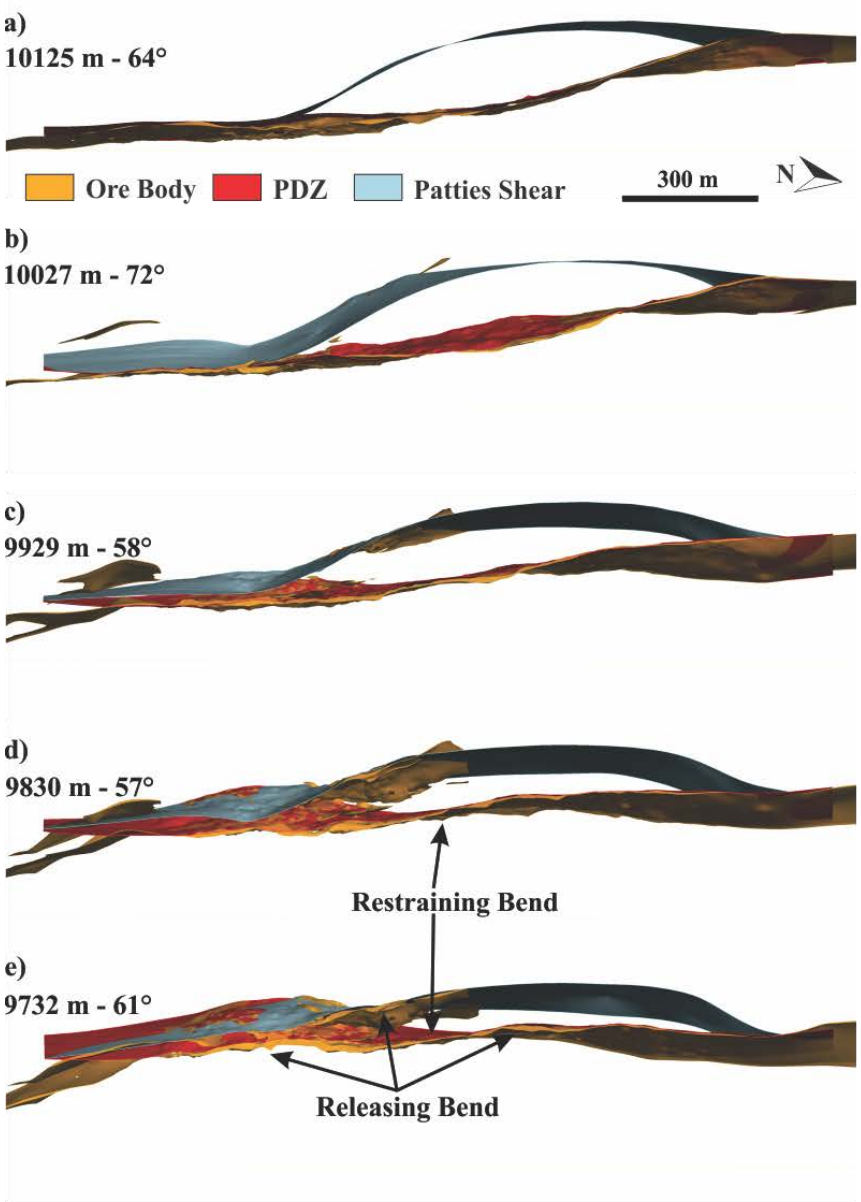
a)
10125 m - 64°
Ore Body
PDZ
Patties Shear
300 m
N
b)
10027 m - 72°
c)
9929 m - 58°
d)
9830 m - 57°
Restraining Bend
e)
9732 m - 61°
Releasing Bend

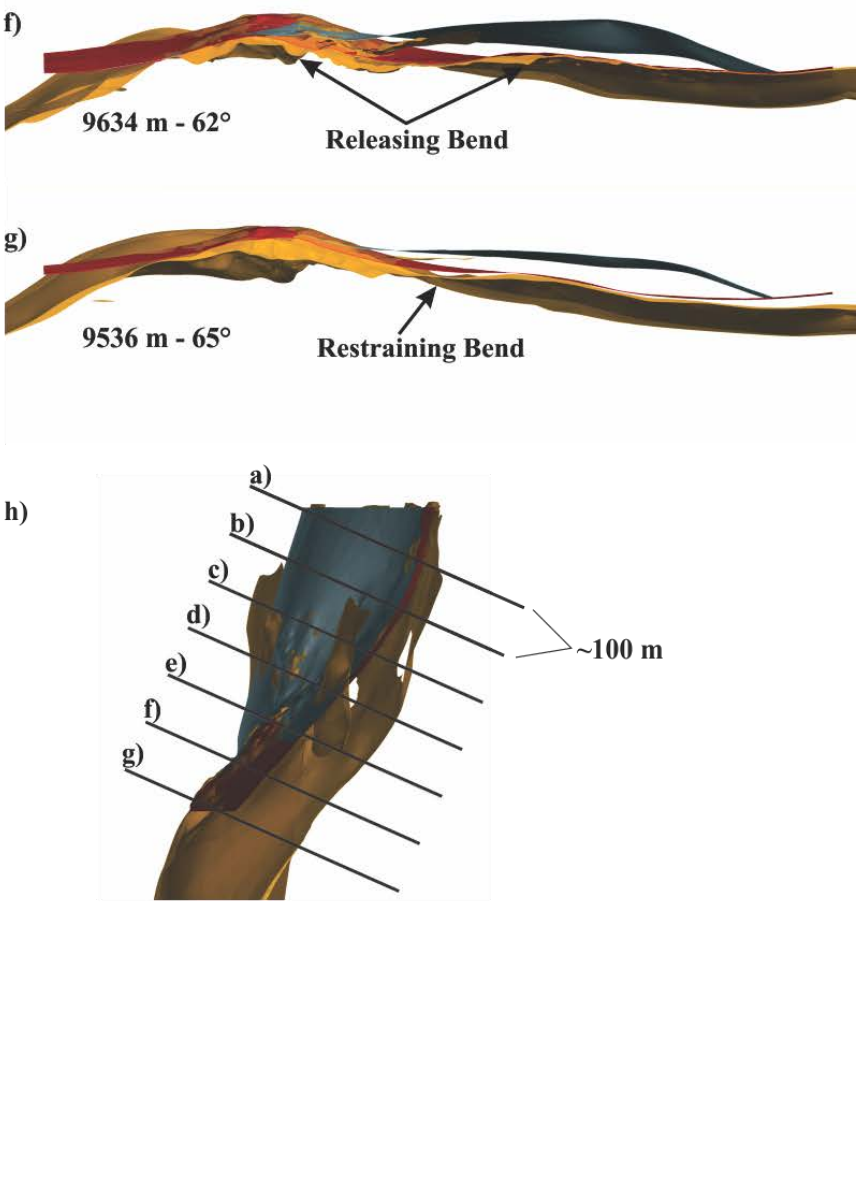
f)
9634 m - 62°
Releasing Bend
g)
9536 m - 65°
Restraining Bend
h)
a)
b)
c)
d)
e)
f)
g)
~100 m

The position of lenses of high-grade Zn mineralisation within the Dugald River Shear Zone can be predicted based on the geometry of the Y-shears. It should be noted that where the shear zone is steep, thick high-grade Zn lenses are unlikely to occur as the shear zone was near orthogonal to the sub-horizontal WSW – ENE shortening direction and coaxial deformation dominated to produce the transposition related Phase 2 mineralisation (Fig. 3.17a -c). Ford et al. (2009) found that maximum dilation occurred in faults with a dip angle of ~45° which at Dugald River occurs in the South Mine as indicated by the thickest part of the ore body and the shear zone dips at around 45° (Fig. 3.8, 3.18). Thus, the South Mine represents a macro-scale releasing bend indicated by the development of a thick sulphide lens within a right-handed bend of the principal displacement zone (Fig. 3.17f, 3.19). Subordinate lenses have developed from this thick sulphide lens along Y-shears, with releasing and restraining bends developing (Fig. 3.17d – e, 3.19).

Fig. 3.18: a) ENE view of the principal displacement zone with the face dip of interconnected triangles colour coded according to dip angle. The Dugald River Shear Zone geometry is mirrored by the principal displacement zone and is steeper to the north and the surface. The flexure in the South Mine is illustrated by lower angle dips for the shear zone and due to the zones of S_3 intensification that were reactivated as low-angle thrust arrays during D_4. Remnant P-shear segments towards the east of the principal displacement zone were reactivated during D_5 together with the low-angle thrusts and locally segmented the shear zone and ore body as illustrated by localised lower angle dips. b) Interval midpoints for drilling data used to generate the high-grade Zn wireframe volume provided by Dugald River Mine. Only the intervals for the main ore lens that occurs along the footwall of the principal displacement zone are shown with the true thickness of the ore lens at a respective point calculated and colour coded. In general, the ore body is thicker where lower angle dips occur as indicated in the scatter plot (c) and supports the conclusion by Ford et al. (2009) that maximum dilation occurs at ~45° dip angles for faults. The e2 value, from the stereoplots (Fig. 3.6c), can be used as a localised exploration vector for trends in the ore lenses as indicated by the black boxes in (b).

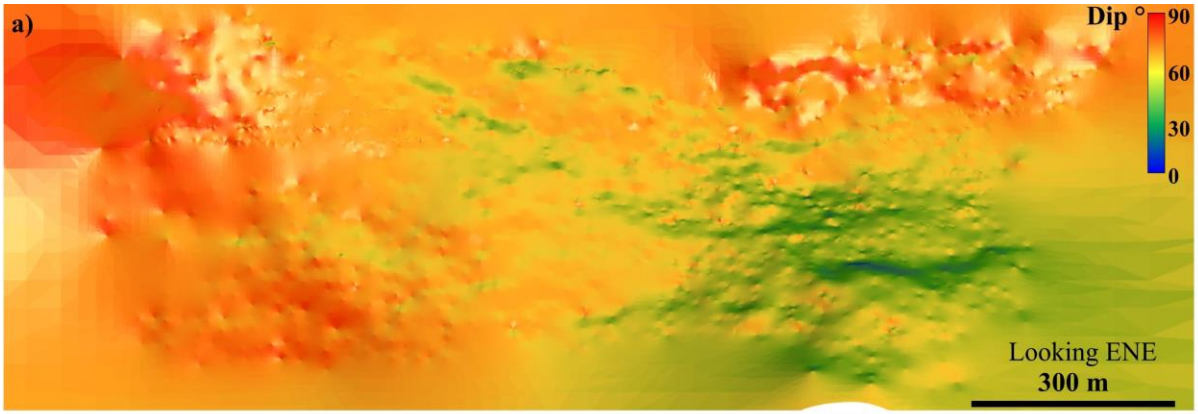
a)
Dip °
90
60
30
0
Looking ENE
300 m

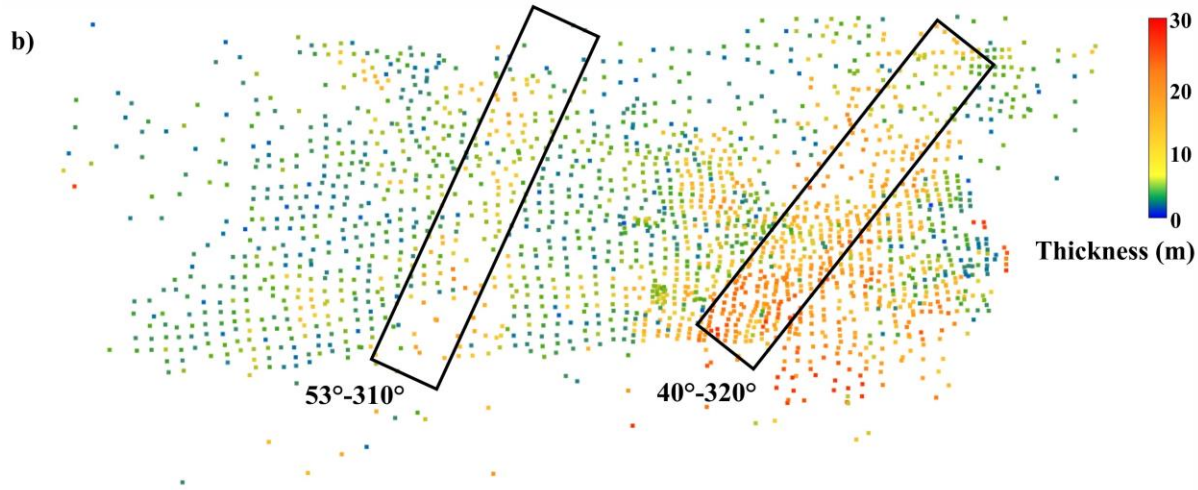
b)
30
20
10
0
Thickness (m)
53°-310°
40°-320°

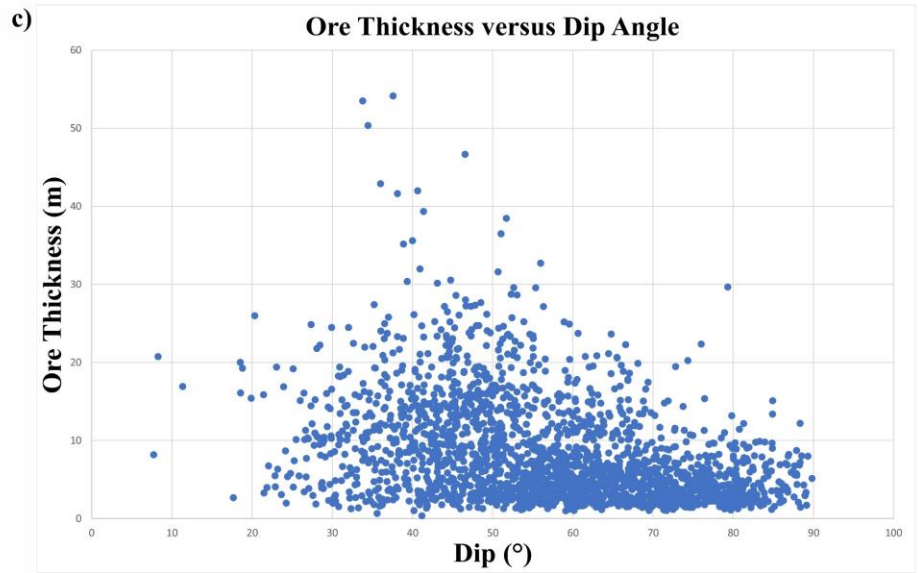
c)
Ore Thickness versus Dip Angle
Ore Thickness (m)
Dip (°)
0
10
20
30
40
50
60
70
80
90
100

The predictive character of Riedel shear networks and how they can be used in exploration vectoring is illustrated in Fig. 3.19. The data cut-off for the 3D modelling in this thesis was December 2019 and included in Fig. 3.19 is the high-grade Zn volume for December 2020 as well as the logged ore textures from drilling up to November 2021. The Y-shear to the west (i.e. Patties Shear) was constructed as bifurcating towards the NNE from the principal displacement zone, using high confidence drilling and mapping data available at the time. Based on the observation from underground mapping and subsequent 3D modelling, the Y-shear was modelled to "merge back" into the principal displacement zone towards the north using limited surface drilling available at the time. By undertaking a detailed structural analysis (i.e. Fig. 3.6) and concluding that the shear zone developed as a Riedel shear network and applying a comprehensive understanding of the 3D geometry of Riedel shear zones, a releasing bend was modelled and confirmed with post data cut-off drilling (Fig. 3.19).

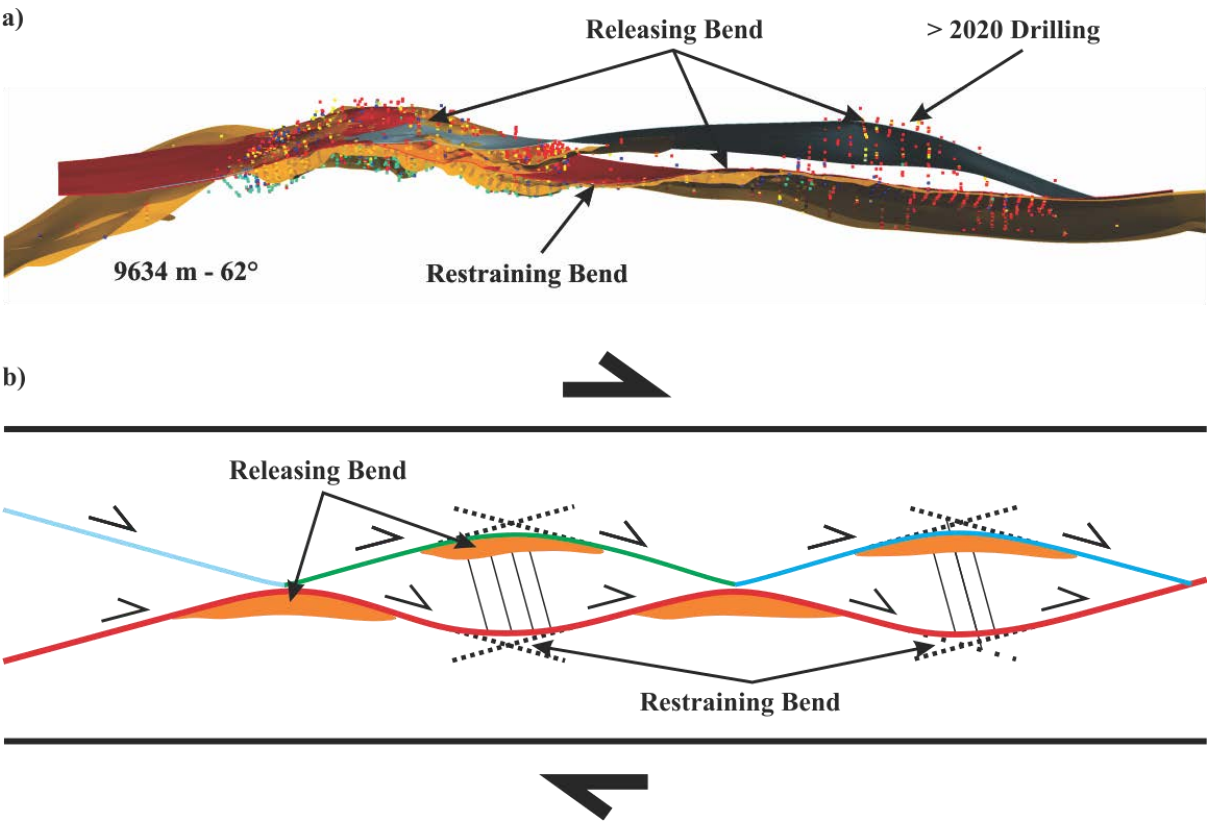

Fig. 3.19: a) Down dip view of the Dugald River Shear Zone. Included are the principal displacement zone and Patties Shear modelled for this study and using a data cut-off of December 2019; the high-grade Zn wireframe volume of December 2020 (provided by Dugald River Mine); and logged intervals for ore textures up to November 2021. b) Idealised model of a dextral Riedel shear network showing where releasing and restraining bends may form as Y-shears propagate during development. The high-resolution 3D modelling of the Dugald River Shear Zone allows releasing bends in the shear zone to be predicted and therefore sites for targeted drilling campaigns.

3.8. Conclusion

The Dugald River Shear Zone provides insights into the relationship between mineralisation and dilational sites that are created within an anastomosing Riedel shear zone as it develops. The structural complexity of the shear zone necessitates dense drilling and combined with high-grade Zn ore lenses occurring along the footwall of continuous Y-shears, results in a robust dataset of drilling and mapping data, including virtual outcrops from SfM-MVS. A high-resolution 3D model of the shear zone was constructed and serves to highlight existing areas of dilation (i.e. releasing bends; e.g. Fig. 3.14b, 3.15b, 3.16c, 3.17, 3.19) as well as being predictive when extrapolating shears into areas of sparse data (e.g. Fig. 3.19). Furthermore, within active mining fronts, compressive zones (i.e. restraining bends; Fig. 3.16) that developed within the shear zones can also be predicted and used to guide risk mitigation.

The main outcomes from the chapter are:

- The geometry of the Riedel shear zone determines the distribution of the ore lenses and their thickness. The ore is thickest within right-handed bends within throughgoing shears and where the shear zone has a ~45° dip.
- The en-echelon characteristic of Riedel shear zones means that dilational and compressive zones within the shear zone can be predicted and allow for targeted drilling along the e3 (41°-192°) direction, which is determined from structural analysis of D_4 related fabric.

3.9. References

Abu Sharib, A. S. A. A. & Bell, T. H. (2011). Radical changes in bulk shortening directions during orogenesis; significance for progressive development of regional folds and thrusts. Precambrian Research, 188(1-4), 1–20. https://doi.org/10.1016/j.precamres.2011.03.008

Abu Sharib, A. S. A. A. & Sanislav, I. V. (2013). Polymetamorphism accompanied switching in horizontal shortening during Isan Orogeny; example from the Eastern fold belt, Mount Isa Inlier, Australia. Tectonophysics, 587, 146–167. https://doi.org/10.1016/j.tecto.2012.06.051

Arboleya, M. L. & Engelder, T. (1995). Concentrated slip zones with subsidiary shears; their development on three scales in the Cerro Brass fault zone, Appalachian Valley and Ridge. Journal of Structural Geology, 17(4), 519–532. https://doi.org/10.1016/0191-8141(94)00079-F

Barcos, D. A., Diaz Azpiroz, M., Balanya, J. C., Exposito, I., Jimenez Bonilla, A. & Faccenna, C. (2016). Analogue modelling of inclined, brittle-ductile transpression; testing analytical models through natural shear zones (external Betics). Tectonophysics, 682, 169–185. https://doi.org/10.1016/j.tecto.2016.05.021

Basson, I. J., Creus, P. K., Anthonissen, C. J., Stoch, B. & Ekkerd, J. (2016). Structural analysis and implicit 3D modelling of high-grade host rocks to the Venetia kimberlite diatremes, Central Zone, Limpopo Belt, South Africa. Journal of Structural Geology, 86, 47–61. https://doi.org/10.1016/j.jsg.2016.03.002

Basson, I. J., Lourens, P., Paetzold, H.-D., Thomas, S., Brazier, R. & Molabe, P. (2017). Structural analysis and 3D modelling of major mineralizing structures at the Phalaborwa copper deposit. Ore Geology Reviews, 83, 30–42. https://doi.org/10.1016/j.oregeorev.2016.12.002

Basson, I. J., McCall, M. J., Andrew, J. & Daweti, E. (2018a). Structural controls on mineralisation at the Namib lead and zinc mine, Damara Belt, Namibia. Ore Geology Reviews, 95, 931–944. https://doi.org/10.1016/j.oregeorev.2018.03.028

Basson, I. J., Thomas, S. A. J., Stoch, B., Anthonissen, C. J., McCall, M. J., Britz, J., Macgregor, S., Viljoen, S., Nel, D., Vietze, M., Stander, C., Horn, J., Bezuidenhout, J., Sekoere, T., Gous, C. & Boucher, H. (2018b). The structural setting of mineralisation at Kolomela Mine, Northern Cape, South Africa, based on fully-constrained, implicit 3D modelling. Ore Geology Reviews, 95, 306–324. https://doi.org/10.1016/j.oregeorev.2018.02.032

Bell, T. H., Reinhardt, J. W. & Hammond, R. L. (1992). Multiple foliation development during thrusting and synchronous formation of vertical shear zones. Journal of Structural Geology, 14(7), 791–805. https://doi.org/10.1016/0191-8141(92)90041-T

Bell, T. H. (1983). Thrusting and duplex formation at Mount Isa, Queensland, Australia. Nature (London), 304(5926), 493–497. https://doi.org/10.1038/304493a0

Bell, T. H. (1991). The role of thrusting in the structural development of the Mount Isa Mine and its relevance to exploration in the surrounding region. Economic Geology, 86(8), 1602–1625. https://doi.org/10.2113/gsecongeo.86.8.1602

Bell, T. H. & Hickey, K. A. (1998). Multiple deformations with successive subvertical and subhorizontal axial planes in the Mount Isa region; their impact on geometric development and significance for mineralization and exploration. Economic Geology, 93(8), 1369–1389. https://doi.org/10.2113/gsecongeo.93.8.1369

Betts, P. G., Giles, D., Mark, G., Lister, G. S., Goleby, B. R. & Ailleres, L. (2006). Synthesis of the Proterozoic evolution of the Mt Isa Inlier. Australian Journal of Earth Sciences, 53(1), 187–211. https://doi.org/10.1080/08120090500434625

Blake, D. H. (1987). Geology of the Mount Isa Inlier and environs, Queensland and NorthernTerritory. BMR Bull. 225, 83.

Blake, D. H. & Stewart, A. J. (1992). Stratigraphic and tectonic framework, Mount Isa Inlier. Detailed Studies of the Mount Isa Inlier. Australian Geological Survey Organisation, 1–11.

Blenkinsop, T. G. (2000). Deformation microstructures and mechanisms in minerals and rocks. Kluwer Academic Publishers.

Blenkinsop, T. G., Oliver, N. H. S., Dirks, P. G. H. M., Nugus, M., Tripp, G. & Sanislav, I. (2020). Structural Geology applied to the evaluation of hydrothermal gold deposits. Reviews in Economic Geology, 21, 1- 23. https://doi.org/10.5382/rev.21.01

Carson, C. J., Hutton, L. J., Withnall, I. W. & Perkins, W. G. (2009). Joint GSQ-GA NGA geochronology project, Mount Isa region, 2007 – 2008. Queensland Geological Record 2008/05.

Carson, C. J., Hutton, L. J., Withnall, I. W., Perkins, W. G., Donchak, P. J. T., Parsons, A., Blake, P. R., Sweet, I. P., Neumann, N. L. & Lambeck, A. (2011). Summary of results: Joint GSQ-GA NGA geochronology project, Mount Isa Region, 2009-2010. Queensland Geological Record 2011/03.

Cave, B., Lilly, R. & Barovich, K. (2020). Textural and geochemical analysis of chalcopyrite, galena and sphalerite across the Mount Isa Cu to Pb-Zn transition: Implications for a zoned Cu-Pb-Zn system. Ore Geology Reviews, 124, 103647–. https://doi.org/10.1016/j.oregeorev.2020.103647

Chemenda, A.I., Cavalie, O., Vergnolle, M., Bouissou, S. & Delouis, B. (2016). Numerical model of formation of a 3-D strike-slip fault system. Comptes Rendus Geoscience 348, 61–69. https://doi.org/10.1016/j.crte.2015.09.008

Cho, N., Martin, C. D., & Sego, D. C. (2008). Development of a shear zone in brittle rock subjected to direct shear. International Journal of Rock Mechanics and Mining Sciences (Oxford, England : 1997), 45(8), 1335–1346. https://doi.org/10.1016/j.ijrmms.2008.01.019

Cowan, E. J., Beatson, R. K., Ross, H. J., Fright, W. R., McLennan, T. J., Evans, T. R., Carr, J. C., Lane, R. D., Bright, D. V., Gillman, A. J., Oshust, P. A. and Titley, M. (2003). Practical implicit geological modelling. 5th International Mining Geology Conference, Bendigo, Victoria, 17 - 19 November 2003

Creus, P. K. (2011). Geology and structural controls of lode-gold mineralization around the Navachab Gold Mine in the Pan-African Damara Belt of Namibia. Unpublished Msc thesis. University of Stellenbosch

Creus, P. K., Basson, I. J., Koegelenberg, C. K., Ekkerd, J., de Graaf, P. J. H., Bester, M. & Mokele, T. (2019). 3D fabric analysis of Venetia Mine, South Africa; using structural measurements and implicitly-modelled surfaces for improved pit slope design and risk management. Journal of African Earth Sciences (1994), 155, 137–150. https://doi.org/10.1016/j.jafrearsci.2019.04.009

Creus, P. K., Basson, I. J., Stoch, B., Mogorosi, O., Gabanakgosi, K., Ramsden, F. & Gaegopolwe, P. (2018). Structural analysis and implicit 3D modelling of Jwaneng Mine; insights into deformation of the Transvaal Supergroup in SE Botswana. Journal of African Earth Sciences (1994), 137, 9–21. https://doi.org/10.1016/j.jafrearsci.2017.09.010

Creus, P. K. Sanislav, I. V. & Dirks, P. H. G. M. (2021). Application of SfM-MVS for mining geology: Capture set-up and automated processing using the Dugald River Zn-Pb-Ag mine as a case study. Engineering Geology, 293, 106314–. https://doi.org/10.1016/j.enggeo.2021.106314

Cuomo, S., Galletti, A., Giunta, G. & Marcellino, L. (2017). Reconstruction of implicit curves and surfaces via RBF interpolation. Applied Numerical Mathematics, 116, 157–171. https://doi.org/10.1016/j.apnum.2016.10.016

Davidson, G. J., Davis, B. K. & Garner, A. (2002). Structural and geochemical constraints on the emplacement of the Monakoff Oxide Cu-Au(-Co-U-REE-Ag-Zn-Pb) deposit, Mt Isa Inlier, Australia, in: Porter, T. M. (Ed.), Hydrothermal Iron Oxide Copper-Gold & Related Deposits: A Global Perspective. PGC Publishing, Adelaide, pp. 49–75.

Davis, B. K. (2017). Dugald River - Orebody Knowledge Study (DROKS). Unpublished report by Orefind.

Davis, G. H. & Reynolds, S. J. (1996). Structural geology : of rocks and regions (2nd ed.). John Wiley.

Davis, G. H., Bump, A. P., Garcia, P. E. & Ahlgren, S. G. (2000). Conjugate Riedel deformation band shear zones. Journal of Structural Geology, 22(2), 169–190. https://doi.org/10.1016/S0191-8141(99)00140-6

Davis, T. P. (2004). Mine-Scale Structural Controls on the Mount Isa Zn-Pb-Ag and Cu Orebodies. Economic Geology, 99(3), 543–559. https://doi.org/10.2113/99.3.543

Dewey, J. F., Holdsworth, R. E. & Strachan, R. A. (1998). Transpression and transtension zones. Geological Society Special Publications, 135(1), 1–14. https://doi.org/10.1144/GSL.SP.1998.135.01.01

Dirks, P. G. H. M., Charlesworth, E. G. & Munyai, M. R. (2009). Cratonic extension and Archaean gold mineralisation in the Sheba-Fairview mine, Barberton Greenstone Belt, South Africa. South African Journal of Geology, 112(3 - 4), 291 - 316. https://doi.org/10.2113/gssajg.112.3-4.291

Dirks, P. H. G. M., Charlesworth, E. G., Munyai, M. R. & Wormald, R. (2013). Stress analysis, post-orogenic extension and 3.01 Ga gold mineralisation in the Barberton greenstone belt, South Africa. Precambrian Research, 226, 157–184. https://doi.org/10.1016/j.precamres.2012.12.007

Ford, A., Blenkinsop, T. G. & McLellan, J. G. (2009). Factors affecting fluid flow in strike-slip fault systems: coupled deformation and fluid flow modelling with application to the western Mount Isa Inlier, Australia. Geofluids, 9(1), 2–23. https://doi.org/10.1111/j.1468-8123.2008.00219.x

Fossen, H. (2010). Structural geology. Cambridge University Press.

Foster, D. & Austin, J. (2008). The 1800–1610Ma stratigraphic and magmatic history of the Eastern Succession, Mount Isa Inlier, and correlations with adjacent Paleoproterozoic terranes. Precambrian Research, 163(1-2), 7–30. https://doi.org/10.1016/j.precamres.2007.08.010

Gibson, Meixner, A. J., Withnall, I. W., Korsch, R. J., Hutton, L. J., Jones, L. E. A., Holzschuh, J., Costelloe, R. D., Henson, P. A. & Saygin, E. (2016). Basin architecture and evolution in the Mount Isa mineral province, northern Australia; constraints from deep seismic reflection profiling and implications for ore genesis. Ore Geology Reviews, 76, 414–441. https://doi.org/10.1016/j.oregeorev.2015.07.013

Giles, D., Betts, P. G., Ailleres, L., Hulscher, B., Hough, M. & Lister, G. S. (2006). Evolution of the Isan Orogeny at the southeastern margin of the Mt Isa Inlier. Australian Journal of Earth Sciences, 53(1), 91–108. https://doi.org/10.1080/08120090500432470

Grose, L., Ailleres, L., Laurent, G., & Jessell, M. (2021). LoopStructural 1.0: time-aware geological modelling. Geoscientific Model Development, 14(6), 3915–3937. https://doi.org/10.5194/gmd-14-3915-2021

Harris, P. (2015). Dugald River case study - the importance of understanding your orebody and designing your mine for maximum value. In: Polvin, Y. (Ed.), Underground deisgn methods. Australian Centre for Geomechanics, Perth. 21 - 36. doi:10.36487/ACG_rep/1511_0.2_Harris

Hill, E. V., Oliver, N. H. S., Cleverley, J. S., Nugus, M. J., Carswell, J. & Clark, F. (2014). Characterisation and 3D modelling of a nuggety, vein-hosted gold ore body, Sunrise Dam, Western Australia. Journal of Structural Geology, 67, 222–234. https://doi.org/10.1016/j.jsg.2013.10.013

Hillacre, S., Ansdell, K. & McEwan, B. (2020). Geology, structural analysis, and paragenesis of the Arrow uranium deposit, western Athabasca Basin, Saskatchewan, Canada; implications for the development of the Patterson Lake corridor. Economic Geology, 116(2), 285–321. https://doi.org/10.5382/econgeo.4797

Hillier, M. J., Kemp, E. A. De, Schetselaar, E. M. (2017). Implicit 3-D modelling of geological surfaces with the Generalized Radial Basis Functions (GRBF) algorithm. Geological Survey of Canada 1–15. https://doi.org/https://doi.org/10.4095/301665

Hillier, M. J., Schetselaar, E. M., de Kemp, E. A. & Perron, G. (2014). Three-dimensional modelling of geological surfaces using generalized interpolation with radial basis functions. Mathematical Geosciences, 46(8), 931–953. https://doi.org/10.1007/s11004-014-9540-3

Hobbs, B. E. (1987). Principles involved in mobilization and remobilization. Ore Geology Reviews, 2(1-3), 37–45. https://doi.org/10.1016/0169-1368(87)90022-9

Huston, D. L., Stevens, B., Southgate, P. N., Muhling, P. & Wyborn, L. (2006). Australian Zn-Pb-Ag ore-forming systems; a review and analysis. Economic Geology, 101(6), 1117–1157. https://doi.org/10.2113/gsecongeo.101.6.1117

Jackson, M. J., Scott, D. L. & Rawlings, D. J. (2000). Stratigraphic framework for the Leichhardt and Calvert superbasins; review and correlations of the pre-1700 Ma successions between Mt Isa and McArthur River. Australian Journal of Earth Sciences, 47(3), 381–403. https://doi.org/10.1046/j.1440-0952.2000.00789.x

Kirilova, M., Toy, V., Rooney, J. S., Giorgetti, C., Gordon, K. C., Collettini, C. & Takeshita, T. (2018). Structural disorder of graphite and implications for graphite thermometry. Solid Earth (Göttingen), 9(1), 223–231. https://doi.org/10.5194/se-9-223-2018

Kisters, A. F. M. (2005). Controls of gold-quartz vein formation during regional folding in amphibolite-facies, marble-dominated metasediments of the Navachab gold mine in the Pan-African Damara Belt, Namibia. South African Journal of Geology, 108(3), 365–380. https://doi.org/10.2113/108.3.365

Kitt, S., Kisters, A., Vennemann, T. & Steven, N. (2017). Orebody geometry, fluid and metal sources of the Omitiomire Cu deposit in the Ekuja Dome of the Damara Belt in Namibia. Mineralium Deposita, 53(2), 261–276. https://doi.org/10.1007/s00126-017-0731-y

Koegelenberg, C., Basson, I. J., Sinkala, H., Lupapulo, H. & Hornsby, P. (2019). Pan-African structural evolution of Paleoproterozoic basement gneiss and Cu-Co mineralized shear zones in the Domes Region of the Lufilian Belt, Mwombezhi Dome, Zambia. Journal of Structural Geology, 127, 103869–. https://doi.org/10.1016/j.jsg.2019.103869

Laurent, G., Ailleres, L., Grose, L., Caumon, G., Jessell, M., & Armit, R. (2016). Implicit modeling of folds and overprinting deformation. Earth and Planetary Science Letters, 456, 26–38. https://doi.org/10.1016/j.epsl.2016.09.040

Le, T, X., Dirks, P. H. G. M., Sanislav, I. V., Huizenga, J. M., Cocker, H. A. & Manestar, G. N. (2021). Geochronological constraints on the geological history and gold mineralization in the Tick Hill region, Mt Isa Inlier. Precambrian Research, 366, 106422–. https://doi.org/10.1016/j.precamres.2021.106422

Le, T. X., Dirks, P. H. G. M., Sanislav, I. V., Huizenga, J. M., Cocker, H. A. & Manestar, G. N. (2021). Geological setting and mineralization characteristics of the Tick Hill Gold Deposit, Mount Isa Inlier, Queensland, Australia. Ore Geology Reviews, 137, 104288–. https://doi.org/10.1016/j.oregeorev.2021.104288

Lister, G. S., O'Dea, M. G. & Somaia, I. (1999). A tale of two synclines; rifting, inversion and transpressional popouts at Lake Julius, northwestern Mt. Isa Terrane, Queensland. Australian Journal of Earth Sciences, 46(2), 233–250. https://doi.org/10.1046/j.1440-0952.1999.00690.x

Lorensen, W. E. & Cline, H. E. (1987). Marching cubes: A high resolution 3D surface construction algorithm. Computer Graphics (New York, N.Y.), 21(4), 163–169. https://doi.org/10.1145/37402.37422

McKinnon., S. D., & de la Barra, I. G. (1998). Fracture initiation, growth and effect on stress field; a numerical investigation. Journal of Structural Geology, 20(12), 1673–1689. https://doi.org/10.1016/S0191-8141(98)00080-7

Micklethwaite, S., Ford, A., Witt, W. & Sheldon, H. A. (2015). The where and how of faults, fluids and permeability; insights from fault stepovers, scaling properties and gold mineralisation. Geofluids, 15(1-2), 240–251. https://doi.org/10.1111/gfl.12102

Mira Geoscience. (2021). GOCAD Mining Suite. URL https://mirageoscience.com/ (accessed 8.5.21).

Mueller, A. G. (2020). Structural setting of Fimiston- and Oroya-style pyrite-telluride-gold lodes, Paringa South Mine, Golden Mile, Kalgoorlie; 1. Shear zone systems, porphyry dykes and deposit-scale alteration zones. Mineralium Deposita, 55(4), 665–695. https://doi.org/10.1007/s00126-017-0747-3

Murphy, T. E. (2004). Structural and stratigraphic controls on mineralization at the George Fisher Zn-Pb-Ag Deposit, Northwest Queensland, Australia. Unpublished PhD thesis. James Cook University. 443p

Naylor, M. A., Mandl, G. & Sijpesteijn, C. H. K. (1986). Fault geometries in basement-induced wrench faulting under different initial stress states. Journal of Structural Geology, 8(7), 737–752. https://doi.org/10.1016/0191-8141(86)90022-2

Newbery, S.P., Carswell, J.T., Allnutt, S.L. & Mutton, A.J. (1993). The Dugald River zinc-lead-silver deposit; an example of a tectonised Proterozoic stratabound sulphide deposit, in: International Symposium - World Zinc '93. Hobart, pp. 7–21.

O'Dea, M. G., Lister, G., MacCready, T., Betts, P. G., Oliver, N. H. S., Pound, K. S., Huang, W. & Valenta, R. K. (1997). Geodynamic evolution of the Proterozoic Mount Isa terrain. Geological Society Special Publications, 121(1), 99–122. https://doi.org/10.1144/GSL.SP.1997.121.01.05

Page, R. W. & Bell, T. H. (1986). Isotopic and structural responses of granite to successive deformation and metamorphism. The Journal of Geology, 94(3), 365–379. https://doi.org/10.1086/629035

Paradigm. (2021). SKUA-GOCAD. URL https://www.pdgm.com/products/skua-gocad (accessed 8.5.21).

Passchier, C. W. & Trouw, R. A. J. (2005). Microtectonics (2nd rev. and enl. ed.). Springer.

Ponce, C., Druguet, E. & Carreras, J. (2013). Development of shear zone-related lozenges in foliated rocks. Journal of Structural Geology, 50, 176–186. https://doi.org/10.1016/j.jsg.2012.04.001

Riedel, W. (1929). Zur mechanik geologischer Brucherscheinungen. Zentralblatt fur Mineral. Geol. und Palaontolgie 354–368.

Roache, T. J., Blenkinsop, T. G., Vearncombe, J. R. & Reddy, S. M. (2004). Shear zone versus fold geometries at the Cannington Ag-Pb-Zn deposit; implications for the genesis of BHT deposits. Journal of Structural Geology, 26(6-7), 1215–1230. https://doi.org/10.1016/j.jsg.2003.11.013

Rubenach, M. J., Foster, D. R. W., Evins, P. M., Blake, K. L. & Fanning, C. M. (2008). Age constraints on the tectonothermal evolution of the Selwyn Zone, Eastern fold belt, Mount Isa Inlier. Precambrian Research, 163(1-2), 81–107. https://doi.org/10.1016/j.precamres.2007.08.014

Rutter, E. H., Hackston, A. J., Yeatman, E., Brodie, K. H., Mecklenburgh, J. & May, S. E. (2013). Reduction of friction on geological faults by weak-phase smearing. Journal of Structural Geology, 51, 52–60. https://doi.org/10.1016/j.jsg.2013.03.008

Scott, D. L., Rawlings, D. J., Page, R. W., Tarlowski, C. Z., Idnurm, M., Jackson, M. J. & Southgate, P. N. (2000). Basement framework and geodynamic evolution of the Palaeoproterozoic superbasins of north-central Australia; an integrated review of geochemical, geochronological and geophysical data. Australian Journal of Earth Sciences, 47(3), 341–380. https://doi.org/10.1046/j.1440-0952.2000.00793.x

Seequent. (2021). Leapfrog Geo. URL https://www.seequent.com/ (accessed 8.5.21).

Sibson, R. H. (1990). Conditions for fault-valve behaviour. Deformation Mechanisms, Rheology and Tectonics, I–1528(1), 15–28. https://doi.org/10.1144/GSL.SP.1990.054.01.02

Spampinato, G. P. T., Betts, P. G., Ailleres, L. & Armit, R. J. (2015). Structural architecture of the southern Mount Isa Terrane in Queensland inferred from magnetic and gravity data. Precambrian Research, 269, 261–280. https://doi.org/10.1016/j.precamres.2015.08.017

Spelbrink, L. & George, K-L. (2017). Dugald RIver Orebody Knowledge Study (DROKS). Unpublished internal MMG report.

Spence, J. S., Sanislav, I. V. & Dirks, P. H. G. M. (2021). 1750-1710 Ma deformation along the eastern margin of the North Australia Craton. Precambrian Research, 353. https://doi.org/10.1016/j.precamres.2020.106019

Spence, J. S., Sanislav, I. V. & Dirks, P. H. G. M. (2022). Evidence for a 1750–1710 Ma orogenic event, the Wonga Orogeny, in the Mount Isa Inlier, Australia: Implications for the tectonic evolution of the North Australian Craton and Nuna Supercontinent. Precambrian Research, 369, 106510–. https://doi.org/10.1016/j.precamres.2021.106510

Stoch, B., Anthonissen, C. J., McCall, M. J., Basson, I. J., Deacon, J., Cloete, E., Botha, J., Britz, J., Strydom, M., Nel, D. & Bester, M. (2018). 3D implicit modeling of the Sishen Mine; new resolution of the geometry and origin of Fe mineralization. Mineralium Deposita, 53(6), 835–853. https://doi.org/10.1007/s00126-017-0784-y

Swanson, M. T. (2005). Geometry and kinematics of adhesive wear in brittle strike-slip fault zones. Journal of Structural Geology, 27(5), 871–887. https://doi.org/10.1016/j.jsg.2004.11.009

Swanson, M. T. (2006). Late Paleozoic strike-slip faults and related vein arrays of Cape Elizabeth, Maine. Journal of Structural Geology, 28(3), 456–473. https://doi.org/10.1016/j.jsg.2005.12.009

Tchalenko, J. S. (1968). The evolution of kink-bands and the development of compression textures in sheared clays. Tectonophysics, 6(2), 159–174. https://doi.org/10.1016/0040-1951(68)90017-6

Tchalenko, J. S. (1970). Similarities between shear zones of different magnitudes. Geological Society of America Bulletin, 81(6), 1625–1639. https://doi.org/10.1130/0016-7606(1970)81[1625:SBSZOD]2.0.CO;2

Tchalenko, J. S. & Ambraseys, N. N. (1970). Structural analysis of the Dasht-e Bayaz (Iran) earthquake fractures. Geological Society of America Bulletin, 81(1), 41–59. https://doi.org/10.1130/0016-7606(1970)81[41:SAOTDB]2.0.CO;2

Vollgger, S. A., Cruden, A. R., Ailleres, L. & Cowan, E. J. (2015). Regional dome evolution and its control on ore-grade distribution; insights from 3D implicit modelling of the Navachab gold deposit, Namibia. Ore Geology Reviews, 69, 268–284. https://doi.org/10.1016/j.oregeorev.2015.02.020

Vollgger, S. A., Wilson, C. J. ., Micklethwaite, S., Tomkins, A. G. & Cruden, A. R. (2020). Ore shoots in folded and fractured rocks – Insights from 3D modelling of the Fosterville gold deposit (Victoria, Australia). Ore Geology Reviews, 118, 103272–. https://doi.org/10.1016/j.oregeorev.2019.103272

Williams, P. F. & Price, G. P. (1990). Origin of kinkbands and shear-band cleavage in shear zones; an experimental study. Journal of Structural Geology, 12(2), 145–164. https://doi.org/10.1016/0191-8141(90)90001-F

Withnall, I. W. & Hutton, L. J. (2013). North Australian Craton, in: Jell, P.A. (Ed.), Geology of Queensland. Geological Survey of Queensland, pp. 23–112

Xu, G. (1996). Structural geology of the Dugald River Zn-Pb-Ag deposit, Mount Isa Inlier, Australia. Ore Geology Reviews, 11(6), 339–361. https://doi.org/10.1016/S0169-1368(96)00007-8

Chapter 4

Application of SfM-MVS for mining geology: capture set-up and automated processing using the Dugald River Zn-Pb-Ag mine as a case study

Creus, P.K.[a,b], Sanislav, I.V.[a,b], Dirks, P.H.G.M[a,b]

Keywords: Structure-from-Motion; Underground Mining; Digital Mapping; Digital Photogrammetry

Authors Note: This chapter has been published online in Engineering Geology before significant work in interpreting the structural controls on mineralisation was conducted. The content of this chapter is nearly identical to the published version and has minor stylistic and grammatical changes to conform to the rest of the thesis.

DOI: https://doi.org/10.1016/j.enggeo.2021.106314

4.1. Abstract

The use of structure-from-motion, multi-view stereo (SfM-MVS) in the mining industry is well-established for capturing digital data on the surface. However, the application of SfM-MVS in active underground mining has received less attention as there are unique challenges that need to be overcome, especially if a procedure is to be applied daily in active mining. Unique challenges include preparation time, camera positioning, illumination and useability. The faces of active development drives are generally only available for a short period before being prepared and blasted, this information is lost if not mapped immediately. Furthermore, due to safety concerns, unsupported faces cannot be approached for physical mapping. SfM-MVS allows these faces to be viewed and mapped in the form of a virtual outcrop, thus, allowing for remote mapping of underground development, which at the Dugald River mine, located in Queensland, Australia, allowed for mapping continuity as staff worked remotely during COVID-19. This contribution describes how to set-up a capture in an underground mine to produce high-quality SfM-MVS 3D reconstructions of development faces. The methodology can be readily incorporated into a standard operating procedure. While the procedure can be used with most photogrammetry software packages that utilise SfM-MVS algorithms, it is best utilised using the provided Python script and Agisoft Metashape Professional v1.6. The script allows for automation of capture processing, which can free up several hours per day compared to user-interacted processing.

4.2. Introduction

Digital mapping as part of the mining process has become an increasingly important tool for data gathering. Widespread techniques include face photography, stereophotography, structure-from-motion multi-view stereo (SfM-MVS), light detection and ranging (LiDAR) and hyperspectral imaging. In recent years numerous research papers and conferences have discussed the application of digital data capture techniques in Geoscience (James and Robson, 2012; Assali et al., 2014; Bemis et al., 2014; Johnson et al., 2014; Vollgger and Cruden, 2016; Allmendinger et al., 2017; Cawood et al., 2017; James et al., 2017; Novakova and Pavlis, 2017; Whitmeyer et al., 2019), with the use of photogrammetry in underground mining gaining attention (Slaker and Mohamed, 2017; García-Luna et al., 2019; Whaanga et al., 2019). They cover a wide range of topics including comparisons between different digital techniques (e.g., Assali et al., 2014; Cawood et al., 2017), structural data collection using smartphones (e.g., Allmendinger et al., 2017; Whitmeyer et al., 2019) and comparisons between digital and traditional (i.e. structural compass, pen and paper) mapping techniques. In general, most authors agree that digital mapping delivers similar results as traditional mapping, and the observed differences can be eliminated by improving sensors, devices, and algorithms.

Studies on surface outcrop are usually done where lighting, rock exposure and environmental conditions are optimal for data capture, or can be delayed until environmental conditions are favourable. In underground mining, environmental conditions, including humidity and dust are variable, and due to ongoing mining activity, data collection must be performed within tight timeframes. For example, the face of an active drive can be prepared and charged for firing at the subsequent shift change. Thus, the on-duty Mine Geologist is typically the only Geoscientist that will see and record the information from the face. This information is commonly recorded using hand sketches, which may be rushed, untidy and subjective with structural orientations estimated rather than measured due to safety reasons as an unsupported face may not be approached (Robertson, 2017). Furthermore, automation and smart mining are increasingly becoming vital due to stricter mining regulations around safety and ongoing pressure within companies to reduce operating costs.

Face photography, LiDAR, stereophotography and SfM-MVS are the main techniques used for underground digital data capture. Face photography allows for a georeferenced 2D image to be viewed in 3D modelling software and is a quick method to view a development face and digitise objects onto. However, 2D images are inadequate in capturing the 3D complexity of a development cut and have limited use in structural geology analysis (i.e. orientated data points). LiDAR imaging requires expensive equipment and software, specialised training and data capture is time-consuming (e.g., James and Robson, 2012; Assali et al., 2014; Johnson et al., 2014; Cawood et al., 2017), making this technique less attractive for underground mining. Furthermore, with LiDAR point clouds, there is a disconnect between point positions and colour, which needs to be added from a different source during post-processing. Stereophotography, a precursor to SfM-MVS, is error-prone due to the requirement that camera locations and orientation must be known as well as its susceptibility to erroneous camera calibration (e.g., Iglhaut et al., 2019; James and Robson, 2012). While software packages like Agisoft Metashape (Metashape) can perform auto-calibration of cameras, the limitation of two images results in occlusion and the unlikelihood that both the face of a tunnel and ground control points are included in either image. Thus, SfM-MVS is ideally suited for underground digital data capture. It can be done using off-the-shelf digital cameras or unmanned aerial vehicles (UAV) and handheld GPS devices making it a cost-effective solution. SfM-MVS makes use of a series of overlapping images, taken at different angles to the face and sidewalls, reducing occlusion as well as creating redundancy if some images in a capture are low-quality (see section 2). There is also a direct relationship between calculated points and colour as they are from the same source (i.e. the images). The digital data can be processed using a wide variety of commercial and open-source software, as well as cloud-based services. Furthermore, SfM-MVS provides a continuous “virtual outcrop” of the underground development.

In this contribution, we investigate the application of SfM-MVS to underground mining by using the Dugald River mine as a case study. The Dugald River Zn-Pb-Ag mine is located ~90 km

northeast of Mount Isa in the Eastern Subprovince of the Mount Isa Inlier, NW Queensland, Australia (Fig. 4.1). The mineralisation style is interpreted as a shear-zone hosted epigenetic (Xu, 1997) with the 2020 resource stated as being 67 Mt @ 11.6 % Zn, 1.2 % Pb and 25 g/t Ag with potential remaining open to the north, south and at depth (MMG, 2020). The mine is operated entirely underground and is structurally complex making it ideal for testing and developing underground digital mapping tools. Dugald River begun underground development in 2012 with production of Zn concentrate in 2017, and recently moved into mine ramp up with an expected throughput of 170 kt Zn concentrate per year, while averaging 317 m of underground development per month in 2020. SfM-MVS has been used at the Dugald River mine since the end of 2016 (Robertson, 2017), However, recent review of the quality of the virtual outcrops found that the images used to produce the outcrops were noisy and unfavourably exposed.

At Dugald River mine, an average of 7 captures are recorded per day, requiring 20 min per capture to process. Thus, automating the processing of the captures can free up several hours a day. While semi-automated methods of processing dense point clouds and meshes for discontinuity/plane mapping is well-discussed in the literature (e.g., Jaboyedoff et al., 2009, 2007; Riquelme et al., 2014), recent developments in full-automation (e.g., Kong et al., 2020; Umili et al., 2013) potentially allows for the entire digital mapping process to be automated. In full-automation, 3D scene reconstruction is done using SfM-MVS followed by rock mass analysis and characterisation of generated point clouds using machine learning algorithms. Notably, this is done in an objective manner resulting in reproducible results.

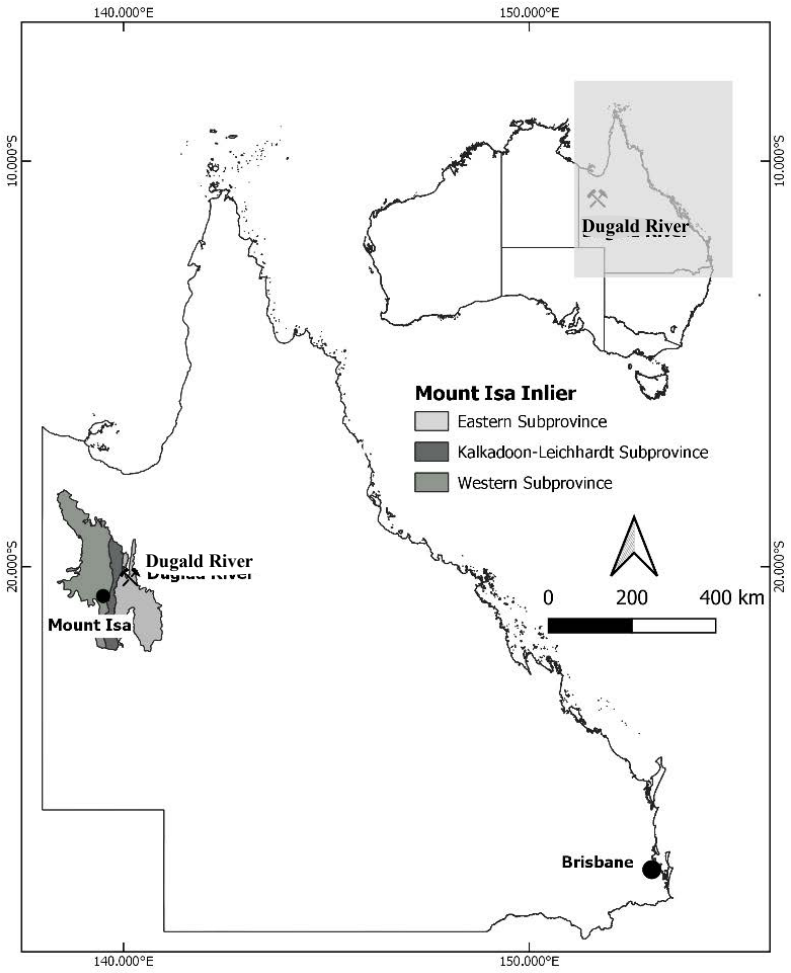

Fig. 4.1: Locality of the study area. Dugald River Zn-Pb-Ag mine is situated in the Eastern Subprovince of Mount Isa Inlier, NW Queensland, Australia. The shaded area in the inset shows the area covered by the map, in NE Australia.

In this manuscript, we present two aspects of SfM-MVS in underground mining; Section 3 is a modified version of the procedure described by Robertson (2017) to improve the overall quality of captures in which optimal camera settings and suggested capture set-ups are discussed and in Section 4 we discuss automated processing of captures, which uses the Python API provided with the professional version of Metashape. The methodology described in this manuscript can be readily applied to any underground mine in the form of a standard operating procedure. An example dataset including photographs and ground control points are included as supplementary data and can be processed with the downloadable Python script, provided the user has a Metashape Professional license.

4.3. Structure-from-Motion – Overview

SfM-MVS has widespread uses in geoscience to capture and store data for viewing in 3D software. By capturing a series of images of an object, SfM-MVS can be used to produce a "virtual outcrop" (Cawood et al., 2017). This allows development to be viewed by Geoscientists that are not able to go underground regularly, e.g., senior geoscientists, consultants etc. The methodologies and processes behind SfM-MVS are discussed in concise detail by numerous authors (e.g., Bemis et al., 2014; James and Robson, 2012; Smith et al., 2015; Vollgger and Cruden, 2016; Whaanga et al., 2019).

In the context of this study, the use of SfM-MVS can be described in 3 phases (Table 4.1). The first phase (Section 3) involves the capturing of images and surveying of ground control points (GCPs). Note, the first phase is not limited to using Metashape and serves as a guide on how to capture high-quality images of development faces that can be processed by most photogrammetry software such as Pix4DMapper (www.pix4d.com), RealityCapture (www.capturingreality.com) and mining industry-specific software such as 3DM Analyst (www.adamtech.com.au) and PixPro (www.dataminesoftware.com). The second phase requires populating a spreadsheet (see Section 4; Table 4.2) with parameters used by the Python script. The final phase involves the processing of images and survey information to produce 3D data in the form of a dense point cloud or mesh and is described in detail in section 4. Note, in the context of this study a mesh refers to interconnected vertices, edges and faces that define a polyhedral object, which in literature may be termed a wireframe, 3D object, 3D mesh, 3D model or surface.

Table 4.1: Phases taken to capture and process development headings.

1. Image Capture	2. Processing Preparation	3. Automated Processing via Python Script and Metashape
• Camera settings • Place GCPs and lights • Survey GCPs • Wash face • Acquire images	• Copy data to folders • Populate spreadsheet	• Import spreadsheet • Create project and export folder • Import images • Estimate image quality • Detect markers and import survey data • Align images (sparse point cloud) • Trim data • Generate depth maps • Build dense point cloud and/or mesh • Export dense point cloud and/or mesh

In literature, software processing is generally described as a 2-step process. The first step involves the detection of distinct features (key points) in images and alignment (Smith et al., 2015; Vollgger and Cruden, 2016; Agisoft, 2019). Distinct features in images that are most likely to be matched in other images are detected and assigned 3D coordinates from which a network of tie points are generated (Cawood et al., 2017). This is done iteratively, by starting with two images and incrementing as the computation continues. Bundle block adjustment uses the features to estimate the internal and external camera parameters to determine the camera positions and orientation as well as the 3D geometry of the scene (Förstner and Wrobel, 2016; Vollgger and Cruden, 2016). The result of this step is a sparse point cloud. Step two involves generating a dense point cloud and/or a mesh. Multi-view stereo algorithms (Smith et al., 2015; Vollgger and Cruden, 2016) are used to generate a dense point cloud and meshes are generated using algorithms such as Marching Cubes (Lorensen and Cline, 1987).

4.4. Structure-from-Motion - Capturing

The precision and resolution of a generated dense point cloud or wireframe are dependent on several factors: 1) the resolution and quality of input images; 2) the distance of the camera to the object 3) the overlap of the images; 4) the angle of the camera position relative to the object; 5) the number and distribution of control and check points, i.e. ground control points; and 6) illumination (Smith et al., 2015; James et al., 2017). The texture of the object to be captured and the processing settings are important for SfM-MVS to produce acceptable results. Examples of poor surfaces to capture are reflective, semi-reflective and glossy surfaces such as reflective tape, surface glare, and gloss paper, respectively. These surfaces lack surface details for the software to identify key points or commonly produce erroneous key points with water pools (e.g., Fig. 4.6a). Non-static textures (usually people) must be avoided, however, these can be manually masked in Metashape, if the image cannot be excluded. Additionally, dusty drives, water dripping from backs and high humidity may also impact the quality of images and ability of SfM-MVS to produce acceptable results.

4.4.1. Digital Camera Settings

The type of camera and settings play a crucial role in the quality of the images that are captured and, subsequently, the point cloud that is generated. The quality of dense point clouds and meshes is facilitated by higher quality images, thus the sensor resolution and size factor into the quality of the images. In this study, a Canon EOS 550D camera was used with a focal length of 18 mm.

To achieve high-quality imagery, the exposure of an image needs to be correct. Three camera settings: ISO, aperture and shutter speed can be adjusted to ensure correctly exposed images and together are referred to as the "exposure triangle" (Fig. 4.2a; Marsh, 2014; Schofield, 2018). ISO refers to the sensitivity of the imaging sensor to given light (Marsh, 2014). Increasing the ISO results in brighter images, but also noise, i.e., it may result in grainy images in low light conditions. Aperture, measured in f/stop, refers to the opening of a lens' diaphragm through which light passes, thereby changing the depth of field of an image (Modrak and Anthes, 2010; Marsh, 2014). Setting a high value, increases the exposure time and depth of field of an image, resulting in a sharper background to the point of focus (i.e., object being photographed). Shutter speed is the speed at which the shutter of the camera closes, which controls the amount of light that will reach the camera sensor. A slower shutter speed allows more light through but can result in blurry images unless a tripod is used. Notably, adjusting one of the settings of the exposure triangle affects the other two (Marsh, 2014). A correctly exposed image will have a balanced exposure histogram similar to a bell curve, whereas underexposed or overexposed images will be distributed towards black or white tones, respectively (Fig. 4.2b - g; Marsh, 2014).

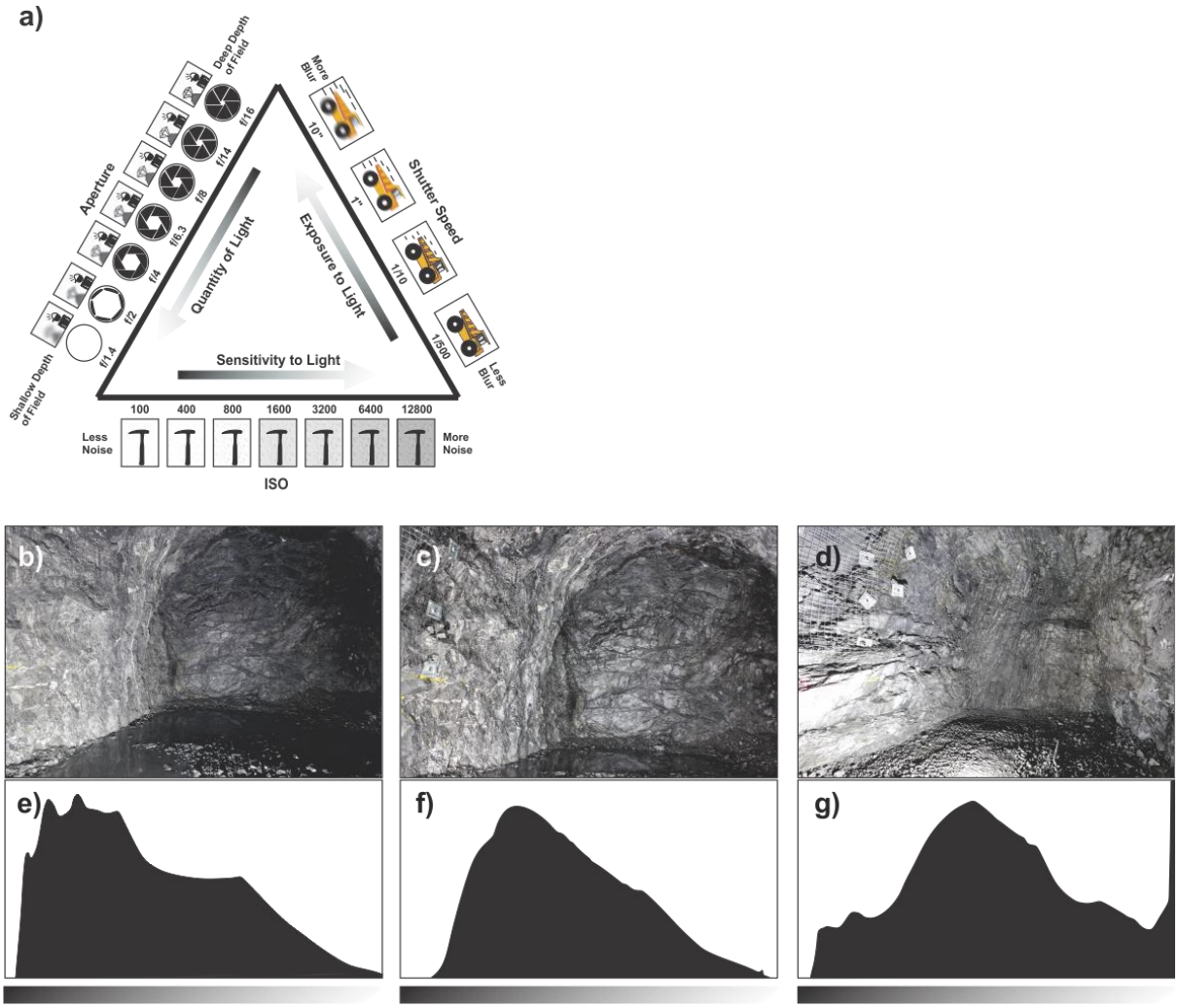

Fig. 4.2: a) Exposure triangle comprising the variables ISO, aperture, and shutter speed. The 3 variables determine the exposure of an image and changing 1 requires adjusting at least 1 of the others. Images b, c, d represent captures with associated exposure histograms e, f, g. b) Capture in which large shadows are created resulting from a poorly lit scene, with its associated exposure histogram e) distributed towards black, indicating an underexposed image. c) Capture of a well-lit scene in which the associated exposure histogram f) is distributed in the mid-tone range. d) Capture in which the lights are focused on part of the scene, creating an area that is brighter than the rest of the scene, which is indicated by the shift towards white in the associated exposure histogram g)

Digital cameras have predefined camera modes that are designed to make a camera user-friendly. However, the automatic mode should not be used in SfM-MVS as the camera flash may be triggered. For the successful rendering of a dense point cloud or mesh, the images need to be sharp for the entire image, i.e. the depth of field of the image. Accordingly, Aperture Priority (Av) should be used, which allows the user to change the aperture and ISO values, with the shutter speed adjusted automatically by the camera. In low light conditions, the exposure time may be increased significantly, which may result in blurry images if the camera is moved slightly. Thus, setting the camera on a tripod is recommended as well as using a remote trigger.

4.4.2. Ground Control Points

Ground control points (GCPs) allow for georeferencing of the 3D reconstruction produced by SfM-MVS and auto-calibration of the camera. Georeferencing requires a minimum of 3 GCPs (James and Robson, 2012). For this study 4 GCPs were used, 2 on either side of the tunnel (Fig. 4.4a).

A preliminary test using laser pointers to record additional GCPs in the unsupported ground was conducted. In the test, an additional 12 lasers, spread across the face, sidewall and back (see Fig. 4.4 for terminology) were used to increase the number of GCPs to 16, of which 4 were used as check points (refer to Agisoft (2019) for a description on control and check points). The results show that using additional GCPs with the laser pointer method in underground SfM-MVS did not justify the extra time required to set-up a capture, which may impact other mining processes. The laser pointers require manual tagging of multiple GCPs on most images, resulting in a longer processing time. Furthermore, the visual quality of the point clouds and meshes produced are not markedly different. Whereas automated processing of captures is more advantageous when considering that 3D reconstructions can be used in downstream semi-automated and automated processes (e.g., Riquelme et al., 2014, 2018; Guo et al., 2017; García-Luna et al., 2019; Thiele et al., 2019; Kong et al., 2020). Although the use of laser pointers for GCPs in underground mining is unsuitable, they can be used in other inaccessible areas such as open-pit highwalls and cliffs.

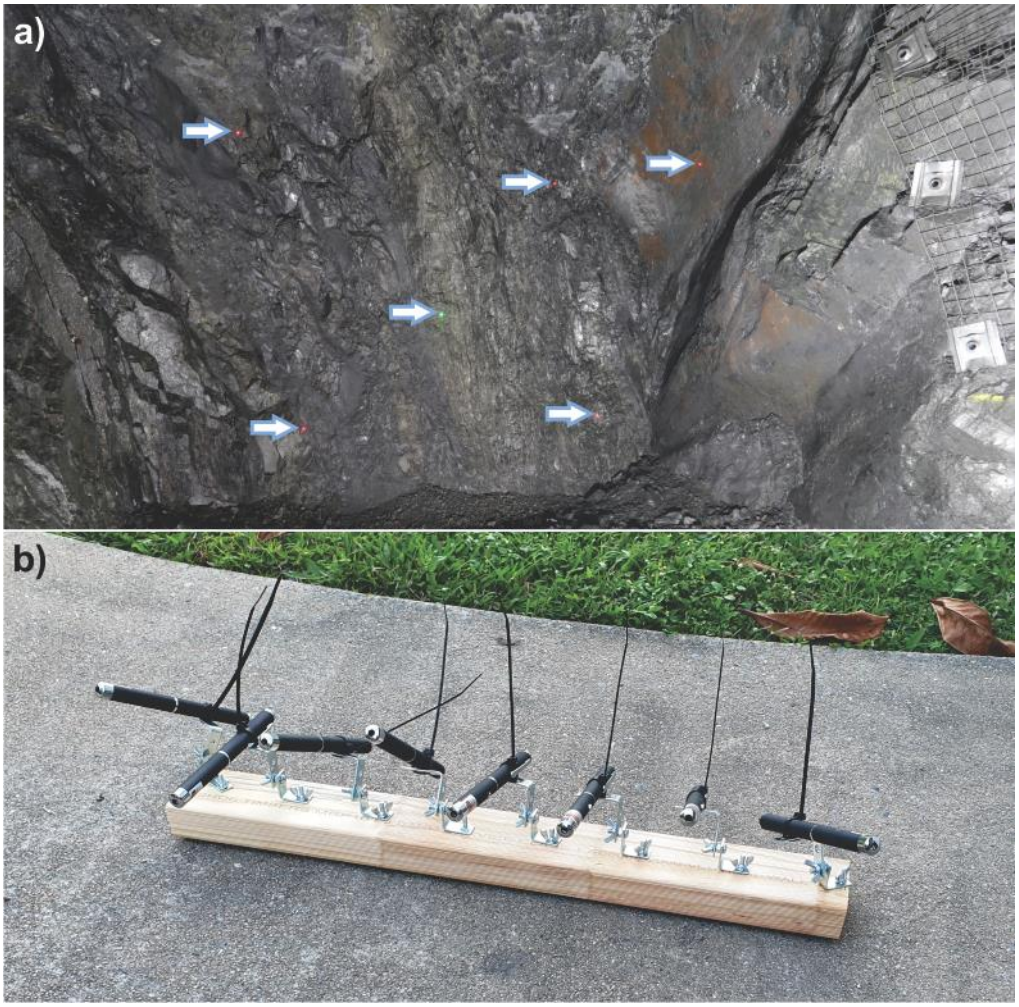

Fig. 4.3: a) Laser pointers used to mark GCPs on the face and sidewall. Shown here are 5 red and 1 green laser. Tagging the GCPs on images is time-consuming as each image has several laser points. b) Laser pointer set-up using wood and stainless-steel brackets. The brackets are attached using bolts and wingnuts so that the laser pointers can be angled.

4.4.3. Camera Position

The camera position governs several factors that are important when considering SfM-MVS. Changing the position of the camera, as well as the angle relative to an object of interest (e.g. development face) provides perspective, or depth information (e.g., James and Robson, 2012; Bemis et al., 2014; Johnson et al., 2014). James and Robson (2012) suggest short distances of 2 – 3 m when capturing objects further than 20 m and use angular intervals of 10 -20° over a wide range of angles. Furthermore, they suggest capturing more images necessary to reduce the chance of omitting areas.

With SfM-MVS, the order in which the images are taken is not important, however, it is suggested that all features to be recorded occur in at least two or more images to avoid blind spots. The recommendation by most authors is that there is at least 60 – 80 % overlap between images (e.g., Agisoft, 2019; Bemis et al., 2014; Slaker and Mohamed, 2017; Whaanga et al., 2019).

The distance of the camera to an object of interest plays an important role in the resolution of the 3D reconstruction. In photogrammetry, the term ground sampling distance (GSD) is commonly used and is a metric that describes the distance between the centre of adjacent pixels. A smaller GSD results in a higher resolution and generally more visible detail. Note, visible detail can be affected by other factors such as motion blur and illumination. Camera lenses are either prime lenses or zoom lenses. Prime lenses have a fixed focal length and cannot be zoomed, whereas a zoom lens allows for variable focal lengths within the range of the lens by adjusting the zoom ring.

In an underground setting, there are limitations on where the camera can be set-up, as well as the positioning of lights to ensure maximum illumination without causing overexposed or underexposed images and lens flares. A typical decline accessed mine has tunnel widths of ~6 m. For captures in these operations, we suggest a tripod-mounted camera and 4 stations that are spaced roughly 1 m apart and in line with the second row of mesh bolts from the unsupported ground (Fig. 4.4), however, this is dependent on camera and camera lens combination. With the camera and lens combination used in this study (see section 4.5), 6 photos were taken at each station for a total of 24 per capture. This provides sufficient overlap, minimal angular change between overlapping images, and enough depth information to result in an acceptable perspective.

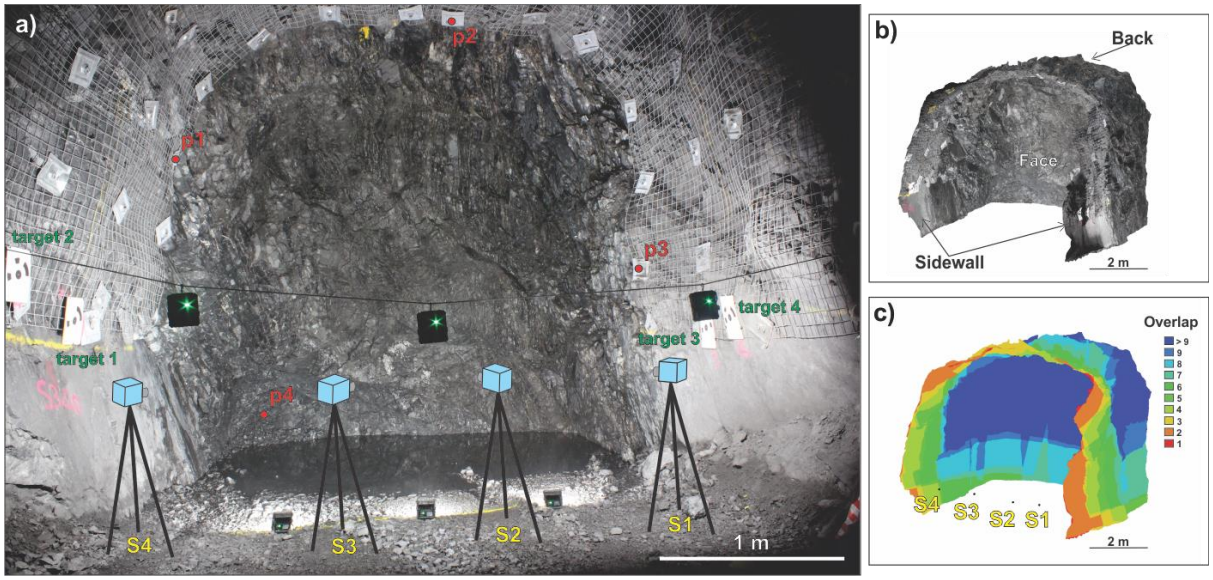

Fig. 4.4: a) Suggested set-up for SfM-MVS image acquisition in underground mining. b) is the output mesh for a). GCPs are placed on either side of the tunnel in line with the 4 camera stations (S1 – S4), which are spaced ~1 m apart. The camera stations are placed between the lights on the floor and in this study, the lights were hung from a rope spanning the tunnel (lights mounted on a stand are recommended for production purposes). p1 to p4 are additional points that may need to be surveyed (see section 4.65). For this study, six images were captured per station ensuring sufficient overlap, e.g., a sequence of images may follow: i) targets 1 and 2; ii) p1; iii) p2; iv) p1 and p4; v) centre of the face; vi) region covering face and back. Using this example resulted in the image overlap shown on c), where the image overlap on the face exceeds 9 images. Note, this may differ when using a different camera and/or lens.

4.4.4. Illumination

Illumination poses one of the greatest challenges when conducting SfM-MVS in underground mining. Inherently lighting must be produced, sufficient yet portable - and battery-powered - to ensure timely captures that will not delay other mining processes. Furthermore, the lighting set-up must not change during the entire capture as changing the lighting may result in features differing between images.

The use of LED lights is recommended. In this study, 6 lights were used that consisted of portable LED lights obtained from a general hardware store. Arlec 30W 2100 lumens rechargeable LED work lights were used. The lights have a CRI rating of > 80 and a colour temperature of 5000 K. The CRI of the LED's should be as high as possible so that colours under LED light resembles natural light as closely as possible. With a known colour temperature, the white balance can be set in the camera and colours adjusted to look more natural. While adjusting the colour temperature is sensical, at Dugald River using auto white balance resulted in sulphide types that are easier to distinguish, including from the host rock. Thus, when first implementing SfM-MVS it may be useful to experiment with white balance.

Three lights were placed on the ground with the remaining lights hung from a rope spanning the width of the tunnel, roughly 1.8 m off the ground. The lights were placed in an arc with the camera tripod placed between the set on the ground and the rope (Fig. 4.4). 6 lights were chosen as they produced sufficient illumination given the dark grey colour of the graphitic slate at Dugald River and the dark brown colour of high-grade ore. Furthermore, 6 lights create diffuse lighting as opposed to fewer lights that may create dark halos (e.g. Fig. 4.2b, d). Hanging lights from a rope is not recommended outside of testing, as they are susceptible to moving due to draft and accidental bumps. Rather the lights should be mounted on a stand.

4.4.5. Summary of Equipment

A capture can be completed by a single user using off-the-shelf equipment. The off-the-shelf equipment required is: 1) a high-resolution camera with a fixed focal length, which is mounted on a tripod; 2) Rugged and portable waterproof LED lights, which are mounted on stands to create diffuse lighting; 3) Four, A3 size GCPs printed on corflute signs as they are hard wearing and inexpensive. Dry faces will not produce optimal results, thus attaching hoses to mine services is required. A dedicated Total Station is highly recommended to ensure GCPs are surveyed correctly and without delay.

4.5. Structure-from-Motion – Processing

Processing of captures was done in Agisoft Metashape Professional v1.6. Metashape adopts a workflow-based methodology that processes the images and survey data with parameters set by the user. These parameters can be standardised to allow for consistency between users of the software on a mine site, or mining company. While section 3 describes a method to capture high-quality images that can be processed in most photogrammetry software, Metashape was chosen, because the professional version has a Python API (Application Programming Interface) that allows for customisation of how and when Metashape functions are used.

4.5.1. Python Script

Due to multiple captures per day, the use of the Python script included with this manuscript is recommended. Included with the supplementary data is the modifiable Python script (sfm_automated_processing.py), a standalone executable (sfm_automated_processing.exe) and a readme file. The modifiable Python script requires the installation of Python and several libraries listed in the readme. The standalone executable does not require the installation of Python, nor the libraries. Unless specified, the Python script refers to either file. When running the Python script, a GUI (graphical user interface) will open which will update the user of the progress of the script. The reader is referred to the readme file for an overview of the GUI.

The parameters that need to be applied during the script are defined within an Excel spreadsheet (included as supplementary data), which is selected by the user via the GUI, thereby not requiring direct modification of the script. The script iterates through the rows of the spreadsheet to: 1) name the project; 2) import images; 3) import GCPs; 4) set image alignment quality; 5) trim data; 6) set depth maps quality; 7) generate a dense point cloud; and 8) generate a textured mesh. Optional parameters that can be defined include estimating image quality and exporting dense point cloud normals.

4.5.2. Project Set-Up

Each capture needs to be set-up in its own project directory. The images and GCP survey information are stored within the directory that the Python script will use to import and export relevant data. Generally, a suitable naming convention for a project is the mine level followed by the drive name and the date that the face was fired (e.g., S240_OD435_N2_230919; Table 4.2). Note, the default export format for a mesh is *object* (.obj), which requires a filename with no whitespaces. The script is designed to create a new project in the project directory. If a project with the same filename already exists, the script will skip the iteration and move onto the next project to avoid accidental overwriting. In addition, an export folder is created if one does not exist in the project directory. All data imported and processed is stored within a single chunk in Metashape, which shares reference information and a region (bounding box).

Table 4.2: Example of the project set-up spreadsheet.

Project Name	Project Directory	Estimate Image Quality	Align Quality	Trim Data	Trim Buffer	Depth Map Quality	Dense Point Cloud	Export Dense Point Cloud	Include Point Normals	Textured Mesh	Export Textured Mesh
S240_OD435_N2_050820	D:\Dugald River \Photogrammetry Tests\Capture 2	Y	1	Y	0.5	2	Y	Y	Y	Y	Y
S440_OD400_N1_120820	D:\Dugald River \Photogrammetry Tests\Capture 5	N	1	N	0.5	2	N	N	N	Y	Y

4.5.3. Import Images

The script is intended for an equal number of images per station. This study used 6 images per station for a total of 24-images. The images are saved using the default, sequential naming convention of a camera (e.g. IMG_1804; IMG_1805… IMG_1819). The Python script sorts the images sequentially and adds them to camera stations 1 to 4 also considering instances where the sequence resets due to exceeding 10 000 images, or 100 000 for newer cameras (e.g. IMG_9999 is followed by IMG_0001). Images are grouped into camera stations as this significantly improves the alignment process, which may otherwise produce artefacts (tie points within the rock mass).

Optional image quality estimation provides a rudimentary method to determine if an adjustment of the capture process is required. Given the harsh environment in underground mining, cameras and lenses will have accelerated degradation. In addition, consistent low-quality images may reflect a user requiring further training in the standard operating procedure. Image quality is important in the photogrammetry process and poor images should be excluded. However, excluding images will require that the capture be processed manually within Metashape as the Python script is designed for an equal number of images per station. Metashape can automatically estimate image quality by returning a value calculated based on the level of sharpness of the most focused part of the image (Agisoft, 2019). By using this tool, poor images can be excluded, but this is only recommended if it does not create "blind spots".

4.5.4. Detect Markers and Import Ground Control Points

The Python script is intended to be used with coded targets printed from Metashape. The coded targets allow for full automation of the processing, which would otherwise require manual tagging of GCPs on images. Metashape provides a set of pre-generated targets, with an associated number (target 1, target 2, target 3, target 4 etc.). Four targets were used in this study, thus providing redundancy if a target is not detected by Metashape. Agisoft (2019) provides several guidelines on the correct use and positioning of the coded targets. In this study 12-bit coded targets with a centre point radius of 28 mm were printed in A3 and clipped to cardboard (Fig. 4.5), however, printing the patterns on a harder wearing surface such as corflute plastic is recommended for production purposes. The centre of the coded target was surveyed – in the local mine grid - using a Leica Total Station.

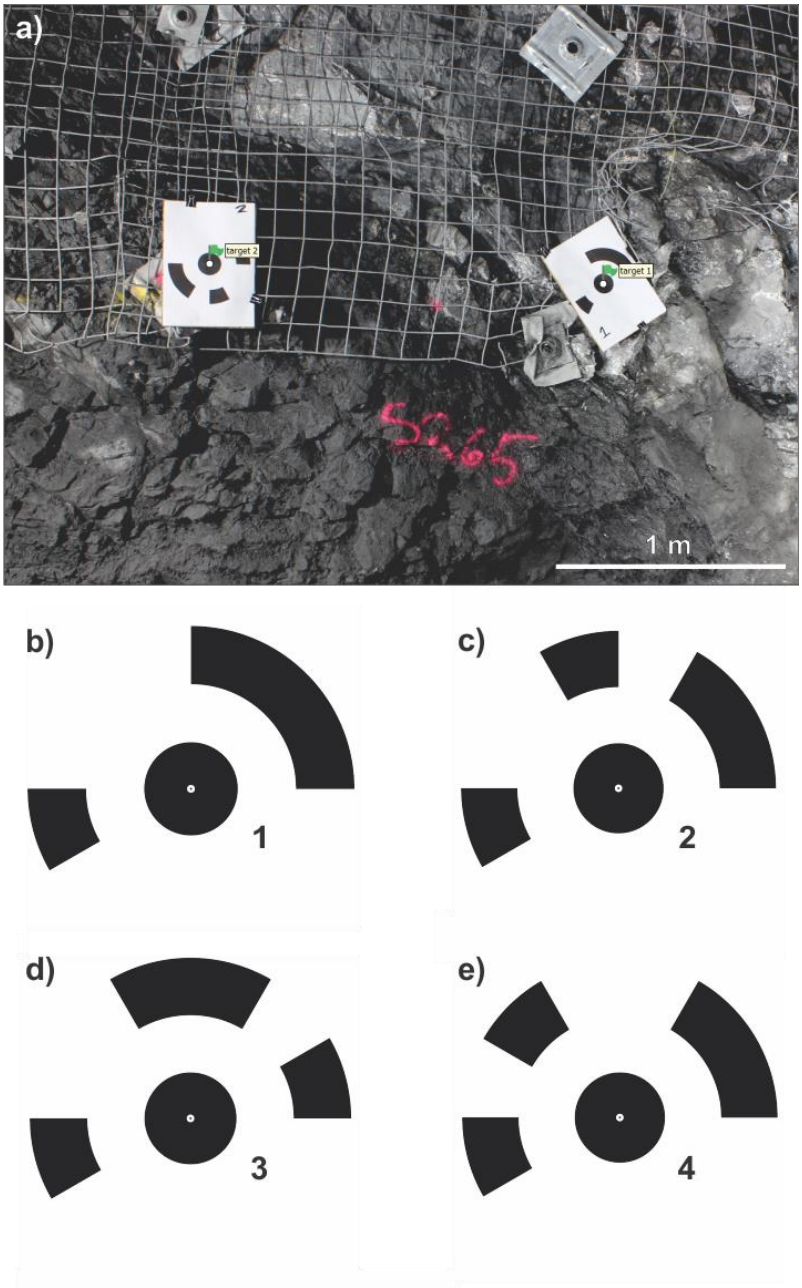

Fig. 4.5: Coded targets printed from Metashape with markers detected in the centre of the target. The coded targets are circular patterns. Thus, the orientation of the target is not important as highlighted in a). Target 1 (b) is inclined while target 2 (c) is inversed. d) and e) are targets 3 and 4, respectively, which occur on the opposite sidewall to that shown in a).

The four coded targets for each test were successfully detected, except in Test 3 (section 5.1.3) where coded target 3 was not detected. This is most likely due to the angle of the coded target relative to the camera station. In subsequent tests, the cameras stations were placed in a position that is near orthogonal to the coded targets. However, it should be noted that Metashape's coded targets are sensitive to pixel size and the dimensions of the target may need to be adjusted to the GSD.

When a unique coded target is detected in an image, an associated marker is created by Metashape. Once the coded targets are detected, reference information for the targets can be imported. The default setting of the Python script is to import csv/txt files with a comma as the delimiter. The markers created by Metashape are sequentially named target 1, target 2 etc. Thus, when surveying the coded targets, this naming convention must be used (see survey text file included with the supplementary data for formatting and naming convention).

4.5.5. Sparse Point Cloud

A sparse point cloud is generated by detecting and matching key points in overlapping images (Bemis et al., 2014; Vollgger and Cruden, 2016). This is done iteratively within an arbitrary local coordinate system defined by Metashape.

When generating the sparse point cloud there may be errors in the sparse point cloud, which can be corrected using Optimise Camera. Possible non-linear deformations are removed to minimise the reprojection error and improve the georeferencing accuracy.

Generation of the sparse point cloud is done in 3 steps: 1) match photos; 2) align cameras; and 3) optimise cameras. The accuracy of the alignment is set in the spreadsheet included as supplementary data (Table 4.2). The number is directly linked to the alignment accuracy as per the Metashape Python Reference for v1.6 (Table 4.3). The suggested value for the script is *downscale = 1*, which refers to high accuracy with Metashape using the original resolution of the images. When the images are aligned, Metashape applies a chunk transformation to the chunk, which includes a translation, scale, and rotation component (see section 4.6).

Table 4.3: Downscale number settings for image alignment (sparse point cloud) and depth maps.

	Sparse Point Cloud	Depth Maps
Highest (Ultra for depth maps)	0	0
High	1	2
Medium	2	4
Low	4	8
Lowest	8	16

4.5.6. Modify Region

Metashape automatically generates a region (bounding box) when images are aligned. The region encapsulates the sparse point cloud and is rotated and sized to represent a rectangle. The position of the camera stations and GCPs, combined with the requirement for significant overlap between images, results in the wire mesh (steel ground support) and the floor of the tunnel being included in several images. The wire mesh results in a chessboard pattern in the dense point cloud and mesh, and the floor provides no geological significance as it is comprised of blasted material and may contain puddles of water. Water represents a reflective surface that is problematic for SfM-MVS and may result in erroneous points (Vollgger and Cruden, 2016). Fortunately, the apparent, or generated position of tie points and dense point clouds computed from water puddles in tunnels will occur below the physical position of the water (Fig. 4.6). Thus, excluding these points from further processing simply requires that a lower elevation limit be set for the region.

Modifying the region, or bounding box is an optional parameter in the Python script. In addition to excluding wire mesh and cropping the 3D reconstruction, resizing the region reduces the overlap that is visible when loading several successive captures as the face of the previous capture will generally be at the unsupported ground line of a current capture. Furthermore, the wire mesh represents a complex surface, which significantly increases the number of points in the dense point cloud and is reflected in the file size of the exported dense point cloud and mesh. For example, in this study, the median file size for the untrimmed dense point cloud and mesh is 2221 MB and 415 MB, respectively. The file size for the trimmed dense point cloud and mesh is 977 MB and 352 MB, respectively.

Tunnel heading directions can be in any cardinal direction. Therefore, modifying the region needs to be dynamic, because the rotation, translation and scale of the transformation matrix will be different for each capture as Metashape uses an arbitrary local coordinate system. The coordinate system at Dugald River mine is modified from the GDA84 datum with an eastward shift of 9° to align the strike of the orebody with True North. Thus, ore drives and footwall drives are developed "north-south", and crosscuts and access drives are "east-west". The parameters used to modify the region are determined from the generated sparse point cloud and 4 additional points in the imported survey file. Parameters include vertices of the region as well as the size and rotation of the region.

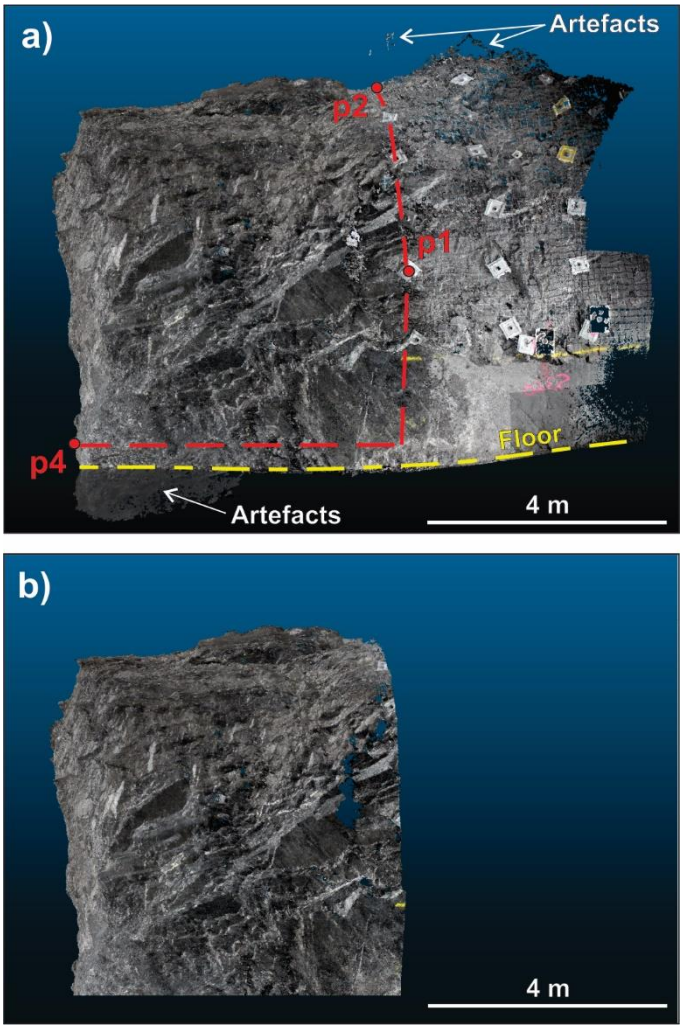

Fig. 4.6: Mesh of the same capture shown in Fig. 4.4 in which a puddle of water occurs near the face. a) The wire mesh and puddles may produce artefacts within the rock mass. The red dashed line in a) delineates the region shown in b), which is the output mesh if trim data is enabled in the script. Trimming the data excludes the wire mesh and floor of the capture, which would otherwise have little to no geological significance. Refer to Fig. 4.7 for a description of p1, p2 and p4. Screenshots taken in open-source software, CloudCompare (www.danielgm.net/cc).

The additional points do not need to have an associated coded target, rather the position of where the points are surveyed is important (Fig. 4.7a, b). The points must be labelled p1 to p4 as the script uses index labels (see survey text file included in supplementary data). The first 3 points (p1 to p3) must be surveyed on the first row of bolts on both sides of the tunnel and the back of the tunnel to form a triangle, orthogonal to the heading direction. p4 is recorded on the tunnel face (Fig. 4.7a, d) and the elevation of p4 is used as the lower limit of the region and should consider any rubble that may occur between the camera stations and the face as this should be excluded from further processing.

The points, p1 to p4, are used to calculate a rigid transformation matrix. In 3D space the rigid transformation matrix comprises a rotation (3 X 3 matrix) and a translation (3D vector), together written as a 4 X 4 matrix (Förstner and Wrobel, 2016) of the form:

$$T = \begin{bmatrix} a1 & a2 & a3 & t1 \\ b1 & b2 & b3 & t2 \\ c1 & c2 & c3 & t3 \\ 0 & 0 & 0 & 1 \end{bmatrix} \tag{4.1}$$

Where the upper part of the first 3 columns represents the rotation matrix (a1 to c3) and the upper part of the last column the translation vector (t1 to t3). The lowest row is used to complete the 4 X 4 matrix as multiplying a 3D spatial vector by a 3 X 4 matrix is not possible. The purpose of the transformation matrix is to rotate the sparse point cloud parallel to the y-axis of the local mine coordinate system. To achieve this, the origin of the coordinate system is translated to a point within the sparse point cloud around which the sparse point cloud will be rotated. This new origin is the centroid of triangle p1, p2 and p3, calculated using:

$$\mathrm{C} = \frac{\mathrm{p1} + \mathrm{p2} + \mathrm{p3}}{3} \tag{4.2}$$

The translation component of the transformation matrix is calculated by multiplying the centroid vector by -1. To align the sparse point cloud parallel to the y-axis of the coordinate system, the sparse point cloud is rotated in the xy-plane using:

$$R = \begin{bmatrix} cos\theta & -sin\theta & 0 \\ sin\theta & cos\theta & 0 \\ 0 & 0 & 1 \end{bmatrix} \tag{4.3}$$

Where theta (θ) is determined using the x- and y- components of the normal to the triangle centroid. The normal is calculated using the cross product of two vectors originating from the centroid:

$$v1 = centroid - p1 \quad (4.4)$$
$$v2 = centroid - p2 \quad (4.5)$$
$$normal = v1 * v2 \quad (4.6)$$
$$\theta = \arctan\left(\frac{y}{x}\right) \quad (4.7)$$

Where y is the y-component and x is the x-component of the normal. However, equation 7 is only true when x > 0, i.e. the first and fourth quadrant. To return unique values for all quadrants, the sign of x and y are used (Dinechin et al., 2015; Förstner and Wrobel, 2016) together with the two-argument function atan2(y,x) that is widely used in computer programming. In the script the numpy library of Python is used for mathematical operations with equation 7 modified for clockwise rotation:

$$\theta = \frac{\pi}{2} - atan2\left(\frac{y}{x}\right) = atan2\left(\frac{x}{y}\right) \quad (4.8)$$

The transformation matrix is determined by multiplying the rotation matrix with the matrix form of the translation vector:

$$T = \begin{bmatrix} a1 & a2 & a3 & 0 \\ b1 & b2 & b3 & 0 \\ c1 & c2 & c3 & 0 \\ 0 & 0 & 0 & 1 \end{bmatrix} * \begin{bmatrix} 1 & 0 & 0 & t1 \\ 0 & 1 & 0 & t2 \\ 0 & 0 & 1 & t3 \\ 0 & 0 & 0 & 1 \end{bmatrix} = \begin{bmatrix} a1 & a2 & a3 & t1 \\ b1 & b2 & b3 & t2 \\ c1 & c2 & c3 & t3 \\ 0 & 0 & 0 & 1 \end{bmatrix} \quad (4.9)$$

A transformation matrix of 3D space is a 4 X 4 matrix, thus the extra elements shown in equation 9 are required to adhere to matrix multiplication rules. Similarly, when applying the transformation matrix to the sparse point cloud, an additional column of ones needs to be added. Finally, the sparse point cloud can be transformed using:

$$\begin{bmatrix} x' \\ y' \\ z' \\ 1 \end{bmatrix} = \begin{bmatrix} x \\ y \\ z \\ 1 \end{bmatrix} * T' \tag{4.10}$$

Where T' is the transposed matrix of transformation matrix T.

The size of the region is determined from the minimum and maximum coordinates of the transformed sparse point cloud. The sparse point cloud comprises tie points, which may not necessarily reflect the final shape of the dense point cloud or mesh. Thus, a buffer is included in determining the size of the region. The buffer value is set in the spreadsheet (Table 4.2), with a recommendation of 0.5 m. Outlier tie points beyond 0.5 m from the tunnel are rare, with exceptions being water puddles (Fig. 4.6) that are removed by setting a lower elevation limit to the region. The outputs if the script is intended to be used with manual digitising for mapping, thus outliers will be easily identified by the user. When using automated mapping techniques from dense point clouds, the outliers will need to be removed, which is beyond the scope of this manuscript.

For simplification, the shape of the region represents a cube, therefore the size of the region will be the maximum distance of either:

$$d1 = (\max(x) + b) - (\min(x) - b) \tag{4.11}$$
$$d2 = \max(y) + b \tag{4.12}$$
$$d3 = (\max(z) + b) - p4(z) \tag{4.13}$$

Where x, y and z refer to transformed x-, y- and z- coordinates of the sparse point cloud, p4(z) is the transformed z-coordinate of p4 and b is the buffer assigned from the spreadsheet. Note, the distance of the y-coordinate is determined from the origin (i.e. y = 0) as the region is designed to exclude the wire mesh. Similarly, the lower elevation of the region is assigned from the z-coordinate of p4.

The region size is used to determine the vertices (corners) of the region, which in turn are used to determine the region centre (Fig. 4.7c, d). In addition to the region size and centre, the rotation of the region is required by Metashape. Python script modifications from Pasumasnky (2018, 2019) are used to determine the region centre and the rotation of the region. Given the clockwise transformation of the sparse point cloud and the lower elevation of the region is the z-coordinate of p4, the coordinates of the

first two corners are calculated using equation 14 and 15, respectively, with the region centre (equation 16) calculated as the midpoint of line c1 – c2 (Pasumasnky, 2019):

$$c1 = (\min(x) - b, 0, p4(z)) \quad (4.14)$$
$$c2 = ((\min(x) - b) + \max(d1, d2, d3), \max(d1, d2, d3), p4(z) + \max(d1, d2, d3)) \quad (4.15)$$
$$region\ centre = \frac{c1 + c2}{2} \quad (4.16)$$

The rotation of the region requires 3 orthogonal corners. As c1 is already calculated, the two additional corners are determined using (Fig. 4.7c, d):

$$c3 = ((\min(x) - b) + \max(d1, d2, d3), 0, p4(z)) \quad (4.17)$$
$$c4 = ((\min(x) - b), \max(d1, d2, d3), p4(z)) \quad (4.18)$$

The z-coordinate of the 3 corners are set to that of the calculated region centre to define a plane with two vectors as the sides:

$$v3 = c1 - c3 \quad (4.19)$$
$$v4 = c1 - c4 \quad (4.20)$$

From which the rotation of the region is determined using Pasumasnky (2018, 2019):

$$normal2 = v3 * v4 \quad (4.21)$$
$$v5 = -(v4 * normal) \quad (4.22)$$
$$R = \begin{bmatrix} v4(x) & v4(y) & v4(z) \\ v5(x) & v5(y) & v5(z) \\ normal(x) & normal(y) & normal(z) \end{bmatrix} \quad (4.23)$$

Note the results of the cross products are normalised and x, y, z refer to the x, y, and z components of the respective vectors. The existing region in the chunk is overwritten by R.

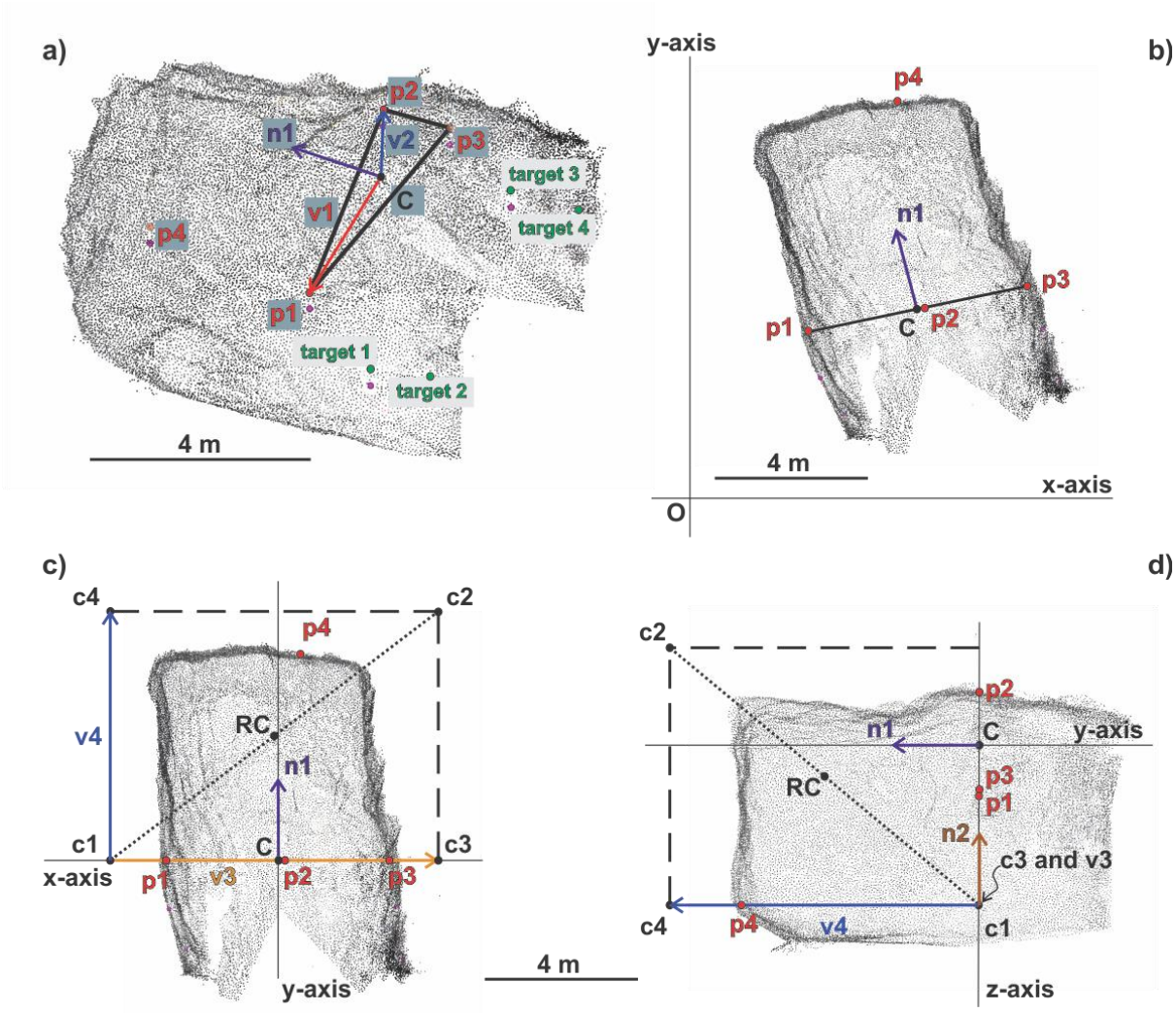

Fig. 4.7: Steps involved in modifying the region when trim data is selected. Shown here is a subsampled dense point cloud with screenshots taken in open source software CloudCompare. a) Oblique view showing the positioning of GCPs (target 1 – target 4) and additional points (p1 - p4) required to determine a transformation matrix (T) (Eq. 4.1). p1 – p3 form a triangle with centroid C (Eq. 4.2), from which the normal (n1) can be calculated as the cross product of vectors v1 and v2 (Eq. 4.6). The negative coordinates of C are used as the translation component of T and the normal is used to calculate the rotation component of T using Equations 3 – 8. b) Plan view of the same capture. In this instance the capture occurs within the first quadrant of the Dugald River coordinate system (Note: coordinate axes not to scale). The tunnel heading direction is north-northwest, which after applying T is transformed to north with the origin of the coordinate system now C. c) Plan view and d) side view of the transformed point cloud. The region centre (RC), size and rotation are required by Metashape. The region size, shown as the long-dashed line and calculated as the maximum of Eq. 4.11, 4.12, or 4.13. Corners c1 and c2 are determined using Eq. 4.14 and 4.15, respectively and RC is the midpoint of line c1 to c2 (small dashed line). Finally, the rotation of the region is calculated using additional corners, c3 and c4, that are orthogonal to c1. The corners are used to determine vectors v3 and v4 from Eq. 4.19 and 4.20, respectively with the cross product of these vectors defining n2 (Eq. 4.21). The x, y and z components of v4, n2 and a final vector (v5) determined from Eq. 4.22 define the rotation matrix R (Eq. 4.23).

4.5.7. Dense Point Cloud and Textured Mesh

This step represents the longest computational time. The spreadsheet can be used to inform the script whether a dense point cloud, textured mesh, or both are required (Table 4.2). Depth maps are generated before a dense point cloud, or mesh can be built. The quality of the depth maps is also defined in Table 4.2, which is linked to the depth maps reconstruction quality as per the Metashape Python Reference for v1.6. (Table 4.3). We suggest a default setting of 2 ('*high*'). The setting '*ultra*' represents a significant increase in computational time and number of points in the dense point cloud and vertices of the mesh, without providing a significant visual improvement. The setting '*medium*', although taking less time to compute, results in a noticeable drop in the quality of the dense point cloud and mesh. The dense point cloud, by default includes point colours determined from the images.

Textured mesh building is recommended as it is easier to view and digitise the capture in 3D modelling software than in the dense point cloud. In the Python script the textured mesh is constructed in 3 steps: 1) generate a model; 2) generate uv mapping for the model; and 3) generate texture for the model.

4.5.8. Exporting

The final part of the script is to export the results. A dense point cloud and/or textured mesh can be exported. If required, calculated normals for the points within the dense point cloud can be included. The files are exported to the export folder created within the project directory. The default file formats for the exports are ASCII (txt) for the dense point cloud and .obj for the mesh as they are widely used in the software. Note, if exporting a texture with the mesh, 2 additional files are included (.mtl and .jpg) that need to be in the same folder as the .obj file with the same file name and no white spaces. The default file formats can be changed, but this will require modification of the Python script.

4.5.9. Log File

An optional log file can be saved after the processing is complete. Table 4.4 is an example log file for the captures processed in Table 4.2. The log file is saved as a .csv file in the same folder as the Python script. The log file provides a summary of the processing steps taken, and it records any issues that may have occurred during processing, such as an existing project, which will return TRUE if a project was detected in the project folder.

Table 4.4: Example of the log file using the captures shown in Table 2.

Project Name	Project Exists	Images	Image Quality Estimated	GCP	Trim Data	Dense Point Cloud	Textured Model	Export Files	Total Time
S240_OD435_N2_050820	FALSE	24 images	TRUE	4 markers	TRUE	TRUE	TRUE	Files exported	12.456
S440_OD400_N1_120820	FALSE	24 images	FALSE	4 markers	FALSE	FALSE	TRUE	Files exported	14.367

4.6. Dugald River Case Study

The methodology described in section 3 was tested in five active headings at the Dugald River mine. Several lighting set-ups and camera settings were tested at each capture. The results of capture 1 were used to guide the set-up and camera settings of capture 2 and so forth. In total 68 tests were done and processed for trimmed and untrimmed versions using the Python script. A Canon EOS 550D using an 18 – 55mm zoom lens set at a focal length of 18mm was used to capture images. Due to lengthy experiment times, a different camera was used to that of the mine which uses a Canon EOS 6D and wide-angle lens set at 20mm. The ISO and f/stop are the primary camera settings that were changed, with the shutter speed adjusted automatically by the camera.

A review of historical captures at Dugald River mine found that the images used are noisy and unfavourably exposed, due to a camera setting of ISO 2000 and a 2-light set-up on the ground. Features such as banded ore, veins and large clasts in images do not have sharp boundaries and the 2 lights set-up produces uneven exposure (e.g. Fig. 4.2b, d). Hence, a baseline camera setting of f/ 8 and ISO 1600 was used, which for the Canon EOS 550D is the closest ISO value that can be set to that of the Canon EOS 6D.

Image quality is an important factor in a high-quality capture, however, estimating image quality is a complicated subject, particularly when considering objective methods. Metashape provides a tool that can be used to estimate image quality by returning a sharpness value of the most focused part of the image. While this facilitates in determining whether an individual image is blurry, it has limited use in comparing image quality between captures, and tests within a capture using different camera settings and light set-ups. Thus, a subjective approach was taken. Select images from the same capture were visually compared using several criteria: 1) depth of field (sharpness); 2) colour range; and 3) boundaries of features in the images. Distinct features such as veins, faults/shears and sulphides bands were used as comparators. The dense point clouds and mesh products from the script were compared similarly. A flow diagram was used for comparing the images (Fig. 4.8). Note that the same image number was compared (e.g. station 3, image 4 was compared with station 3, image 4 of another test).

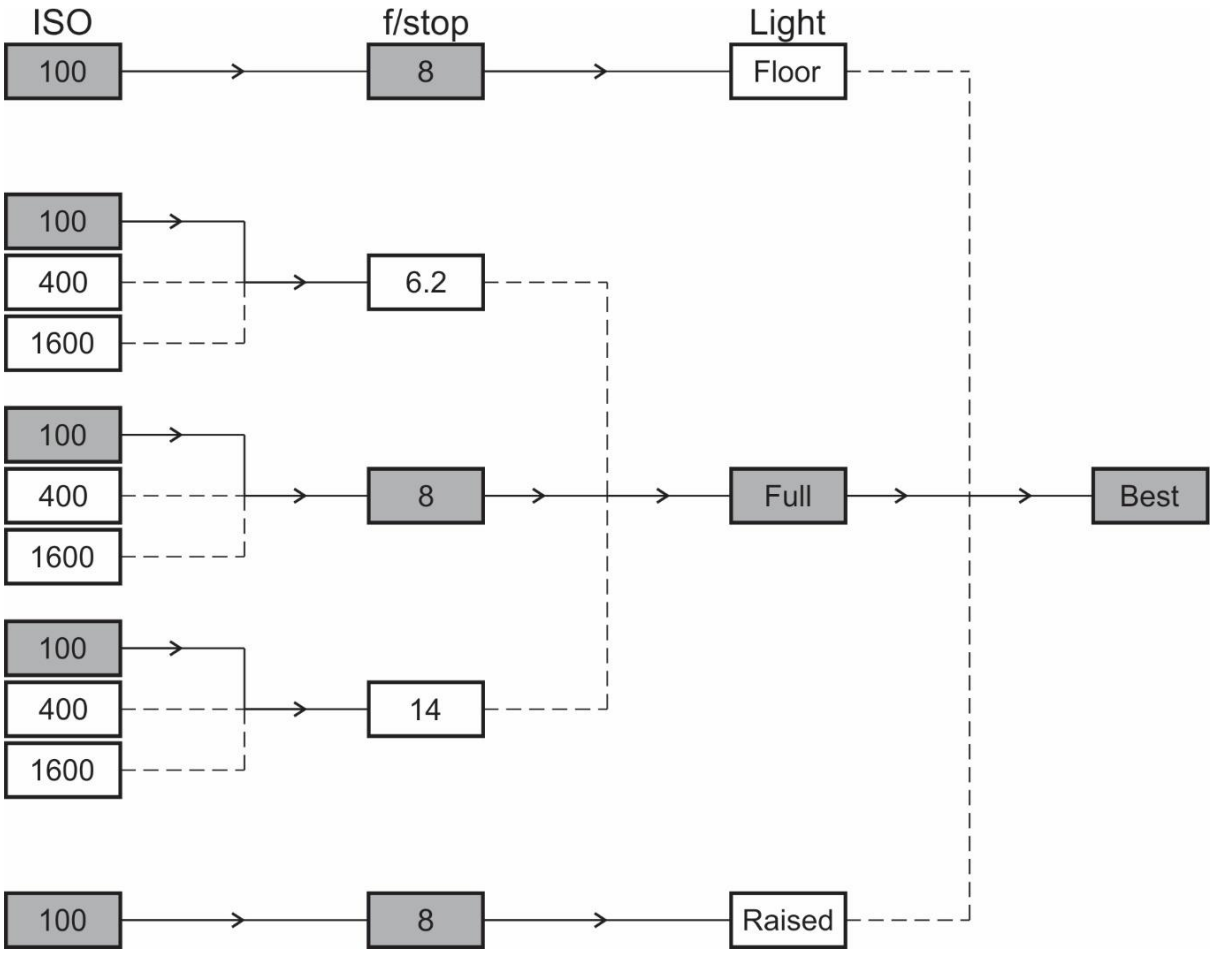

Fig. 4.8: Flow diagram of Capture 3 (see Section 5.1.3). In the first comparison, the ISO values for each light set-up and f/stop value are compared. In the second comparison, the best ISO value for each f/stop value are compared and finally, the best light set-up is compared. For Capture 3 the highest quality images were determined to be ISO 100 with a f/stop of 8 and a full light set-up.

4.6.1. Results and Interpretation

4.6.1.1. Capture 1

The purpose of the first capture was to ascertain whether Metashape will pick up printed coded targets in an active underground mining setting. In addition, while f/ 8 used in the mine procedure provided sufficient depth of field, the ISO value of 2000 resulted in noisy images and, therefore, loss of detail. Thus, lowering of the ISO value was also tested (Table 4.5) in this capture with criteria 2 and 3 used as estimators. All lights were used in the capture. The results from capture 1 indicate that lowering the ISO value produces a visual improvement in the sharpness of the images as well as clearer colour variation (Fig. 4.9), which is reflected in the dense point cloud and mesh.

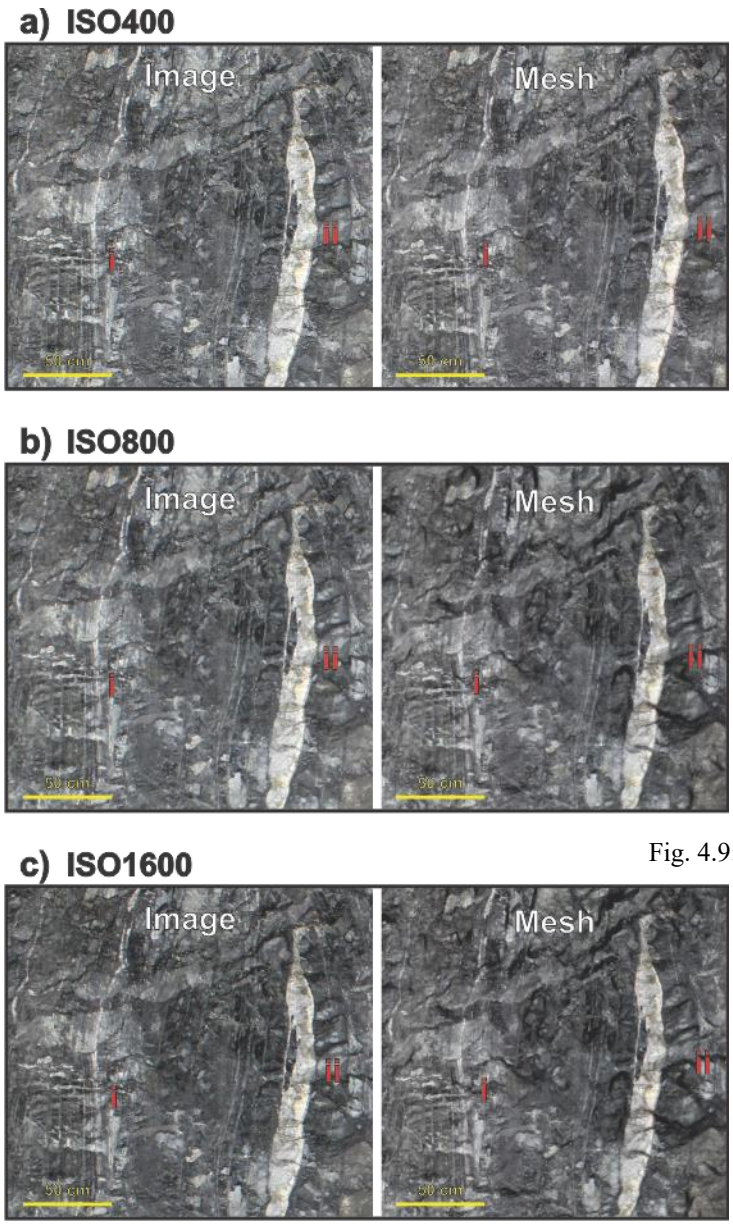

Fig. 4.9: Selected images and screenshots of associated textured meshes from Capture 1. In this capture f/stop, 8 was used with 3 different ISO values: a) ISO 400; b) ISO 800; and c) ISO 1600. Distinct features used to compare the images and textured meshes are indicated with (i) and (ii). The banding indicated by (i) is clearer with ISO 400 (a). Similarly, the colour variation of the carbonate vein shown at (ii) is clearer with ISO 400 (a).

4.6.1.2. Capture 2

The ISO settings were the same as Capture 1. The f/stop was incrementally increased from f/ 7.1 to f/ 16 and all lights were used in this capture (Table 4.5; Fig. 4.10). Here all criteria were applied with the result indicating that f/ 8 ISO 400 has the best image quality, dense point cloud and mesh. Furthermore, the results of testing a range of aperture diameters shows that there is no significant visual improvement in the image quality and similar to Capture 1, the improvement is due to a lower ISO value (viz. ISO 400) (Fig. 4.10a - c).

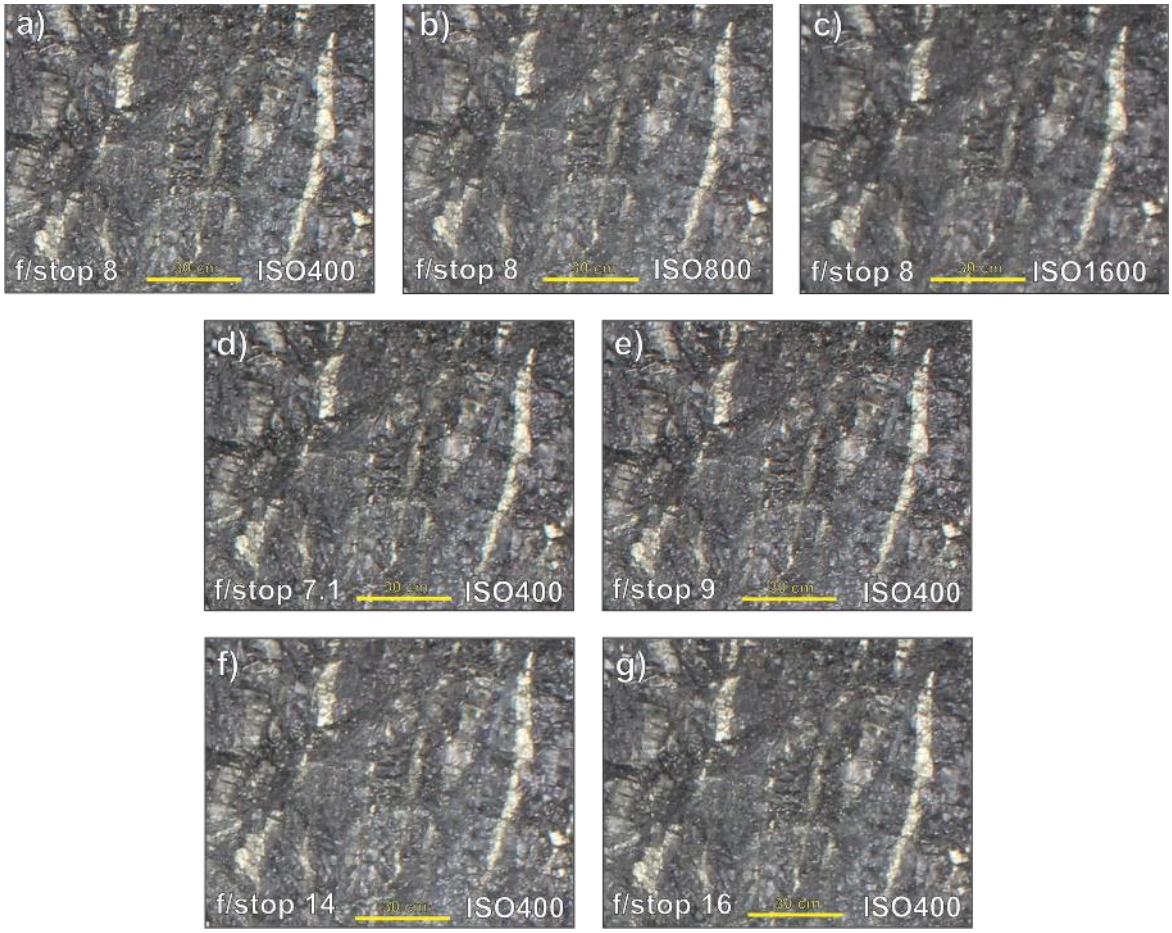

Fig. 4.10: Selected images from Capture 2. In this capture, the f/stop was incrementally increased from 7.1 to 16 (a, d – g), with ISO 400, 800 and 1600 tested with each f/stop. Using ISO 400 as a constant, the f/stop values shown in (a, d – g) show little quality improvement. However, when comparing the different ISO values using f/stop 8 as a constant (a – c), by increasing the ISO values there is a noticeable increase in noise and fuzzier boundaries between distinct features (indicated here with sulphide bands).

4.6.1.3. Capture 3

The results from Captures 1 and 2 indicate that the ISO value is the primary factor determining the image quality. Thus, for Capture 3 the lighting set-up was tested to ascertain if more lights and/or the height at which the lights were placed have a significant impact on image quality with all criteria used in estimating image quality. Placing lights on the ground is simpler and more efficient than using a light stand or hanging lights from a rope. Furthermore, as ISO 400 was found to be the best ISO setting from the previous captures, ISO 800 was replaced by ISO 100, the lowest possible setting for the camera, and f/ 6.2, 8 and 14 were used (Table 4.5). From the previous captures, the aperture diameter did not visibly influence the quality of the images, thus a lower f/stop of 6.2 was tested with results indicating that with this f/stop value, there was a noticeable drop in image quality. However, this may in part be due to the distance from the supported ground being further than previous captures (~5.5 m vs. ~4.5 m).

An ISO value of 100 produced the best image quality for this capture combined with f/ 8 and a full light set-up. Using a full light set-up results in a diffuse capture, whereas only using a floor, or raised set tends to create shadows towards the corner of the sidewall and the face (Fig. 4.11). Shadows are included in the computation but tend to produce dark areas, which are reflected in the textured mesh if interpolation is used.

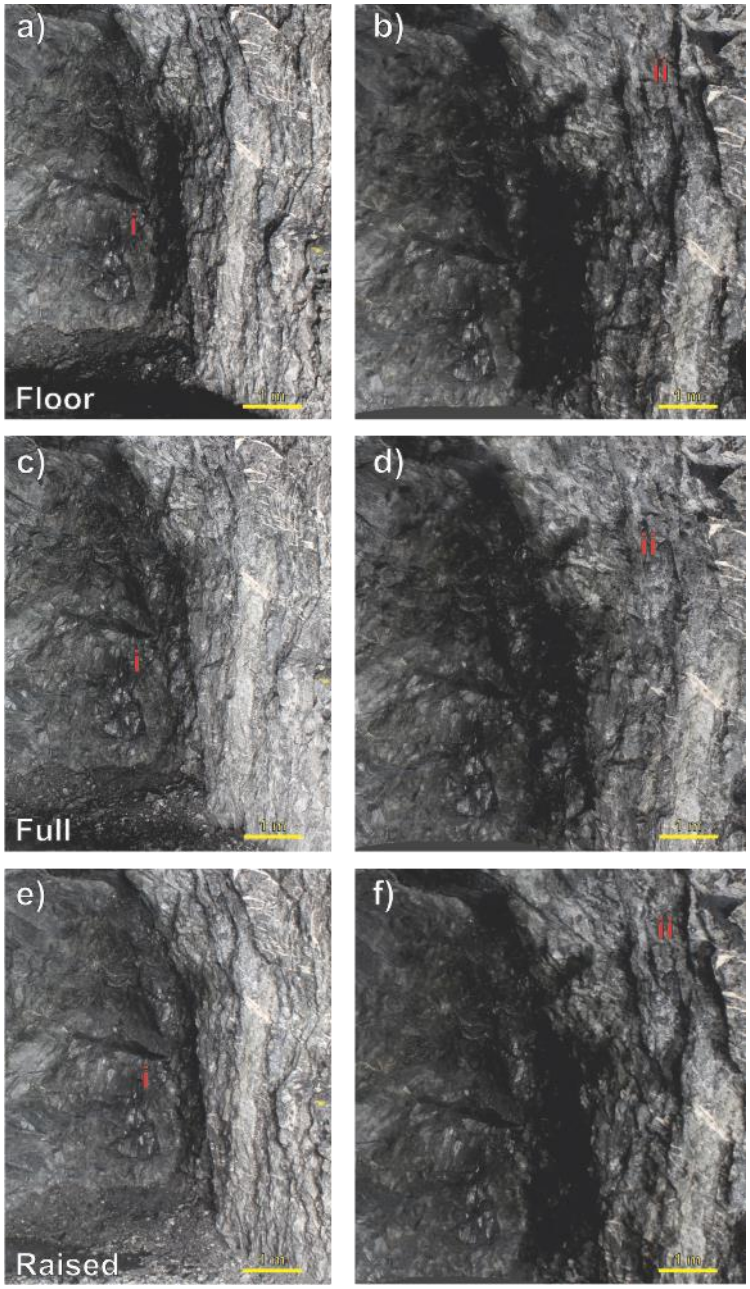

Fig. 4.11: Selected images (a, c, e) and meshes (b, d, f) from Capture 3. f/ 8 and ISO 100 are shown here with a floor light set-up (a, b), full light set-up (c, d) and raised light set-up (e, f). A full light set-up has diffuse lighting as indicated at (i, ii) when compared to a floor or raised set-up where shadows are visible. The shadows are accentuated in the mesh.

4.6.1.4. Capture 4

Capture 4 was performed to provide additional tests for a full light set-up and raised lights (Table 4.5). The floor-only set-up produced more shadows than the raised set-up while conducting Capture 3, with a noticeable drop in illumination towards the back of the tunnel. Thus, the floor set-up was excluded from the onset in Capture 4. f/ 6.2 resulted in lower quality images than f/ 8 and 14, but not as significant as observed in Capture 3. Thus, a lower limit of f/ 7.1 can be inferred for underground mining settings. Similar to Capture 3, f/ 8 and ISO 100 using a full light set-up was found to have the best quality images, dense point cloud and mesh, however, f/ 14 with ISO 1600 for a raised set-up has comparable image quality. However, as highlighted in Fig. 4.12, less diffuse light from fewer light sources results in shadows.

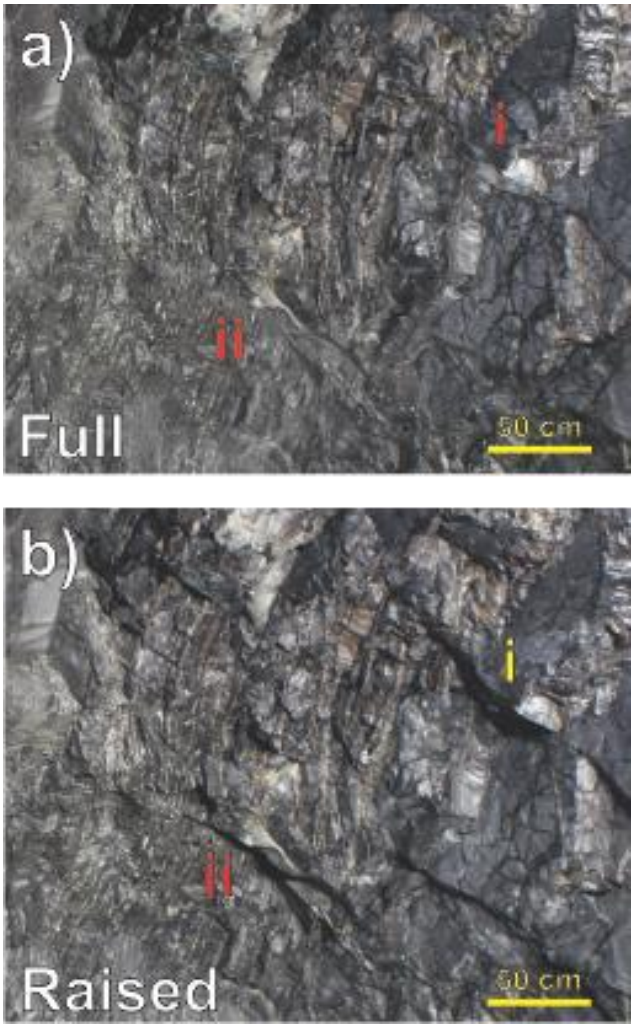

Fig. 4.12: Selected images from Capture 4. f/ 8 and ISO 100 images are shown. A full light set-up (a) produced a diffuse scene compared to a raised light set-up (b) where shadows are noticeable (see i and ii). Furthermore, using a full light set-up produced a clearer colour variation.

4.6.1.5. Capture 5

The final capture was performed to target a high-grade ore drive. Due to time constraints, only a full light set-up and f/ 8 and 14 were tested. Comparing ISO 100, 400 and 1600 results, ISO 100 returned the best image quality. There is no noticeable difference in image quality between f/stop 8 and 14.

4.6.1.6. Capture Processing

A high-end gaming desktop was used in this study to process the 68 tests. The total processing time is shown in Fig. 4.13 and includes trimmed and untrimmed versions. The custom-built system includes an i9 9900KF CPU, 64Gb DDR4 RAM, m2.NVME SSD, RTX 2080 Super GPU and 12Tb of HDD in RAID 5 with a cost of AUD$ 5500. The trimmed version has a median processing time of ~14 min and untrimmed of ~16 min, therefore not a significant increase in processing time per project, however, untrimmed is associated with a significant increase in data storage requirements.

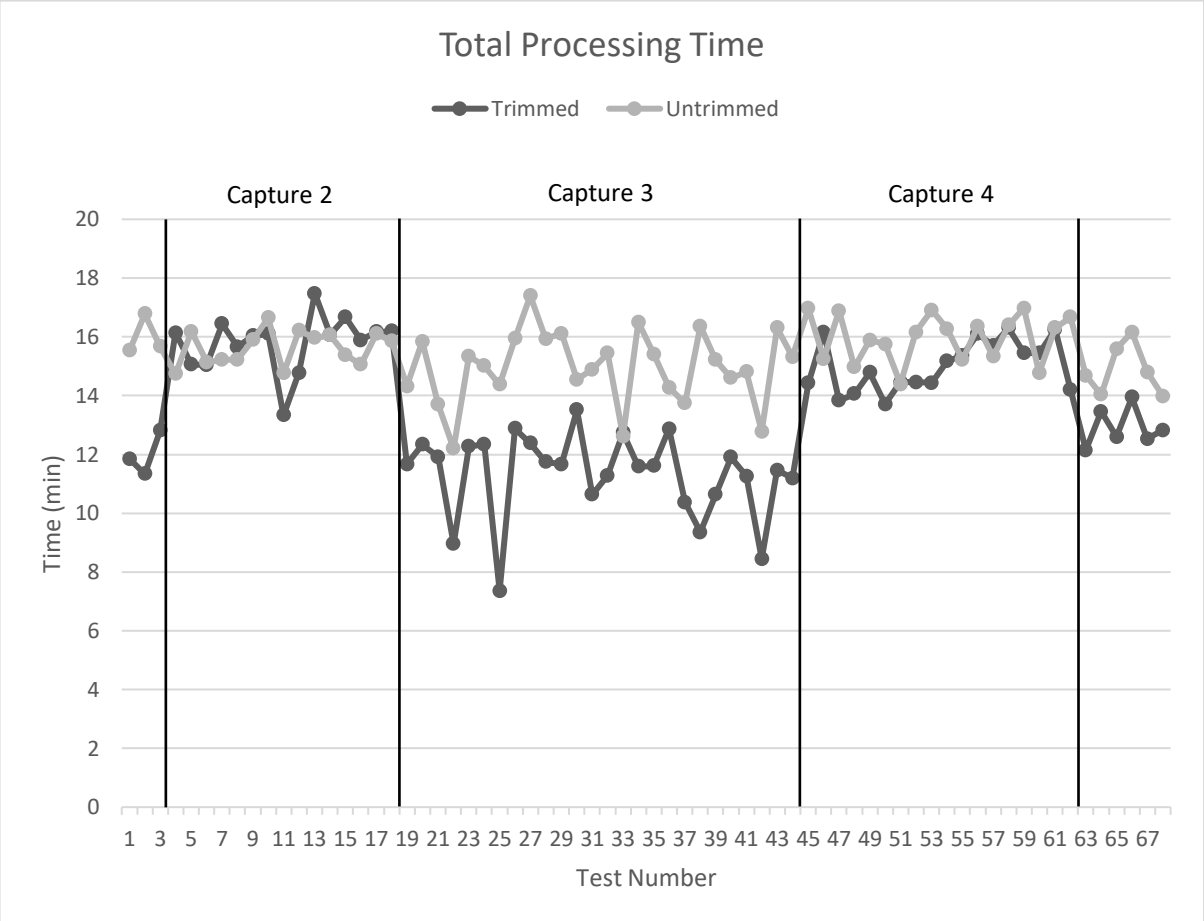

Fig. 4.13: Chart displaying the total processing time for each test with trimmed and untrimmed versions. The trimmed version has a median processing time of ~14 min and untrimmed of ~16 min.

4.6.2. Summary

Based on the results from the 5 captures, having a low ISO value with a f/stop greater than 8 results in high-quality images, and a dense point cloud and mesh. While the objective of SfM-MVS is to produce the highest quality virtual outcrop, additional factors need to be considered in an active mine setting. Primarily, the time to set-up and conduct a capture.

The process followed in this study is setting up the lights, connecting the hose to a water valve, mounting the camera and Total Station to its tripod, and placing the coded targets on the sidewall. Before georeferencing the Total Station and surveying the coded targets, the face is washed and allowed to dry to avoid glare on images. The final step is to capture images.

An aperture value of f/ 8 and ISO 400 produced the highest quality images. However, as shown in Table 4.5, increasing the f/stop value may result in long exposure times. For example, using f/ 14 (small diameter lens diaphragm) and ISO 100 (low light sensitivity) will produce high-quality images, but is associated with shutter speeds of up to 30 seconds. This may result in captures taking up to 30 min using a 24 image methodology. In high-grade ore drives, this may be problematic as they are usually high priority drives for charge-up. Thus, using f/8 and ISO 400 is recommended with a full-light set-up, with a capture taking < 20 min and processing of the capture in Metashape taking ~15 min.

Table 4.5: f/stop and ISO values used in the 5 captures. For each capture, the light set-ups are indicated in parentheses. The minimum, maximum and median shutter speeds are included in the table.

Capture	f/stop	ISO	Shutter Speed (seconds)		
			Minimum	Maximum	Median
1 (full light set-up)	8	400	0.6	3.2	2
		800	0.6	2	1
		1600	0.125	0.6	0.5
2 (full light set-up)	7.1	400	0.5	2.5	1.6
		800	0.25	1	1
		1600	0.125	0.6	0.5
	8	400	1	3.2	2
		800	0.3	1.6	1
		1600	0.2	0.8	0.6
	9	400	1	4	3.2
		800	0.5	2	1.6
		1600	0.25	1	0.8
	14	400	3.2	10	8
		800	2	5	4
		1600	1	2.5	2
	16	400	2.5	13	10
		800	1.6	6	5
		1600	1	3.2	2.5
3 (full, floor and raised light set-up)	6.3	100	1	4	2.5
		400	0.25	1	0.6
		1600	0.016	0.3	0.166
	8	100	2	6	4
		400	0.4	1.6	1
		1600	0.1	0.3	0.25
	14	100	5	20	13
		400	1.6	5	2.85
		1600	0.3	1.3	0.8
4 (full and raised light set-up)	6.3	100	1.3	6	5
		400	0.3	1.6	1.3
		1600	0.08	0.5	0.275
	8	100	1.3	10	8
		400	0.5	2.5	2
		1600	0.125	0.6	0.45
	14	100	6	30	25
		400	1.6	8	6
		1600	0.5	2	1.6
5 (full light set-up)	8	100	4	10	8
		400	0.8	2.5	2
		1600	0.166	0.6	0.5
	14	100	10	30	25
		400	4	8	5.5
		1600	0.6	2	1.6

4.7. Discussion

This study provides a detailed methodology to apply SfM-MVS in underground mining with a script that allows for automation of the processing. The move towards safer and cost-effective mining in the digital age will require that mapping evolves from physically mapping every cut, to mapping important areas of development and using virtual outcrops to populate the regions between. This is emphasised in structurally complex deposits where robust data collection is required while keeping up with high rates of underground development.

In structurally complex deposits, there are large areas of the underground mine development where the planar fabric has a consistent orientation and structures are not observed. In these areas, the cuts can be mapped quickly using virtual outcrop format, thus, providing more time for areas that are deemed structurally complex where detailed mapping is required. Furthermore, development faces may have multiple structures that need to be mapped, however, due to safety concerns, orientation data for these structures cannot be measured directly, but are rather estimated. Notably, estimated data should not be used in downstream processes such as 3D models, highlighting the value of virtual outcrops as they provide a reference surface on which polylines or orientated points can be digitised.

Virtual outcrops are displayed in true colour, thus they can be used to accurately delineate lithological and ore-waste contacts and can be used to characterise structures, particularly the scale of a structure. The direct digitising of structures and lithological contacts aid in constraining 3D models with the added advantage of viewing additional data within the same view (e.g. drilling data, modelled surface/volumes). Furthermore, virtual outcrops allow for knowledge-driven, highly detailed 3D models to be produced from faces that would otherwise no longer be mappable.

The combination of the detailed description of how to set-up a capture for high-quality images and automated processing provides a significant improvement over previous work (e.g., García-Luna et al., 2019; Slaker and Mohamed, 2017; Whaanga et al., 2019). Captures require GCPs if the virtual outcrops are to be used in 3D modelling software. Replacing spray painted GCPs with coded targets is straightforward and p1 – p4 can be captured at the same time as the GCPs are surveyed. The points, p1 – p4 are used in geometry calculations, thus the technique can be applied to any underground mine using the Python script or coded into other software. Furthermore, with the spreadsheet provided in the supplementary data, the captures can be batch processed, e.g., all tests in this study were processed overnight in a single run.

Detailed in this study are 68 tests done at the Dugald River mine. The purpose of this was to firstly, determine if, in underground mines, a low ISO value resulted in less noise in images and, therefore, sharper boundaries between features and, secondly, to determine what influence the f/stop value has on the sharpness of images. Lowering the ISO value has a noticeable effect on reducing the noise in images with sharper boundaries between features. Lowering the f/stop value below 8 gradually results in images becoming blurry as the aperture of the lens widens and the depth of field becomes shallower. Conversely, increasing the f/stop value above 8 does not result in noticeably sharper images, but is associated with decreasing shutter speeds. Time to set-up and capture a heading, factor into the applicability of SfM-MVS in underground mining, thus higher f/stop values are not suggested. Consequently, the result of f/ 8 and ISO 400 are ideal for the camera and lens used in this study and the light set-up. However, minor adjustments of the camera settings suggested may need to be made when using a different camera and/or lens and light set-up, following the logic shown on the exposure triangle (Fig. 4.2).

4.8. Conclusion

- A procedure for capturing high-quality images to be used in SfM-MVS is described in the paper. The procedure can be used in a standard operating procedure in any underground mine using off-the-shelf equipment.
- A Python script that uses Agisoft Metashape Professionals Python API is provided. The Python script allows for automated processing of captures using minor tweaks to the procedure for capturing high-quality images. The Python script allows for batch processing of captures with each capture taking 15 min to process.
- Camera settings are an important factor in capturing high-quality images. The ISO and f/stop settings are the most important settings that govern image quality. Aperture priority allows the user to set the ISO and f/stop value with the camera automatically adjusting the shutter speed. Results from this paper indicate that f/8 and ISO 400 produce high-quality images with acceptable shutter speeds, given the camera and lens used in this study as well as the light set-up.
- The procedure and automated processing allow for virtual outcrops to be available for mapping remotely, within the same day.

4.9. References

Agisoft, 2019. Agisoft Metashape User Manual. 139.

Allmendinger, R.W., Siron, C.R., Scott, C.P., 2017. Structural data collection with mobile devices : Accuracy , redundancy , and best practices. Journal of Structural Geology 102, 98–112. https://doi.org/10.1016/j.jsg.2017.07.011

Assali, P., Grussenmeyer, P., Villemin, T., Pollet, N., Viguier, F., 2014. Surveying and modeling of rock discontinuities by terrestrial laser scanning and photogrammetry: Semi-automatic approaches for linear outcrop inspection. Journal of Structural Geology 66, 102–114. https://doi.org/10.1016/j.jsg.2014.05.014

Bemis, S.P., Micklethwaite, S., Turner, D., James, M.R., Akciz, S., T. Thiele, S., Bangash, H.A., 2014. Ground-based and UAV-Based photogrammetry: A multi-scale, high-resolution mapping tool for structural geology and paleoseismology. Journal of Structural Geology 69, 163–178. https://doi.org/10.1016/j.jsg.2014.10.007

Cawood, A.J., Bond, C.E., Howell, J.A., Butler, R.W.H., Totake, Y., 2017. LiDAR, UAV or compass-clinometer? Accuracy, coverage and the effects on structural models. Journal of Structural Geology 98, 67–82. https://doi.org/10.1016/j.jsg.2017.04.004

Dinechin, F. De, Istoan, M., Dinechin, F. De, Istoan, M., Dinechin, F. De, Istoan, M., 2015. Hardware implementations of fixed-point Atan2. 22nd IEEE Symposium on Computer Arthmetic.

Förstner, W., Wrobel, B.P., 2016. Photogrammetric Computer Vision - Statistics, Geometry, Orientation and Reconstruction, Geometry and Computing 11. Springer. https://doi.org/10.1007/978-3-319-11550-4

García-Luna, R., Senent, S., Jurado-Piña, R., Jimenez, R., 2019. Structure from Motion photogrammetry to characterize underground rock masses: Experiences from two real tunnels. Tunnelling and Underground Space Technology 83, 262–273. https://doi.org/10.1016/j.tust.2018.09.026

Guo, J., Liu, S., Zhang, P., Wu, L., Zhou, W., Yu, Y., 2017. Towards semi-automatic rock mass discontinuity orientation and set analysis from 3D point clouds. Computers and Geosciences 103, 164–172. https://doi.org/10.1016/j.cageo.2017.03.017

Iglhaut, J., Cabo, C., Puliti, S., Piermattei, L., O'Connor, J., Rosette, J., 2019. Structure from Motion Photogrammetry in Forestry: a Review. Current Forestry Reports 5, 155–168. https://doi.org/10.1007/s40725-019-00094-3

Jaboyedoff, M., Couture, R., Locat, P., 2009. Structural analysis of Turtle Mountain (Alberta) using digital elevation model: Toward a progressive failure. Geomorphology 103, 5–16. https://doi.org/10.1016/j.geomorph.2008.04.012

Jaboyedoff, M., Metzger, R., Oppikofer, T., Couture, R., Derron, M.H., Locat, J., Turmel, D., 2007. New insight techniques to analyze rock-slope relief using DEM and 3D-imaging cloud points: COLTOP-3D software. Proceedings of the 1st Canada-US Rock Mechanics Symposium - Rock Mechanics Meeting Society's Challenges and Demands 1, 61–68. https://doi.org/10.1201/noe0415444019-c8

James, M.R., Robson, S., 2012. Straightforward reconstruction of 3D surfaces and topography with a camera: Accuracy and geoscience application. Journal of Geophysical Research: Earth Surface 117, 1–17. https://doi.org/10.1029/2011JF002289

James, M.R., Robson, S., d'Oleire-Oltmanns, S., Niethammer, U., 2017. Optimising UAV topographic surveys processed with structure-from-motion: Ground control quality, quantity and bundle adjustment. Geomorphology 280, 51–66. https://doi.org/10.1016/j.geomorph.2016.11.021

Johnson, K., Nissen, E., Saripalli, S., Arrowsmith, J.R., McGarey, P., Scharer, K., Williams, P., Blisniuk, K., 2014. Rapid mapping of ultrafine fault zone topography with structure from motion. Geosphere 10, 969–986. https://doi.org/10.1130/GES01017.1

Kong, D., Wu, F., Saroglou, C., 2020. Automatic identification and characterization of discontinuities in rock masses from 3D point clouds. Engineering Geology 265, 105442. https://doi.org/10.1016/j.enggeo.2019.105442

Lorensen, W.E., Cline, H.E., 1987. (~ ~ Computer Graphics, Volume 21, Number 4, July 1987. 21, 163–169.

Marsh, N., 2014. Forensic Photography : A Practitioner's Guide. John Wiley & Sons, Incorporated, Hoboken, UNITED KINGDOM.

MMG, 2020. MMG LIMITED MINERAL RESOURCES AND ORE RESERVES STATEMENT AS AT 30 JUNE 2020.

Modrak, R., Anthes, B., 2010. Reframing Photography : Theory and Practice. Routledge, London, UNITED KINGDOM.

Novakova, L., Pavlis, T.L., 2017. Assessment of the precision of smart phones and tablets for measurement of planar orientations: A case study. Journal of Structural Geology 97, 93–103. https://doi.org/10.1016/j.jsg.2017.02.015

Pasumansky, A., 2018. Creating region/bounding box/LiDAR import [WWW Document]. URL https://www.agisoft.com/forum/index.php?topic=8679.0 (accessed 9.6.20).

Pasumasnky, A., 2019. Resize and move region [WWW Document]. URL https://www.agisoft.com/forum/index.php?topic=11409.0 (accessed 9.6.20).

Riquelme, A., Tomás, R., Cano, M., Pastor, J.L., Abellán, A., 2018. Automatic Mapping of Discontinuity Persistence on Rock Masses Using 3D Point Clouds. Rock Mechanics and Rock Engineering 51, 3005–3028. https://doi.org/10.1007/s00603-018-1519-9

Riquelme, A.J., Abellán, A., Tomás, R., Jaboyedoff, M., 2014. A new approach for semi-automatic rock mass joints recognition from 3D point clouds. Computers and Geosciences 68, 38–52. https://doi.org/10.1016/j.cageo.2014.03.014

Robertson, M., 2017. The practical use of underground 3D photogrammetry data at MMG Rosebery polymetallic mine , Tasmania , Australia. Tenth International Mining Geology Conference. 409–412.

Schofield, A., 2018. The Exposure Triangle in Summary -- Photo Tips by Austin [WWW Document], Gale General OneFile. URL https://link.gate.com/apps/doc/A564688035/ITOF? (accessed 11.28.19).

Slaker, B.A., Mohamed, K.M., 2017. A practical application of photogrammetry to performing rib characterization measurements in an underground coal mine using a DSLR camera. International Journal of Mining Science and Technology 27, 83–90. https://doi.org/10.1016/j.ijmst.2016.09.032

Smith, M.W., Carrivick, J.L., Quincey, D.J., 2015. Structure from motion photogrammetry in physical geography. Progress in Physical Geography 40, 247–275. https://doi.org/10.1177/0309133315615805

Thiele, S.T., Grose, L., Cui, T., Cruden, A.R., Micklethwaite, S., 2019. Extraction of high-resolution structural orientations from digital data: A Bayesian approach. Journal of Structural Geology 122, 106–115. https://doi.org/10.1016/j.jsg.2019.03.001

Umili, G., Ferrero, A., Einstein, H.H., 2013. A new method for automatic discontinuity traces sampling on rock mass 3D model. Computers and Geosciences 51, 182–192. https://doi.org/10.1016/j.cageo.2012.07.026

Vollgger, S.A., Cruden, A.R., 2016. Mapping folds and fractures in basement and cover rocks using UAV photogrammetry, Cape Liptrap and Cape Paterson, Victoria, Australia. Journal of Structural Geology 85, 168–187. https://doi.org/10.1016/j.jsg.2016.02.012

Whaanga, A., Vigor-Brown, W., Nowland, S., 2019. The implementation of photogrammetry and automated data analysis functions at the Waihi Underground Gold Mine. AusIMM Mining Geology 2019. 1–13.

Whitmeyer, S.J., Pyle, E.J., Pavlis, T.L., Swanger, W., Roberts, L., 2019. Modern approaches to field data collection and mapping: Digital methods, crowdsourcing, and the future of statistical analyses. Journal of Structural Geology 125, 29–40. https://doi.org/10.1016/j.jsg.2018.06.023

Xu, G., 1997. Microstructural evidence for an epigenetic origin of a Proterozoic zinc-lead-silver deposit, Dugald River, Mount Isa Inlier, Australia. Mineralium Deposita 32, 58–69. https://doi.org/10.1007/s001260050072

Chapter 5

Visualisation and communication of geological data confidence in 3D geological modelling

Creus, P.K., Sanislav, I.V. and Dirks, P.H.G.M.

Keywords: Python, Data Visualisation, Geological Data Confidence

5.1. Introduction

In the mining industry, geological data are used to generate 3D geological models of the subsurface with models used in varied downstream processes such as mine design, rock mass stability and resource modelling. Thus, a well-constrained and accurate 3D model is of paramount importance to ensure safe and optimised mining. Furthermore, due to a 3D model being an interpretation of the subsurface using available data, it will inherently have uncertainty associated with it (Bowden, 2004; Lindsay et al., 2012). According to Bowden (2004), uncertainty may arise due to incomplete, sparse, inconsistent or quality of data with Lindsay et al. (2012) suggesting that the reliability of the model is heavily dependent on the input data.

Traditional methods of collecting geological data are increasingly being augmented by digital methods. Digital methods include SfM-MVS/LiDAR (e.g., Vollgger and Cruden, 2016; Cawood et al., 2017; Creus et al., 2021), hyperspectral imaging of drillcore and faces (e.g., Kirsch et al., 2018; Harraden et al., 2019; Thiele et al., 2021) and downhole televiewer (e.g., Bendedicto et al., 2021). However, digital methods of capturing geological data can produce large datasets of raw digital data, which can be reduced by semi-automated (e.g., Riquelme et al., 2014; Vollgger and Cruden, 2016) and automated (e.g., Thiele et al., 2019; Kong et al., 2020) methods through post-processing, although they can produce uncertainty in geological interpretation (Bond et al., 2007b) as representative samples may not adequately describe the local geology (Lindsay et al., 2012). The visualisation of multiple datasets in 3D modelling software can be cumbersome and usually, only the 3D model is presented without showing the data on which the models were constructed (Bond, 2015) with 3D models in the industry often used by non-geology end users (Savage et al., 2013).

There are numerous publications discussing uncertainty in geological data and 3D models, which includes empirical or quantifiable approaches (e.g., Jones et al., 2004; Lindsay et al., 2012; Randle et al., 2018). The uncertainty to a large degree can be reduced by adding more data. In this study, we present a practical method for visualising where uncertainty may exist in a 3D model by generating a regular grid of points to which a confidence rating can be assigned. Using the grid-based system, the uncertainty in a model in comparison to the underlying data can be communicated to various stakeholders within an organisation. For instance, if new development needs to be planned, mine engineers can quickly view the data confidence that geologists have within the volume to be developed into. That way a risk analysis can be done on whether development should continue or more data needs to be collected through drilling or other appropriate methods.

In this study, we are not trying to determine or quantify whether data is correct or how accurate an interpretation of geology is towards true geology. Rather we are providing a method to practically communicate the uncertainty of geological data in mining to various stakeholders that do not have an intimate knowledge of the geological data, or the 3D model produced from the data. The method uses a data distribution approach with 3 categories defining low, moderate and high confidence in the data and its distribution.

5.2. Uncertainty

Uncertainty in a 3D model or data appears to be a topic that is discussed disproportionately in the oil and gas industry and is seldom covered in the mining industry. For instance, McManus et al. (2021) analysed 142 Joint Ore Reserves Committee (JORC) reports released in 2019 and found that no reports used quantitative assessments of uncertainty in geological models and stated that it is not understood why quantitative methods of uncertainty assessment are not used in public reports for mining projects. Many 3D modelling software packages with an oil and gas focus include tools for quantifying uncertainty, something that is generally lacking in mining-focused software packages. This is despite the requirement of codes like JORC providing guidelines in assessing and communicating the confidence and uncertainty in geological models and the underlying geological data and understanding (McManus et al., 2021).

Uncertainty analysis is well-researched covering a wide range of topics and the references provided within this chapter are by no means an exhaustive list but serve to provide an overview of the uncertainty of geological data relevant to 3D structural modelling in the framework of this study. Uncertainty is not just the absence of knowledge and can prevail where a lot of information is available (van Asselt and Rotmans, 2002; Walker et al., 2003) and can be grouped into aleatoric and epistemic uncertainty (Walker et al., 2003; Bowden, 2004; Bond, 2015). Aleatoric uncertainty refers to known uncertainty and is hard to reduce, e.g. such as uncertainty in analytical equipment due to precision error. Mathematical methods to quantify aleatoric uncertainty are well established (e.g., Bowden, 2004) and in this study, we are more concerned with epistemic uncertainty. Epistemic uncertainty refers to uncertainty due to imperfect knowledge and can be reduced if more, or improved information is gathered. For instance, a fault modelled from sparse drilling data with no direct observations from mapping will have uncertainty associated with it, which can be reduced by intercepting the fault with more drilling, or directly observing the fault during face mapping. The Dugald River deposit is a good example of how the lack of knowledge resulted in

operational risk with the mine entering care and maintenance to increase the knowledge and thus reduce the uncertainty with the Dugald River Shear Zone and ore body (Harris, 2015).

Inconsistent data within an acceptable distance and from different sources is worth mentioning as it is a common occurrence in underground mining, particularly between drilling data and mapping (Fig. 5.1). Inconsistency may be due to spatial discrepancies, the measured feature characteristic or interpretation error. Spatial discrepancies are difficult to reduce as they will mostly be due to instrument precision and processing issues and typically, given the precision required in mining, insignificant. Measured feature characteristic in this context refers to characteristics such as the scale of a fault/shear being measured, *viz.* a mine-scale fault versus a small-scale fracture in the damage zone of the mine-scale fault. While both characteristics are required in structural analysis, the ability to filter out small-scale structures is invaluable in 3D modelling.

One way to look at uncertainty is in how many possible alternative interpretations can be made from the same dataset. Lindsay et al. (2012) used a range of 10° for strike and dip of geological data measurements to generate several 3D models for a volume of interest and evaluated the models onto a 3D grid to quantify and visualise uncertainty in regions within the volume of interest. Multiple interpretations from the same dataset can also be due to prior training and experience of a Geoscientist (e.g., Bond et al., 2007a). Ultimately, uncertainty translates into risk and the objective is to reduce risk as much as possible and it should be noted that uncertainty is created at each step of the mining process which accumulates and propagates (Jones et al., 2004). Lastly, epistemic uncertainty can be divided into uncertainty related to the data itself and interpretation from the data (also Clarke, 2004). The rest of this section briefly outlines uncertainty related to the interpretation and the data types relevant to this study.

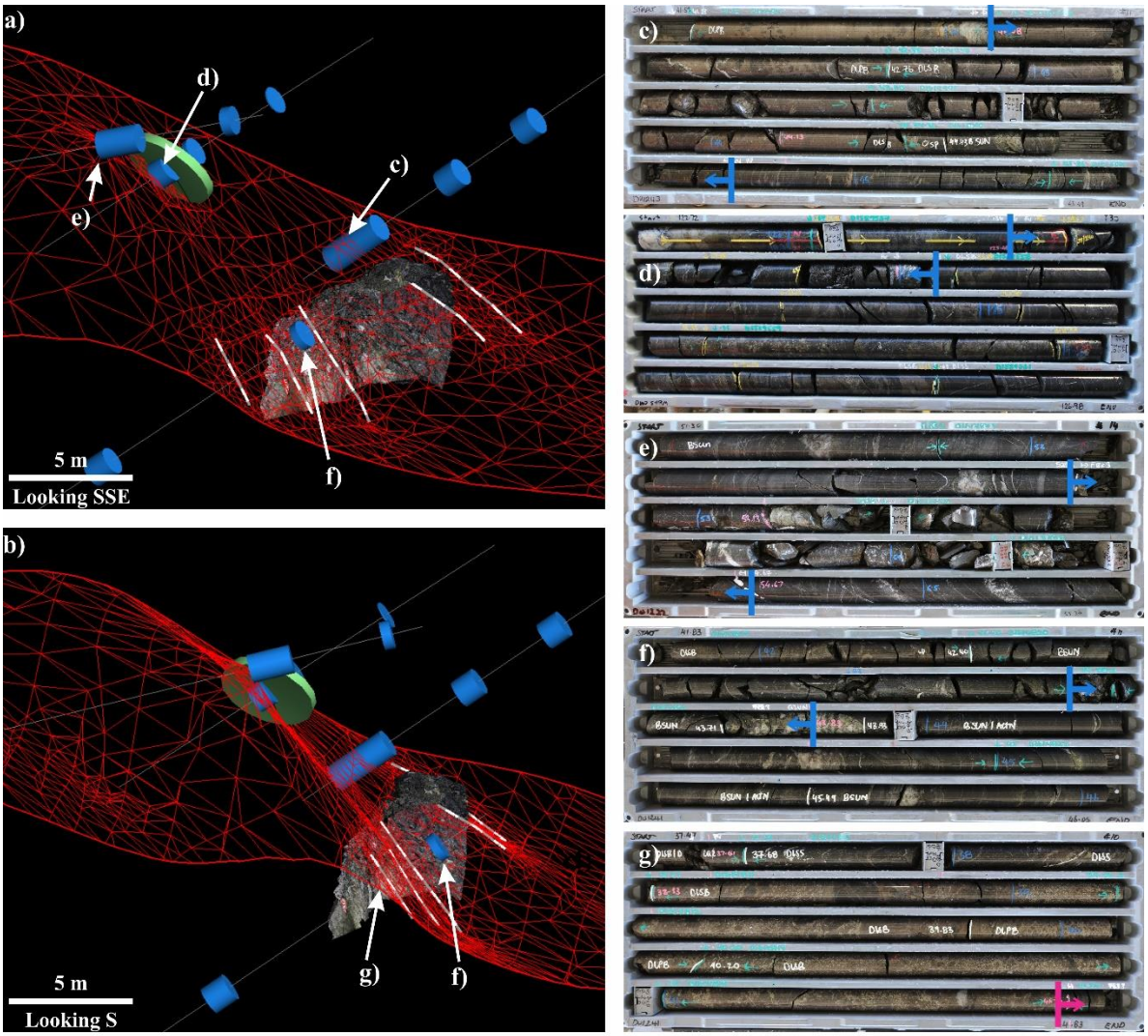
a)
d)
e)
c)
f)
5 m
Looking SSE
b)
g)
f)
5 m
Looking S
c)
d)
e)
f)
g)

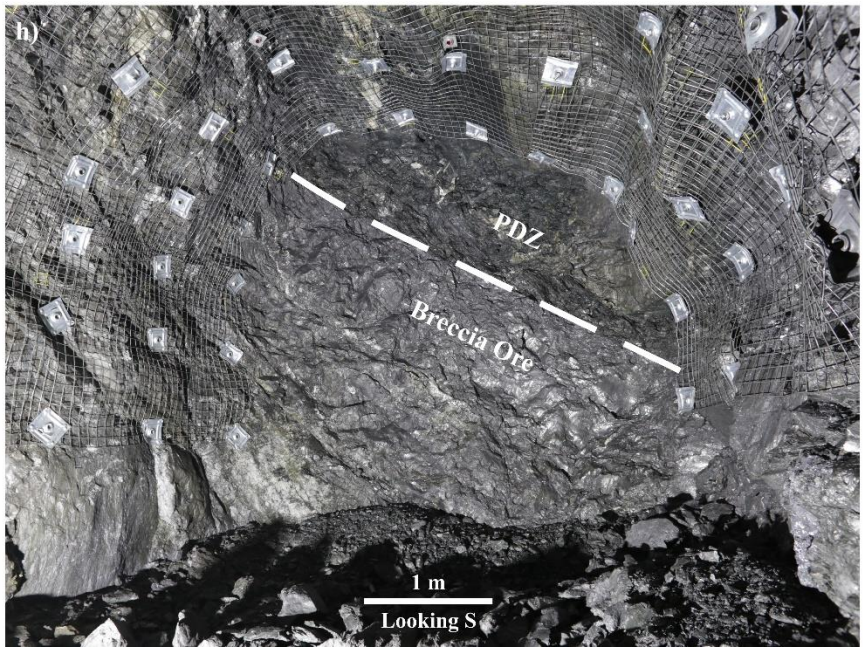
h)
PDZ
Breccia Ore
1 m
Looking S

Fig. 5.1: a) Example of inconsistency between mapping and drilling data. a and b) are an SSE and S view, respectively of a modelled shear with drilling data and digitised polylines shown. There are several instances of inconsistent data within this small area. c) is a logged interval that should be several discrete shears but was logged as one interval. Note the blue arrows in the core photos indicate the start and end of a logged interval with downhole from left to right. d) has an inconsistent orientation to the modelled wireframe, however, the evaluation of the structural measurement using drillcore photos confirms that it is a small fracture and should be excluded from wireframe construction. f) is converse to c) as the interval was too small and should have started at the pink interval in the previous core tray (i.e., g). h) the structure (PDZ) and the breccia ore have a sharp contact and are easily recognisable in the virtual outcrops and the contact was digitised in the location of g) as indicated by the white polyline on the wireframe.

5.2.1. Interpretation Uncertainty

Geology is a subjective science with an interpretation of data based on prior experience and knowledge (Jones et al., 2004) with the type of experience more important than the length of experience (Bond et al., 2007). Witter et al. (2019) suggest that uncertainty associated with geological interpretation is greater than uncertainty due to data acquisition and processing. Interpretation includes the recording of observations of drillcore, outcrop, geophysics surveys and interpreting multi-disciplinary datasets to produce a cross-section, 3D model and reports or publications.

Uncertainty in interpretation is important to consider in 3D modelling during active mining. While implicit modelling engines have greatly simplified the modelling process and allow for multiple hypotheses to be tested, usually a single interpretation (i.e., 3D model) is required for downstream processes. Generally, a single geologist has ownership of modelling a volume of interest as having multiple geologists working on the same volume of interest may result in conflicting interpretations (also Bond et al., 2007b). Thus, a single person has the most intimate knowledge of the underlying data used in generating the 3D model.

Spatially and geometrically accurate cross-sections developed by a geologist on mines are becoming rare due to the ease of using 3D modelling software powered by implicit modelling engines. Creating an accurate cross-section can be time-consuming with modern mining datasets that in places can be dense and given that 3D modelling software can be used to create cross-sections, it is simpler to build a 3D model and then create a 2D section to use in a report. The topic of this paragraph is not to add to the debate on the value of cross-sections but rather to state that in legacy datasets, cross-sections are common as at the time they were the best method for presenting conceptual models of the subsurface. Inherently, uncertainty is

introduced into cross-sections while they are constructed by a geologist and includes both epistemic and aleatoric uncertainty. Notably, aleatoric uncertainty includes spatial and data measurement errors and epistemic uncertainty can be derived from geological interpretation of regional geology and history, and lack of knowledge or experience (Clarke, 2004).

Similarly, as in the previous paragraph on cross-sections, a geological map also includes a component of interpretation by a geologist and is influenced by previous experience and knowledge (Jones et al., 2004). The most obvious uncertainty in a geological map is the extrapolation under cover between measured points for geological contacts and that uncertainty will increase with increasing geological complexity. Furthermore, geological maps are 2D representations of the surface geology and extrapolation of uncertainty to depth during 3D modelling has an increasing range of geometrical possibilities (Fig. 5.3; Lindsay et al., 2012).

5.2.2. Drilling Data Uncertainty

Uncertainty in drilling data can be divided into construction and logging (Pakyuz-Charrier et al., 2018). According to Pakyuz-Charrier et al (2018), construction uncertainty is affected by several factors including equipment and technical expertise. In the mining industry, uncertainty related to drillcore orientation is the most common construction uncertainty followed by the type of drilling (*viz.* diamond core, percussion and air core). While modern downhole survey tools such as north-seeking gyros are accurate, drilling data used in 3D modelling may span several decades and include older surveying tools such as magnetic surveying and often older surveys are labelled as unknown in the database as hard copies of the logs are no longer available.

Geological logging of drillcore includes quantitative and qualitative data collection often with both types of data collected simultaneously. For instance, a lithological contact within a drillhole may have comments and a structural measurement associated with it, i.e., measured data (depth and structural measurement) with descriptive/interpreted (lithology A and lithology B with a description of the lithologies). In mining, the uncertainty created by measurement precision of depth of structural reading and the orientation of a measured feature can be considered insignificant given the scale of a stope and open-pit cut - a few millimetres or degrees is acceptable. A greater cause for concern is the uncertainty created

due to human error when logging (e.g., Fig. 5.1c and g), such as assigning incorrect lithology, alteration and structural features or uncertainty created by the subjective nature of drillcore logging as geologists apply personal biases to logging (Lark et al., 2014). It is self-evident that with percussion and air core drilling structural measurements are impossible as is determining the exact downhole depth of a geological contact.

Generally, incorrect logging of lithology can be identified when viewing logging data in 3D. Unless there is a structural reason for an abrupt difference in lithology between adjacent, close-spacing drillholes, the incorrect assignment of lithology can be seen when viewing data in 3D (Fig. 5.2). However, where drilling data are sparse it will become harder to ascertain, if at all, whether the lithology is correctly logged. While incorrect logging of lithology can generally be improved by training and supervision, typos are a common error that can affect anyone during logging, particularly with the direct typing of logs into a server-based database (e.g., Fig. 5.1c and g). Depending on the feature logged, the typos can be easily validated using drillcore photos when using the data (e.g., a fault interval that is 30 m wide when the median for the deposit is 2 m), however, hidden uncertainty can be created with features that are harder to validate with drillcore photos (e.g., foliation measurements) or if photos are not available (e.g., if the photo for Fig. 5.1d was not available). A worthwhile habit to incorporate when logging is to include logging sections with up-to-date wireframes included in the sections (Fig. 5.2).

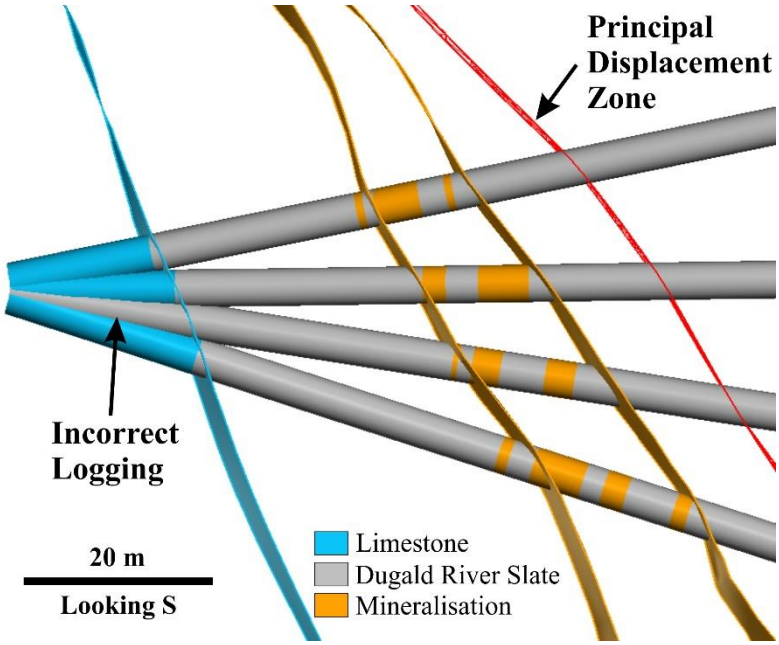

Fig. 5.2: Example of logging error. A limestone unit was erroneously logged as slate. Due to the interval being near the collar and that several other drillholes can be used as a reference, the log can confidently be changed to limestone in the drillhole database. Using current interpretations of wireframes with drilling sections is good practice to ensure accurate and consistent logging.

5.2.3. Virtual Outcrop Mapping Uncertainty

The use of photogrammetry in mining, particularly underground mining represents a paradigm shift in how mapping data are collected. Photogrammetry provides a method to view and store outcrops in virtual format (e.g., Cawood et al., 2017; García-Luna et al., 2019; Whaanga et al., 2019; Creus et al., 2021). The process is simple to set up and processing can be automated (e.g., Creus et al., 2021) and recent advancements in semi-automated (Vollgger and Cruden, 2016; Riquilme et al., 2016) and automated (Kong et al., 2020). Thus, full automation from data capture, processing and discontinuity extraction of virtual outcrops will most likely become standard mining practice.

The value in using virtual outcrops is that as they are georeferenced, polylines and structural discs representing contacts and structural features can be digitised in 3D modelling software using current interpretations as a reference, thereby allowing new mapping data to be characterised using for instance the approved identifier for a fault or ore lens. Furthermore, the storing of virtual outcrops allows for quality assurance by senior geologists and managers in the office at any time as opposed to at the outcrop that may be exposed and blasted within a 24hr cycle in underground mining. Furthermore, virtual outcrops allow for the mapping of inaccessible areas (e.g., pit walls, unsupported ground and cliffs).

In underground mining, digitising features on virtual outcrops can result in a significant increase in 3D data. The accuracy of virtual outcrops to real outcrops has been investigated by numerous publications (e.g., Assali et al., 2014; Cawood et al., 2017) and for the precision required in the mining industry, the accuracy of using virtual outcrops versus real outcrops for mapping can be regarded as acceptable. Uncertainty created during the use of virtual outcrops will mainly occur due to interpretation errors such as incorrect lithology assignment or structural features.

5.2.4. Traditional Mapping Uncertainty

In this study, traditional mapping refers to mapping using a compass-clinometer or a mapping app on a smartphone. The applicability, accuracy and precision of smartphones versus a compass-clinometer has been the topic of research by numerous authors (e.g., Allmendinger et al., 2017; Cawood et al., 2017)

There are several ways that uncertainty can arise from mapping. Often with legacy data, metadata is no longer available or never existed, specifically whether measurements were taken in magnetic, true or grid north. While with many mines, the differences may be double digits and can be deduced by plotting the data on a stereonet and comparing it to known data, this is not the case at Dugald River, which has a ~N-S trending fabric and ore body, which resulted in a mine grid north modified to 9.366° west of north. At the time of mapping for this study, data were collected in true north, which was 5.789° west of magnetic north. Thus, the spread of measuring dip direction is 15.155°, which given a Riedel Shear network can mean characterising a data point to an incorrect Riedel shear fracture (see Chapter 3). We highly recommend that mapping tables regardless of the method used to capture data include designations of what north system the measurements in a column are in (e.g., Table 5.1) and if they were estimated, which is common in inaccessible localities. It should be noted that mapping conducted during active mining will most likely be in grid north and legacy data collected before mining may not necessarily be within a mine grid as mine grids are typically established at an advanced stage of mine planning.

The lack of comments in mapping tables is a common source of creating uncertainty in interpretation and confidence in using the data points. Comments provide a user of the data with descriptive information about a feature measured, which may assist in determining the applicability of using the data point in modelling or analysis.

Outcrop and face mapping has several significant challenges and is discussed in great detail by Jones et al. (2004) when constructing geological maps. In summary, they mention that interpretations by geologists are rarely translated into the final product (also Bond, 2015), which includes uncertainty in the data and the geological maps and if any uncertainty is mentioned it is qualitative. They suggest ways to quantify uncertainty during geological mapping and it is highly recommended that the suggestions are implemented in an organisation-level work quality requirement.

When considering mapping data to be used in 3D modelling, we suggest that input data are subdivided into characterised and orientation-only datasets. Characterised mapping data refers to descriptive data which includes coordinates, orientation, structure type, kinematic information, comments, material

properties, classification of what was recorded and any additional descriptive data relevant to a mine site or organisation. Accordingly, the characterised dataset represents high confidence data that can be used in interpretations and to determine modelling parameters. Orientated mapping data generally only includes coordinates, orientation, and lithology or structure type and represents data that may potentially create uncertainty in a model or analysis, particularly if no photographic evidence is available.

5.2.5. Data Downsampling

In the context of this study, data downsampling refers to extracting representative data points from a dataset appropriate to the scale of the 3D model (e.g., Lindsay et al., 2012). The advantage and disadvantage of using digital methods to capture geological data are that numerous data points can be captured rapidly. If we consider mapping using a compass-clinometer versus a smartphone app, recording a measurement with a smartphone simply requires typing in relevant descriptors for the feature to be measured and placing the device flat on a surface and clicking a button on the screen. Using a compass-clinometer requires ensuring the compass is level and recording two separate angles (depending on the make of the compass) and writing the descriptors for the measurement into a notebook. Thus, in the time it takes to record a measurement using a compass-clinometer, several measurements can be recorded using a smartphone app. The advantage is that mapping with a smartphone can cover a larger area and multiple measurements can be recorded for a structure, thereby constraining the geometrical variance of the structure (e.g., Jones et al., 2004), allowing for data redundancy (e.g., Allmendinger et al., 2017) and creating a better representation of the local geology (e.g., Lindsay et al., 2012). The disadvantage is that in most cases to create a 3D model, the data will need to be downsampled to a few representative points that may fail to adequately represent the geology (e.g., Lindsay et al., 2012). While the previous statement may appear contradictory, if one considers a situation where an outlier measurement is picked from a set of points representing a fault intercepted by an underground tunnel, the geometrical error of the modelled fault will propagate into the rock mass (Fig. 5.3).

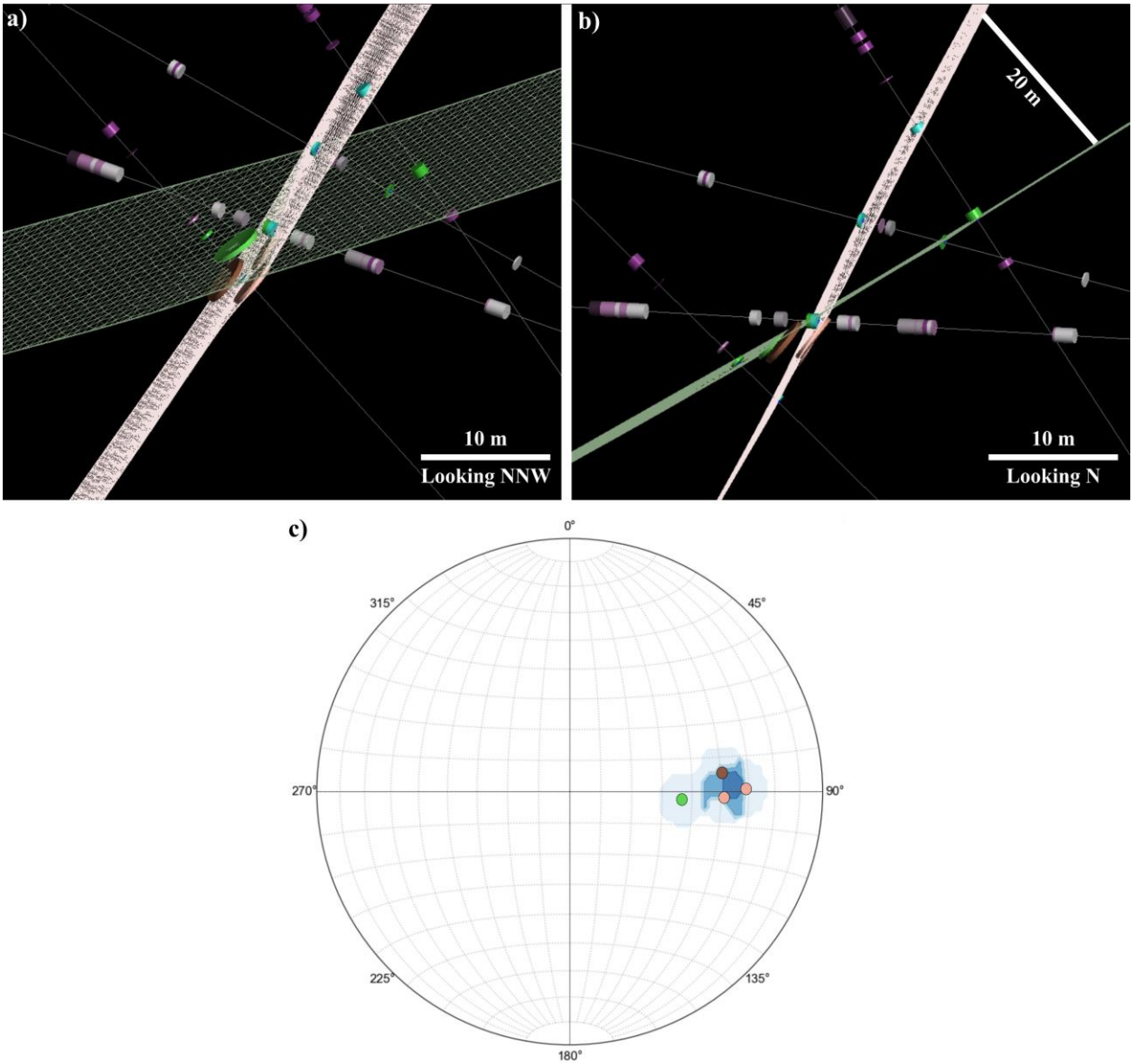

Fig. 5.3: Example comparing the trajectory of two modelled wireframes into the rock mass from mapping data. The outlier data (green point on the steroenet (c)) is on the opposite side of a drive to the brown point and both are measurements of the hangingwall plane of a major structure. The pink points are measurements from the footwall of the same major structure as the green and brown. Both wireframes incorporate fault intercepts in drilling without changing the trajectory too much but the distance between the two wireframes increases significantly within the rock mass. In a complex, anastomosing shear zone this may lead to incorrect assignment of drilling data to discrete structures.

5.3. Dugald River Dataset

Before the commencement of underground development at the Dugald River mine in 2012, data were collected from orientated drillcore and surface mapping. With the commencement of underground development, data were collected from drill fans and traditional mapping using underground development, however, soon after reaching the ore body, it was realised that the structural complexity of the ore body was inadequately understood and a technical risk mitigation study was initiated (Harris, 2015). One of the findings of the study was to reduce the drill spacing from 25 X 25 m to 15 m along strike and 10 m down-dip where the geology is structurally complex. Thus, there is considerable drilling data for the 2 km strike length deposit (Fig. 5.4).

Face mapping was the primary method of underground mapping until 2017 when digital mapping using photogrammetry phased out face mapping. The primary reason for this is due to the structural complexity of the deposit, which makes mapping time-consuming, thereby making it difficult to keep up with development while maintaining data integrity. Furthermore, given that that fabric is NNW-trending and that ore lenses occur adjacent to the footwall of shears in the Dugald River Shear Zone, development drives are designed with an NNW-trend and usually with a shear and partial ore lens within the drive (e.g., Fig. 2.18 in Chapter 2; Fig. 3.10 in Chapter 3). Notably, development faces cannot be mapped due to safety concerns as they occur under unsupported ground.

Fig. 5.4: Drilling completed at Dugald River up to December 2019. a and b) Drilling completed before the feasibility study conducted in 2009 was from the surface only. b) Principal displacement zone (PDZ) represented by the grey plane. c) There was a significant increase in completed drilling from underground development. d) Histogram of completed drilling at Dugald River. A lower cut-off for drilling is set in 1988. In 2013 the mine was placed into care and maintenance while a detailed structural study was conducted.

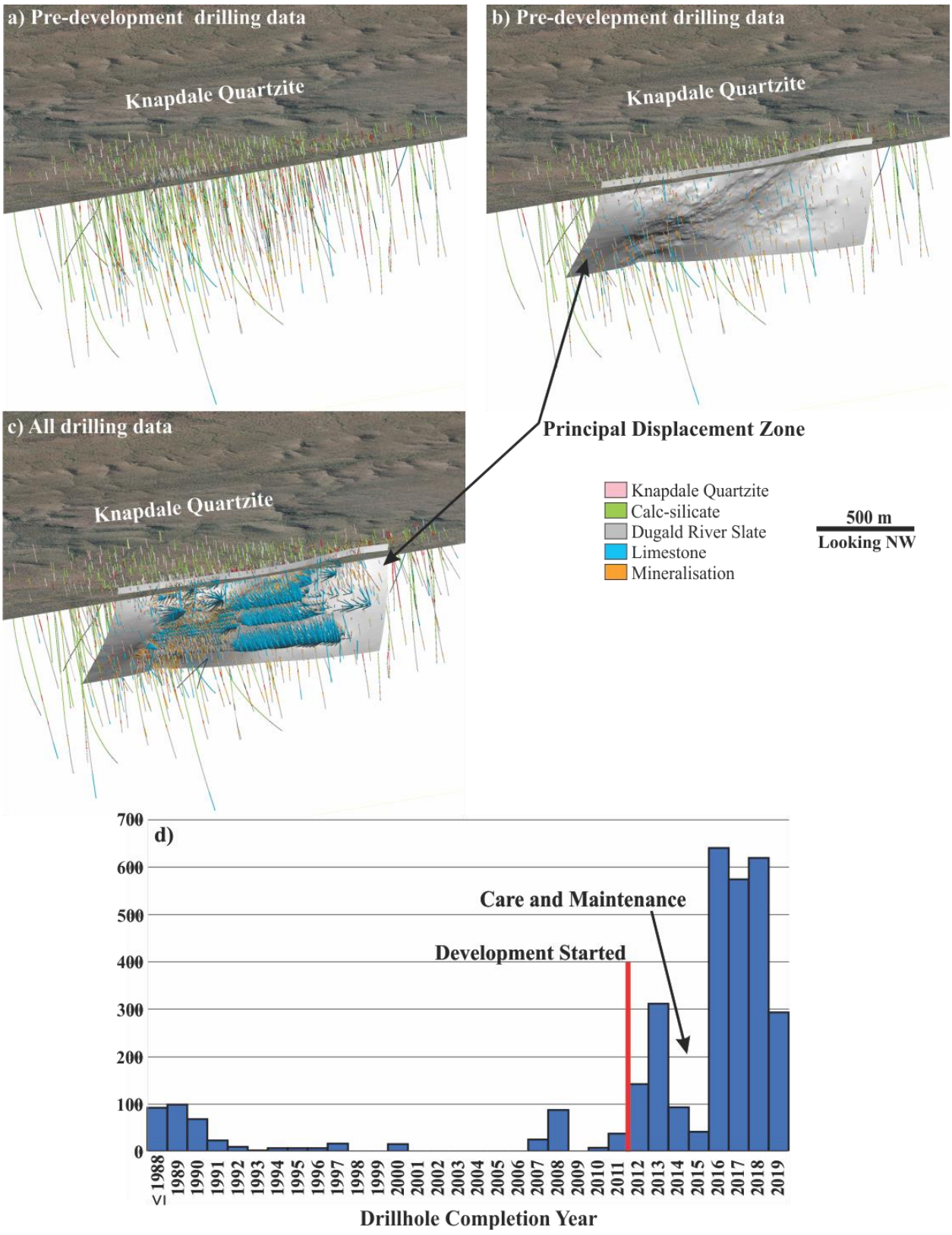
a) Pre-development drilling data
Knapdale Quartzite
b) Pre-develepment drilling data
Knapdale Quartzite
c) All drilling data
Knapdale Quartzite
Principal Displacement Zone
Knapdale Quartzite
Calc-silicate
Dugald River Slate
Limestone
Mineralisation
500 m
Looking NW
d)
Care and Maintenance
Development Started
700
600
500
400
300
200
100
0
≤ 1988
1989
1990
1991
1992
1993
1994
1995
1996
1997
1998
1999
2000
2001
2002
2003
2004
2005
2006
2007
2008
2009
2010
2011
2012
2013
2014
2015
2016
2017
2018
2019
Drillhole Completion Year

5.3.1. Drilling Data

The drilling data at Dugald River comprises surface-based drilling and the bulk of the drilling was conducted from underground development (Fig. 5.4c). The underground drilling uses a drill fan methodology with a standard design of primary drilling at 40 m along strike and 30 m down-dip for the initial assessment of new targets. Infill drilling follows and is done at either 20 m along strike and 15 m down-dip or on a reduced spacing of 15 m along strike and 10 m down-dip where initial assessments indicate increased structural complexity.

Primary drilling has been orientated allowing for structural measurements to be recorded. However, drillcore runs are often dominated by broken pieces if drilled through the shear zone due to the graphitic nature of the anastomosing shear zone and that discrete shears may be comprised of fault cores of fault breccia or cataclasites, including incohesive varieties (Chapter 2, 3). Furthermore, structural measurements, if possible, are only recorded within 20 m of the ore body and intercepts of shears can range from sub-centimetre to several metres wide which need to be reflected in the 3D model. Thus, to make the primary and infill drilling compatible, Spelbrink and George (2017) developed a method to display fault/shear/fracture intervals (herein referred to as structures) in a meaningful manner by adding an intensity of damage rating to each interval, which effectively creates categorical data that can be filtered and displayed in 3D modelling software. Each structure interval is given an intensity rating of 1 (weak) to 5 (strong) and only structures with an intensity rating of 3 or higher are generally included in structural modelling. Even with the > 3 intensity rating cut-off and by compositing intervals < 1 m, the number of structure intervals is 23 948. Thus, it can be time-consuming to model the structures, especially in areas that do not have direct observations such as outside of development drives and where structural measurements from the orientated core could not be recorded. It should be noted that the recording of structure planes is rare due to the lack of orientated core and the sparse spacing of primary drilling.

Data representing planar fabric, which includes S_0 and S_2, are sporadic given the 20 m exclusion rule for taking measurements of orientated drillcore as well as the drill spacing and the difficulty in orientating drillcore pieces within the shear zone. This is compounded by the fact that typically within a core tray a single data point is recorded unless folding is noticeable. Data points outside the 20 m exclusion zone of the ore body are only available for older drillholes when production targets were not prioritised. Thus, in areas where there are no direct observations from underground development, a good understanding of the geology is vital in ensuring high confidence in the structural model.

Lastly, a drillhole is a line through a rock mass and limited information about the 3D geometry of a planar feature such as a shear can be extracted. Particularly when considering a Riedel shear network with anastomosing shear zones in which it is not unreasonable to assume that a structure that is measured in a drillhole may have a bifurcation within the rock mass, or the expected orientation of the structure deviates.

5.3.2. Underground Mapping

Before 2017, underground mapping at the mine was undertaken using grade line mapping. With grade line mapping structural and lithological information are recorded at the grade line and information transferred to level plans and data transferred to spreadsheets that are loaded in modelling software as categorised data (i.e., fault, shear, fracture, S_0, S_2 etc.). However, at the mine, the scale of the structures was not transferred and therefore incompatible with the intensity rating methodology of the drilling data. In addition, due to the structural complexity of the deposit, the grade line method was time-consuming and could not keep up with the development. Thus, SfM-MVS photogrammetry was adopted at the mine.

Detailed underground mapping that was conducted by consultants and researchers is sporadic as this type of mapping is usually not part of the production cycle. Generally, mapping by specialists tends to, in addition to recording spatial and orientation information, including comments, kinematics, polarity (younging, facing, vergence), the scale of the structure as well as small-scale features such as crenulations and striations. The addition of scale is important as it can retroactively be made compatible with the structure intensity rating for the drilling, or at the very least a keyword search can be run on the comments.

While underground mapping represents 3D mapping, it can be difficult to ascertain the 3D geometry of a geological feature that is mapped as the development walls are in effect a 2D plane and with the ventilation system, the roof of the tunnels may be visibly blocked. Thus, apparent geometries may need to be considered when mapping underground.

5.4. Methods

In this section, we provide several methods to aid in communicating data distribution and confidence that a modeller has in the surface/volumes produced. The first method is purely subjective and compiled by the geologist while they model and in this study has specific reference to faults and shears.

5.4.1. Discrete Structure Table

Geological structures such as faults and shears occur in most 3D models (e.g., Basson et al., 2016, 2017; Creus et al., 2018, 2019). Not only are the structures important for mine design purposes, but they are often used within the model to create litho-structural domains in which specific modelling parameters are applied (e.g., Basson et al., 2016), or used to model representations of the 3D fabric (e.g., form surfaces; Creus et al., 2019). Faults and shears are represented in 3D as surfaces (discrete planes) or enclosed volumes (damage zones) and depending on the capabilities of the software may represent finite objects (Fig. 5.5a) or be required to terminate against another object, including the model boundary (Fig. 5.5b). A finite surface for instance is restricted within known points with minor extrapolation and the confidence of the structure related to the data confidence. With a non-finite surface, significant extrapolation by the software away from known points may be required with confidence in the accuracy of the surface decreasing away from the known points.

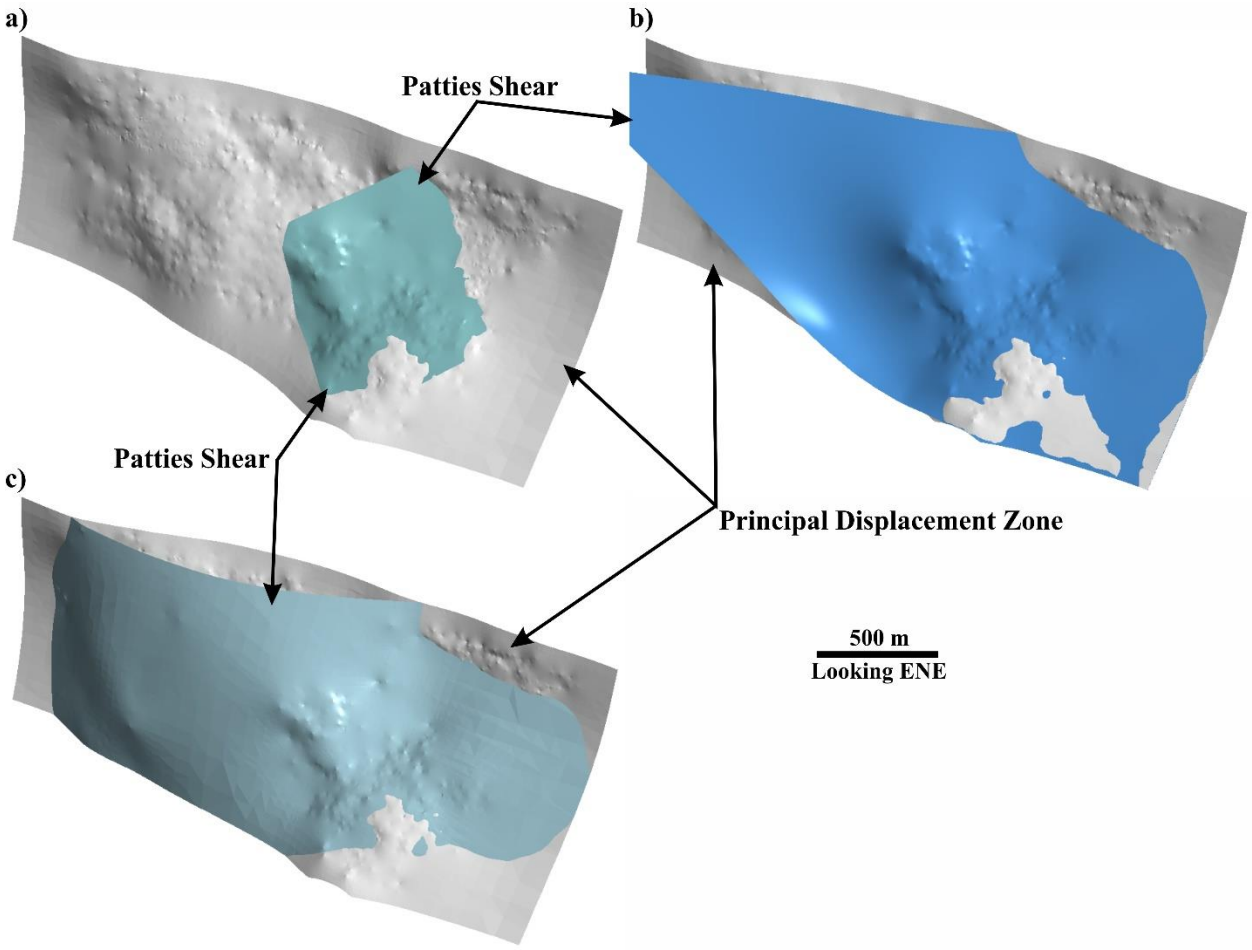

Fig. 5.5: a) Finite surface of the Patties Shear versus a non-finite surface (b) in which the modelling software required significant extrapolation from known data points. c) The interpretation of Patties Shear with all data considered and based on observations and interpretation that the Dugald River Shear Zone developed as a Riedel shear zone. The geometry of Patties Shear is significantly different in the north of the deposit and highlights how extrapolation by the software when generating non-finite surfaces can have an impact on the design of drill plans and underground infrastructure.

From experience, it can be a source of frustration in inheriting a 3D model with numerous structures. In particular, what data has been used to construct the structure and what is the confidence in the structure and the underlying data. We propose using a "*discrete structure table*" (Table 1) that provides a single table of information for each discrete structure and can also be used for version control. As a template, the table includes the structure ID/name, data point and type, location/drilling interval of the data point, any comments, and confidence in the data point. The table is used to provide information rather than an interpretation.

Table 1 is an example of a discrete structure table used in constructing the 3D model for this thesis. By including coordinates for each data point, the table can be loaded into 3D modelling software and displayed with the structure to visualise areas of lower confidence (Fig. 5.6, 5.7). For instance, the Dugald River Shear Zone is an evolved Reidel shear zone with a principal displacement zone that developed at the interface between a continuous, thick sulphide horizon that occurs adjacent to the shear zone (see Chapter 2, 3). Given that the development occurs along the footwall of the shear zone that spans at least 2 km along strike, and that most drilling is through the ore body and shear zone, the result is that the number of data points used to constrain the principal displacement zone is 189 mapping points, 2278 digitised polylines and 1787 drill intercepts. Each data point has been given a user-defined confidence rating which for most of the principal displacement zone is high (Fig. 5.6a), except in the area where there is a flexure in the shear zone where numerous anastomosing shears creates uncertainty in assigning data points to discrete structures (Fig. 5.6b and c, 5.7a and b).

Table 5.1: Abridged discrete structure table showing several data entries for the principal displacement zone (PDZ). The comments are shortened so that the table is print-friendly.

Structure ID	General Structure Description	Source	Structure Type	Intensity	Data ID	Depth	From	To	Dip	Dip Direction (MG)	East	North	RL	Data Comment	Confidence
PDZ	Mine scale…	Drilling	Fracture	3	DU0209		127.17	130.1			10707.7	14724.7	10050.2	Westward shift…	Medium
		Drilling	Fracture	5	DU0693		149.06	152.1			10685.7	14714.4	10017.3	Core loss	High
		Drilling	Fault	4	DR476	109.14	106.88	109.15	72.88	255.89	10757.4	14651.1	10108.5	FW plane…	High
		Drilling	Breccia	4	DU0500		126.76	127.15			10701.9	14706.0	10035.4		High
		Drilling	Fault	4	DU0683		137.31	137.6			10713.4	14705.5	10048.6	Several splays…	High
		Drilling	Fault	5	DU0496		118.78	118.85			10713.3	14663.4	10038.6	Large zone…	Medium
		Creus - PhD	Fault	4	N150_OD486_S				62	271	10718.4	14748.9	10077.9	Major structure…	High
		Creus - PhD	Shear	5	N150_OD486_S				71	252	10690.5	14812.0	10076.8	Major shear…	High
		Photogrammetry	Fault	5	191007_S340_XC398_W_1						10769.8	13936.3	9964.9	HW_FW…	High
		Photogrammetry	Fault	5	191024_S340_OD398_N2_1						10689.6	14002.7	9887.7	HW_FW…	High
		Photogrammetry	Fault	5	191024_S340_OD398_N2_1						10692.0	13998.9	9888.1	HW_FW…	High
		Photogrammetry	Fault	5	191024_S340_OD398_N2_1						10686.0	14009.6	9887.8	HW_FW…	Medium
		Geology 2013 - STH_Lode	Fault		S125_OD413_S1				76	256	10830.7	13839.8	10107.2		High
		Geology 2015 - STH_HWSL	Fault		S125_OD413_S1				74	291	10830.8	10830.8	10107.8	Low conf…	Medium

Fig. 5.6: a) Confidence rating for the principal displacement zone (PDZ). The section line for Fig. 5.7c is shown as a dashed line. b and c) Large area of the PDZ in the South Mine that has several input data points that are labelled as moderate or low confidence. A major reason is that this part of the shear zone has numerous shears and was initially a termination point of a R- and P-shear that as shear zone development progressed developed into a Y-shear and then a principal displacement zone and through abrasion, numerous meso-scale shears developed. The effect of which is indicated by underperforming stopes (Fig. 5.7; also Chapter 3). S390, S440, and S490 are levels in the South Mine and the section line for Fig. 5.7a and b are shown as a dashed line.

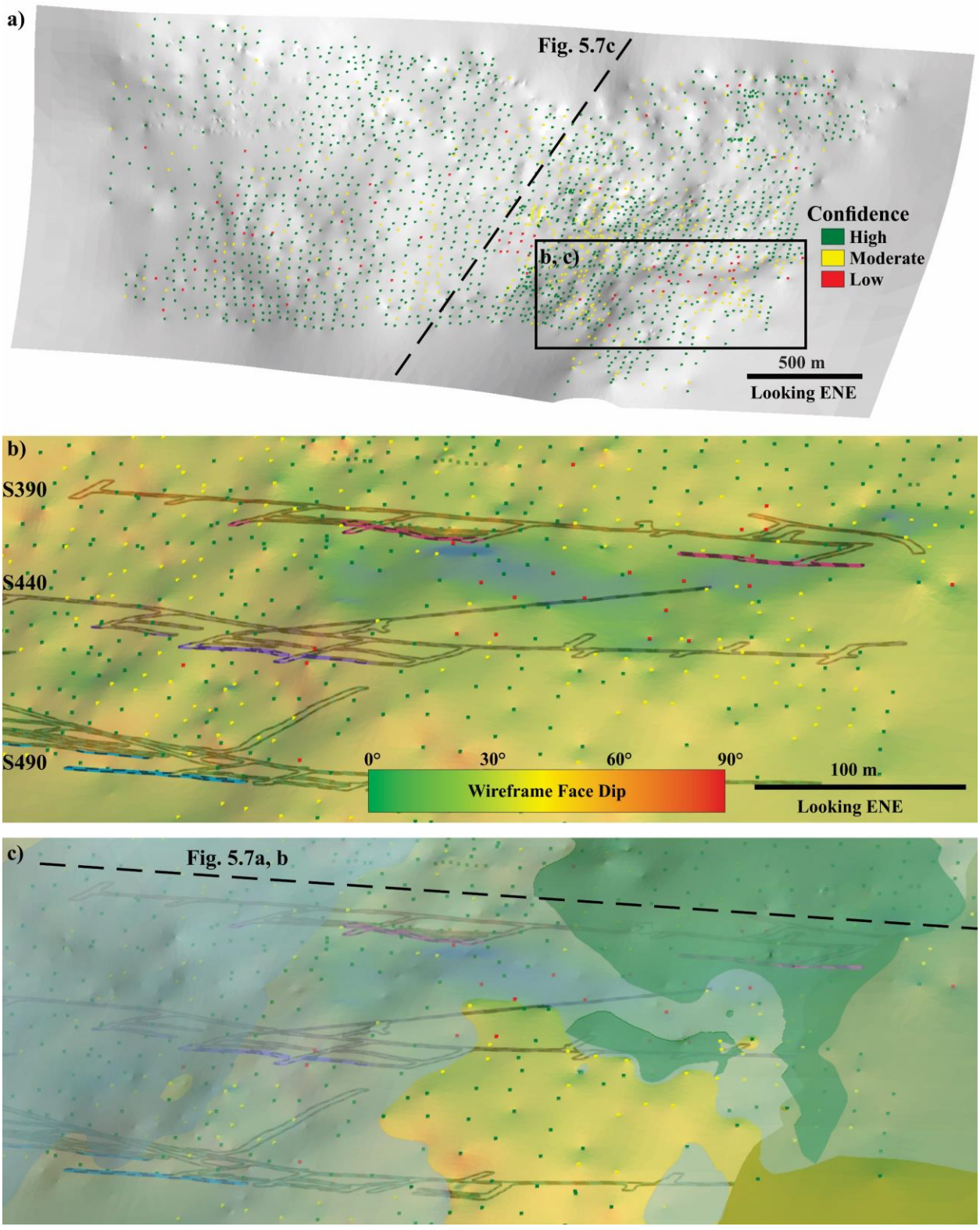
a)
Fig. 5.7c
Confidence
High
Moderate
Low
b, c)
500 m
Looking ENE
b)
S390
S440
S490
0°
30°
60°
90°
Wireframe Face Dip
100 m
Looking ENE
c)
Fig. 5.7a, b

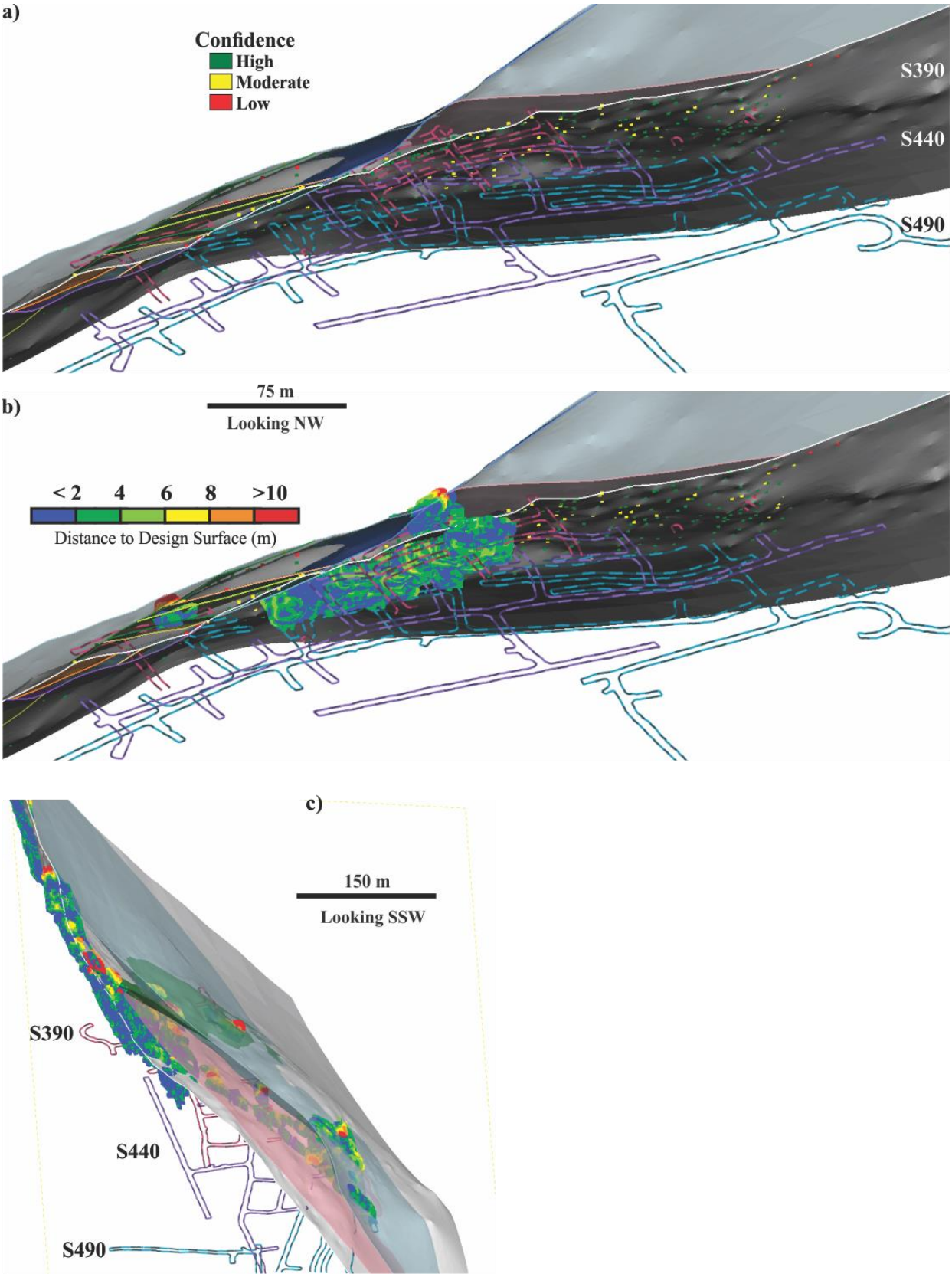
a)
Confidence
High
Moderate
Low
S390
S440
S490
b)
75 m
Looking NW
< 2
4
6
8
>10
Distance to Design Surface (m)
c)
150 m
Looking SSW
S390
S440
S490

Fig. 5.7: a) Large area of the principal displacement zone (PDZ) that has several points that are low or moderate confidence. b) This area is a zone of abrasion that formed during the evolving Riedel shear network and is marked by numerous mesoscale shears with associated cataclastic and fault breccia development. Zones such as these are marked by under-performing stopes and follow the general trend of the e3 and e2 eigenvalues (41°-192° and 41°-328°, respectively; Chapter 3).

Explicitly stating the data points used to construct a structure is necessary where data are clustered, which is often the case with outcrop mapping. Outcrop mapping can result in uncertainty brought on by conflicting evidence, particularly if drilling data are nearby or multiple geologists have collected data from the same outcrop. From experience working with multiple datasets from active mining operations, a common issue is the incorrect identification of a structural feature, usually fine-grained rocks with bedding and one or more tectonic fabrics. Unfortunately, mapping by geologists is subjective and largely based on experience and pre-conceived notions (Bowden, 2004), e.g., a graduate geologist versus a consultant with decades of experience who will collect higher quality data and readily identify important features to record. For instance, in the mining industry, common geological features that are overlooked are the measurement of lineations and kinematics.

With a structurally complex shear zone such as the Dugald River Shear Zone, the data inputs into a structure may change as new data are added, or as modelling of the shear zone continues. The shear zone developed as an evolved, dextral Riedel shear network with a bulk shear direction trending NNW, which means that synthetic shears will occur within a roughly ±20° range of the bulk shear trend i.e., NW through NNW to N for P-, Y- and R-shears respectively, and a dip range of ~45° to 90°. Thus, while modelling a shear zone such as the Dugald River Shear Zone the geometry of a modelled shear, the data inputs, or the interactions with other modelled shears may change as the modelling process progresses (Fig. 5.8), which is further compounded when using a dataset that changes as mining progresses (Fig. 5.9). In Figure 5.8a, an earlier interpretation of a few major shears towards the west of the principal displacement zone is shown, which was modified to the current interpretation (Fig. 5.8b) after the interpretation of Patties Shear started to take “shape”. Notably, when modelling a complex shear zone, interpretation and construction of shears start in areas with high confidence data from multiple sources.

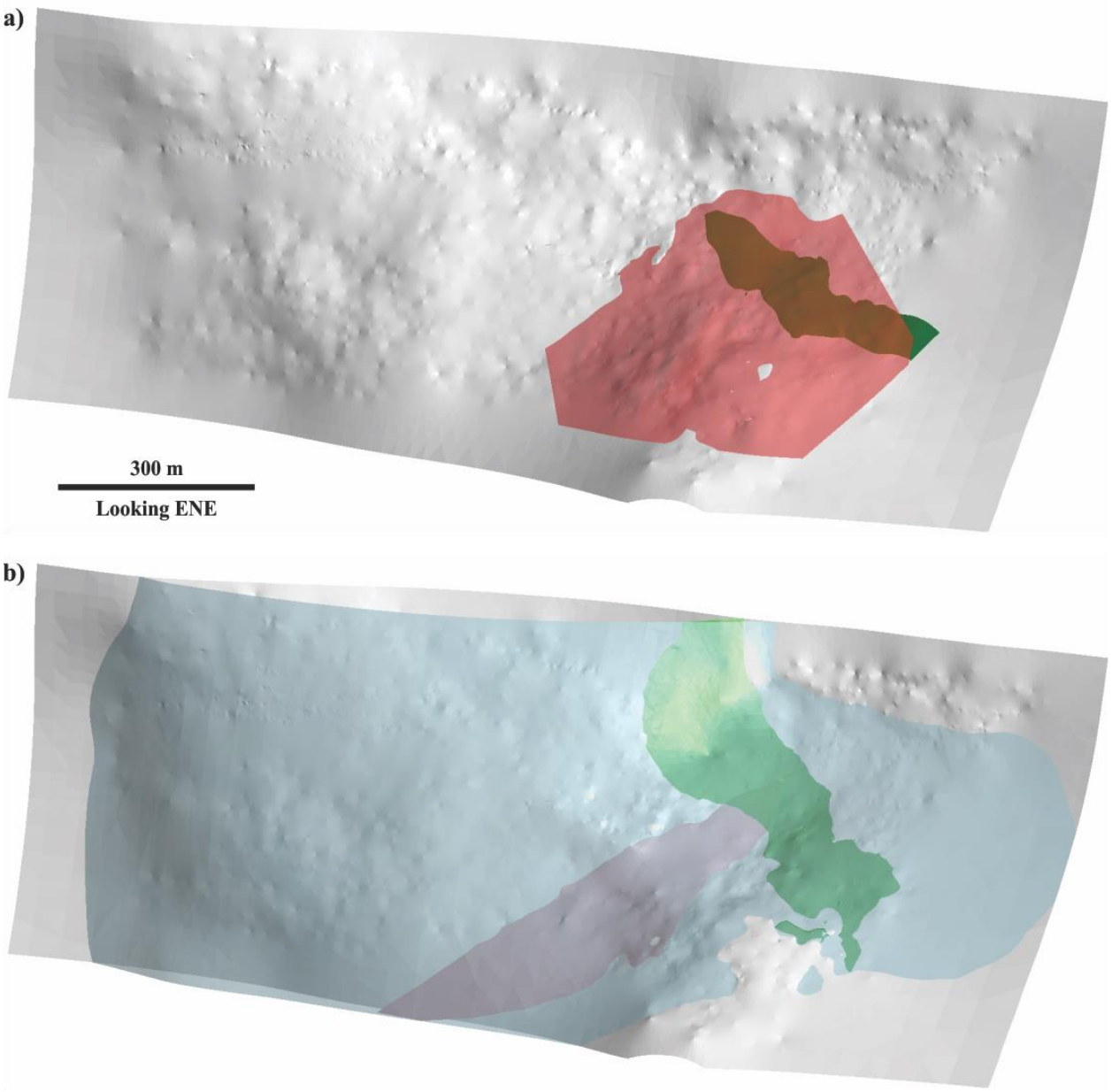

Fig. 5.8: a) Early interpretation and model of shears in the South Mine. b) Current interpretation for this thesis. The difference is largely due to the progressive inclusion of data points (drilling data) away from areas that have directly observed data (mapping) and a clearer understanding of the geometry of the shear zone.

While the inclusion of a confidence rating for data points is a retroactive approach, it should ideally be included moving forward at the time of data collection (also Jones et al., 2004). Geoscientists should include their confidence in the point measured, or when logging drillcore as this will help downstream users with assigning their confidence to the data point as it is added to the discrete structure table and populated onto the wireframe when communicating to stakeholders. In addition, it allows a modeller to make informed decisions on downsampling data where data points are clustered. The discrete structure table has several uses that can be grouped into 1) communication; 2) visualisation; and 3) verification.

5.4.1.1. Communication

The table is populated independently of modelling software and licensing requirements. Thus, various stakeholders can access and view the table. Because the table includes information such as structure classification and comments it can be used to aid in mine design. For instance, if litho-structural domains are required in a model, the structures need to be modelled as surfaces, which fails to display the extent of the damage zone, and general comments about the structure and data points can be used to estimate the geomechanical properties of structures within an area.

5.4.1.2. Visualisation

Each data point that is added to the table includes coordinates so that the table can be imported into 3D modelling software. The primary purpose is to display the confidence rating for each data point used to model a structure and is used to ascertain parts that may require attention (e.g. Fig. 5.6, 5.7). By assigning a confidence rating of low, medium or high the user is providing a subjective view of uncertainty. The principal displacement zone represents a high confidence modelled surface, however, several parts of the surface are defined as medium to low confidence and may require attention to improve the confidence, either with mapping campaigns or orientated drilling. At Dugald River, the lower confidence parts are usually where the shear zone is flatter and numerous anastomosing shears developed and it is difficult to confidently assign data points to a specific shear.

5.4.1.3. Verification

Verification is concerned with ensuring data accuracy not only in the confidence of individual points but also in the confidence of a modelled surface, particularly with non-finite surfaces that are extrapolated from known data points. One purpose of converting the relevant data sources used to construct a modelled surface into a single table allows for simpler information extraction such as distance to data along a surface (Fig. 5.9).

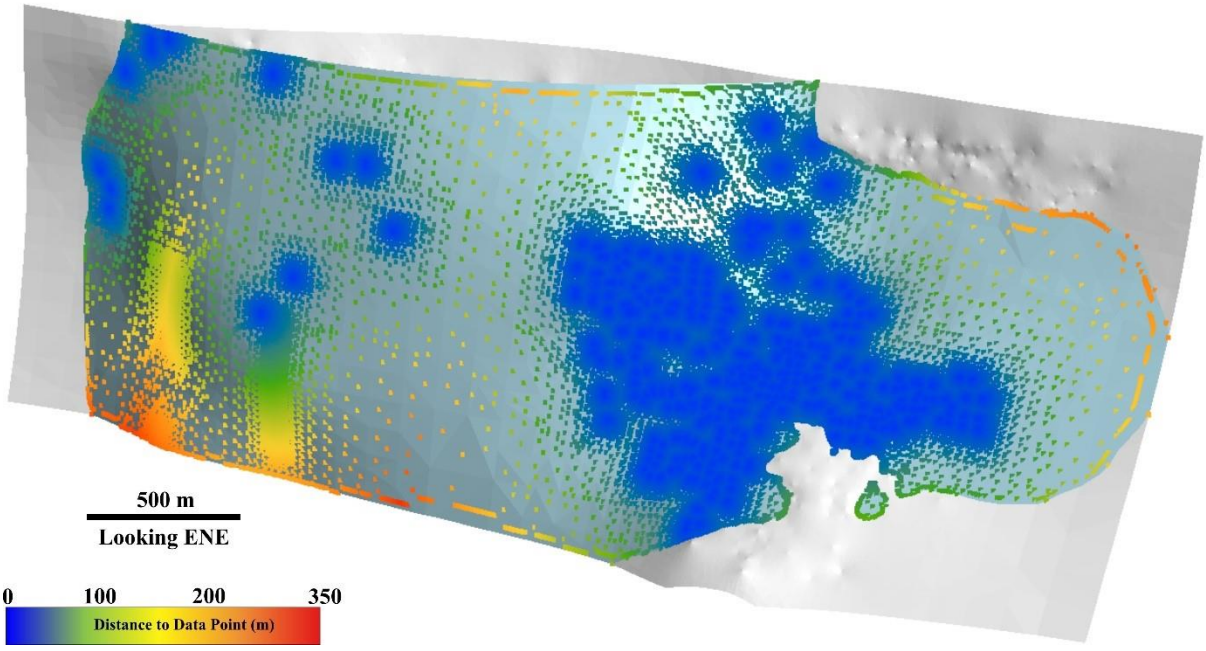

Fig. 5.9: Distance to data for each triangle centroid of the wireframe for Patties Shear giving rough spatial confidence in the wireframe.

A wireframe is a network of interconnected triangles and calculating the centroid of each triangle can be done with most 3D software or with Python using the library *ezdxf* (Moitzi, 2022) to access a dxf format of a wireframe and running a nearest neighbour search using the *scipy.spatial* (Virtanen et al., 2020) library to determine the distance from a centroid to the nearest data point. Viewing the result in 3D modelling software gives one an idea of the spatial confidence in a structure (Fig. 5.9). The centroid is calculated using Equation 1:

$$centroid = \frac{vx1 + vx2 + vx3}{3} \tag{5.1}$$

Where vx refers to a vertex of a triangle and (vx1; vx2; vx3) are the three vertices that constitute the triangle. In addition, the vertices can be used to determine the orientation of the triangles i.e., the dip and dip direction. The three vertices define a plane and the normal vector to the plane can be converted into dip and dip direction using Equations 2 - 6:

$$u = vx2 - vx1 \tag{5.2}$$

$$v = vx2 - vx3 \tag{5.3}$$

$$n = v \; x \; u \tag{5.4}$$

$$dip = \cos^{-1} nz \tag{5.5}$$

$$dip\ direction = \tan^{-1} \frac{nx}{ny} \tag{5.6}$$

Where u and v are vectors from vx2 to vx1 and vx3, respectively and n is the normal to the plane created by vx1, vx2 and vx3. The normal to the plane is calculated using the cross product of vectors u and v and if using Python to calculate the normal, n needs to be normalised to avoid null values when using Equation 5.5 as the distances to the vertices can be greater than 1 and will return vector components (nx, ny and nz) greater than 1 (values outside the range of -1 to 1 for $\cos^{-1}$ are not valid). In addition, the dip direction may be returned outside of the range 0 to 360, thus the values need to be corrected by adding or subtracting 360, respectively.

The provided script, *tri_ori.py* (Appendix B) can be used to calculate the triangle orientations for wireframes added in the *tri_ori.xlsx* project setup table (Table 5.2; included as supplementary data) and evaluated to the discrete structure table. The script uses *ezdxf* which for large *.dxf* files can take a few minutes to load.

Table 5.2: Project setup table for the *tri_ori.py* script. The table is included as supplementary data

Wireframe	**Discrete Structure Table**	**X**	**Y**	**Z**	**Dip**	**Dip_Direction**
*File path to wireframe	*File path to discrete structure table	*Easting/X column name	*Northing/Y column name	*Elevation/RL/Z column name	*Dip column name	*Dip Direction/Azimuth column name

5.4.2. Data Confidence Distribution

In this section, we describe a method to firstly categorise data into low, medium and high confidence, which is then populated in 3D using a regular grid of points. The criteria for grouping data into low, moderate or high presented in this study is a baseline and modification of groups is expected based on mine site requirements or work quality requirements of an organisation. Table 5.3 is an example table that can be used for categorising data and is designed to simplify the process and resembles a risk matrix used frequently in the mining industry. A similar approach is employed by Clarke (2004) that used a linguistic score for data quality and quantity to determine a certainty score, which itself is a variation of Bowden (2004) that assessed data quality versus quality indicator to assess uncertainty.

In rows, data are categorised based on the reliability of the data source and in the columns, the quality of the data is categorised. The examples given for each cell are not exhaustive and may need to be modified depending on the requirements of the organisation. Data used to construct models can be from varied sources (geologists and disciplines) and may include historical data, thus using an approach of categorising data based on the source and quality allow for rapid assigning of confidence as it simply requires a new column to be created in a database or data table (e.g., Table 5.4). The subtables in Table 5.4 were compiled in Microsoft Excel by assigning a data source and data quality reliability rating to each data point and then running a function to assign data confidence to each point. In addition, a column for photographic evidence was included. The tables with the additional columns can be loaded into 3D modelling software and meaningful information communicated (Fig. 5.10).

Table 5.3: Table used to categorise the reliability of a data source and quality into low, moderate and high. Included are several examples that are expected to be modified by the requirement of the mine site or organisation. At Dugald River, the relevant data sources are characterised and orientation mapping, orientated and non-orientated drilling. The data quality is a mix of measured data from both experienced and inexperienced geologists. However, data are predominantly from orientation mapping and non-orientated drillcore thus for a purpose of a detailed structural analysis (see Table 5.4) such as this study, the data is classified as moderate reliability.

		Data Quality		
		High • Measured (experienced) • High-precision analytical equipment	Moderate • Measured (inexperienced/unknown) • Interpreted (experienced) • Portable analytical equipment	Low • Interpreted (inexperienced/unknown) • Low precision analytical equipment (legacy)
Data Source	High • Characterised mapping • Orientated drillcore • Geochemical data (fresh rock) • High-resolution geophysics • High-resolution spectral data	**High**	**Moderate**	**Low**
	Moderate • Orientation mapping • Non-orientated drillcore • Geochemical data (weathered rock and soil/stream) • Low-resolution geophysics • Low-resolution spectral data	**Moderate**	**Moderate**	**Low**
	Low • Legacy data • Regional scale geophysics	**Low**	**Low**	**Low**

Table 5.4: Data tables used in this study. Each data point in a table was assigned a data source and quality reliability factor, which were combined into a data confidence rating for each data point. Tables 5.4A and D are the only data sources that have high confidence data as the data sources and quality are reliable for the detailed structural analysis required in this thesis.

Table 5.4A: Selected data from this study and consultants to showcase the criteria for a high-quality source as the data includes additional information (kinematics, feature classification, comments) lacking from orientation-only mapping (Tables 5.4B and C).

Table 5.4A: Characterised Mapping													
X	**Y**	**Z**	**Structure**	**Lithology**	**Kinematics**	**Classification**	**Dip**	**Dip Direction (MG)**	**Comment**	**Data Source**	**Data Quality**	**Data Confidence**	**Photos**
10609.1	14239.11	9811.1144	Shear	DLMS		Minor	87	129	Thin shear…	High	High	High	Yes
10606.88	14239.11	9812.2	Shear	DLMB	Dextral	Minor	81	61	Splay off…	High	High	High	Yes
10768.62	14246.12	10008.9749	Fault	BSUN	Reverse	Major	63	261	Major structure…	High	High	High	Yes
10772.48	14284.98	10008.2194	Shear	BSUN		Major	74	280	Shear zone…	High	High	High	Yes
10883.03	13886.76	10210.57246	Shear	LMST			72	293	dextral, shear…	High	High	High	No
10813.22	14358.35	10214.46294	Shear	LMST			49	54	Fe altered…	High	High	High	No

Table 5.4B: Mapping table compiled from various mapping data tables found in the Dugald River database. The mapping data only has the structure type and orientation data associated with it and as it is measured data, the data quality was assigned moderate (measured with the unknown label; see Table 5.3). Due to the overlap between face mapping and photogrammetry, while face mapping was phased out, some of the face mapping points will have photographic evidence.

Table 5.4B: Orientation Only Mapping (Face Mapping)									
X	**Y**	**Z**	**Structure**	**Dip**	**Dip Direction (MG)**	**Data Source**	**Data Quality**	**Data Confidence**	**Photos**
10894.44	13925.24	10183.75291	Fault	60	320	Moderate	Moderate	Moderate	No
10903.45	13912.08	10182.38704	Fault	10	225	Moderate	Moderate	Moderate	No
10896.76	13922.61	10182.31771	Fault	58	303	Moderate	Moderate	Moderate	No
10843.4	13986.75	10149.95	Shear	70	75	Moderate	Moderate	Moderate	Yes
10664.22	15048.1	10128.32	Fault	64	310	Moderate	Moderate	Moderate	Yes

Table 5.4C: Mapping table compiled from digitising structures on photogrammetry virtual outcrops. The digitising was done as part of this thesis, and thus is of high-quality data, however, as there is limited information that can be extracted from the data for structural analysis, the data has moderate confidence.

Table 5.4C: Orientation Only Mapping (Photogrammetry)										
x	**y**	**z**	**dip**	**azimuth (MG)**	**Classification**	**Polyline ID**	**Data Source**	**Data Quality**	**Data Confidence**	**Photos**
10803.19	14394.72	10109.25156	15	356	Minor	N125_OD487…	Moderate	High	Moderate	Yes
10698.74	13977.13	9888.388334	43	262	Major	S340_OD398…	Moderate	High	Moderate	Yes
10696.21	13978.7	9885.993378	54	274	Major	S340_OD398…	Moderate	High	Moderate	Yes

10712.28	14179.89	9917.564	29	263	Moderate	S315_OD419…	Moderate	High	Moderate	Yes
10626.06	13975.12	9837.726716	34	276	Moderate	S390_OD395…	Moderate	High	Moderate	Yes

Table 5.4D: Table of selected structural logging from orientated drillcore. The table is a separate input table to the non-orientated drillcore logging table (Table 5.4E), however in some instances data was erroneously input into the table, which should be reflected in the data source and quality by running a check empty cell condition function.

Table 5.4D: Orientated Drillcore Logging

HoleID	Depth	Feature	Dip	DipDirection (MG)	Comment	Data Source	Data Quality	Data Confidence	Photos
DU1773	28.11	Fault_3	55.75	100.38	polished	High	High	High	Yes
DU1697	115.54	Fracture_3	28.73	323.83		High	Moderate	Moderate	Yes
DU1673	25.55	Breccia_4			fine gouge…	Moderate	Moderate	Moderate	Yes
DU1695	115.13	Fracture_4	58.23	268.52		High	High	High	Yes

Table 5.4E: Table of selected non-orientated drillcore intervals. Due to the lack of orientation data, the data will always have moderate confidence regardless of the data quality. The structures are logged as intervals with a feature type recorded with an intensity rating assigned scaling from 1 to 5.

Table 5.4E: Non-Orientated Drillcore Logging

HoleID	From	To	Structure_Intensity	mid_x	mid_y	mid_z	Data Source	Data Quality	Data Confidence	Photos
DU1567	4.59	9.79	Breccia_3	10728.52	14523.32	9752.362	Moderate	High	Moderate	Yes
DU1567	78.06	78.36	Breccia_3	10658.25	14517.63	9760.942	Moderate	High	Moderate	Yes
DU1489	3.75	4.22	Breccia_2	10623.49	15143.56	9733.744	Moderate	Moderate	Moderate	Yes
DU1489	4.22	4.37	Breccia_4	10623.21	15143.7	9733.79	Moderate	Moderate	Moderate	Yes
DU1489	4.37	5.57	Fracture_1	10622.62	15143.99	9733.89	Moderate	Moderate	Moderate	Yes

Table 5.5: Template for the project setup table for the *data_distribution.py* script. The columns below are required, except the *Structure* and *Structure_Filter* columns and all columns in the data will be loaded but only the required columns for the script to function will be used. The column names in the cells will be renamed in the script to avoid a *KeyError* in Python.

Path	X	Y	Z	Dip	Dip_Direction	Structure	Structure_Filter	Data_Source	Data_Quality	Photos
*File path	*Easting/X column name	*Northing/Y column name	*Elevation/RL/Z column name	*Dip column name	*Dip Direction/Azimuth column name	*Structure/Feature column name	*Structure/Feature filter list; in format S0;S1;S2	*Data source column name	*Data quality column name	*Photo column name

While the subtables shown in Table 5.4 are simple to set up and load into 3D modelling software, they can be cumbersome to view where data are clustered and from multiple sources and confidence ratings (Fig. 5.10). In addition, changing the column focus in multiple tables can be restrictive when communicating data to stakeholders. Lastly, depending on the 3D modelling software used, a *.csv* file format may be required when importing tables, which only stores values in cells and therefore does not keep formulas. Thus, included in this thesis is a python script (*data_distribution.py*) that loads the tables in either *.xlsx* or *.csv* format and performs several queries on the tables with the results populated onto a regular 3D grid of points. The output is a *.csv* file that contains the grid coordinates and the query results. Examples of useful queries are included in the rest of the section. The complete *data_distribution.py* script is included in Appendix B and includes detailed comments for the steps of the script with the important steps summarised in this section. The script requires *numpy* (Harris et al., 2020), *pandas* (Mckinney, 2010) and *scipy.spatial* (Vertanen et al., 2020) libraries to be installed on the computer and uses a project set-up table (Table 5.5) to load data tables.

At the beginning of the script, several variables will require user modification before the first run as they are mine site-specific: 1) the boundary of the volume of interest (e.g., 3D model boundary); 2) the spacing between grid points (default is 20; *viz.* 20 m in the mine grid of Dugald River); 3) the query percentage cut-off for assigning "Yes" to queries ; 4) the cut-off for multiple high or moderate reliability points to define high or moderate data confidence (default is 3); and 5) the file path to project set-up table (Table 5.5; also included as supplementary data).

The script iterates through the project set-up table and concatenates the tables into a master DataFrame (see McKinney (2010) for a description of a DataFrame structure). It should be noted that the data reliability from the data source and data quality columns is applied to the data tables during this step as it is simpler to code in Python than Microsoft Excel, which can have issues with the "*fill series*" function and as many software packages export *.csv* files, the formulas would need to be retyped each time the tables are to be used.

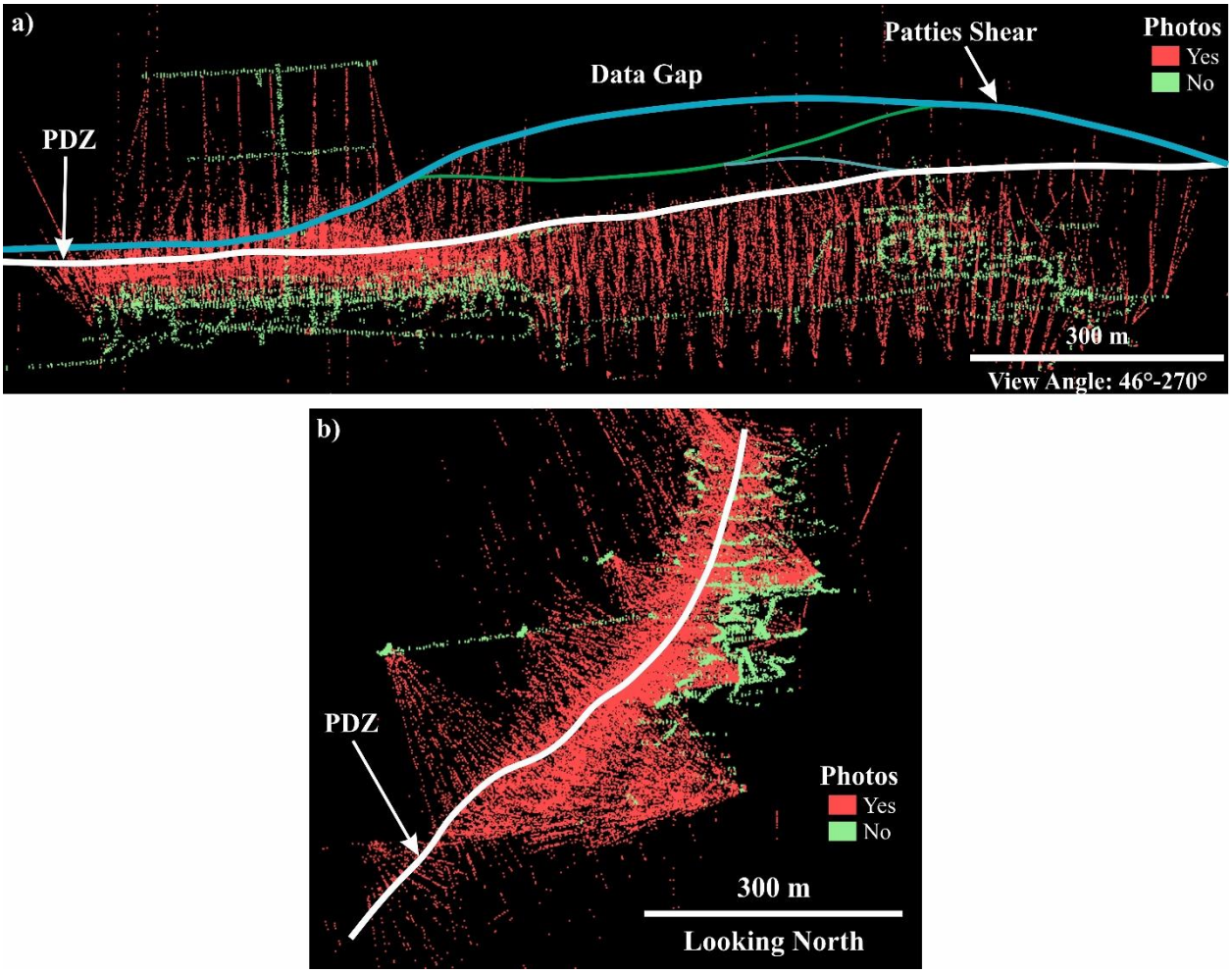

Fig. 5.10: Data tables (Table 5.4) used in this study colour coded according to whether the data have photos. The lack of photos can make it difficult to interpret the applicability of assigning a data point to a structure if no descriptors (e.g., comments, scale classification) are available. Furthermore, there is a large ~300 m data gap in the volume of interest which is reflected in the distance-to-data method illustrated for the Patties Shear (Fig. 5.9). Two subordinate shears are shown between the Patties Shear and the principal displacement zone (PDZ) which will have some uncertainty with it as there is limited data used to construct them.

A nearest neighbour search is executed on the master DataFrame to determine all the data points that occur within a grid point's "space" (i.e., half the spacing between adjacent grid points). If no points occur within the grid point's "space", the grid point is discarded to reduce processing times. Queries are then executed with the primary query determining the data confidence for each respective grid point (Table 5.6). The data confidence query is hierarchical, thus if the criteria for high are satisfied the next iteration (grid point) will begin and it includes a failsafe condition that if no criteria are met, it will return '*Fail*'. Table 5.6 is an example used for this study and due to the requirements for the structural analysis, only one criterion exists for high confidence data. Thus, it is expected the criteria will be modified based on the requirement of a mine site and that changes will need to be reflected in the *data_distribution.py* script.

Table 5.6: Criteria for assigning confidence in the data for a grid point's "space". The cut-off value of 3 is was decided based on the 20 m spacing between grid points and to avoid the assignment of high for sporadic orientated drillcore measurements. Thus, a high confidence rating was assigned where characterised mapping and/or regular orientated drillcore logging for structures occurs.

Confidence Rating for Data Distribution		
High	**Moderate**	**Low**
• Multiple (>=3) high confidence data with supporting photographic evidence	• Multiple (>=3) moderate confidence data with supporting photographic evidence • High confidence data without supporting photographic evidence • <3 high confidence data with supporting photographic evidence	• Low confidence data only • Multiple moderate confidence data without photographic evidence • Single datum without supporting photographic evidence (high and moderate confidence) • <3 moderate confidence data with supporting phtographic evidence

Additional useful queries are included in the script: 1) density of data points in the grid point's "space"; 2) the number of data sources; 3) if data points contain orientation measurements; and 4) if data points contain photos. The former two return a numerical value and the latter two use a user-specified query percentage cut-off to return "Yes" or "No". The output of the script is a *.csv* file that is exported into the same folder where the project setup table is located and saved as *data_confidence* with the current date (e.g., *data_confidence_2022-01-20.csv*).

It should be noted that the project setup table includes a structure filter column. The purpose is to account for tables that include multiple feature types, some of which are not necessary for the script. In the context of this study, these are features related to planar features such as bedding and foliation as the concern here is faults and shears.

5.5. Discussion

The methods presented in this chapter assist with visualising and communicating the confidence in the geological data distribution used to construct 3D models and highlight areas in the volume of interest that may need attention to increase confidence in the data. In this study, we are focused on structural data used to construct the Dugald River Shear Zone.

The first method is a *discrete structure table* (e.g., Table 5.1), which is a subjective method of communicating the variation in the confidence that a geologist has in the assignment of data points to construct a wireframe (also Savage et al., 2013). Assigning a confidence rating to each data point is a form of expert elicitation (see Randle et al., 2019) as the mental uncertainty that a modeller has in assigning a data point to a respective wireframe is categorised into low, moderate or high. The factors that influence a decision are variable and at Dugald River are mainly due to multiple discrete shears that developed where the shear zone is flatter (Fig. 5.6) which is compounded by the fact that measurable, direct observations of discrete shears are limited to underground development that is largely along the footwall of the principal displacement zone (Fig. 5.11 and 12). Thus the interpretation of discrete shears within the rock mass is largely from non-orientated drillcore and uncertainty will increase further away from underground development. By using the *discrete structure table*, uncertain areas of a structure's interpretation can be communicated to stakeholders so that they can be informed that with future iterations of the 3D model, or as new data are made available, the geometry (e.g., Fig. 5.5) and possibly the continuation of the structure as modelled may change (e.g., Fig. 5.8). Additional factors that may influence the decision of assigning confidence includes the data source and type, availability of photographic evidence, and the number of data points supporting an interpretation.

The second method uses the *discrete structure table* for a structure and triangle centroids of its wireframe to display the distribution of data used to construct the wireframe (Fig. 5.9). The method uses the assumption that where data are sparse there will be uncertainty in the interpretation of a structure. However, data density is less problematic at Dugald River given the close spatial relationship of the ore body with the shear zone (Chapters 2 and 3) and that drilling mostly intercepts both the ore body and most of the shear zone. The Patties Shear is an exception and has variable data distribution (Fig. 5.9) with higher modelling confidence of the wireframe geometry in the south where the shear is intercepted by underground drilling and development, and decreasing towards the north where there is a data gap of ~300 metres before surface drilling data was available and used to constrain the shear (e.g., Fig. 5.10), which is interpreted to merge with the principal displacement zone (Fig. 5.11 - 13). Similarly to the first method, the second method assists in communicating uncertain areas in a structure's interpretation from a data distribution perspective and if more data are added to sparse areas,

the certainty in the interpretation may increase by either constraining the geometry of the structure or if need be the interpretation of a single structure versus multiple structures (e.g., Fig 5.8).

The final method populates the reliability of the geological data onto a regular 3D grid (Fig. 5.11 - 13). It serves as a practical method to display confidence in the geological data independent of an interpretation of a structure and allows for querying of information related to uncertainty (e.g., data density, data sources, photographic evidence, orientation data). Its main purpose is to highlight areas within a volume of interest that may need attention concerning creating potential uncertainty in interpretation (e.g., Fig. 5.13).

5.5.1. Dugald River Case Study

For the Dugald River deposit, an appropriate grid spacing is 20 m and five tables were processed with the *data_distribution.py* script. The maximum confidence rating for each 20 m^3 grid point is shown in Figure 5.11a and Figure 5.12a and indicates that the data confidence for the volume of interest is predominantly moderate due to the close drill spacing of non-orientated drillcore and limited structural measurements from orientated drillcore. In addition, virtual outcrops are captured regularly while developing drives, which are digitised to increase the distribution of moderate confidence data between drilling. Low confidence areas in the volume of interest occur where face mapping was done (green dots on Fig 5.11a - b and Fig 5.12a - b), which predominantly do not have photos for supporting evidence and as they are classified as moderate confidence data and using the criteria of Table 5.6 during the execution of the script will result in a grid point being assigned low confidence if face mapping is the sole data source.

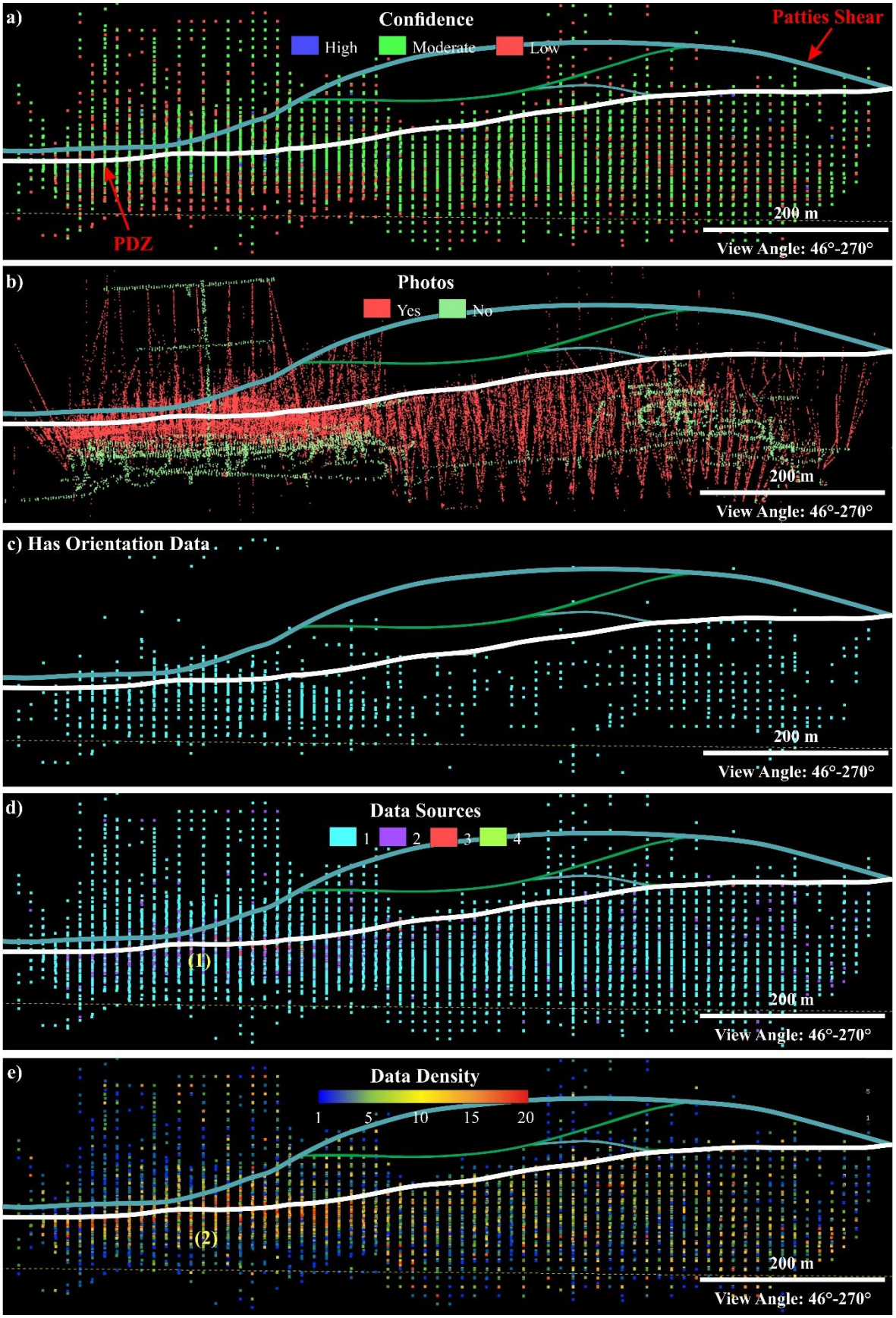
a)
Confidence
High
Moderate
Low
Patties Shear
PDZ
200 m
View Angle: 46°-270°
b)
Photos
Yes
No
200 m
View Angle: 46°-270°
c) Has Orientation Data
200 m
View Angle: 46°-270°
d)
Data Sources
1
2
3
4
(1)
200 m
View Angle: 46°-270°
e)
Data Density
1
5
10
15
20
(2)
200 m
View Angle: 46°-270°

Fig. 5.11 and Fig 5.12: Output examples of the *data_distribution.py* script. In Fig. 5.11, the images are roughly down-dip of the principal displacement zone (PDZ) and in Figure 5.12, the images are looking north. Note gaps in the regular grid of points are due to NULL values for the grid point (i.e., no queried data occurs within its "space"). Included in the images are the Patties Shear and two subordinate shears which have variable confidence in their interpretation due to a data gap in the volume of interest (Fig. 5.10a). Fig. 5.11b and Fig. 512b provide a comparison with Fig 5.11a and Fig. 5.12a to highlight that low-confidence areas are generally where face mapping dominates as they lack supporting photographic evidence. Fig 5.11c and Fig. 5.12c highlight the bias of orientation data within the footwall of the PDZ. Fig. 5.11d - e and Fig. 5.12d - e shows the number of data sources and density of data points within a grid point "space". The number of data sources (yellow 1 in Fig. 5.11d) and data density (yellow 2 in Fig 5.11e) is higher in the southern part of the mine particularly in the upper levels as traditional face mapping and photogrammetry overlapped in this area.

The distribution of data with orientation measurements is disproportionately along the footwall of the principal displacement zone and upper portions of the mine where surface drilling dominates over underground drilling (Fig. 5.11c and Fig. 5.12c). The surface drilling was mostly done before underground development and when production targets were less important, thus generally representing data with higher confidence as it will have comments and care was taken to take frequent measurements. Most of the development occurs along the footwall of the principal displacement zone, thus mapping data can be captured regularly. It should be noted that for a detailed structural analysis a representative spread of data should be available. Fortunately, at the time of this study, many mine levels were available with drives developed through the shear zone (blue grids on Fig. 5.11a and Fig. 5.12a) and a good representation of structural data could be captured. Ideally, high confidence structural data should be captured regularly and using a data confidence distribution method such as the one presented here can assist in determining areas that require attention (e.g., Fig. 5.13).

Additional queries that are useful and included in the default script are the data sources and density of data (Fig. 5.11d - e and Fig. 5.12d - e). The outputs show the robustness of the data rather than the confidence of the data and are useful in identifying areas that may need targeted mapping or drilling campaigns to increase the data distribution.

Fig. 5.12: See caption for Figure 5.11. Presented here are north views from the southern end of the mine.

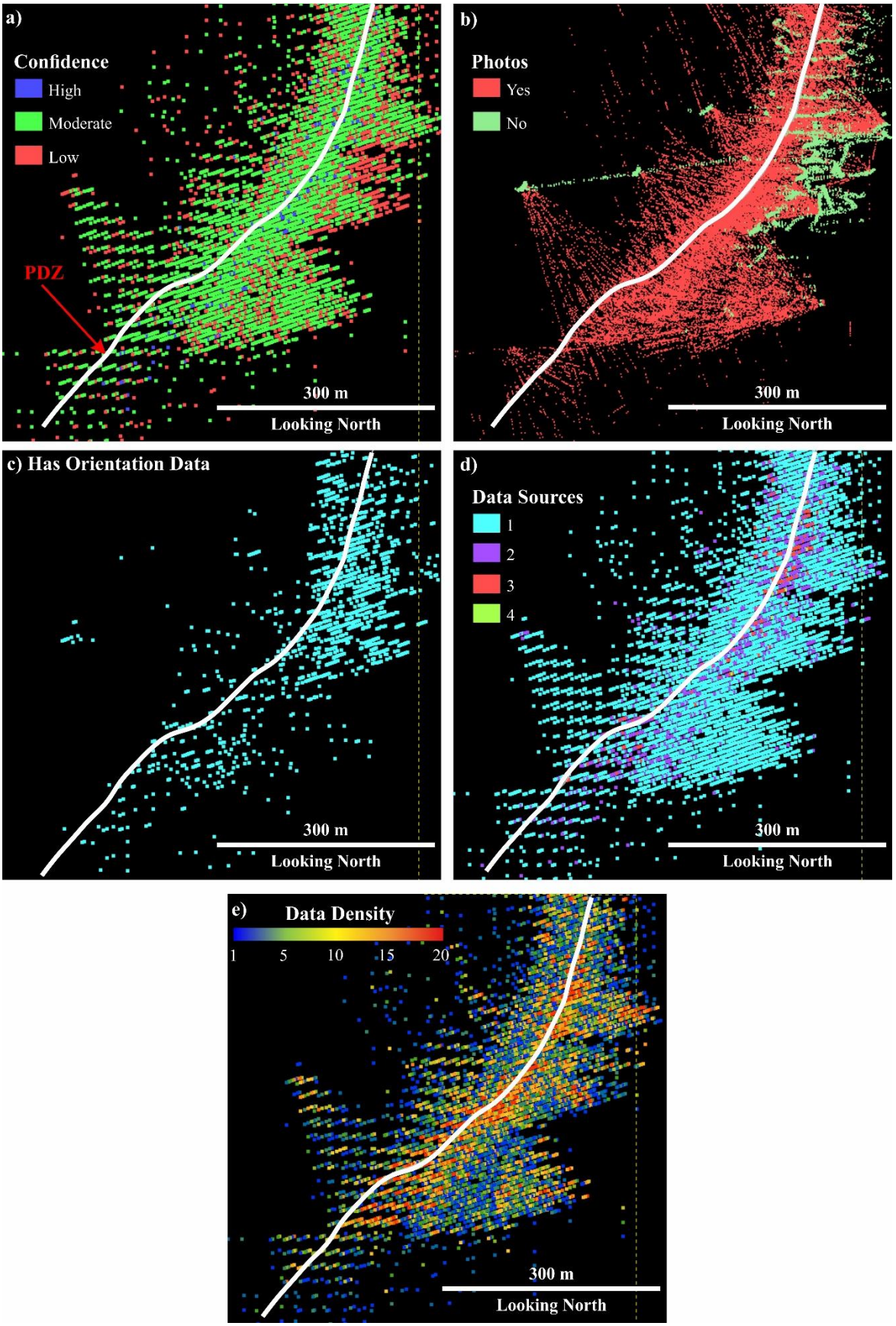
a)
Confidence
High
Moderate
Low
PDZ
300 m
Looking North
b)
Photos
Yes
No
300 m
Looking North
c) Has Orientation Data
300 m
Looking North
d)
Data Sources
1
2
3
4
300 m
Looking North
e)
Data Density
1
5
10
15
20
300 m
Looking North

Figure 5.13 is an example of how the data confidence distribution can be used to communicate confidence in an interpretation of interconnecting structures and plan where targeted data collection campaigns should be conducted to improve the confidence in the data and therefore the interpretation. The example is from the northern boundary of the 3D model where data distribution is sparser compared to the rest of the model (e.g., compare the southern side of Figure 5.13a to the northern side). In this region several macro-scale R- and P- shears were modelled with the principal displacement zone marked by a westward shift in the strike of the structure (see Fig. 5.5) with the interpretation that the principal displacement zone has propagated along a P-shear (yellow number 1 on Fig 5.13a; also see Chapter 3) and then along an R-Shear to a more northerly strike. An alternative and plausible interpretation may be that the principal displacement zone propagated along the P-Shear and rather propagated along a more southern R-Shear (white number 2 on Figure 5.13a). It is important to accurately interpret the geometry of the principal displacement zone as the high-grade ore lenses occur adjacent to it (see Chapters 2 and 3), and although it appears that the northern flexure in the shear zone is contractional, it is nonetheless important in a detailed structural analysis to constrain the exploration vectors for predictive ore targetting (Chapter 3).

The results of the *data_distribution.py* script indicate that the areas of low confidence (Fig. 5.13d) are where face mapping data dominates (Fig. 5.13a and b) and as the data lacks photos it is difficult to confidently assign data points to a structure. Thus to improve the data confidence, it is suggested that a mapping campaign be planned in the large areas of low confidence and given the importance of the area for a comprehensive structural analysis, it should be conducted using traditional methods (characterised mapping) and using photogrammetry for reference.

There are several caveats with the methods proposed and using the Dugald River mine dataset. The Dugald River mine is a recently exploited deposit (less than 10 years at the time of the start of the study), thus the techniques of capturing data are modern (e.g., photogrammetry, high resolution core photos). The majority of the data available for the Dugald River mine is classified as moderate confidence using the criteria of Tables 5.3 and 5.5 as the data are measured by experienced geologists from non-orientated drillcore and photogrammetry. The data is recorded regularly along drillcore runs and most development cuts and due to the data also including photographic evidence, the data is evaluated to the regular grid of points with moderate data confidence (Table 5.6). Thus, the methods presented in this study should ideally be tested on older mines that have a wider range of data types and methods of capturing data.

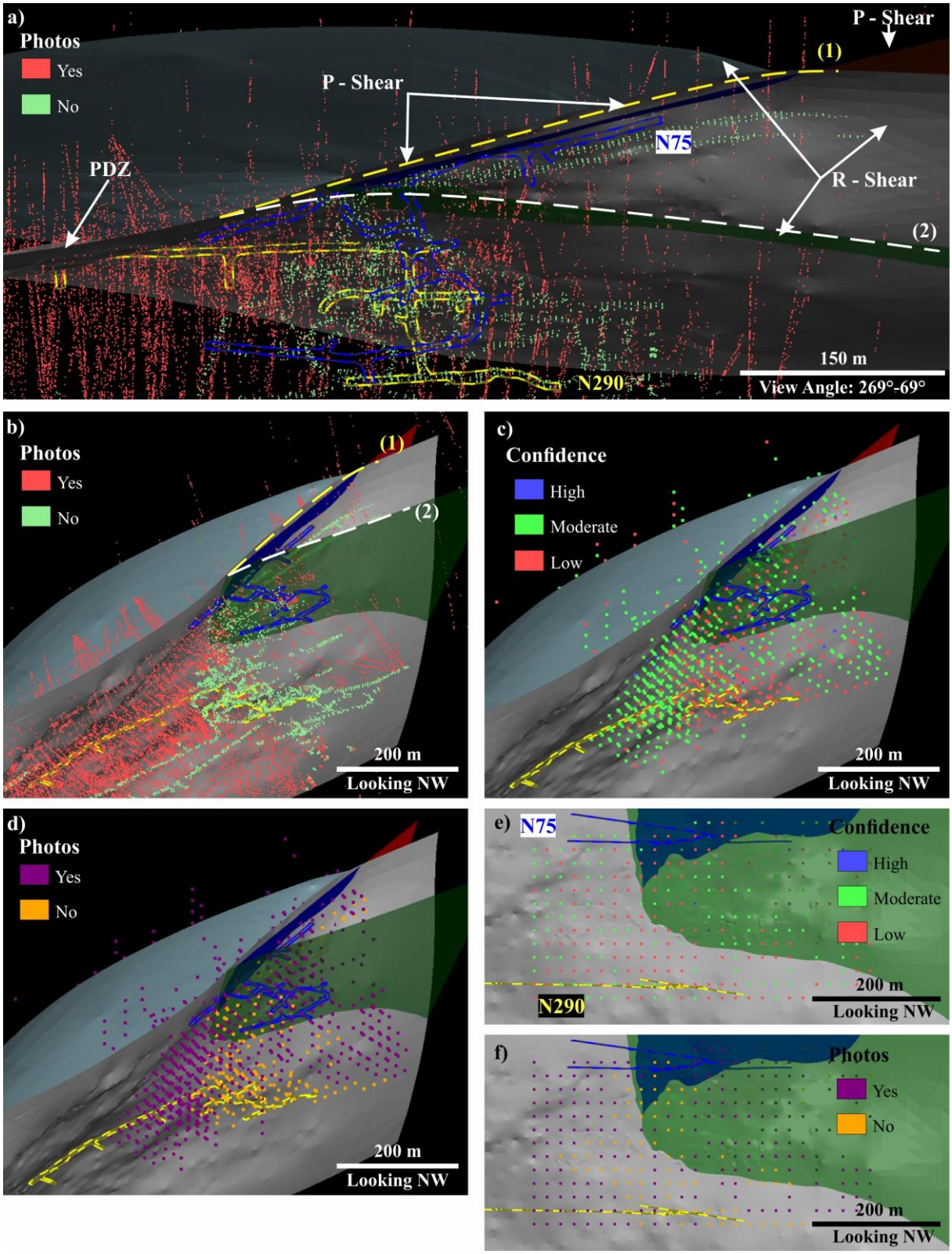
a)
Photos
Yes
No
P - Shear
(1)
P - Shear
N75
PDZ
R - Shear
(2)
150 m
N290
View Angle: 269°-69°
b)
Photos
Yes
No
(1)
(2)
200 m
Looking NW
c)
Confidence
High
Moderate
Low
200 m
Looking NW
d)
Photos
Yes
No
200 m
Looking NW
e)
N75
Confidence
High
Moderate
Low
200 m
N290
Looking NW
f)
Photos
Yes
No
200 m
Looking NW

Fig. 5.13: Output examples of the *data_distribution.py* script for the northern boundary of the model. a) Inclined west view of the photo distribution of the data tables (Table 5.4). Labels for the principal displacement zone (PDZ) and R- and P- shears are included for reference and the same for the rest of the figures. The Patties Shear is the light blue surface to the west. Two levels, namely N75 and N290, are included to provide a visual aid of the scale of low confidence data. b) NW view of the photo distribution of the data tables (Table 5.4). c and d) NW view of the output of the *data_distrution.py* script showing the distribution of the photos and the data confidence distribution, respectively. e and f) West view of the output of the *data_distrution.py* script showing the distribution of the photos and the data confidence distribution, respectively. The west view provides a sense of the scale of low confidence data in this part of the model.

5.6. Conclusion

- Several methods are presented in this chapter for geologists to communicate the confidence that they have in the geological data within a volume of interest.
- The first method uses a discrete structure table which is populated while a structure is modelled. A confidence rating of low, moderate or high is given to each data point and is a subjective way of communicating the confidence a geologist has in individual data points.
- The second method uses a provided python script (*tri_ori.py*) to calculate the distance of triangle centroids of a wireframe (structure's surface) to the data points of its associated discrete structure table. The output provides an estimate of the variability in the confidence in a structure by displaying the distance to data along its wireframe.
- The third method uses a provided python script (*data_distribution.py*) to generate a regular 3D grid of points to which data within its "space" is queried. Each data point is first assigned a reliability rating for data quality and source as well as if the data has supporting photographic evidence. The script queries the data and outputs a confidence rating for the data within each grid point "space".
- The methods provided can be used to determine areas within a volume of interest that may require additional data collection campaigns to improve the geological data confidence and thus reduce uncertainty in a 3D model. An example of the Dugald River Shear Zone is provided in the chapter.

5.7. References

Allmendinger, R. W., Siron, C. R. & Scott, C. P. (2017). Structural data collection with mobile devices; accuracy, redundancy, and best practices. Journal of Structural Geology, 102, 98–112. https://doi.org/10.1016/j.jsg.2017.07.011

Assali, P., Grussenmeyer, P., Villemin, T., Pollet, N. & Viguier, F. (2014). Surveying and modeling of rock discontinuities by terrestrial laser scanning and photogrammetry; semi-automatic approaches for linear outcrop inspection. Journal of Structural Geology, 66, 102–114. https://doi.org/10.1016/j.jsg.2014.05.014

Basson, I. J., Creus, P. K., Anthonissen, C. J., Stoch, B. & Ekkerd, J. (2016). Structural analysis and implicit 3D modelling of high-grade host rocks to the Venetia kimberlite diatremes, Central Zone, Limpopo Belt, South Africa. Journal of Structural Geology, 86, 47–61. https://doi.org/10.1016/j.jsg.2016.03.002

Basson, I. J., Lourens, P., Paetzold, H.-D., Thomas, S., Brazier, R. & Molabe, P. (2017). Structural analysis and 3D modelling of major mineralizing structures at the Phalaborwa copper deposit. Ore Geology Reviews, 83, 30–42. https://doi.org/10.1016/j.oregeorev.2016.12.002

Benedicto, A., Harrison, G., Eccles, B. & Ledru, P. (2021). Advanced use of borehole acoustic televiewer (ATV) for structural interpretation of unconformity-related uranium deposits. Economic Geology, 116(6), 1435–1453. https://doi.org/10.5382/econgeo.4832

Bond, C. E. (2015). Uncertainty in structural interpretation; lessons to be learnt. Journal of Structural Geology, 74, 185–200. https://doi.org/10.1016/j.jsg.2015.03.003

Bond, C. E., Gibbs, A. D., Shipton, Z. K. & Jones, S. (2007). What do you think this is? "Conceptual uncertainty" in geoscience interpretation. GSA Today, 17(11), 4–10. https://doi.org/10.1130/GSAT01711A.1

Bond, C. E., Shipton, Z. K., Jones, R. R., Butler, R. W. H. & Gibbs, A. D. (2007). Knowledge transfer in a digital world; field data acquisition, uncertainty, visualization, and data management. Geosphere (Boulder, Colo.), 3(6), 568–576. https://doi.org/10.1130/GES00094.1

Bowden, R. A. (2004). Building confidence in geological models. Geological Prior Information: Informing Science and Engineering, 239(1), 157–173. https://doi.org/10.1144/GSL.SP.2004.239.01.11

Cawood, A. J., Bond, C. E., Howell, J. A., Butler, R. W. H., & Totake, Y. (2017). LiDAR, UAV or compass-clinometer? Accuracy, coverage and the effects on structural models. Journal of Structural Geology, 98, 67–82. https://doi.org/10.1016/j.jsg.2017.04.004

Clarke, S.M. (2004). Confidence in geological interpretation. A methodology for evaluating uncertainty in common two and three-dimensional representations of subsurface geology. British Geological Survey Internal Report, IR/04/164. 33pp

Cowan, E. J., Beatson, R. K., Ross, H. J., Fright, W. R., McLennan, T. J., Evans, T. R., Carr, J. C., Lane, R. D., Bright, D. V., Gillman, A. J., Oshust, P. A. and Titley, M. (2003). Practical implcit geological modelling. 5th International Mining Geology Conference, Bendigo, Victoria, 17 - 19 November 2003

Creus, P. K., Basson, I. J., Koegelenberg, C. K., Ekkerd, J., de Graaf, P. J. H., Bester, M. & Mokele, T. (2019). 3D fabric analysis of Venetia Mine, South Africa; using structural measurements and implicitly-modelled surfaces for improved pit slope design and risk management. Journal of African Earth Sciences (1994), 155, 137–150. https://doi.org/10.1016/j.jafrearsci.2019.04.009

Creus, P. K., Basson, I. J., Stoch, B., Mogorosi, O., Gabanakgosi, K., Ramsden, F. & Gaegopolwe, P. (2018). Structural analysis and implicit 3D modelling of Jwaneng Mine; insights into deformation of the Transvaal Supergroup in SE Botswana. Journal of African Earth Sciences (1994), 137, 9–21. https://doi.org/10.1016/j.jafrearsci.2017.09.010

Creus, P. K. Sanislav, I. V. & Dirks, P. H. G. M. (2021). Application of SfM-MVS for mining geology: Capture set-up and automated processing using the Dugald River Zn-Pb-Ag mine as a case study. Engineering Geology, 293, 106314–. https://doi.org/10.1016/j.enggeo.2021.106314

Funtowicz, S. O. & Ravetz, J. R. (1990). Uncertainty and Quality in Sciencefor Policy. Kluwer Academic Publishers, Dordrecht

Garcia-Luna, R., Senent, S., Jurado-Pina, R. & Perez-Jimenez, R. (2019). Structure from motion photogrammetry to characterize underground rock masses; experiences from two real tunnels. Tunnelling and Underground Space Technology, 83, 262–273. https://doi.org/10.1016/j.tust.2018.09.026

Grose, L., Ailleres, L., Laurent, G., & Jessell, M. (2021). LoopStructural 1.0: time-aware geological modelling. Geoscientific Model Development, 14(6), 3915–3937. https://doi.org/10.5194/gmd-14-3915-2021

Harraden, C. L., Cracknell, M. J., James, L., Berry, R. F., Carey, R. & Harris, A. C. (2019). Automated core logging technology for geotechnical assessment; a study on core from the Cadia East porphyry deposit. Economic Geology, 114(8), 1495–1511. https://doi.org/10.5382/econgeo.4649

Harris, P. (2015). Dugald River case study – the importance of understanding your orebody and designing your mine for maximum value. In: Polvin, Y. (Ed.), Underground 193rrang methods. Australian Centre for Geomechanics, Perth. 21 – 36. Doi:10.36487/ACG_rep/1511_0.2_Harris

Harris, C. R., Millman, K. J., van der Walt, S. J., Gommers, R., Virtanen, P., Cournapeau, D., Wieser, E., Taylor, J., Berg, S., Smith, N. J., Kern, R., Picus, M., Hoyer, S., van Kerkwijk, M. H., Brett, M., Haldane, A., Del Río, J. F., Wiebe, M., Peterson, P., … Oliphant, T. E. (2020). Array programming with NumPy. Nature (London), 585(7825), 357–362. https://doi.org/10.1038/s41586-020-2649-2

Jones, R. R., McCaffrey, K. J. W., Wilson, R. W., & Holdsworth, R. E. (2004). Digital field data acquisition; towards increased quantification of uncertainty during geological mapping. Geological Prior Information: Informing Science and Engineering, 239(1), 43–56. https://doi.org/10.1144/GSL.SP.2004.239.01.04

Kirsch, M., Lorenz, S., Zimmermann, R., Tusa, L., Moeckel, R., Hoedl, P., Booysen, R., Khodadadzadeh, M. & Gloaguen, R. (2018). Integration of terrestrial and drone-borne hyperspectral and photogrammetric sensing methods for exploration mapping and mining monitoring. Remote Sensing (Basel, Switzerland), 10(9), 1366–. https://doi.org/10.3390/rs10091366

Kong, D., Wu, F. & Saroglou, C. (2020). Automatic identification and characterization of discontinuities in rock masses from 3D point clouds. Engineering Geology, 265, 105442–. https://doi.org/10.1016/j.enggeo.2019.105442

Lark, R. M., Mathers, S. J., Thorpe, S., Arkley, S. L. B., Morgan, D. J., & Lawrence, D. J. D. (2013). A statistical assessment of the uncertainty in a 3-D geological framework model. Proceedings of the Geologists' Association, 124(6), 946–958. https://doi.org/10.1016/j.pgeola.2013.01.005

Laurent, G., Ailleres, L., Grose, L., Caumon, G., Jessell, M., & Armit, R. (2016). Implicit modeling of folds and overprinting deformation. Earth and Planetary Science Letters, 456, 26–38. https://doi.org/10.1016/j.epsl.2016.09.040

Lindsay, M. D., Ailleres, L., Jessell, M. W., de Kemp, E. A., & Betts, P. G. (2012). Locating and quantifying geological uncertainty in three-dimensional models; analysis of the Gippsland Basin, southeastern Australia. Tectonophysics, 546-547, 10–27. https://doi.org/10.1016/j.tecto.2012.04.007

McKinney, W. (2010) Data structures for statistical computing in python. Proceedings of the 9th Python in Science Conference, Volume 445

McManus, S., Rahman, A., Coombes, J., & Horta, A. (2021). Uncertainty assessment of spatial domain models in early stage mining projects; a review. Ore Geology Reviews, 133, 104098–. https://doi.org/10.1016/j.oregeorev.2021.104098

Moitzi, M. (2022). ezdxf. URL https://ezdxf.mozman.at/docs/setup.html (accessed 20.09.2022)

Pakyuz-Charrier, Giraud, J., Ogarko, V., Lindsay, M., and Jessell, M. (2018). Drillhole uncertainty propagation for three-dimensional geological modeling using Monte Carlo. Tectonophysics, 747-748, 16–39. https://doi.org/10.1016/j.tecto.2018.09.005

Randle, C.H., Bond, C.E., Lark, R.M., and Monaghan, A.A. (2018). Can uncertainty in geological cross-section interpretations be quantified and predicted? Geosphere, v. 14, no. 3, p. 1087– 1100, doi:10.1130/GES01510.1.

Randle, C.H., Bond, C.E., Lark, R.M., and Monaghan, A.A. (2019). Uncertainty in geological interpretations: Effectiveness of expert elicitations. Geosphere, v. 15, no. 1, p. 108–118, https://doi.org/10.1130/GES01586.1

Riquelme, A. J., Abellan, A., Tomas, R. & Jaboyedoff, M. (2014). A new approach for semi-automatic rock mass joints recognition from 3D point clouds. Computers & Geosciences, 68, 38–52. https://doi.org/10.1016/j.cageo.2014.03.014

Savage, N., Nicholas, L., Wilson, A. & Seery, J. (2013). Visual communication of geological confidence - A move toward a less subjective approach. Iron Ore Conference, 12 - 14 August 2013. Perth, Western Australia.

Spelbrink, L. & George, K-L. (2017). Dugald River Orebody Knowledge Study (DROKS). Unpublished internal MMG report.

Thiele, S. T., Grose, L., Cui, T., Cruden, A. R. & Micklethwaite, S. (2019). Extraction of high-resolution structural orientations from digital data; a Bayesian approach. Journal of Structural Geology, 122, 106–115. https://doi.org/10.1016/j.jsg.2019.03.001

Van Asselt, M. B. A. & Rotmans, J. (2002). Uncertainty in integrated assessment modelling: From positivism to pluralism. Climatic Change, 54(1-2), 75–105. https://doi.org/10.1023/A:1015783803445

Virtanen, P., Gommers, R., Oliphant, T. E., Haberland, M., Reddy, T., Cournapeau, D., Burovski, E., Peterson, P., Weckesser, W., Bright, J., van der Walt, S. J., Brett, M., Wilson, J., Millman, K. J., Mayorov, N., Nelson, A. R. J., Jones, E., Kern, R., Larson, E., … van Mulbregt, P. (2020). SciPy 1.0: fundamental algorithms for scientific computing in Python. Nature Methods, 17(3), 261–272. https://doi.org/10.1038/s41592-019-0686-2

Vollgger, S. A. & Cruden, A. R. (2016). Mapping folds and fractures in basement and cover rocks using UAV photogrammetry, Cape Liptrap and Cape Paterson, Victoria, Australia. Journal of Structural Geology, 85, 168–187. https://doi.org/10.1016/j.jsg.2016.02.012

Walker, W. E., Harremoës, P., Rotmans, J., van der Sluijs, J. P., van Asselt, M. B. A., Janssen, P. & Krayer von Krauss, M. P. (2003). Defining uncertainty: A conceptual basis for uncertainty management in model-based decision support. Integrated Assessmentm. 1389-5176/03/0000-000$16.00

Whaanga, A., Vigor-Brown, W., Nowland, S. (2019). The implementation of photogrammetry and automated data analysis functions at the Waihi Underground Gold Mine. AusIMM Mining Geology 2019. 1–13.

Witter, J. B., Trainor-Guitton, W. J., & Siler, D. L. (2019). Uncertainty and risk evaluation during the exploration stage of geothermal development; a review. Geothermics, 78, 233–242. https://doi.org/10.1016/j.geothermics.2018.12.011

Chapter 6

Conclusion

Creus, P.K., Sanislav, I.V., Dirks, P.H.G.M.

The primary research question for this thesis is to present the 3D structural geometry of the Dugald River Shear Zone and provide a paragenesis of its associated high-grade Zn-Pb-Ag ore body. The core chapters (Chapters 2 and 3) approach the research question from different perspectives and in this concluding chapter, we summarise the interpretations in chronological order. Chapter 2 details the structural paragenesis of the Dugald River deposit and we present a new genetic model for Mount Isa Inlier Zn-Pb mineralisation during the Isan Orogeny, which we term the Dugald River style Zn-Pb mineralisation. Chapter 3 focuses on the fourth deformational event, D_4, which we suggest was responsible for high grade Zn mineralisation during which dilational sites were created within the evolving Riedel shear zone, namely, the Dugald River Shear Zone.

While Chapters 2 and 3 are the core chapters of this thesis, the final data chapters (Chapters 4 and 5) are nonetheless significant. Virtual outcrops are becoming an invaluable resource as part of data interpretation and smart/automated mining is a common theme in conferences. At the time of publishing Chapter 4, we could not find any formal research into automated processing of SfM-MVS in underground mining or civil engineering. Subsequent to publishing Chapter 4, we have made advances in downstream applications of the 3D reconstructions generated from the SfM-MVS processing to automatically characterise ore and waste in the development faces as presented by Creus et al. (2021). Similarly, the python scripts in Chapter 5 represent unique ideas to overcome geological data visualisation and present difficulties that occur across most mines that exploit complex ore bodies. Furthermore, the concepts presented in Chapters 4 and 5 provide opportunities for future development with machine learning algorithms.

6.1. The Dugald River-type Zn-Pb Mineralisation

The host rocks of the Dugald River deposit record several, successive deformation events during the Isan Orogeny. We propose five deformation events with D_2 to D_4 creating favourable extensional sites for mineralisation (Chapter 2), with high grade Zn mineralisation associated with Riedel shearing during D_4 (Chapters 2 and 3). Two phases of mineralisation are suggested with the first phase, Phase 1, occurring during D_2 and the second phase, Phase 2, during D_4. While Phase 1 is a distinct mineralisation phase, we infer that the wallrock to sulphide ratio was high, thereby making this phase sub-economic, while, Phase 2 resulted in significant enrichment of Zn mineralisation.

Phase 1 mineralisation occurred during D_2 when E-W directed sub-horizontal shortening resulted in peak metamorphism and the sub-vertical, N-S trending regional ductile fabric within the Mount Isa Inlier. We suggest that various secondary space accommodating mechanisms, resulting from progressive fold tightening, developed quartz-carbonate veins, boudins and separation of fold hinges (saddle reefs) that were coevally replaced by sulphides that were transported within metamorphic/hydrothermal fluid. Fold tightening during D_2 records a strain gradient that firstly resulted in coalescing of sulphide replaced quartz-carbonate veins with boudin necks and saddle reefs as the veins were rotated into parallelism with the pervasively developed steep S_2. Secondly, tight to isoclinal folds with associated coalesced sulphide veins resembled a crackle breccia, which created a heterogenous rock mass that during D_3 sub-vertical orogenic collapse preferentially developed zones of intensified, low to moderate SW-dipping S_3.

The second phase of mineralisation, Phase 2, occurred during D_4 and the waning stages of the Isan Orogeny, which was marked by the transition from ductile to brittle-ductile deformation. Mineralisation during D_4 is marked by progressive deformation as finite strain shifted from coaxial to non-coaxial deformation. The coaxial history is recorded by the development of a transposed fabric and planar ore dominant in the steeper parts of the shear zone such as the North Mine and towards the surface in the South Mine. Whereas the non-coaxial history is recorded by the development of breccia ore dominant in the flatter parts of the shear zone such as the South Mine.

During early D_4, the continuation of sub-horizontal shortening resulted in the reactivation of zones of intensified S_3 as low-angle thrust arrays that recorded top-to-the-NE sense of shear. Opposing shear along the stacked thrusts created areas of extension and compression, which promoted the remobilisation of sulphides from areas of high mean rock stress (contractional zones) to low mean rock stress (dilatant zones) and combined with synthetic shear along steeper, W-dipping S_0 and S_2 resulted in zones of concentrated sulphides.

Transposition in the northern part of the deposit and towards the surface preserves the coaxial deformation history during D_4 and developed high and low strain domains. The high strain domains are discernible by the development of S_4 that transposed earlier fabric with rootless F_2 often observed. D_2 and D_4 are co-planar, which makes differentiating S_4 and S_2 difficult outside of outcrop scale low strain domains where F_2 are preserved as well as axial planar S_2. Increasing D_4 strain further tightened F_2 with the areas where tight to isoclinal folds developed during D_2, producing a transposition fabric with subsequent high strain zone widening as D_4 progressed and is marked by a low wall rock to sulphide ratio producing the planar ore texture.

The shift from coaxial to non-coaxial deformation is associated with the transition from ductile to brittle-ductile deformation, which we infer resulted in P-T conditions under which the sulphides could continue to deform through ductile mechanism versus the siliciclastic host rock that deformed through brittle mechanisms. This effect is pronounced in the South Mine where the thickened sulphide horizon created by the opposing shear along low-angle thrusts, synthetic slip along steep, W-dipping S_0 and S_2 and the planar ore texture developed through transposition, resulted in an interface with a pronounced competency contrast to the host rock. At this interface fractures developed in slate that were infilled by sulphides with clasts developing where fractures enveloped the slate which was subsequently incorporated into the sulphide horizon and through a process of kneading, milling and rotation, the clasts were rounded.

The thick ductile deforming sulphide horizon could accommodate strain at a rate that was faster than the enveloping slate, which resulted in the development of en-echelon Riedel shears. The first Riedel shears to develop were R-shears with R'-shears developed within overlap zones of R-shears as displacement progressed. With increasing strain, P-shears developed and as the shear segments grew, they interconnected with R-shears to develop thoroughgoing Y-shears, eventually forming an anastomosing shear zone. Notably, the various geometric arrangements of Riedel shear fractures provided additional planes along which opposing shear provided widespread development of contractional and extensional sites, further promoting mechanical remobilisation of sulphides.

We suggest that the thoroughgoing Y-shears, in particular, the principal displacement zone were important for transporting sulphides from depth. The flexure in the South Mine was at a favourable geometry (*viz*. ~45°) to create a dilational zone within the shear zone further promoting the thickening of the sulphide horizon.

In summary, the proposed Dugald River-type, shear zone hosted Zn-Pb mineralisation model represents a unique style of mineralisation in the Mount Isa Inlier. Exploration for this style of mineralisation should be focused in areas of the Mount Isa Inlier that have been subjected to intense deformation and moderate to high grade metamorphism. In other words, the Eastern Fold Belt, opens a new prospective area of the Mount Isa Inlier as previous models and exploration for Zn-Pb mineralisation has been focused in the Western Fold Belt where lower metamorphic, SEDEX and reworked SEDEX deposits are targeted.

6.2. 3D Geometry of the Dugald River Shear Zone

A high-resolution 3D model was constructed of the Dugald River Shear Zone to understand the 3D architecture of the shear zone and ore body and the impact the shear zone has on the quality of the rock mass enveloping the stopes. In this section, we summarise the findings of the 3D model.

There is an apparent 3D distribution of the ore textures within the Dugald River deposit. Towards the north and surface of the deposit where the shear zone is steeper, the dominant ore texture is planar ore. Whereas in the flatter parts of the shear zone, the dominant ore texture is breccia ore. We suggest that this is due to the South Mine having an important structural control on mineralisation development that is lacking in other parts of the deposit, namely, the low-angle thrust arrays. Furthermore, the steep fabric is not conducive to dilational jog development.

Structural analysis of D_4-related shears provides several important values that assist in 3D modelling and exploration vectoring. The eigenvalue, e1, can be used to determine a recommended slice angle when modelling a Riedel shear network, which for the Dugald River Shear Zone is 081°/23°. In Chapter 3, we highlight the importance of using an appropriate slice angle, which provides a view angle that assists in linking data points when modelling the shears. The eigenvalue, e3, provides an exploration vector as it is sub-parallel to the bulk shear direction and releasing bends may develop along that trend, which for the Dugald River Shear Zone is 40°-192°.

In Chapter 3 we suggest that the Dugald River Shear Zone developed as an evolved Riedel shear zone with numerous Y-shears developing as well as a principal displacement zone (PDZ). The PDZ was an important structural control on the distribution of high-grade Zn lenses as releasing and restraining bends within the PDZ promoted sulphide remobilisation. Furthermore, because the PDZ is a thoroughgoing structure, we suggest that Zn-rich sulphides from depth were transported within the permeable shear zone and deposited within the flatter part of the shear zone, *viz.*, the South Mine (area of comparatively lower mean rock stress).

Riedel shear networks develop fracture surfaces in distinctive geometric arrangements as displacement progresses. The geometry and development of the shears relative to the underground infrastructure have an impact on rock mass stability. For instance, R'-shears develop within overlap zones between R-shears and are SE-dipping, which with the N-trending orientation of R- and Y-shears as well as the design of underground development means that the R'-shears are susceptible to creating wedges which may cause fall of ground with development drives, or impact the stability of hangingwalls to stopes. The terminations of R- and P-shears to form the Y-shears are initially sharp, which as displacement continues, abrades the rock mass as a Y-shear erodes to an orientation that parallels the bulk shear direction. Within these zones of abraded rock, the rock mass quality will be poor as these zones contain cataclastic and fault breccia as well as small-scale shears and faults. The findings in this thesis for Dugald River are that these zones of lower rock mass quality occur within a similar trend as the e3 eigenvalue, *viz.*, 40°-192°.

The final deformation event, D_5, has significant bearing on the rock strength quality of the shear zone as the shears underwent brittle reactivation to produce incohesive fault breccia and cataclasite. The first event, D_1, has negligible influence on the mineralisation and shear zone development and is not discussed further in the concluding chapter.

6.3. Reference

Creus, P. K. Sanislav, I. V. & Dirks, P. H. G. M. (2021). Automated processing of SfM-MVS in underground mining geology using Agisoft Metashape. 4th Virtual Geoscience Conference (VGC 2021).

Appendix A

Drill Core and Hand Sample Location and Descriptions

PhD Sample ID	Thin Section ID	Polished	Drillhole	Orientation (True North)	Puck ID	LA-ICP-MS	Sample Level	Sample Number	Comments
DRCS_01	DRCS_01	Yes	DU2579_7.7					DU2579_01	Oblique to S0. Wispy S3 cleavage at high angle to S0/S2.
DRCS_02	DRCS_02	Yes	DU2579_15.98					DU2579_02	Foliation that appears to have crenulation folds.
DRCS_03	DRCS_03	Yes	DU2579_23.61					DU2579_04	High strain zone that has flattened porphyroblasts into almost a mylonitic fabric.
DRCS_04	DRCS_04	Yes	DU2579_42.5					DU2579_05	Stringer ore texture. The bands (1.5cm) are sphalerite+pyrite+pyrrhotite. The bands are parallel to aligned porphyroblasts, suggesting that the porphyroblasts and bands represent a transposed fabric. The slate clasts (or bands) in this zone are fractured and are infilled by pyrite or (later pyrite?). The fractures seem to only contain one type of sulphide. Fractures are normal to bands.
DRCS_05	DRCS_05	Yes	DU2579_74.7					DU2579_08	Foliation boudinage. Flattened pyrite minerals appear to bend toward the boudin neck. Absent of any rheological contrast, thus S2 foliation boudinage.
DRCS_06	DRCS_06	Yes	DU2579_149.77					DU2579_09	Boudinage in DLSS. Looks like shearband boudinage. Shears (Sb) are graphitic and easily break. Boudins retain folding as shown by folding of carbonate veins in boudin (a). The folds have axial planar cleavage, parallel to wispy carbonate outside (b) of shearband area (boudin)
DRCS_07	DRCS_07	Yes	DU2533_23.9					DU2533_02	S0/S2 parallel carbonate veins that have large sub-rounded black spots (0.5cm scale). The spots are replaced by sulphides
DRCS_08	DRCS_08	Yes	DU2533_31.1					DU2533_03	Small-scale folding that appears to have an axial planar cleavage. Breccia clasts shows considerable strain in the form of high strain domains, which includes deflection of slate and carbonate bands. More pyrite here than usual. Does the sulphide concentration affect the degree of brecciation and strain in the rock? More pyrite, larger clasts, more sphalerite smaller clasts?
DRCS_09	DRCS_09	Yes	DU2639_112.04					DU2639_03	Large porphyroblasts with carbonate trails that define S2. Thick carbonate vein that has pyrite along the vein wall, but in localised zones.
DRCS_10	DRCS_10	Yes	DU2639_311			Yes		DU2639_06	LA-ICP-MS data is available on request. Breccia ore taken for sample. Has late-stage veins. Different colours, but not sure why (iron-rich sphalerite?).
DRCS_11	DRCS_11	Yes	DU2639_318.70					DU2639_07	Sheared slate ore.
DRCS_12	DRCS_12	No	DU0789_46.85					DU0789_02	Flattend light bands with enveloping green bands.

DRCS_13	DRCS_13	No	DU2638_275.95					DU2638_02	Fold, includes pyrrhotite infill in a vein. Disharmonic fold and a hook fold. Looks like the carbonaceous infilled some high strain zones in this folded area. Or the folds are due to strain increase in the 10cm zone.
DRCS_14	DRCS_14	Yes	DU2557_125			Yes		DU2557_05	LA-ICP-MS data is available on request. Layered sulphides. Sphalerite within pyrrhotite intercalations
DRCS_15	DRCS_15	No	DU0789_249					DU0789_07	Stockwork breccia in high strain zone. Disseminated sulphides parallel to S2. Partial replacement of carbonate by sulphides.
DRCS_16	DRCS_16	No	DU1606_4.8					DU1606_01	Limestone with wispy S3 carbonate fracture cleavage. Low-angle to bedding
DRCS_17	DRCS_17	No	DU0789_32.63					DU0789_01	Foliation in Calc-silicate. Mild metamorphism of calc-silicate. Defined by darker bands and lighter bands that tend to be altered.
DRCS_18	DRCS_18	No	DU2557_125					DU2557_08	Stringer/slatey breccia type ore. Flattened slate clasts with small sphalerite infilled fractures in clasts. Enveloped by thicker sulphide stringers. Fractures in clasts have two prominent directions. Orthogonal and parallel to the long axis
DRCS_19	DRCS_19	No	DU0789_247.62					DU0789_06	Small-scale version of the sample picked from S265 (folded clasts in DLCB). Discordant mineralisation.
DRCS_20	DRCS_20	No	DU2557_94.32		2	No		DU2557_07	Composite bedding and S2 in BSUN. Small-scale folding
DRCS_21	DRCS_21	Yes	DU1606_29			Yes		DU1606_03	Folded slate clasts with thick sulphide stringers. Slate clasts have carbonate infilled micro-fractures. Some appear to be replaced
DRCS_22	DRCS_22	Yes	DU0789_249			Yes		DU0789_08	Stockwork breccia in high strain zone. Disseminated sulphides parallel to S2. Partial replacement of carbonate by sulphides.
DRCS_23			DU2579_42.34		7	Yes		DU2579_06	Stringer ore with S0/S2 parallel bands. Slate bands/clasts are folded as well as the carbonate veins. Extension fractures in the slate are infilled by (remobilised?) sphalerite and pyrite.
DRCS_24			DU0509_71.6		10	Yes		DU0509_01	Banded ore. Coarse-grained pyrite with finer-grained sphalerite and possibly galena. Fine sphalrite veinlets. Dark siltstone(?) clasts.
DRHS_01	DRHS_01	Yes		(a)121/41; (b)250/65; c)010/64			N200_OD489_N	PC2019_05	3 planes interact to create a blocky fracture pattern. The SE dipping planes daylight into the development. Crenulation developed on plane b
DRHS_02	DRHS_02	Yes		358/46			S390_XC395	PC2019_08	Sample of slate in a fold between two major shear zones. Crenulation oblique to S0 plane (358/46)?
DRHS_03	DRHS_03	Yes				Yes	Unknown	PC2019_13	LA-ICP-MS data is available on request. High-grade DLMB. Possible fabric
DRHS_04	DRHS_04	Yes		034/68			S340_OD398_N1	PC2019_09	Sample of S0/S2

DRHS_05	DRHS_05	Yes				Yes	S290_DHS437	PC2019_11	LA-ICP-MS data is available on request. High-grade massive breccia. Possible fabric.
DRHS_06	DRHS_06	No		085/84			S125_OD414_N1	PC2020_01	Sampled near Test 2 of the photogrammetry testing area
DRHS_07	DRHS_07	No		085/84			S125_OD414_N1	PC2020_02	Sampled near Test 2 of the photogrammetry testing area
DRHS_08					8	Yes	South Mine	PC2020_03	Picked off ground
DRHS_09					9	No	S415_XC411	PC2020_04	Between N1 and N3
DRHS_10					1	No	S390_OD395_N3	PC2020_05	S/C slate with sphalerite
DRHS_11					5	Yes	S290_OD425_S2	PC2019_14	Pb breccia
DRHS_12					3 and 4	Yes	South Mine	PC2020_06	Sheared pyrrhotite. Location unknown, but it is South Mine
DRHS_13					6 and 11	Yes	S415_XC423	PC2019_01	LA-ICP-MS data available on request
DRHS_13					12 and 13	Yes	S465_XC423_W	PC2020_07	Small scale folded pyrite
DRHS_14					14 and 15	Yes	South Mine	PC2020_08	Small scale folded pyrite

Appendix B

Python Scripts

data_confidence.py

```
import numpy as np
import pandas as pd
from scipy.spatial import cKDTree
from datetime import date



#########################################################################################################################
#Change values to define the boundary and the spacing of the grid points
##np.arange(min, max, spacing)
spacing = 20
grid_points = {'x_array' : np.float32(np.arange(10233, 10927, spacing).T),\
               'y_array' : np.float32(np.arange(13836, 15228, spacing).T),\
                'z_array' : np.float32(np.arange(9500, 10200, spacing).T)}


#File path to project setup table
##Must be in the example format
project_setup_path = 'C:/Users/piete/OneDrive/Desktop/Data Confidence/Final Data/data_confidence_project_list.xlsx'


#Query percentage for a "Yes" assignment in additional queries
query_percentage = 0.3


#Cut-off for high and moderate
cut_off = 3
#########################################################################################################################
#Create Grid from X,Y,Z and combine to single Dataframe
xv, yv, zv = np.meshgrid(grid_points['x_array'], grid_points['y_array'], grid_points['z_array'], indexing='xy')


grid = pd.DataFrame()


grid['grid_X'] = np.ravel(xv)
grid['grid_Y'] = np.ravel(yv)
```

```
grid['grid_Z'] = np.ravel(zv)

del xv, yv, zv

#Path to project setup spreadsheet
project_setup_table = pd.read_excel(project_setup_path)

#Extract data table names from project setup table
data_name_list = project_setup_table['Path'].tolist()

#Create empty DataFrame to append data tables to
concat_df = pd.DataFrame(columns = ['X', 'Y', 'Z', 'Dip', 'Dip_Direction', 'Structure', 'Data_Source', 'Data_Quality', 'Photos', 'Table_Name'])

#Iterate through project setup table and append tables to concat_df
##Adds tables to an interim DataFrame that is replaced each iteration
for project_idx, project_row in project_setup_table.iterrows():

    #Checks file format and imports using appropriate function
    if project_row['Path'].endswith('.csv'):

        interim_data = pd.read_csv(project_row['Path'])

    elif project_row['Path'].endswith('.xlsx'):

        interim_data = pd.read_excel(project_row['Path'])

    #Test for tables that are missing columns and populates the created with 'nan'
    for count, column_name in enumerate(list(project_row.values)):

        if str(column_name) == 'nan':

            interim_data[project_row.index[count]] = 'nan'
```

```
    #Ensures the interim DataFrames will have consistent headers
    column_names = {project_row['X'] : 'X', project_row['Y'] : 'Y', project_row['Z'] : 'Z',\
                                    project_row['Dip'] : 'Dip', project_row['Dip_Direction'] : 'Dip_Direction',\
                                      project_row['Structure'] : 'Structure', project_row['Structure_Filter'] : 'Structure_Filter',\
                                        project_row['Data_Source'] : 'Data_Source', project_row['Data_Quality'] : 'Data_Quality',\
                                          project_row['Photos'] : 'Photos'}

    interim_data = interim_data.rename(columns = column_names).copy()

    interim_data['Table_Name'] = project_row['Path'].rsplit('\\',1)[1].rsplit('.',1)[0]

    #Drops structure features that are not necessary
    if str(project_row['Structure_Filter']) != 'nan':

        structure_filter = project_row['Structure_Filter'].split(';')
        interim_data = interim_data[interim_data['Structure'].isin(structure_filter)]

    #Concat the interim_data to the expanding concat_df
    concat_df = pd.concat([concat_df, interim_data[['X', 'Y', 'Z', 'Dip', 'Dip_Direction', 'Structure', 'Data_Source', 'Data_Quality', 'Photos',
'Table_Name']]])

del interim_data

#Resets the index of the complete concat_df
concat_df = concat_df.reset_index(drop = True)

#Query of data source and data quality to populate a column with data confidence
concat_df['Data_Confidence'] = np.where(((concat_df['Data_Source'] == 'High') & (concat_df['Data_Quality'] == 'High')), 'High',\
                                (np.where((concat_df['Data_Source'] == 'High') & (concat_df['Data_Quality'] == 'Moderate'), 'Moderate',\
                                 (np.where((concat_df['Data_Source'] == 'Moderate') & (concat_df['Data_Quality'] == 'High'), 'Moderate',\
                                   (np.where((concat_df['Data_Quality'] == 'Moderate') & (concat_df['Data_Quality'] == 'Moderate'), 'Moderate',
'Low')))))))

#Combines the data confidence and phots values for each row
```

```
##Used in populating the data confidence distribution

concat_df['Header_Concat'] = concat_df['Data_Confidence']+'__'+concat_df['Photos']


#Nearest neighbour search within each grid points space

##Returns the indices of the relevant data points

##p refers to the Minkowski p-norm with p = np.inf the maximum coordinate difference (i.e., Chebychev distance)

tree = cKDTree(np.array([concat_df['X'], concat_df['Y'], concat_df['Z']]).T)

nn_ii = tree.query_ball_point(grid, r = spacing / 2, p = np.inf)


#Add the indices to the grid DataFrame

grid['nn_ii'] = nn_ii


del tree, nn_ii


#Dicitonaries for adding query data to

grid_result_dict = {}

grid_density_dict = {}

grid_photos_dict = {}

grid_orientation_dict = {}

grid_sources_dict = {}


#Drops grid points that have empty lists

grid = grid[grid.astype(str)['nn_ii'] != '[]']


#Iterates through the grid points populating the dictionaries with results

##Fail conditions coded in case of anomalies

for grid_idx, grid_row in grid.iterrows():


    data_df = concat_df.loc[grid_row['nn_ii']]


    count_unique = data_df['Header_Concat'].value_counts()


###############################################################################
```

```
#Query for data confidence distribution

##Add/move elif conditions as required

if 'High__Yes' in list(count_unique.index):

    if count_unique['High__Yes'] >= cut_off:

        grid_result_dict[grid_idx] = 'High'

    elif (count_unique['High__Yes'] < cut_off) & (count_unique['High__Yes'] > 0):

        grid_result_dict[grid_idx] = 'Moderate'

    else:

        grid_result_dict[grid_idx] = 'Fail'

elif ('High__No' in list(count_unique.index)) & (len(count_unique) == 1):

    grid_result_dict[grid_idx] = 'Low'

elif 'Moderate__Yes' in list(count_unique.index):

    if count_unique['Moderate__Yes'] >= cut_off:

        grid_result_dict[grid_idx] = 'Moderate'

    elif (count_unique['Moderate__Yes'] < cut_off) & (count_unique['Moderate__Yes'] == 1):

        grid_result_dict[grid_idx] = 'Low'

    elif (count_unique['Moderate__Yes'] < cut_off) & (count_unique['Moderate__Yes'] > 0):

        grid_result_dict[grid_idx] = 'Moderate'
```

```
        else:

            grid_result_dict[grid_idx] = 'Fail'

    elif 'Moderate__No' in list(count_unique.index):

        grid_result_dict[grid_idx] = 'Low'



    elif ('Low__No' in list(count_unique.index)) |  ('Low__Yes' in list(count_unique.index)):

        grid_result_dict[grid_idx] = 'Low'

    else:

        grid_result_dict[grid_idx] = 'Fail'
################################################################################
    #Additonal columns for communication of data
    ##Data density
    grid_density_dict[grid_idx] = sum(count_unique)

    #Orientation data
    ##Yes if >= query_percentage
    if any(data_df['Dip'] != 'nan') & any(data_df['Dip_Direction'] != 'nan'):

        if (len(data_df[data_df['Dip'] != 'nan']) / len(data_df)) >= query_percentage:

            grid_orientation_dict[grid_idx] = 'Yes'

        else:

            grid_orientation_dict[grid_idx] = 'No'
```

```
    else:

        grid_orientation_dict[grid_idx] = 'No'

    #Photos
    ##Yes if >= query_percentage
    if 'Yes' in list(data_df['Photos']):

        if (len(data_df[data_df['Photos'] == 'Yes']) / len(data_df)) >= query_percentage:

            grid_photos_dict[grid_idx] = 'Yes'

        else:

            grid_photos_dict[grid_idx] = 'No'

    else:

        grid_photos_dict[grid_idx] = 'No'

    #Number of sources
    grid_sources_dict[grid_idx] = len(data_df['Table_Name'].value_counts())
################################################################################
#Add dictionaries as columns to grid DataFrame
grid['Confidence_Distribution'], grid['Density'], grid['Photos'], grid['Orientation'], grid['Sources'] = grid_result_dict.values(),
grid_density_dict.values(),\
    grid_photos_dict.values(), grid_orientation_dict.values(), grid_sources_dict.values()

del grid['nn_ii']

grid.to_csv('C:/Users/piete/OneDrive/Desktop/Data Confidence/confidence_test.csv', index = False)
```

```
#Export grid of points to the same folder as the project setup folder

##Saves file with the current date on the machine

grid.to_csv(str(project_setup_path.rsplit('/', 1)[0])+'/'+'data_confidence_'+str(date.today())+'.csv', index = False)
```

tri_ori.py

```
import numpy as np

import pandas as pd

import ezdxf

import scipy.spatial as sps

import os

import time



#Function used in script

##Triangle centroids of wireframes

def triangle_orientation(dxf):


    msp = dxf.modelspace()

    faces = msp.query()


    tri_cen = list()

    normal_list = list()


    for i in faces:


        centroid = (i.dxf.vtx0 + i.dxf.vtx1 + i.dxf.vtx2) / 3


        tri_cen.append(np.array(centroid))


        u = i.dxf.vtx1 - i.dxf.vtx0

        v = i.dxf.vtx1 - i.dxf.vtx2


        n = np.cross(u,v) / np.linalg.norm(np.cross(u,v))


        normal_list.append(np.array(n))
```

```
    df1 = pd.DataFrame(tri_cen, columns = ['X', 'Y', 'Z'])

    df2 = pd.DataFrame(normal_list, columns = ['nx', 'ny', 'nz'])


    output_df = pd.concat([df1, df2], axis = 1)


    return output_df


#Import parameters and data

##Path to project set-up spreadsheet

###Shift+right click xlsx file. Select copy as path

project_setup_path = str(input("Please paste project path: ")).replace('"', '')


project_setup_table = pd.read_excel(project_setup_path) #xlsx format


for project_index, project_parameters in project_setup_table.iterrows():


    start = time.time()


    dxf_df = triangle_orientation(ezdxf.readfile(project_parameters['wireframe']))


    end = time.time()


    total = (end - start)


    ##Column names based on the entries in the project setup table

    ##Remove nan values to avoid errors

    col_list = [project_parameters['X_coordinate'], project_parameters['Y_coordinate'], project_parameters['Z_coordinate'],\

            project_parameters['Dip'], project_parameters['Dip Direction']]

    col_list = [i for i in col_list if str(i) != 'nan']


    column_names = {project_parameters['X_coordinate'] : 'X', project_parameters['Y_coordinate'] : 'Y',
project_parameters['Z_coordinate'] : 'Z',\

                project_parameters['Dip'] : 'Dip', project_parameters['Dip Direction'] : 'Dip Direction'}
```

```
for k in list(column_names.keys()):


    if str(k) == 'nan':

        del column_names[k]



discrete_table = pd.read_excel(project_parameters['discrete structure table'], usecols = col_list)

discrete_table = discrete_table.rename(columns = column_names)

discrete_table = discrete_table[column_names.values()]


nn_tree = sps.cKDTree(np.array([discrete_table['X'], discrete_table['Y'], discrete_table['Z']]).T)


nn_dd, nn_ii = nn_tree.query(np.array([dxf_df['X'], dxf_df['Y'], dxf_df['Z']]).T, k = 1, workers = -1)


#Calculate dip and dip direction

dxf_df['nx'] = np.where(dxf_df['nz'] < 0, dxf_df['nx'] * -1, dxf_df['nx'])

dxf_df['ny'] = np.where(dxf_df['nz'] < 0, dxf_df['ny'] * -1, dxf_df['ny'])

dxf_df['nz'] = np.where(dxf_df['nz'] < 0, dxf_df['nz'] * -1, dxf_df['nz'])


dxf_df['Dip'] = np.degrees(np.arccos(dxf_df['nz'].astype(np.float64)))

dxf_df['DipDir'] = np.degrees(np.arctan2(dxf_df['nx'].astype(np.float64), dxf_df['ny'].astype(np.float64)))


dxf_df['DipDir'] = np.where(dxf_df['DipDir'] < 0, dxf_df['DipDir'] + 360, dxf_df['DipDir'])


#Add distance column to dataframe

dxf_df['distance'] = nn_dd


#Export to same folder as the wireframe. Saves as a csv

##Checks for export folder before creating a new one

###Will overwrite any existing files with the same name

wireframe_name_split = project_parameters['wireframe'].rsplit('\\', 1)
```

```
export_folder = str(wireframe_name_split[0]+'\Export')


try:
    os.makedirs(export_folder)


except:
    pass


export_path = str(export_folder+'\\'+wireframe_name_split[1].rsplit('.', 1)[0]+'_distance.csv')


dxf_df.to_csv(export_path, index = False)
```